Second Moment Modelling for the Numerical Simulation of Passive Scalar Dispersion of Air Pollutants in Urban Environments

Dissertation
zur Erlangung des akademischen Grades
DOKTOR-INGENIEUR

vorgelegt von
MSc.-Ing. Rafael Izarra
aus Venezuela

eingereicht dem
Fachbereich Maschinenbau
der Universität Siegen

Referent: Dr.-Ing. J. Franke
Korreferent: Univ.- Prof. Dr. F. Dinkelacker

Tag der mündlichen Prüfung
18. Dezember 2009

Acknowledgments

The present work was done during my scientific fellowship in the Institut für Fluid- und Thermodynamik of Universitaet Siegen (Germany) and financially supported by the German Academic Exchange Service (DAAD).

I would like to express my gratitude to my two supervisors Prof. h.c. Univ.-Prof. Dr.-Ing. habil. Wolfram Frank and Dr.-Ing. Joerg Franke. Thank you for giving me the opportunity to work as a PhD candidate in the institute and for the support and guidance received during my time there.

I would like to thank Prof. Dr.-Ing. Friderich Dinkelaker for his pertinent advice and his willingness to be a co-referent of this work. Furthermore, I thank Prof. Dr.-Ing. habil. Peter Betsch and Prof. Dr.-Ing Claus-Peter Fritzen for their assistance during my doctoral examination.

Many thanks are due to all my colleagues and friends for the useful discussions and suggestions as well as their technical and moral support during my time in Siegen. They are Dr.-Ing. Thorsten Kray, Dipl.-Ing. Thomas Gora, Dipl.-Ing. Mehdi Agami, Frau Reinhild Hoof, Dipl.-Ing Herman Geppert and others. I had a wonderful time working together with all and every one of you.

I gratefully acknowledge DAAD for honouring me with the scholarly award to pursue my PhD. Similarly, I would like to thank the team of COST Action 732 for the useful material and the technical and friendly discussions.

I am also thankful to my family, especially to my parents Rafael and Yasmin, sisters Tibisay and Tahiana, cousins, aunts and grandmothers. Their love, blessing and stimulating words encourage me to achieve the best throughout my stay in Germany.

This dissertation would not have been possible without the unconditional support of my wife Elizabeth. Therefore, I dedicated this work to her and to our daughter Victoria. Thank you for your love, constant support, patience and faith in me. Both of you represent my main source of happiness, motivation and achievements.

I wish God bless this book and every one of the persons who collaborate with its realization and receive the double of successfulness.

Rafael Izarra

Summary

Since the Industrial Revolution mankind has needed to deal with increasing air pollution problems as a result of manufacturing, mining, transportation, and power production. Air pollution concerns the interaction of gases and particles emitted into the atmosphere with the surrounding environment. This interaction can redirect pollutants toward sensitive areas, concentrate different species above acceptable levels, or even mitigate concentration levels by enhancing diffusion and dispersion. The present EU environmental legislation has been implemented to control these high pollutant concentrations and improve the air quality conditions in urban areas. The numerical simulation of dispersion has shown to be a useful tool for both the scientific description of pollution phenomena and for planning and decision making.

The numerical simulation of pollution dispersion in urban environments by means of solution of the statistically steady Reynolds Averaged Navier Stokes (RANS) equations is known to be strongly dependent on turbulence models. If pollution dispersion is modelled, the turbulence models do not only have to be used for the Reynolds stresses, but also for the turbulent scalar fluxes. While the influence of several turbulence models for Reynolds stresses on pollution dispersion in urban environments has already been examined several times, the turbulent scalar fluxes are usually modelled by the simple gradient diffusion assumption. In the present work, the influence of more advanced models for the turbulent scalar fluxes on the dispersion of pollutants is examined. Two different wind tunnel experiments, a two-dimensional (2D) street canyon and a three-dimensional (3D) urban area model, were selected for the validation of the models' performance. In total, five anisotropic algebraic flux models and two second moment models were implemented in the commercial software FLUENT 6.3. All these models together with the simple gradient diffusion model (with different turbulent Schmidt numbers) are used and the results are compared with measurements using statistical performance measures to assess their predictive capability.

All evaluated models showed good general agreement in comparison to the experiments. The anisotropic models provided better concentration predictions than the isotropic models in 2D simulations. However, these improvements were very small in 3D simulations and usually disappeared. In the end, modelling improvements based on the sensitivity analysis of model coefficients, numerical and experimental model limitations and other parameters and assumptions relevant for the simulation of passive scalar pollution dispersion are presented and discussed.

Key words: Turbulent scalar fluxes, anisotropic modelling, RANS, CFD, MUST, atmospheric dispersion, model improvement.

CONTENTS

1 Introduction

1.1 Pollution in the Environment

Historical records show that the impact of air pollutants in the environment has been observed by human beings for a very long time. In the Old Testament of the Bible, Abraham says "…behold, the smoke of the land ascended like the smoke of a furnace" (Gen 19:28). During 79 AD, the eruption of Mount Vesuvius is recorded to have asphyxiated people with volcanic fumes. In England during the reign of Edward I (1272-1307) and Edward II (1307-1327), legal penalties were sentenced after the nobility protested against the use of highly "pestilential odorous sulphurous coal" [Mero99]. In 1661 John Evelyn published *Fumifugium* one of the earliest known books on air pollution, which describes the effects of pollution in the city of London. In Europe the earliest legislation to control pollution emissions was established during the 19th century as simple local rules in big cities such as Paris, London and Berlin [Feng98]. Since then, air pollution has become widely recognized as a national and international public health risk, in part due to some large killer urban smog events. Smog emissions caused 268 deaths in London, UK in 1873, more than 1000 deaths in Glasgow, UK in 1909, and 60 deaths in Meuse Valley, Belgium in 1930. A similar recent example was in 1986 when the release of radioactivity during the Chernobyl reactor accident exposed millions of people to radio active pollution.

Pollution is defined [Camb08] as any damage caused to water, air, etc. by harmful substances or waste. Thus, air pollution deals with particulates, chemicals, or biological materials introduced into the atmosphere that cause harm or discomfort to humans or other living organisms, or damage the natural environment. In general, almost all human activities make some direct or indirect impact on the natural environment and almost all industrial processes which transform natural resources into products for man's use give rise to some pollution [Wood89]. However, air pollution sources can be either natural or man-made [US-EPA]. Air pollutants may take the form of solid particles, liquid droplets or gases and can be classified as either primary (substances directly emitted from a process) or secondary (when primary pollutants react or interact, e.g. ozone). The main factors which determine the severity of a pollutant are its chemical nature, its concentration and its persistence [Mill95]. Some pollutants are biodegradable and therefore will not persist in the environment in the long term. Air pollution emissions can also be classified for modelling purposes as buoyant plumes (plumes which are lighter than air, e.g. methane), dense gas plumes (plumes which are heavier than air, e.g. carbon dioxide) and passive or neutral plumes (plumes which are neither lighter nor heavier than air).

Pollutant emissions are produced not only during big events but also during small everyday releases as a consequence of production, transportation, handling or storage of gases, particles and chemical substances. The impacts of these pollutant emissions on the environment are usually measured by their effects on the human standard of living and the number of people affected [Feng98]. Since 1960, the world population has been doubled and due to improvements in standard of living and the world economy, the global number of pollutant sources like car emissions[1] have risen by a factor of 10. The resulting increases in air pollution have led to important impacts on human health and well-being, which may be immediate (respiratory diseases) or delayed (cancer). They also have caused material damages on economical/technical structures of cultural heritage and large scale environmental phenomena such as acidification, depletion of the ozone layer and an imminent global warming.

The most direct impacts of air pollution are felt for those who live in cities. The United Nations' 2006 report stated that already 48.7% of the world's population were living in urban areas in 2005. This development was expected to continue in the subsequent years, and some statistical estimates said that more than half of the world population would be living in urban areas by 2008. Thus, this period marks the first time in history when the world has more urban residents than rural residents.

In urban areas, the wind flow around individual and/or groups of buildings governs the local dispersion of pollution and pedestrians' comfort. Present EU environmental legislation intends to control the high pollutant concentrations and air quality conditions in urban environments. Mathematical modelling of dispersion has shown to be a useful tool for both scientific description of pollution phenomena and planning and decision making. Dispersion models can provide useful information to assist in the delineation of hazard zones (toxic corridors) resulting from contaminant releases in accidents or everyday activities.

---

[1] A European Environment Agency report from September 2008 shows that road transport remains Europe's single largest air polluter [EEA08].

Accordingly, in the next two subsections several engineering applications of pollutant dispersion modelling are summarized, emphasizing some specific geometries relevant for this work and taking into account previous experiences from these and similar applications.

1.2 The Engineering Problem

If air pollutant is a “problem”, mathematical modelling cannot claim to be the solution to this problem. However, mathematical modelling is an indispensable instrument for important air quality analysis and beside wind tunnel experiments, it is the most practical tool to predict pollution dispersion and answer many of the subsequent “what if” questions.

Historically, pollution dispersion has been studied as a part of meteorology or specifically micrometeorology. The micrometeorology, also well known as micro-scale meteorology, deals with the atmospheric flow phenomena but it is limited to the processes at the lower end of the spectrum of the atmospheric scales. It means the study of small-scale, short-lived atmospheric conditions and processes in the layer of frictional influence adjoining the earth’s surface, commonly known as the Atmospheric Boundary Layer (ABL). Important topics in micrometeorology include heat transfer and gas exchange between soils, vegetation and/or surface water with the atmosphere.

Discussion of the layers in the Earth's atmosphere is needed to understand where air pollution dispersion takes place. The main layers of the Earth's atmosphere from the surface of the ground upwards are the troposphere (0 to 15 Km), the stratosphere (15 to 50Km), the mesosphere (50 to 85Km), the thermosphere and others (more than 85Km) [Nasa-url]. The lowest part of the troposphere is the Atmospheric Boundary Layer or Planetary Boundary Layer (PBL) which extends from the Earth's surface to about 1.5 to 2.0 km in height [Stul88]. The ABL is made up of the mixing layer capped by the inversion layer and they are separated by a change in temperature behaviour in the vertical direction. Almost all of the pollutants emitted into the ambient atmosphere are transported and dispersed within the mixing layer. Some of the emissions penetrate the inversion layer and enter the free troposphere above the ABL. Many atmospheric dispersion models are referred to as boundary layer models because they mainly model air pollutant dispersion within the ABL [Wik-ADM]. The study of pollutant transport in the very low part of the ABL, i.e. inside and over urban areas, has attracted great concern during the past few decades, mainly due to increasing concentrations of pollutants and their adverse impacts on human health.

The study of pollution dispersion is normally accomplished in three main ways: field (full scale) measurements, laboratory-scale or reduced-scale experimental measurements (e.g. wind-tunnel or water-tunnel analysis) and computational modelling. Within computational modelling there are several different approaches. The most common are the Gaussian models, Lagrangian models and Eulerian models [Feng98].

- The Gaussian models are probably the oldest and most common way to estimate buoyant pollution dispersions. These models calculate a three-dimensional steady-state concentration field from a single source point by approximating the dispersion of contaminants with a Gaussian shaped curve, meaning that the pollutant distribution has a normal probability distribution. Some representative examples of this kind of models are [Sutt32], [Pasq61], [Pasq74], and [Turn94].
- The Lagrangian models calculate the air pollution dispersion by tracking the statistical trajectory of a large number of particles as they are transported within the atmospheric flow, which is typically generated by a meteorological model. The Lagrangian models use a moving frame of reference as the particles move from their initial location. Some versions of this kind of model are the Lagrangian Puff Models (e.g. [Scir96]), Lagrangian Particle Dispersion Models (e.g. [Mora96]), Lagrangian Transport-Chemistry Models (e.g. [Hov94]) and the hybrid dispersion models which are a combination of Lagrangian and Eulerian dispersion models (e.g. [Trem93]).
- The Eulerian dispersion models are similar to the Lagrangian models because they also track the movement of a large number of pollution plume particles as they move from their initial location. The most important difference between the two models is that the Eulerian model uses a fixed three-dimensional frame of reference rather than a moving frame of reference. The Eulerian models are the typical approach used in Computational Fluid Dynamics (CFD) codes and it is employed to compute transport involving fluid flow, heat transfer, mass transport and associated convective-diffusive phenomena by the use of computer based numerical methods.

The Computational Fluid Dynamics technique is a useful tool to study wind flow and pollutant dispersion. In fact, with the ever-increasing computational power, high resolution CFD models have become a common practical tool to explain the detailed processes occurring in urban environments. It is now feasible, using state-of-the-art computers, to simulate building-scale flow and dispersion in real urban settings. [Xian06].

This work is based on the idea of applying CFD codes to simulate pollution dispersion on the micrometeorology scale with the intention of overcoming some of the well known limitations of the commonly used atmospheric dispersion models. It is expected that the CFD simulations will provide additional information from their higher capability to manage more geometrical details of the flow domain in comparison to simpler non-CFD dispersion models.

1.3 State of the Art

The study of pollution dispersion in urban environments is, at present, a very active area within the scientific community. Other than the above mentioned health and political/economical reasons, one motive are continuing computer speed improvements that have made it possible to use the CFD technique in a relatively new engineering application like the simulation of contaminant dispersions in detailed urban areas. The CFD application in wind engineering, better known as Computational Wind Engineering (CWE), is a relatively new area with a short history of just over 20 years, meaning that like in the early stages of any other application area, a lot of research for models' validation and improvement is still missing. Ten to fifteen years ago, the most commonly studied geometries in this area were street canyons or flow around single blocks/buildings. However, more complicated geometries can now be easily found like the regular arrays of buildings (e.g. [Leit02],[Chua05]), street intersections (e.g.[Fran05]), the section of a real street (e.g. [Louk01],[Kast99]) and also less common, but possible to find are simulations of bigger real city areas, e.g. Oklahoma City [Urba08], New York City [Came06], [Coir06], [Coir06b], Kawasaki City [Huan06], etc.

In spite of these and many other experiences, the accurate prediction of urban flow and dispersion is currently an unresolved issue due to its inherent complexity of formulating physically sound turbulence models added to the complex wind flows from intricate arrays of structures or urban canopies with arbitrary configuration of groups of buildings and street canyons. The two most common approaches used to simulate turbulent flow in CFD are Reynolds-Averaged-Navier-Stokes (RANS) and Large Eddy Simulation (LES) [Xi06] [Hsie07]. Turbulence modelling improvement in urban areas is as well as in many other engineering application a very important and tricky part in most CFD simulations.

Street canyons are a typical pollutant dispersion case of interest in urban environments because they are regions of the largest street-level pollutant concentrations and are hence a place with high pollution exposure of people. Furthermore, the simplest building blocks of cities are street canyons and it has been the geometry of main interest in several recent pollution dispersion studies of atmospheric boundary layer wind tunnel experiments [Mero96], [Pava99], [Kast99], [Grom07]. These studies usually present street canyons with several geometrical aspects affecting the flow behaviour, like different building roof shapes, isolated or urban street canyons, the influence of obstacles/trees and others[2].

One of the first and probably most complete works on RANS numerical simulations for two-dimensional street canyons was presented by Sini et al. using the code CHENSI with the standard k-ε turbulence model [Sini96]. This work was an important contribution by presenting a parameterization of the flow field within an isolated street canyon as a function of its aspect ratio (W/H, where W is the canyon's width and H is the building's height). However, their experimental validation of results was poor. Leitl et al. performed two-dimensional (2D) and three-dimensional (3D) simulations using the Standard and RNG k-ε turbulence models, but emphasising the improvement of the wind tunnel set up and failing in providing many geometrical and computational details [Leit97]. Hassan et al. reports a series of simulations for velocities and the concentration of pollutants in a 2D isolated street canyon using the Standard k-ε turbulence model but they recognized that they did not have enough experimental measurements to compare results [Hass98]. Chang and Meroney present a 3D numerical simulation of an urban street canyon with perpendicular streets with a small domain [Chan01]. Additionally, they compare turbulence models and point out considerable changes between RNG and Standard k-ε results. Chan et al. use the commercial software FLUENT to compare the numerical simulation of an urban area street canyon with the aspect ratio of one and measurements from [Mero96], but with some geometry simplifications in source line design [Chan02]. They also compare the Standard, RNG and Realizable k-ε models for pollutant concentrations on the walls and show better agreement for the RNG model. Liu et al. report an LES study of passive scalar dispersion in a street canyon with ratio one using a 3D cubic cavity [Liu02] and compare their results with [Pava99]. They describe the formation of a primary vortex and three smaller vortices in the bottom corners of the canyon and in the top-leeward corner. They also test different locations for the pollutant inlet and declare that turbulent diffusion is the

---

[2] The works of [Mero96] and [Pava99] are the wind tunnel experimental measurements selected in this work for the comparison and evaluation of the numerical simulations.

predominant mechanism for pollutant removal from the canyon. Walton et al. present LES for an idealised urban street canyon (W/H= 1.2) [Walt02]. They report that the vortex formed within the canyon region is unsteady and that it meanders along the length of the canyon. Comparisons with the Standard k-ε model reveal that this model predicts a slightly weaker recirculation within the canyon. However, [Walt02] use a very close symmetry boundary condition at the top (=2H), which definitely influences the results. Additionally, in this work the grid resolution used was not fine enough to resolve all the turbulence features accurately. Sahm et al. present five different CFD software results to compare with a street canyon experiment [Sahm02]. They study a street canyon of W/H=2 and highlight the influence of the turbulence model as main reason for the deviation between measurements and model predictions. Nazridoust and Ahmadi present numerical simulations of three different arrays of 2D street canyons using FLUENT 6.3 [Nazr06]. In one of them, they use the urban geometry model from [Mero96]; however, they fail to contrast the measurements with the simulation results from the second street canyon where most probably a fully developed flow for the atmospheric boundary layer cannot be found. They compare the pollution predictions qualitatively using a simplified source design of the pollutants and changing its composition from ethane (in the experiments) to CO_2 (in simulations). More recently [Izar07a] present an extensive comparison of pollution dispersion predictions using several turbulence models (Standard k-ε, RNG k-ε, Realizable k-ε, Standard k-ω, SST k-ω, Spalart-Allmaras and differential Reynolds stress model) together with different computational conditions in a 2D street canyon with W/H=1. Further details of this work are given in Chapter 7.

In addition to the study of a variety of street canyon configurations and similar geometries, there are also many studies about the prediction of pollutant dispersion in bigger domains. A good example is the Mock Urban Setting Test (MUST), which belongs to the group of regular arrays of buildings and is the second case selected in the present work to evaluate the CFD model performance. The original MUST field experiment was carried out in September 2001 in a flat area located in the Great Basin desert of western Utah (USA). The experiment consists of an array of 12 by 10 shipping containers with gaps between and is fully equipped to measure air velocities and the dispersion of a contaminant [Yee04] (further details are given in Chapter 8). Although it is a very recent work, a considerably large amount of research groups have made use of this experiment. For example, the MUST case with some geometry simplifications was studied in a wind tunnel experiment at scale 1:50 by the Defence Science and Technology Organization of Australia at Monash University [Gail06]. A similar water-channel experiment of MUST was performed at scale 1:102.5 at Canada R&D Corporation [Yee06]. With more rigorous geometrical details, the MUST case was studied in a wind-tunnel experiment (scale 1:75) at the Meteorological Institute of the University of Hamburg (Germany)[3] [Bezp07].

The MUST field experiment has also been the motivation of many computational modelling studies. Some examples are the evaluation of empirical urban dispersion models [Warn06]; Gaussian and Lagrangian micro- or meso-scale dispersion models [Baum08], [Amic08], [Eich08]; RANS and Unsteady-RANS approaches [Hsie07], and the prediction capabilities for different computational approximations like the models for turbulence [Mill07], for heat [Mill06], for dispersion [Izar08], for dispersion variance [Mill08], variable grid conditions [Barm08] and many other parameters needed to set up an appropriate CFD numerical simulation of pollution dispersion [Salo07], [Coir06], [Efth08]. The MUST experiment was also selected by the Cost Action 732 (Quality assurance and improvement of micro-scale meteorological models) [Cost732], where it was modelled by more than a dozen research groups (see e.g. [Oles08], [Disa08], [Fran08]). Some of the first LES studies of the MUST experiment were published by [Dejo09], [Sant07] and a VLES study was published by [Came05]. In most of these pollutant transport studies the usual discussed topics are Euler or Lagrange dispersion modelling for gaseous emissions or different sizes of particle emissions in conjunction with the effects of building size and shape, street width, wind velocity variation, wind direction, heat transfer and viscous turbulence models.

The numerical prediction of pollution dispersion in urban environments by means of the solution of the statistically steady RANS equations has shown to be strongly dependent on the selected turbulence models. In the case of pollution dispersion, turbulence models do not only have to be used for the Reynolds stresses, but also for the turbulent scalar fluxes. While the influence of several turbulence models for the Reynolds stresses on the dispersion in urban environments has already been examined several times, the turbulent scalar fluxes are usually modelled by the simple gradient diffusion assumption. This model assumes isotropic diffusion behaviour for species transport in analogy to the turbulent transport behaviour of momentum. It means that the scalar diffusivity is proportional to the eddy diffusivity with a factor equivalent to the inverse of the (usually constant) turbulent Schmidt number (Sc_t). Different isotropic scalar flux models were recently applied in pollution dispersion using various constant values of the turbulent Schmidt number by [Tomi07], [Disa07], and one anisotropic scalar flux model by [Wang09]. Also the recent publications from Rossi [Ross09a], [Ross09b], [Ross10a], [Ross10b] present a

---

[3] This last wind tunnel experiment is the one used in the present work for comparison and evaluation of numerical results.

very good analysis of two anisotropic scalar flux models in pollution/mass dispersion. To the knowledge of the author, only [Izar07b] and [Izar08] have published a qualitative and quantitative comparison of the performance for several isotropic and anisotropic scalar flux models for pollution dispersion including algebraic and second moment modelling. Further details and the complete list of turbulent models employed in those publications are described in the present work.

Fortunately, the lack of references using advanced scalar flux models is not the same in other engineering applications. Many different approximations of these terms have been studied for the analogue heat flux term in heat transfer applications, when the temperature is approximated as a passive scalar. Formally discussed, a passive heat transfer approximation is not real but under very low temperature variations and neglecting buoyancy effects, it can yield relatively good estimations. In such heat transfer applications, the variation of the turbulent Prandtl number Pr_t (analogue to Sc_t) is usually computed by using different constant values. Additional and less common options to model heat fluxes include empirical equations or more advanced first and second order anisotropic heat flux models. The simulation improvements obtained by the implementation of those advanced heat flux models in heat transfer applications may also occur for the transport of passive pollutants in the atmosphere. This idea represents the original hypothesis and main motivation of the present work.

In this dissertation, the effects of several numerical parameters involved in the CFD simulation of atmospheric pollution dispersion are analyzed. The numerical parameters under consideration are the selection of turbulent stress models, active/passive pollutant, first/second order spatial discretization schemes and grid uncertainty in combination with different isotropic/anisotropic algebraic/differential scalar flux models. The anisotropic scalar flux models were implemented for passive scalar transport conditions using the commercial CFD package FLUENT 6.3 [Flue06]. The well known geometries of a bi-dimensional street canyon and the already widespread MUST experiment have been selected for this purpose due to the considerable literature available to evaluate the influence of the previously mentioned elements. The model predictions are compared with experimental measurements using statistical performance measures to assess their predictive capability. As a final goal this dissertation is intended to evaluate the effort/improvement relation by the selection of advanced models, to propose a criterion for the selection of the suitable model for pollutant dispersion modelling, and to contribute to the experience in this topic for further practical engineering and research.

1.4 Structure of the Dissertation

The information is presented in the following order. Chapter 2 presents the governing equations and computational approach needed to compute the fluid and contaminant transport. It introduces the reader to the turbulence problem and explains the necessity of turbulence models. Chapter 3 presents the different options available to model the turbulence effects in fluid flow equations (Reynolds stresses), in the pollutant transport equation (scalar flux term), and in the near wall region. Chapter 4 gives a short overview of how the previous equations are solved through a Computational Fluid Dynamics (CFD) analysis and presents the numerical approximations included in it. Chapter 5 explains how the advanced scalar flux models were implemented in the commercial CFD software. Chapter 6 shows the model validation employed for the evaluation of the numerical results. Chapter 7 and 8 present the details of the numerical simulation setups and analyze the results for the two studied test cases, the dispersion in a 2D street canyon and in the 3D urban MUST experiment. Finally, Chapter 9 presents some general observations and analysis of results for both test cases, and Chapter 10 states the conclusions drawn and gives recommendations for future works. The appendices contain some details of the implemented anisotropic scalar flux models, additional images from the results chapters and the source codes for the implemented models.

2 Simulation of Pollution Dispersion Using CFD

Pollution dispersion in the atmosphere is a good example of a scalar quantity dragged by a turbulent flow. Therefore, the turbulent flow field must be calculated with the intention to estimate the pollutants' movement.

In fluid dynamics turbulent flow is a fluid regime characterized by chaotic, unstable, and 3D property changes. It consists of convection transport that is many times higher than its diffusion transport and a rapid variation of pressure and velocity in space and time. Some dictionary definitions already associate turbulence with the atmosphere and identify it as an irregular motion of the atmosphere characterized by gusts and lulls or up-and-down currents of the wind. After a century of experience, it has been seen that the “turbulence problem” is notoriously difficult to estimate, and still there are not prospects of a simple analytic theory. Consequently, in last the 30 years, there have been a lot of efforts to use the increasing power of digital computers to find an approximated solution to this problem through CFD analysis.

2.1 Governing Equations and Computer Approach

To simulate fluid flow and pollution dispersion in CFD, the fundamental equations of fluid mechanics must be solved. First, these fundamental equations must be regarded for a continuum medium, which means that the behaviour of fluid is considered with macroscopic properties, i.e. velocities, pressure, density, viscosity, temperature and species fraction have macroscopic length scale (approx. 1μm or larger). These may be thought as averages over suitably large numbers of molecules. The governing equations needed to describe the fluid flow motion are the conservation of mass (or continuity equation), conservation of momentum, conservation of energy and conservation of species:[4]

$$\frac{\partial(\rho)}{\partial t} + \frac{\partial}{\partial x_i}(\rho u_i) = 0 \qquad \text{Eq. 2-1}$$

$$\frac{\partial(\rho u_j)}{\partial t} + \frac{\partial}{\partial x_i}(\rho u_i u_j) = -\frac{\partial}{\partial x_i}(\tau_{ij}) - \frac{\partial p}{\partial x_j} + f_j \qquad \text{Eq. 2-2}$$

$$\frac{\partial(\rho h)}{\partial t} + \frac{\partial(\rho u_i h)}{\partial x_i} = -\frac{\partial}{\partial x_i}(j_{ih}) + S_h + \Phi \qquad \text{Eq. 2-3}$$

$$\frac{\partial(\rho c)}{\partial t} + \frac{\partial(\rho u_i c)}{\partial x_i} = -\frac{\partial}{\partial x_i}(j_{ic}) + S_c \qquad \text{Eq. 2-4}$$

where ρ is the density, u_i are the three velocity components, p is the pressure, f_i are the body forces and any additional momentum sources, h is the enthalpy, c is a scalar contaminant, and S_T and S_c represent the generation/destruction rate of energy and species respectively. The τ_{ij} is the momentum shear stress tensor, j_{ih} is the diffusion flux of energy transport, and j_{ic} is the diffusion flux of species transport. These equations have been written in a general form for easier recognition of the terms. The first and second terms in the left side of all equations are the local time change and convective transport respectively. The first term on the right in every equation corresponds to the diffusion transport of the term between brackets. The rest of the terms are computationally considered or treated as source terms.

In a Newtonian fluid, the viscous stress is proportional to the rate of deformation. This means that the momentum equation (Eq. 2-2) for Newtonian fluids the shear stress tensor τ_{ij}, is calculated from:

$$\tau_{ij} = \mu\left(\frac{\partial u_i}{\partial x_j} + \frac{\partial u_j}{\partial x_i}\right) - \frac{2}{3}\mu\frac{\partial u_k}{\partial x_k}\delta_{ij} \qquad \text{Eq. 2-5}$$

where μ is the fluid viscosity and δ_{ij} is the Kronecker delta (δ_{ij}=1 if $i=j$ and δ_{ij} =0 if $i \neq j$). Substituting Eq. 2-5 in Eq. 2-2, the transport equation becomes the same form as the well known Navier-Stokes equations.

In the energy equation (Eq. 2-3), the diffusion flux of energy transport term (j_{ih}) includes the energy transfer due to conduction and species diffusion. Similarly, in the species equation (Eq. 2-4) the diffusion flux arises due to the concentration of gradients. Finally, they are calculated as:

---

[4] Continuity, momentum, and energy equations are usually considered the fundamental equations of fluid mechanics. However, in the case of pollutant dispersion in an isothermal atmosphere, the energy equation plays no role but the species equation must be solved. The deductions of these equations can be found in any basic fluid mechanics book.

$$j_{ih} = \Gamma_h \frac{\partial T}{\partial x_i} - \sum_j h_j j_{jc} \qquad \text{Eq. 2-6}$$

$$j_{ic} = \Gamma_c \frac{\partial c}{\partial x_i} \qquad \text{Eq. 2-7}$$

where the factors Γ_h and Γ_c are the diffusion coefficients for the enthalpy (Fourier's law) and species (Fick's law) transport respectively. The second term on the right side in Eq. 2-6 represent the energy transport by the diffusion. The last term in Eq. 2-3 is the viscous dissipation Φ, it is defined as [Cebe02]:

$$\Phi = 0.5 \cdot \mu \cdot \left(\frac{\partial u_i}{\partial x_j} + \frac{\partial u_j}{\partial x_i} \right)^2 - \frac{2}{3} \mu \frac{\partial u_k}{\partial x_k} \frac{\partial u_l}{\partial x_l} \qquad \text{Eq. 2-8}$$

To describe turbulent flows in CFD, the governing equations of mass, momentum, energy and species concentration are estimated using a numerical method. The selection method will depend on the level of description, completeness, computational cost, ease of use, range of applicability, and accuracy. The methods to simulate turbulent flows can be grouped into three categories: the Direct Numerical Simulation (DNS), the Large Eddy Simulation (LES), and the Reynolds-Averaged Navier-Stokes (RANS) simulations. The RANS approach was the method selected in the present work for the numerical simulations of the flow field and pollution dispersions. Therefore, this approach will be better explained in the next chapter.

Direct numerical simulation (DNS) is a simulation technique in CFD in which the Navier-Stokes equations are numerically solved without any turbulence model. This means that the whole range of spatial and temporal scales of turbulence is resolved. All the spatial scales of the turbulence must be resolved in the computational mesh, from the smallest dissipative scales (Kolmogorov micro-scales η), up to the integral scale L, associated with the motions containing most of the kinetic energy. In case of homogeneous turbulence, the number of grid points in each direction must be at least L/η. It can be shown that this ratio is proportional to $\mathrm{Re}_L^{3/4}$. Here Re_L is a Reynolds number based on the magnitude of the velocity fluctuations and the integral length scale. Since this number of points must be employed in each of the directions of the three coordinates, and the time step is related to the grid size, the cost of a simulation typically scales as Re_L^3 [Ferz02].

Consequently, the computational cost of DNS is very high, even at low Reynolds numbers. For the Reynolds numbers encountered in most industrial applications, the computational resources required by a DNS would exceed the capacity of the most powerful computers currently available. However, DNS is a useful tool in fundamental research of turbulence. Using DNS it is possible to perform "numerical experiments" and extract information from them that is difficult or impossible to obtain in the laboratory, allowing a better understanding of the physics of turbulence. Also, DNS is useful in the development of turbulence models for practical applications, such as sub-grid scale models for LES and models for methods that solve the RANS equations.

The next step of lower computer demanding modelling is the Large Eddy Simulation (LES). LES is a numerical technique used to solve the partial differential equations governing turbulent fluid flow. It was initially formulated in the late 1960s and early 1970s by the meteorologist Smagorinsky and his co-workers to simulate atmospheric air currents and climate predictions [Smag70]. Therefore, the primary use of LES was for meteorological applications but later, during the 1980s and 1990s, it became widely used in the field of engineering.

The deduction of this approach is based on Kolmogorov’s (1941) famous theory of self similarity, which is that large eddies of flow are dependent on flow geometry, while smaller eddies are self similar and have a universal character [Kolm41]. For this reason, it became a practice to solve only for the large eddies explicitly, and model the effect of the smaller and more universal eddies on the larger ones. Thus, in LES, the large scale motions of the flow are calculated, while the effect of the smaller universal scales (the so-called sub-grid scales) are modelled using a sub-grid scale (SGS) model. In practical implementations, one is required to solve the filtered Navier-Stokes equations with an additional sub-grid scale stress term. The most commonly used SGS models are the Smagorinsky model and its dynamic variants. They compensate for the unresolved turbulent scales through the addition of an “eddy viscosity” into the governing equations.

LES requires less computational effort than DNS but more effort than those methods that solve the Reynolds-averaged Navier-Stokes equations (RANS). The computational demands also increase significantly in the vicinity of walls, and simulating such flows for practical engineering applications is usually only possible in modern supercomputers today. This method has a big potential for the next generation of CFD simulations. The main advantage of LES over computationally cheaper RANS approaches is the increased level of detail it can deliver. While RANS methods provide “averaged” results, LES is able to predict instantaneous flow characteristics and resolve turbulent flow structures.

In the particular case of pollution dispersion modelling in urban environments, LES is currently possible and recommended. However, the demanding computational resources of typical micro-scale meteorological geometry reduce the applicability to small and simplified cases. The RANS approach has been selected in the present work as a manageable computational method to simulate fluid flow motion and to maximize the applicability of currently available computational resources in a relatively new CFD application such as a real city section or a similar 3D urban area.

2.2 Reynolds Averaged Navier-Stokes Equations

Using the Reynolds averaged approach to turbulence, all of the unsteadiness is averaged out, meaning all unsteadiness is regarded as part of the turbulence. The Reynolds-averaged Navier-Stokes (RANS) equations govern the transport of the averaged flow quantities, with the whole range of the scales of turbulence being modelled. The RANS-based modelling approach therefore greatly reduces the required computational effort and resources, and has been widely adopted in practical engineering applications. When applying Reynolds averaging, also called Reynolds decomposition, the solution for any variable in the Navier-Stokes equations are decomposed into the mean (ensemble-averaged or time-averaged) and its fluctuating components.

$$\phi(x,t) = \bar{\phi}(x) + \phi'(x,t) \qquad \text{Eq. 2-9}$$

where

$$\bar{\phi}(x) = \lim_{T\to\infty} \frac{1}{2T} \int_{-T}^{T} \phi(x,t)\,dt \qquad \text{Eq. 2-10}$$

Here t is the time and T is the averaging interval. This interval must be very large compared to the typical time scale of the fluctuations. The mean value (Eq. 2-10) will depend only on the spatial coordinate x.

Applying the definition presented in Eq. 2-9 and Eq. 2-10 for the velocity, enthalpy and any scalar contaminant yields:

$$\begin{aligned} u_i &= \bar{u}_i + u_i' \\ h &= \bar{h} + h' \\ c &= \bar{c} + c' \end{aligned} \qquad \text{Eq. 2-11}$$

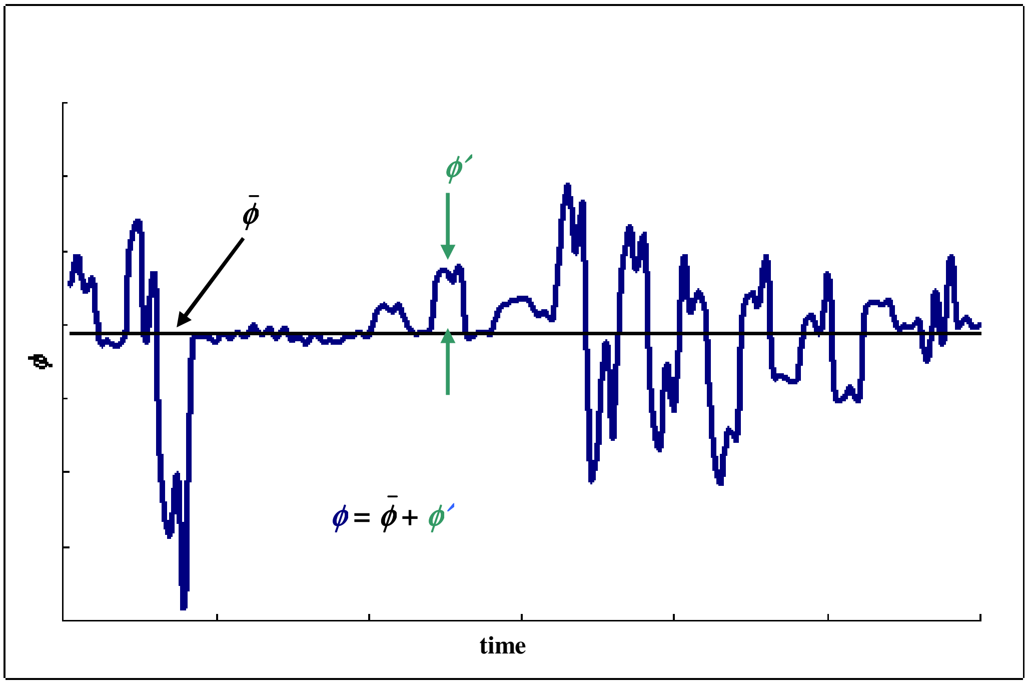

Figure 2-1. Averaged and fluctuating parts of a property ϕ under a steady state flow conditions.

Then, starting from the fundamental equations, the continuity equation (Eq. 2-1) and Navier–Stokes equations (Eq. 2-2 with the substitution of Eq. 2-5) expressed for steady state flow conditions are:

$$\frac{\partial \rho u_i}{\partial x_i} = 0 \qquad \text{Eq. 2-12}$$

$$\frac{\partial \rho u_j u_i}{\partial x_j} = -\frac{\partial p}{\partial x_i} + \frac{\partial}{\partial x_j}\left[\mu\left(\frac{\partial u_i}{\partial x_j} + \frac{\partial u_j}{\partial x_i}\right) - \frac{2}{3}\mu\frac{\partial u_k}{\partial x_k}\delta_{ij}\right] + f_i \qquad \text{Eq. 2-13}$$

Using the time-average definition from Eq. 2-9 these equations can be written as:

$$\frac{\partial \rho \bar{u}_i}{\partial x_i} = 0 \qquad \text{Eq. 2-14}$$

$$\frac{\partial \rho \bar{u}_j \bar{u}_i}{\partial x_j} = -\frac{\partial \bar{p}}{\partial x_i} + \frac{\partial}{\partial x_j}\left[\mu\left(\frac{\partial \bar{u}_i}{\partial x_j} + \frac{\partial \bar{u}_j}{\partial x_i}\right) - \frac{2}{3}\mu\frac{\partial \bar{u}_k}{\partial x_k}\delta_{ij}\right] + \bar{f}_i - \frac{\partial}{\partial x_j}\left(\rho\overline{u_i' u_j'}\right) \qquad \text{Eq. 2-15}$$

where the fluid properties ρ and μ are constants. This set of equations is known as Reynolds Averaged Navier Stokes (RANS) equations. All terms in these equations can be easily recognized as the average quantities of their source equations except for the last term in the right side of Eq. 2-15. The part inside the parenthesis of this term corresponds to the fluctuating component of the turbulence and is known as the

Reynolds stress tensor. In laminar flow conditions, this term does not exist. However, in our case of interest and in most practical fluid flow problems, a turbulence model for the Reynolds stresses term must be used. There are several Reynolds stress turbulent models and most of them have many different variations in model coefficients and/or extra source terms. Seven selected turbulence models for the Reynolds stress have been employed in this work. A short description of each one of the models used is given in Chapter 3.

2.3 Passive Contaminant Transport

Turbulence transport of scalar contaminants is analogue and similar to the transport of momentum. A passive contaminant transport is defined as the movement of a substance (c) that does not affect the dynamical flow field, which is contrary to the case of active scalar (presented in next section), where the contaminant participates in the development of the dynamical flow field. Under the first passive scalar conditions, the mean flow can be computed and analyzed without any attention to the scalar field. The scalar field can subsequently be computed afterwards.

To estimate the transport of pollutants, one extra non-linear differential equation must be solved in addition to the flow field (RANS) equations. This extra equation is the species transport. Performing the Reynolds average (Eq. 2-9) on the species transport equation (Eq. 2-4), in case of a passive scalar and steady state conditions, can be written as:

$$\frac{\partial}{\partial x_j}\left(\rho \bar{u}_j \bar{c}\right) - \frac{\partial}{\partial x_j}\left(\Gamma_c \frac{\partial \bar{c}}{\partial x_j}\right) = -\frac{\partial}{\partial x_j}\left(\rho \overline{u'_j c'}\right) \qquad \text{Eq. 2-16}$$

where Γ_c is the molecular diffusion coefficient of the transported scalar pollutant quantity c. This equation can be easily recognized as a general Reynolds averaged convection-diffusion transport equation. The two terms on the left side are the convection and the diffusion of c respectively, but special attention must be taken in the right side. The new term on the right side comes up from the convective term after performing the Reynolds averages to the species transport equation. The term inside of the right side parenthesis is called turbulent scalar flux term. It is analogue to the Reynolds stress and needs to be modelled with the intention to resolve the transport of pollutants in turbulent flow. In Chapter 3 a detailed description for the deduction of some of the most common models for scalar fluxes is presented.

2.4 Active Contaminant Transport

The CFD calculation of a transport equation for an active scalar contaminant in turbulent flow conditions needs some additional reflections because at this point, this equation becomes fully coupled with the complete flow field. An active scalar contaminant may have different density, viscosity, temperature, chemical composition or concentration than the main fluid; therefore any difference between the fluid properties will affect the main flow field through buoyancy, viscosity, heat, or mass transport.

The first problem that needs to be addressed is the fact that the density varies as a function of position. In the case of turbulent flow, additional to the velocity and scalar fluctuations presented by Eq. 2-12, there would also be density fluctuations. The Reynolds averages for this additional variable would be:

$$\rho = \bar{\rho} + \rho' \qquad \text{Eq. 2-17}$$

It is easy to realise that the use of density fluctuations would introduce additional terms in the continuity, momentum, energy and species equations when the Reynolds average is used. Many of these additional terms are unknown and need to be modelled. To reduce the number of separated terms requiring modelling in active scalar flows with variable density, a density-weighted averaging procedure known as Favre average is used [Vers07].

For density variable simulation, the density-weighted averaging of the mean velocity in *x* direction is defined as:

$$\tilde{u} = \frac{\overline{\rho u}}{\bar{\rho}} \qquad \text{Eq. 2-18}$$

Thus, the instantaneous velocity is written as:

$$u(x,t) = \tilde{u}(x) + u''(x,t) = \frac{\overline{\rho u}}{\bar{\rho}} + u'' \qquad \text{Eq. 2-19}$$

In contrast to the Reynolds average, u'' includes effects of density fluctuations in addition to the velocity fluctuations. Please note that if the flow is incompressible, the density is constant, so $\tilde{u} = \bar{u}$ and $u'' = u'$.

The governing equations presented by Eq. 2-1 to Eq. 2-4, i.e. the continuity, momentum, energy, and species respectively, with the velocity and scalars—but not the density and pressure—decomposed according to density-weighted Favre-averaging yields:

$$\frac{\partial \bar{\rho}}{\partial t} + \frac{\partial}{\partial x_i}(\bar{\rho}\tilde{u}_i) = 0 \qquad \text{Eq. 2-20}$$

$$\frac{\partial \bar{\rho}\tilde{u}_i}{\partial t} + \frac{\partial}{\partial x_j}(\bar{\rho}\tilde{u}_i\tilde{u}_j) = \frac{\partial}{\partial x_j}\left(\bar{\tau}_{ij} - \overline{\rho u_i'' u_j''}\right) - \frac{\partial \bar{p}}{\partial x_i} + \bar{f}_j \qquad \text{Eq. 2-21}$$

$$\frac{\partial \bar{\rho}\tilde{h}}{\partial t} + \frac{\partial}{\partial x_i}\left(\bar{\rho}\tilde{u}_i\tilde{h}\right) = \frac{\partial}{\partial x_i}\left(\tilde{j}_{ih} - \overline{\rho u_i'' h''}\right) + \bar{S}_h \qquad \text{Eq. 2-22}$$

$$\frac{\partial \bar{\rho}\tilde{c}}{\partial t} + \frac{\partial}{\partial x_i}\left(\bar{\rho}\tilde{u}_i\tilde{c}\right) = \frac{\partial}{\partial x_i}\left(\tilde{j}_{ic} - \overline{\rho u_i'' c''}\right) + \bar{S}_c \qquad \text{Eq. 2-23}$$

Special attention must be given to the mixture properties because they are no longer constant. It means that there are different density and viscosity for every species.

The mixture density is calculated in this work based on the ideal gas law for incompressible flow. In this case the density is computed as [Flue06]:

$$\rho = \frac{p_{op}}{RT\sum_i \frac{c_i}{M_{w,i}}} \qquad \text{Eq. 2-24}$$

where R is the universal gas constant (8.3145 J/Kmol), c_i is the mass fraction of species i, $M_{w,i}$ is the molecular weight of the species i, and T and p_{op} are the operation temperature and pressure respectively.

Similarly, the mixture viscosity based on kinetic theory is calculated from:

$$\mu = \sum_i \frac{X_i \mu_i}{\sum_i X_i \varphi_{ij}} \qquad \text{Eq. 2-25}$$

where

$$\varphi_{ij} = \frac{\left[1 + \left(\frac{\mu_i}{\mu_j}\right)^{1/2}\left(\frac{M_{w,j}}{M_{w,i}}\right)^{1/4}\right]^2}{\left[8\left(1 + \left(\frac{M_{w,i}}{M_{w,j}}\right)\right)\right]^{1/2}} \qquad \text{Eq. 2-26}$$

and X_i is the mole fraction of species i.

As can be observed in Eq. 2-20 to Eq. 2-23, the new set of flow field transport equations yields the same form as those for turbulent constant density flows. Here again the momentum fluxes ($\overline{\rho u_i'' u_j''}$), heat fluxes ($\overline{\rho u_i'' h''}$) and scalar fluxes ($\overline{\rho u_i'' c''}$) need to be modelled with a turbulence model. The deduction of these Favre average transport equations is outside of the objective of this thesis but it can be found in any book dealing with simulation of compressible fluid flow e.g. [Cebe02].

3 Closure of Fundamental Equations

As was shown in the previous chapter, after performing the Reynolds or Favre average of the Navier-Stokes equations and of the pollutant transport equation, an additional unknown term arises in each of these equations. To close the complete set of equations and compute the fluid flow field and pollutant transport field, a turbulence model must be used to estimate these unknown terms as a function of known quantities. There are several kinds of turbulence models for the Reynolds stresses and for the scalar fluxes. Models for Reynolds or Favre averaged equations are usually the same. Therefore only the Reynolds average form of the models is shown and for active scalar the fluid density ρ only needs to be replaced by averaged density $\overline{\rho}$. A selected group from some of the most common turbulence models for Reynolds stresses and scalar fluxes are explained in this chapter.

A very important and unfortunate fact to mention at this point is that no single turbulence model has been universally accepted as being superior for all classes of problems. The choice of the best turbulence model in a specific case depends on many considerations. To make the most appropriate choice of a model for an application, one needs to understand the capabilities and limitations of the various options.

3.1 Reynolds Stress Modelling

The Reynolds stress tensor appears in the RANS equations after determining the Reynolds average of the convective term in the Navier-Stokes equation. It is determined by a turbulence model, either via the turbulent viscosity hypothesis or more directly from modelling the Reynolds-stress transport equations. Within the turbulent viscosity based models the number of additional equations to solve also varies, while the Reynolds stress transport model always needs to solve one transport equation for every stress (3 equations in 2D and 6 equations in 3D), plus one equation for the turbulent dissipation rate (ε) and sometimes also for turbulent kinetic energy (k). In summary, these turbulent models could be classified as shown in Table 3-1.

Table 3-1. Reynolds stress modelling classification.

No. of extra transport equations	***Model Name***
Zero	Mixing length model
One	Spalart-Allmaras model
Two	k-ε models k-ω models
Seven	Reynolds stress model

The Zero, One and Two equation models are based on the turbulent viscosity hypothesis. This hypothesis, also known as Boussinesq hypothesis, proposes that the Reynolds stresses are proportional to the mean rate of deformation. It is based on the presumption that an analogy exists between the action of viscous stresses and Reynolds stresses on the mean flow. It can be written as:

$$-\rho\overline{u_i'u_j'} = \mu_t\left(\frac{\partial \overline{u}_i}{\partial x_j} + \frac{\partial \overline{u}_j}{\partial x_i}\right) - \frac{2}{3}\left(\rho k + \mu_t \frac{\partial \overline{u}_k}{\partial x_k}\right)\delta_{ij} \qquad \text{Eq. 3-1}$$

where μ_t is a scalar property called the turbulent viscosity (often called eddy viscosity), $k = 1/2\left(\overline{u'^2} + \overline{v'^2} + \overline{w'^2}\right)$ is the turbulent kinetic energy. Eq. 3-1 is analogous in turbulence transport to Eq. 2-5 for viscous stresses. As before, the last terms are equal to zero for incompressible flow. In this form, the Boussinesq hypothesis (Eq. 3-1) provides all missing unknowns in the RANS flow equations (Eq. 2-15). The turbulent viscosity is calculated in a specific way for all turbulent viscosity based models.

The Boussinesq assumption is both the strength and the weakness of two equation models. This assumption is a huge simplification of a turbulent transport and it allows thinking and estimating the effects of turbulence on the mean flow in the same way as molecular viscosity affects laminar flow. The main weakness of the Boussinesq assumption is that it is not valid generally. There is no formal analytical relation which says that the Reynolds stress tensor must be proportional to the strain rate tensor. It is true in simple flows like straight boundary layers and wakes, but in complex flows—such as flows with strong curvature or strongly accelerated or decelerated flows—the Boussinesq assumption is simply not valid. The turbulent viscosity based models present inherent problems to predict strongly rotating flows and other flows where curvature effects are significant. They also often have problems to predict strongly decelerated flows like stagnation flows. In summary, although the turbulent viscosity hypothesis is not correct in detail, it is an easy way to implement turbulence modelling, and with careful application, it can provide reasonably good results for many flows [Vers07].

The simplest kind of model to estimate Reynolds stress is the algebraic or zero equation model. In this model, an algebraic equation is used to compute a turbulent viscosity from a characteristic velocity and a specified mixing length scale of the flow field. The problem with this kind of model is that their range of applicability is extremely limited to very well defined and simplified geometries. Therefore, this kind of model has not been implemented in the present work. For further details about this kind of model, please refer to a turbulence modelling book such as [Pope00].

The next level of complexity is the one equation models, where a transport equation for a turbulent quantity is solved (usually for the turbulent kinetic energy). In this case, a second turbulent quantity (usually the turbulent length scale) is obtained from an algebraic expression. In the next level of complexity are the two equation models where two transport equations are used to estimate the turbulent characteristics of the flow. The eddy viscosity is obtained from an algebraic relation between these two transported turbulent parameters.

Finally, the Reynolds stress transport equation models (also known in the literature as second-order or second-moment closure models) include six transport equations, one for each Reynolds stress. Each transport equation contains turbulent diffusion, production, pressure-strain and dissipation terms whose individual effects are unknown. Then, assumptions are made about these unknown terms and the resulting partial differential equations are solved in conjunction with the rate of dissipation of the turbulent kinetic energy (ε). The application of this kind of model outside of the academy or research is relatively new due to the increase of computer recourses and the increased time demand compared to standard two-equation models.

The turbulence models selected in this work for the simulation of Reynolds stresses are:

1) Spalart-Allmaras model (S-A)
2) Standard k-ε model (SKE)
3) Renormalization-group k-ε model (RNG)
4) Realizable k-ε model (RKE)
5) Standard k-ω model (SKW)

6) Shear-stress transport k-ω model (SST)
7) Differential stress model (LRRIP)

All these turbulence models are already available in the commercial software FLUENT 6.3. The first one, S-A, is a one-equation model. Models 2-6 are two-equation models. The last one, LRRIP, is the most advanced available model and belongs to the category of Reynolds stress transport equations.

3.1.1 One Equations Spalart-Allmaras model

The Spalart-Allmaras (S-A) turbulence model is the only one-equation model used in the present work; therefore it is presented in a separate section. The Spalart-Allmaras model is a relatively simple one-equation model that solves a transport equation for a modified eddy (turbulent) viscosity instead of the turbulent kinetic energy like most of the one-equation turbulent models. It represents a relatively new class of one-equation models in which it is not necessary to calculate a length scale related to the local shear layer thickness which is often a critical assumption in other one equation models. The S-A model was developed specially for aerospace applications but it is currently gaining popularity in other areas. Nevertheless, no claim is made regarding its suitability to all types of complex engineering flows.

The S-A model belongs to the group of turbulent viscosity based models. A peculiar advantage of this model is that it provides economical computations of boundary layer in external aerodynamics and the near-wall gradients of the transported variable in the model are much smaller than the gradients of the transported variables in the k-ε or k-ω models. This might make the model less sensitive to numerical errors when non-well refined meshes near walls are used [Spal94].

The transported variable in the S-A model is a modified turbulent viscosity $\tilde{\nu}$ which is identical to the standard turbulent viscosity except in the near-wall (viscous-affected) region. The transport equation for the S-A model is given by:

$$\frac{\partial}{\partial x_i}\left(\rho \tilde{\nu} u_i\right) = G_\nu + \frac{1}{\sigma_{\tilde{\nu}}}\left[\frac{\partial}{\partial x_j}\left\{\left(\mu + \rho\tilde{\nu}\right)\frac{\partial \tilde{\nu}}{\partial x_j}\right\} + C_{b2\rho}\left(\frac{\partial \tilde{\nu}}{\partial x_j}\right)^2\right] - Y_\nu \qquad \text{Eq. 3-2}$$

where the turbulent viscosity is calculated as:

$$\mu_t = \rho \tilde{\nu} f_{\nu 1} \qquad \text{Eq. 3-3}$$

with

$$f_{v1} = \frac{\chi^3}{\chi^3 + C_{v1}^3} \qquad \chi \equiv \frac{\tilde{\nu}}{\nu} \tag{Eq. 3-4}$$

The additional terms are:

$$\begin{aligned} G_v &= C_{b1}\rho\tilde{S}\tilde{\nu} & \tilde{S} &\equiv S + \frac{\tilde{\nu}}{\kappa^2 d^2} f_{v2} \\ f_{v2} &= 1 - \frac{\chi}{1+\chi f_{v1}} & S &\equiv \sqrt{2\Omega_{ij}\Omega_{ij}} \\ Y_v &= C_{w1}\rho f_w\left(\frac{\tilde{\nu}}{d}\right)^2 & f_w &= g\left[\frac{1+C_{w3}^6}{g^6 + C_{w3}^6}\right]^{1/6} \\ g &= r + C_{w2}\left(r^6 - r\right) & r &= \frac{\tilde{\nu}}{\tilde{S}\kappa^2 d^2} \end{aligned} \tag{Eq. 3-5}$$

Where *d* is the distance to the closest wall and Ω_{ij} is the mean vorticity tensor defined as:

$$\Omega_{ij} = \frac{1}{2}\left(\frac{\partial \overline{u}_i}{\partial x_j} - \frac{\partial \overline{u}_j}{\partial x_i}\right) \tag{Eq. 3-6}$$

The remaining constants are given in Table 3-2:

Table 3-2. Spalart-Allmaras model coefficients.

Some S-A model coefficients	
$C_{b1} = 0.1355$	$C_{w1} = \frac{C_{b1}}{\kappa^2} + \frac{\left(1+C_{b2}\right)}{\sigma}$
$C_{b2} = 0.622$	$C_{w2} = 0.3$
$\sigma = 2/3$	$C_{w3} = 2.0$
$C_{v1} = 7.1$	$\kappa = 0.4187$

3.1.2 Two Equations Models

Historically, many two-equation models have been proposed. By definition, two-equation turbulent models are those in which two extra transport equations that represent the turbulent properties of the flow are solved. They are the simplest "complete models" of turbulence in which the solution of two separate transport equations allows the turbulent velocity and length scales to be independently determined.

The two-equation turbulence models are the most common turbulence models. In most of these models the turbulent kinetic energy *k* is taken as one of the variables, but there are different options for the second. Models like the *k*-ε model and the *k*-ω

model have become industry standards and are commonly used for a variety of different engineering problems. However, two equation turbulence models are also still a research area in progress and new modified two-equation models are continuously being developed.

Within the two-equation transport model category, three different options of the k- ε models and two different options of the k-ω models have been employed in the present work. All these models have a similar form, based on the Boussinesq eddy viscosity or turbulent viscosity assumption, which is computed from an algebraic relation between the two transported turbulence quantities.

3.1.2.1 *k-ε* Turbulence Models

The k-ε models are probably the most commonly used turbulence models in engineering applications and at least one variant of them (usually the standard *k-ε*) is incorporated in most of the commercial CFD codes. It is a two-equation model, which means it makes use of two extra transport equations to model the turbulent characteristics of the flow. The two transported parameters are the turbulent kinetic energy (*k)* and the turbulent dissipation rate (*ε).*

Three different options of k-ε models were employed in the present work: the standard *k-ε* (SKE)[Laun72], the re-normalization group *k-ε* (RNG) [Yakh86], and the realizable *k-ε* (RKE) [Shih95] models.

The SKE model is a semi-empirical model where the model transport equation for *k* is derived from the exact equation, while the model transport equation for *ε* was obtained using physical reasoning and bears little resemblance to its mathematically exact counterpart. In the derivation of the SKE model, the assumption is that the flow is fully turbulent, and the effects of molecular viscosity are negligible. The SKE model is therefore valid only for fully turbulent flows. The main advantage of this model is its simplicity, for which only initial and/or boundary conditions need to be supplied. It has shown excellent performance in many industrial flows, is numerically stable, and is the most widely validated turbulence model. However, the common problem of this model is its poor performance in some kind of flows including unconfined flows, flows with extra large strain (e.g. curved boundary layers [Bern86], swirling flows or rotating flows [Lill84]) and flows driven by anisotropy of normal Reynolds stresses. In wind engineering one of the well known limitations where the SKE model leads to very bad results is for the pressure distribution around buildings. This limitation is a result of the stagnation point anomaly—excessive production of *k* in stagnation flow regions. Therefore the pressures on the windward walls and especially behind the first corners are not well predicted [Fran07b].

The RNG model was developed with the intention to improve the SKE model's problems. It was derived using a rigorous statistical technique called renormalization group theory. It is similar in form to the SKE model, but includes different model coefficients and an additional term (not derived from RNG theory) in its ε equation that significantly enhances accuracy for rapidly strained flows. This additional term reduces the dissipation of ε in regions of high strain and therefore increases ε in those locations. The model consequently alleviates the stagnation point anomaly by leading to higher dissipation in regions of large k production. The RNG theory provides also an analytical formula for turbulent Prandtl numbers to improve diffusion, while the SKE model uses constant values.

Another option to reduce the deficiencies of the SKE model is the realizable k-ε (RKE) turbulent model. The RKE model is the newest of these three models and differs from the SKE model in having a new formulation for turbulent viscosity and a new transport equation for the dissipation rate (ε). The ε equation has been derived from an exact equation for the transport of the mean-square vorticity fluctuation but taking into account two of the realizability conditions for the Reynolds stresses (positivity of normal stresses and Schwarz inequality for shear stresses) [Pope00], [Shih95]. It has shown better predictions for the spreading rate of both planar and round jets. The RKE model is likely to provide superior performance for flows involving rotation, boundary layers under strong adverse pressure gradients, separation, and recirculation. In wind engineering applications, this model has a short history. Some examples of satisfactory applications with predictions of the flow in street intersection and flow around buildings were observed and published by [Fran05] and [Bloc08].

The three k-ε model options have been synthesized in a general expression for easy formulation. Considering incompressible flow, the transport equations for the turbulent kinetic energy k and for the turbulent dissipation rate ε are resumed as:

$$\frac{\partial(\rho k \bar{u}_i)}{\partial x_i} = \frac{\partial}{\partial x_j}\left[\Gamma_k \frac{\partial k}{\partial x_j}\right] + G_k - D_k + G_b \qquad \text{Eq. 3-7}$$

$$\frac{\partial(\rho \varepsilon \bar{u}_i)}{\partial x_i} = \frac{\partial}{\partial x_j}\left[\Gamma_\varepsilon \frac{\partial \varepsilon}{\partial x_j}\right] + G_\varepsilon - D_\varepsilon \qquad \text{Eq. 3-8}$$

where the definition of each term and the constants vary for the k-ε model option selected. The common terms for these three models are the production of turbulent kinetic energy G_k, its dissipation D_k, and the production of turbulent kinetic energy due to buoyancy G_b, which are calculated as:

$$
\begin{aligned}
D_k &= \rho\varepsilon \\
G_k &= -\rho\overline{u_i' u_j'}\frac{\partial \overline{u}_i}{\partial x_j} = \mu_t S^2 \\
G_b &= -g_i \frac{\mu_t}{\rho \cdot \mathrm{Pr}_t}\frac{\partial \rho}{\partial x_i}
\end{aligned}
\tag{Eq. 3-9}
$$

where Pr_t is the turbulent Prandtl number, calculated in a different way according to every model, S is the modulus of the mean rate-of-strain tensor defined as $S \equiv (2S_{ij}S_{ji})^{1/2}$ and the mean rate-of-strain tensor S_{ij}, defined as:

$$
S_{ij} = \frac{1}{2}\left(\frac{\partial \overline{u}_j}{\partial x_i} + \frac{\partial \overline{u}_i}{\partial x_j}\right)
\tag{Eq. 3-10}
$$

Additionally, the turbulent viscosity for these three models is always estimated from the relation:

$$
\mu_t = \rho C_\mu \frac{k^2}{\varepsilon}
\tag{Eq. 3-11}
$$

The definitions for the different parameters and constants are specified in Table 3-3 and Table 3-4.

Table 3-3. Terms from the k-ε transport equations.

Parameters	***SKE***	***RNG***	***RKE***
Γ_k	$\mu+\mu_t/\sigma_k$	$\alpha(\mu+\mu_t)$	$\mu+\mu_t/\sigma_k$
Γ_ε	$\mu+\mu_t/\sigma_\varepsilon$	$\alpha(\mu+\mu_t)$	$\mu+\mu_t/\sigma_\varepsilon$
G_ε	$G_k\,C_1\varepsilon/k$	$G_k\,C_1\varepsilon/k$	$\rho C_1 S\varepsilon$
D_ε	$C_2\rho\varepsilon^2/k$	$[C_2+C_\mu\eta^3(1-\eta/\eta_0)/(1+\beta\eta^3)]\rho\varepsilon^2/k$	$\rho C_2\varepsilon^2/(k+(\nu\varepsilon)^{½})$

Table 3-4. Model coefficients for the k-ε transport equations.

Constants	***SKE***	***RNG***	***RKE***
σ_k	1.3	-	1.0
σ_ε	1.0	-	1.2
C_1	1.44	1.42	$\mathrm{Max}[0.43, \eta/(\eta+5)]$
C_2	1.92	1.68	1.9
C_μ	0.09	0.0845	$1/(A_0+A_S kU^*/\varepsilon)$
Pr_t	0.85	$\left\lvert\frac{\alpha-1.39}{1/\mathrm{Pr}-1.39}\right\rvert^{-0.63}\left\lvert\frac{\alpha+2.39}{1/\mathrm{Pr}+2.39}\right\rvert^{-0.36}$	0.85

where Pr is the molecular Prandtl number. The other parameters are calculated from:

$$\begin{gathered}\eta = Sk/\varepsilon,\ \eta_0 = 4.38,\ \beta = 0.012,\ S = \left(2S_{ij}S_{ij}\right)^{1/2},\ \alpha = 1.393 \\ U^* = \sqrt{S_{ij}S_{ij} + \Omega_{ij}\Omega_{ij}}, \quad A_0 = 4.04, \quad A_S = \sqrt{6}\cdot\cos\phi \\ \phi = \frac{1}{3}\cos^{-1}\left(\sqrt{6}W\right), \quad W = \frac{S_{ij}S_{jk}S_{ki}}{\hat{S}^3}, \quad \hat{S} = \sqrt{S_{ij}S_{ij}}\end{gathered} \qquad \text{Eq. 3-12}$$

3.1.2.2 *k-ω* Turbulence Model

Historically, many two-equation turbulence models have been proposed. In most of these, *k* is taken as one of the variables, but there are diverse choices for the second. The specific dissipation rate ω(≡ε/k) is the second variable to solve for the *k*–ω based models and represent the second most widely used two-equation models. They are well known for their capability to be usable near boundaries without a requirement of near-wall functions. The reason they have this ability is, that different from the *k*-ε models, an extra dissipation term for near-wall flows is included in the *k*–ω models. They are also based on the Boussinesq hypothesis but with a modified turbulent viscosity formulation. Their application to building aerodynamics is still very uncommon [West02]. An example of its application to wind engineering is [Defr10].

In the present work two options of *k*-ω turbulence models are employed: the standard *k*-ω model (SKW) [Wilc98] and the shear-stress transport *k*-ω model (SST) [Ment94]. They have similar forms with transport equations for *k* and ω. The SKW model was the first model originally proposed as superior to the SKE model for boundary layer flows due to the better treatment of the viscous near-wall region, which accounts for the effects of streamwise pressure gradients. This model incorporates modifications for low-Reynolds-number effects, compressibility, and shear flow spreading. However, the treatment of non-turbulent free-stream boundaries is a common limitation of the model.

The SST model is designed to combine the advantages of the SKE and SKW models by means of an accurate formulation of the SKW model in the near-wall region with the free-stream independence of the SKE model in the far field. To achieve this, the SKE model is converted into a SKW formulation, then the SKW model and the transformed SKE model are both multiplied by a blending function and both models are added together. The blending function is designed to be one in the near-wall region, which activates the SKW model, and zero away from the surface, which activates the transformed SKE model. The SST model incorporates a damped cross-diffusion derivative term in the ω equation. The definition of the turbulent viscosity is modified to account for the transport of the turbulent shear stress. The modelling constants are also different. The modifications implemented in the SST model have shown more accurate and reliable results for a wider class of flows (including aerodynamics flows) than the SKW model [Flue06].

The transport equations of the two different k-ω model options have been synthesized for easier explanation in two general expressions—one for each transport parameter. For both of these models, the turbulent kinetic energy k can be calculated from:

$$\frac{\partial(\rho k \bar{u}_i)}{\partial x_i} = \frac{\partial}{\partial x_j}\left[\Gamma_k \frac{\partial k}{\partial x_j}\right] + G_k - Y_k \qquad \text{Eq. 3-13}$$

and the specific dissipation rate ω, from:

$$\frac{\partial(\rho \omega \bar{u}_i)}{\partial x_i} = \frac{\partial}{\partial x_j}\left[\Gamma_\omega \frac{\partial \omega}{\partial x_j}\right] + G_\omega - Y_\omega + D_\omega \qquad \text{Eq. 3-14}$$

where the diffusion coefficients for both models (SKW and SST) are calculated in analogy to the SKE model. It means:

$$\Gamma_k = \mu + \frac{\mu_t}{\sigma_k} \qquad \Gamma_\omega = \mu + \frac{\mu_t}{\sigma_\omega} \qquad \text{Eq. 3-15}$$

The different terms and model coefficients in these equations depend on the selected k-ω model. See Table 3-5.

Table 3-5. - Terms from the k-ω transport equations.

Parameters	***SKW***	***SST***
G_k	$\mu_t S^2$	$min[\mu_t S^2, 10\rho\beta^* k\omega]$
G_ω	$\alpha G_k \omega/k$	$G_k \alpha/\nu_t$
Y_k	$\rho\beta^* f_\beta k\omega$	$\rho\beta^* k\omega$
Y_ω	$\rho\beta f_\beta \omega^2$	$\rho\beta\omega^2$
D_ω	–	$2(1-F_1)(\rho\sigma_{\omega,2}/\omega)(\partial k/\partial x_j)(\partial\omega/\partial x_j)$
μ_t	$\alpha^* \rho k/\omega$	$\rho k/(\omega \cdot max[1/\alpha^*, SF_2/a_1\omega)$

The remaining constants are given in Appendix A.

3.1.3 Differential Stress Models

The most complex classical RANS turbulence model is the Reynolds stress transport equation model, also called the second-order or second-moment closure model. They are usually employed in cases when the two-equation models fail, such as for complex flows with strain field, significant body forces, and high anisotropic flows. This model does not use the isotropic eddy-viscosity hypothesis and closes the RANS equations by solving transport equations for every one of the Reynolds stresses, together with an equation for the dissipation rate ε. It means that five additional transport equations must be solved in 2D flows and seven additional transport equations in 3D flows.

This is the most elaborate turbulence model employed in the present work. The Reynolds stress model used in this work is commonly known as LRRIP model from the proposal of Launder, Reece, and Rodi [Laun75] with the inclusion of an Isotropization of Production (IP) term. This IP model term supposes that one part of the pressure term (presented in Eq. 3-16) partially counteracts the effect of production to increase the Reynolds-stress anisotropy. This effect is introduced as a consequence of observations from the rapid distortion axisymmetric expansion [Pope00].

Since the LRRIP model accounts for the effects of streamline curvature, swirl, rotation, and rapid changes in strain rate in a more rigorous manner than one-equation or two-equation models, it has greater potential to give accurate predictions for complex flows. However, the ability of LRRIP predictions is limited by the closure assumptions employed to model various terms in the exact transport equations for the Reynolds stresses. The models for the pressure-strain and dissipation-rate terms (see Eq. 3-16) are particularly important and often considered to be mainly responsible for the accuracy of the predictions with these kinds of models. For this reason, the LRRIP model might not always yield results that are clearly superior to the simpler models. Therefore, the additional computational effort does not always guarantee better results. However, use of this model is mandatory when the flow characteristics of interest are the result of anisotropy in the Reynolds stresses. Some examples are cyclone flows, highly swirling flows, rotating flow passages, and the stress-induced secondary flows in ducts. In atmospheric flows the LRRIP model has been reported with good agreement to experimental measurements but not necessarily better than all two-equation models [Fran05].

The transport equations of the Reynolds stress tensor can be derived from the subtraction of the RANS equations with the exact momentum equation. Then, the exact momentum equations are multiplied by a fluctuating property and the product is Reynolds averaged. This deduction is not of main interest of this work and has been left out but it can be found in fundamental texts on turbulent flows (see e.g. [Durb01] [Pope00]). The exact transport equation for the Reynolds stresses in statistically steady conditions reads:

$$\underbrace{\frac{\partial}{\partial x_k}\left(\rho\bar{u}_k\overline{u_i'u_j'}\right)}_{C_{ij}}=\underbrace{-\frac{\partial}{\partial x_k}\left[\rho\overline{u_i'u_j'u_k'}+\overline{p\left(\delta_{kj}u_i'+\delta_{ik}u_j'\right)}\right]}_{D_{Tij}}+\underbrace{\frac{\partial}{\partial x_k}\left[\mu\frac{\partial}{\partial x_k}\left(\overline{u_i'u_j'}\right)\right]}_{D_{Lij}}$$

$$\underbrace{-\rho\left(\overline{u_i'u_k'}\frac{\partial\bar{u}_j}{\partial x_k}+\overline{u_j'u_k'}\frac{\partial\bar{u}_i}{\partial x_k}\right)}_{P_{ij}}+\underbrace{\overline{p\left(\frac{\partial u_i'}{\partial x_j}+\frac{\partial u_j'}{\partial x_i}\right)}}_{\Phi_{ij}}\underbrace{-2\mu\overline{\frac{\partial u_i'}{\partial x_k}\frac{\partial u_j'}{\partial x_k}}}_{\varepsilon_{ij}}\underbrace{-\rho\beta\left(g_i\overline{u_j'\phi}+g_j\overline{u_i'\phi}\right)}_{G_{ij}} \qquad \text{Eq. 3-16}$$

Where each term is identified as:

C_{ij} = Convection

D_{Tij} = Turbulent Diffusion

D_{Lij} = Molecular Diffusion

P_{ij} = Stress Production

Φ_{ij} = Pressure Strain

ε_{ij} = Dissipation

G_{ij}=Buoyancy Production

Unfortunately, several of the terms in the exact equation are unknown and modelling assumptions are required in order to close the equations. Of the various terms in these exact equations, C_{ij}, D_{Lij} and P_{ij} do not require any modelling, but D_{ij}, G_{ij}, ε_{ij} and Φ_{ij} need to be modelled. There are several options to model those terms but only the LRRIP model option has been employed in the present work and it is explained next.

Due to numerical stability, the turbulent diffusion transport is not modelled by the original proposal (GGDH) but with the gradient diffusivity relation, presented as:

$$D_{Tij}=\frac{\partial}{\partial x_k}\left(\frac{\mu_t}{\sigma_k}\frac{\partial\overline{u_i'u_j'}}{\partial x_k}\right) \qquad \text{Eq. 3-17}$$

where the turbulent viscosity, μ_t, is computed using the same equation for the SKE model (Eq. 3-9) and the turbulent Prandtl number is specified as a constant (σ_k=0.82).

Similarly, the effects of buoyancy G_{ij} are modelled based on the gradient diffusion relation and the ideal gases assumption as:

$$G_{ij}=-\frac{\mu_t}{\rho\,\mathrm{Pr}_t}\left(g_i\frac{\partial\rho}{\partial x_j}+g_j\frac{\partial\rho}{\partial x_i}\right) \qquad \text{Eq. 3-18}$$

The Pressure-Strain term has been estimated by using the Linear Pressure-Strain Model [Gibs78] [Laun89]. This is probably the most difficult term to model in

Eq. 3-16 and also very important for good model performance. The employed Linear Pressure-Strain model, also called the basic option by some second moment model specialists [Craf02] [Craf93], consists in the decomposition of the Pressure-Strain term as:

$$\Phi_{ij} = \Phi_{ij,1} + \Phi_{ij,2} + \Phi_{ij,w} \qquad \text{Eq. 3-19}$$

where $\Phi_{ij,1}$ is the slow Pressure-Strain term or the return-to-isotropy term, $\Phi_{ij,2}$ is called the rapid Pressure-Strain term, and $\Phi_{ij,w}$ is the near-wall treatment for the model and called the wall-reflection term. The slow Pressure-Strain term, $\Phi_{ij,1}$, is modelled from [Rott51] as:

$$\Phi_{ij,1} = -C_1 \rho \frac{\varepsilon}{k}\left[\overline{u_i' u_j'} - \frac{2}{3}\delta_{ij} k\right] \qquad \text{Eq. 3-20}$$

where C_1=1.8. The model for the rapid Pressure-Strain term, $\Phi_{ij,2}$, is taken from [Fu87] as:

$$\Phi_{ij,2} = -C_2\left[\left(P_{ij} + G_{ij} - C_{ij}\right) - \frac{2}{3}\delta_{ij}\left(P + G + C\right)\right] \qquad \text{Eq. 3-21}$$

where C_2 = 0.60, P_{ij}, G_{ij}, and C_{ij} are defined in the Eq. 3-16, $P = ½P_{kk}$, $G=½G_{kk}$, and $C = ½C_{kk}$.

Finally, the wall-reflection term, $\Phi_{ij,w}$, responsible for the redistribution of normal stresses near the wall, damps the normal stress perpendicular to the wall while enhancing the stresses parallel to the wall. It is approximated as proposed by [Gibs78]:

$$\begin{aligned}\Phi_{ij,w} = {} & C_1' \frac{k}{\varepsilon}\left(\overline{u_k' u_m'} n_k n_m \delta_{ij} - \frac{3}{2}\overline{u_i' u_k'} n_j n_k - \frac{3}{2}\overline{u_j' u_k'} n_i n_k\right)\frac{C_l k^{3/2}}{\varepsilon d} \\ & + C_2'\left(\phi_{km,2} n_k n_m \delta_{ij} - \frac{3}{2}\phi_{ik,2} n_j n_k - \frac{3}{2}\phi_{jk,2} n_i n_k\right)\frac{C_l k^{3/2}}{\varepsilon d}\end{aligned} \qquad \text{Eq. 3-22}$$

where C'_1 = 0.5, C'_2 = 0.3, n_k is the x_k component of the unit normal to the wall, d is the normal distance to the wall, and $C_l = C_\mu^{3/4}/\kappa$, where C_μ = 0.09 and κ is the von Karman constant (= 0.4187). The turbulent kinetic energy is calculated as $k = (1/2)\cdot\overline{u_i' u_i'}$.

The dissipation tensor term is modelled as:

$$\varepsilon_{ij} = -\frac{2}{3}\delta_{ij}\rho\varepsilon \qquad \text{Eq. 3-23}$$

where the scalar dissipation rate, ε, is computed from

$$\frac{\partial(\rho\varepsilon\bar{u}_i)}{\partial x_i}=\frac{\partial}{\partial x_j}\left[\left(\mu+\frac{\mu_t}{\sigma_\varepsilon}\right)\frac{\partial\varepsilon}{\partial x_j}\right]+C_{\varepsilon1}\frac{1}{2}\left[P_{ii}+C_{\varepsilon3}G_{ii}\right]\frac{\varepsilon}{k}-C_{\varepsilon2}\rho\frac{\varepsilon^2}{k} \qquad \text{Eq. 3-24}$$

and $\sigma_\varepsilon=1$, $C_{\varepsilon 1}=1.44$, $C_{\varepsilon 2}=1.92$ and $C_{\varepsilon 3}=tanh|u_g/u|$. The symbol u_g is the component of the flow velocity parallel to the gravitational vector and u is the component of the flow velocity perpendicular to the gravitational vector. With this and all previously mentioned approximations, the transport equations for the Reynolds stresses are in closed form and can be solved with appropriate boundary conditions.

3.2 Passive Scalar Flux Modelling

Similar to the Reynolds stresses in the RANS equation, the scalar flux term ($\overline{u_i'\phi'}$) appears after performing the Reynolds average to any scalar transport equation with the form of the species transport equation (Eq. 2-16). This new term is unknown a priori and needs to be modelled in order to close the set of governing equations. This chapter discusses the different ways to estimate the scalar fluxes.

Most of the research performed on turbulence closure modelling has been focused on momentum transport with much less attention paid to the transport of passive scalars. The main reason of these differences is because the mean velocity and turbulent stresses constitute very important input to the passive scalar flux equations, while the opposite is not true: passive scalar field is mathematically decoupled from the dynamical equations governing the flow field. A solution of the flow field is thus a prerequisite to the solution of the scalar field.

In addition to the passive scalar case, the equation of active scalar transport also brings the new scalar flux term after performing the Favre average. This term should also be modelled when an active scalar field is calculated. However, due to the primary interest of this thesis, the active scalar was only implemented using the simplest isotropic scalar gradient model. Consequently, the deduction of anisotropic scalar flux models is presented here only for passive scalar transport.

The modelling approach of scalar fluxes is usually carried out with the simplest isotropic scalar fluxes model. The simulation of passive pollutant dispersion in an urban environment by means of advanced anisotropic scalar flux models is extremely rare and therefore not well documented. From the literature review it can be observed that this is one of the first times that the second moment models are employed in this engineering application. With the intention to compare and access the prediction capabilities and possible improvement with the use of these advanced models, they have been implemented according to their classification as algebraic scalar flux models and second moment scalar flux models. Their deduction and formulation are explained in next sub-sections.

3.2.1 Algebraic Scalar Flux Models

The algebraic scalar flux models proposed in the present section are based on an explicit algebraic relation for $\overline{u_i'\phi'}$. The relation is not constructed from their traditional simplification of the transport equation for scalar fluxes, but rather from the use of tensor representation theorems based on a rationally assumed functional relationship reduced through the application of appropriate constraints. For the general case of a compressible, reacting flow with consideration of gravitational effects, the scalar fluxes follow a functional relationship as [Youn05]:

$$\overline{u_i'\phi'} = F\left(\overline{u_i'u_j'}, S_{ij}, \Omega_{ij}, \rho, \tau, \bar{\phi}, g_i, \overline{\phi'^2}, \frac{\partial\bar{\phi}}{\partial x_j}, \frac{\partial\bar{p}}{\partial x_j}, \frac{\partial\rho}{\partial x_j}, Ma\right) \qquad \text{Eq. 3-25}$$

where *Ma* is the Mach number, g_i is the gravity vector, τ is the turbulent time scale, $\bar{\phi}$ and $\overline{\phi'^2}$ are respectively the average concentration and its variance and S_{ij} and Ω_{ij} are respectively the mean rate of strain tensor (Eq. 3-10) and mean vorticity tensor (Eq. 3-6).

In the case of incompressible flow of passive scalar and neglecting buoyancy effects, the functional relationship can be written in a mathematical general representation as [Youn05]:

$$\begin{aligned} -\overline{u_i'\phi'} = {} & \alpha_1\frac{\partial\bar{\phi}}{\partial x_i} + \alpha_2\overline{u_i'u_j'}\frac{\partial\bar{\phi}}{\partial x_j} + \alpha_3 S_{ij}\frac{\partial\bar{\phi}}{\partial x_j} + \alpha_4\overline{u_i'u_k'}\,\overline{u_k'u_j'}\frac{\partial\bar{\phi}}{\partial x_j} + \alpha_5 S_{ik}S_{kj}\frac{\partial\bar{\phi}}{\partial x_j} \\ & + \alpha_6 W_{ij}\frac{\partial\bar{\phi}}{\partial x_j} + \alpha_7 W_{ik}W_{kj}\frac{\partial\bar{\phi}}{\partial x_j} + \alpha_8\left(S_{ik}W_{kj} + S_{jk}W_{ki}\right)\frac{\partial\bar{\phi}}{\partial x_j} \\ & + \alpha_9\left(\overline{u_i'u_k'}S_{kj} + \overline{u_j'u_k'}S_{ki}\right)\frac{\partial\bar{\phi}}{\partial x_j} + \alpha_{10}\left(\overline{u_i'u_k'}W_{kj} + \overline{u_j'u_k'}W_{ki}\right)\frac{\partial\bar{\phi}}{\partial x_j} \end{aligned} \qquad \text{Eq. 3-26}$$

where every α_i represent model coefficients with units that depend on the terms they multiply. They can be expressed as:

$$\alpha_i = F\left(k, \varepsilon, \overline{\phi^2}, \rho, I_\alpha\right) \qquad \text{Eq. 3-27}$$

With k and ε as the turbulent kinetic energy and its dissipation rate, respectively, and the density ρ. I_α represent all possible invariants of the relevant tensor variables which appear in Eq. 3-25.

Using additional assumptions in Eq. 3-26, (like negligible anisotropy, very small turbulent time scales, balance between rotational and irrotational strain-rates or for simple evaluation of the relevant terms and their order of magnitude), the majority of the algebraic scalar flux models proposed in the literature may be obtained. The algebraic scalar flux models are the simplest way to estimate the scalar flux term because they have the advantage of their simpler and shorter formulation alternative to the traditional, more complex scalar flux transport models. Table 3-6 presents some of the most common algebraic models with their corresponding coefficients.

Table 3-6: Algebraic Scalar Flux Models

Model Name	α_1	α_2	α_{3a}	α_{3b}	α_4	A_9
1.-Simple Eddy Diffusivity (SED)	μ_t / Sc_t	0.0	0.0	0.0	0.0	0.0
2.-Daly-Harlow (GGDH) [Daly70]	0.0	0.3τ	0.0	0.0	0.0	0.0
3.-Abe-Suga (ABE-SUGA) [Abe01]	0.0	0.0	0.0	0.0	$0.45\tau/k$	0.0
4.-Abe (ABE) [Abe06]	0.0	0.22τ	0.0	0.0	$0.45\tau/k$	0.0
5.-Younis et. Al. (YOUNIS) [Youn05]	$-0.045k\tau$	0.37	$-0.0037k\tau^2$	0.0	0.0	$-0.023\tau^2$
6.-Launder (WET)[5] [Laun88]	0.0	0.3τ	0.0	0.0	0.0	0.0

where Sc_t is the turbulent Schmidt number, τ ($=k/\varepsilon$ for SED model and $Max\left\lfloor k/\varepsilon ,6\sqrt{\nu/\varepsilon}\right\rfloor$ otherwise) is the turbulent time scale and the additional coefficients α_5, α_6, α_7 α_8 and α_{10} were always set to 0. One of the most relevant characteristics of the advance scalar flux models presented in this table (models 2 to 6) is their capability to assess the anisotropic behaviour of scalar transport. Therefore, this condition has been considered for the classification of scalar fluxes in two groups which are the isotropic and the anisotropic scalar flux models.

3.2.1.1 Isotropic Algebraic Scalar Flux Models

The first model presented in Table 3-6 is the simplest scalar flux model, here called the Simple Eddy Diffusivity (SED) model. It is the most common way to calculate the scalar fluxes in practical engineering applications and it is usually the only available model in most Computational Fluid Dynamic codes. The SED

---

[5] The WET model includes an additional term. i.e: $-\overline{u_i'\phi'} = C_\phi \tau\left(\overline{u_i'u_k'}\,\partial\overline{\phi}/\partial x_k + \overline{u_i'\phi'}\,\partial\overline{u}_i/\partial x_k\right)$

approach is numerically very stable, very simple and does not include much computer effort. This model assumes the gradient diffusion analogy between momentum and scalar transport with the proportionality factor of a usual constant turbulent Schmidt number (Sc_t) instead of a molecular Schmidt number (Sc).

The molecular Schmidt number is a dimensionless number defined as the ratio of molecular momentum diffusivity (kinematic viscosity) and molecular diffusivity of mass. The Sc number is used to characterize fluid flows in which there are simultaneous momentum and mass diffusion processes. In a similar way, the turbulent Schmidt number is defined as the ratio of the turbulent momentum diffusivity (eddy viscosity) μ_t and the turbulent mass diffusivity (Γ_t) dealing with the relation between turbulent diffusion by momentum and mass processes. The role of Sc_t in dispersion modelling has not been studied extensively, especially in urban areas. However, different estimates of this parameter have been published based on field or wind tunnel observations and CFD applications for different atmospheric and wind conditions.

Experimental studies of Sc_t are usually presented together or in relation to its heat transfer analogue turbulent Prandtl number (Pr_t). Reynolds [Reyn75] measured the Pr_t and Sc_t under different flow conditions and proposed empirical formulae representing a limited amount of data. Koeltzsch [Koel00] performed wind tunnel experiments in a turbulent boundary layer above a flat plate and found a strong dependence of Sc_t with height in the boundary layer. Wilson et al. [Wils01] and Flesch et al. [Fles02] reported estimated values of Sc_t based on field observations under different flow conditions. They suggested a Sc_t of 0.6 with a standard deviation of 0.31 based on measurements of pesticide concentrations in the atmosphere.

CFD modelling of the turbulent mass transport around building or urban diffusion problems has usually been carried out using constant Sc_t values ranging from 0.7 to 0.9 (e.g. Baik et al., [Baik03]; Kim et al., [Ketz02]; Cheng and Hu, [Chen05] 2005; Wang and McNamara, [Wang06]; Lien et al., [Lien06]; Santiago et al., [Sant07]; Yassin et al., [Yass08]). These values are usually set as the default in most commercial CFD codes. As pointed out by Tominaga and Stathopoulos [Tomi07], it is very surprising that many papers do not report the Sc_t values used in the simulations, although this parameter is known to have a significant effect on the predictions.

There are various CFD research studies which have investigated the sensitivity of Sc_t on the predicted concentration in the empty boundary layer and in the presence of buildings. Riddle et al. [Ridd04] and Di Sabatino et al. [Disa07] studied this problem for a point source within a neutral boundary layer and highlight that the typical underestimation of the turbulent kinetic energy near the ground obtained from most CFD codes strongly affects the dispersion predictions. Therefore, they proposed to artificially increase the plume dispersion by reducing the Sc_t to 0.3 and 0.4 respectively. Tang et al. [Tang06] performed a parametric study using various Sc_t values which he compared with the field data under near-neutral stability conditions and reported the best agreement (on average) using Sc_t=1.

The influence of Sc_t on dispersion around an isolated cubic building was recently investigated by Tominaga and Stathopoulos [Tomi07] and Blocken et al. [Bloc08]. They publish the best agreement with measurements by using Sc_t=0.3 and both studies discuss an observed underestimation of the lateral plume spread.

CFD simulations of dispersion around more complex structures, such as street canyons and building arrays, have presented interesting results. Hanna et al. [Hann04] and Milliez and Carissimo [Mill07] pointed out that a large number of obstacles increase the production of turbulent kinetic energy and these obstacles compensates the underestimation of turbulent diffusion often observed in RANS simulations of open countryside or single buildings. Di Sabatino et al. [Disa08] mention the possibility of artificially reducing Sc_t to increase the turbulent diffusion of species. A change of the turbulent Schmidt number may produce a change in the diffusion coefficient in the scalar diffusion equation, and therefore it would influence only the diffusion mechanism and not the fluid dynamics. In this sense the Schmidt number in CFD models may be considered merely as an adjustment parameter which needs to be evaluated on the basis of field or laboratory experiments, or with other models. Di Sabatino et al. [Disa07] support this conclusion with the obtained variable Schmidt number as a function of the packing density (ratio of built to un-built area), i.e. the larger the packing density the lower the Schmidt number. They suggest that Sc_t =0.4 for low and medium level packing density and they project further lowering the Sc_t for further increasing the density. A similar tendency of Sc_t was found by Gromke et al. [Grom08] in a study of an isolated street canyon with avenue-like tree planting. They found that when the street canyon was filled with vegetation, the optimum Sc_t number (around 0.6 to 0.7) was larger than the typical value used for an empty street canyon.

As shown above, the optimum value provided in previous studies for Sc_t are sometimes very different from the commonly used values of 0.7–0.9. Values from about 0.3 to 1 are recommended in the literature, depending on various flow properties and geometries. Nevertheless, it is clear that the Sc_t has a large influence on the prediction accuracy of mass transfer. In general, the turbulent momentum diffusion is often underestimated when using RANS models. An underestimation of the turbulent diffusion for scalars can be compensated for with a smaller value of Sc_t

in order to provide better predicted results on concentration distribution. Since most commercially available CFD codes operate with default values in the range of $Sc_t = 0.7–1.0$, it is recommended [Disa07] that the turbulent Schmidt number be critically reviewed when using standard turbulence models for pollutant dispersion investigations in urban areas. However, it should be kept in mind that such cancellation of errors cannot be generalized, so the optimum value of Sc_t should be considered from the viewpoint of the dominant effect in the turbulent mass transport.

3.2.1.2 Anisotropic Algebraic Scalar Flux Models

The SED model implies that turbulent diffusivity is isotropic and that turbulent scalar fluxes and mean scalar gradients are aligned (See Table 3-6). It has been proven (see e.g. [Durb01]) that neither result holds true in complex two- and three-dimensional shear flows. Consequently, the second presented model, originally introduced by Batchelor [Batc49], proposes a generalization of the gradient transport hypothesis inserting the new definition of a tensor diffusion coefficient. Subsequently, [Daly70] proposed this tensor diffusion coefficient directly proportional to the Reynolds stresses. This proposal is based on the supposition that all the mean stream and buoyancy generation is obliterated by pressure fluctuations in the scalar flux transport equation. Thus, this model arises as the simplest one that includes anisotropy effects and allows the non-alignment with the gradient of scalar fluxes, overcoming the principal SED model limitation. However, two-dimensional simulation of this model, Generalized Gradient Diffusion Hypothesis (GGDH), has shown that it cannot successfully predict the two components of the scalar flux vector with a single coefficient because near walls the scalar fluxes correlates stronger with the streamwise than with normal Reynolds stresses [Kim89]. Application of this model can be found in many different transport phenomena including the diffusion term in the transport equations of momentum and scalar fluxes (See Chapter 3.1.3 and 3.2.2.2), and as a direct approximation of the analogue heat transfer term called turbulent heat fluxes (e.g. [Abe01], [Rubi91], [Roge89]).

Subsequently, the DNS calculations from [Kim89] were interpreted by [Abe01] to propose the “quadratic” (here called ABE-SUGA) model with the intention to simplify the determination of the model coefficient in the GGDH model. Thus, this model is presented as a modification of the GGDH inserting a scaling factor of Reynolds stresses non-dimensionalized with the turbulent kinetic energy. Also [Abe01] in the same and other posterior publications proposed a combination of GGDH and the “quadratic” models. This new combination of models with their respective model coefficients was finally presented by [Abe06] and it is referred hear as the ABE model. Although these two models were developed for passive scalar transport, their model calibration and applications have been used almost exclusively for heat transfer purposes.

The model from Younis et al. [Youn05] (here called YOUNIS) is based on the enhancement of the isotropic approach of the SED model and corresponds to the most recent and complex algebraic model formulation implemented in the present work. It was developed from the general functional relationship presented by Eq. 3-26 under the assumption of small anisotropic effects, a small turbulent time scale and a balance between rotational and irrotational strain rates. Its final formulation includes the isotropic term with the collaboration of Reynolds stresses and velocity gradients. Due to this very recent model's development, it has not been implemented in many different engineering applications beyond heat transfer (e.g. [Diet07]). This model has recently been improved for the near-wall treatment including a variable model coefficient using Lumley's flatness factor [Youn07].

Finally, the WET [Laun88] model is a little bit special because this model has an additional term which does not perfectly fit in the mathematical general representation of Eq. 3-26. The reason is because its deduction comes directly from the scalar flux transport equation (Eq. 3-28) and it is based on the assumption that the scalar fluxes are proportional to their rate of production. The WET model is distinctive for two main differences in its formulation. First, it is implicit in the scalar fluxes which is an undesirable feature for the algebraic models because it may produce anomalies in complicated geometries [Youn05]. Secondly, the WET model is not of the gradient transport type, which means that it does not allow the model to sustain finite levels of turbulent scalar fluxes in the absence of mean scalar gradient. In practice, it is possible to occur but only when the scalar field is being transported by the mean flow of the turbulence. These transport processes constitute a non-local mechanism that cannot be catered by a rotational algebraic closure. Probably due to this implicit formulation and the convergence problems that it produces, this model is not usually employed in many engineering applications of anisotropic model comparisons for heat transfer purposes.

In general, algebraic scalar flux models can be classified in two main groups. The first group of models depends exclusively on Reynolds stresses (models like GGDH, ABE-SUGA and ABE) and the second group also depends on velocity gradients as an improvement of the SED model (e.g. [Youn05], [Laun88]). The majority of the models in the second groups are not directly applicable for high velocity gradients close to the walls (see e.g. [Diet07]). Therefore damping functions or variable model coefficients are usually implemented for these models in near-wall flows.

As a final note, it must be mentioned that several of the implemented algebraic scalar flux models are probably still under development and therefore they have not been implemented or calibrated in many engineering applications as pollution dispersion in atmospheric environments. This understanding is important because it means that the recommended standard model coefficient is not always the best selection for each model in each specific test case. However, only their standard model coefficients have been used for the model comparison in this work.

3.2.2 Second Moment Models for Passive Scalars

The transport equation for the scalar fluxes can be obtained analogously to the transport equation for the Reynolds stress tensor. It is formulated by: (1) subtracting the species convection-diffusion equation (Eq. 2-4) from the mean scalar transport concentration (Eq. 2-16), (2) multiplying by $u_{i,}$ and (3) adding the result to the *i*-component of the momentum equation, multiplied by ϕ'. The result is the transport equation for the scalar flux:

$$\begin{aligned}\underbrace{\frac{\partial}{\partial x_k}\left(\bar{u}_k\overline{u_i'\phi'}\right)}_{C_{i\phi}}=&\underbrace{-\overline{u_i'u_j'}\frac{\partial\bar{\phi}}{\partial x_j}-\overline{u_j'\phi'}\frac{\partial\bar{u}_i}{\partial x_j}}_{P_{i\phi}}\underbrace{-\frac{1}{\rho}\overline{\phi'\frac{\partial p'}{\partial x_i}}}_{\Phi_{i\phi}}\underbrace{-(\alpha+\nu)\overline{\frac{\partial\phi'}{\partial x_j}\frac{\partial u_i'}{\partial x_j}}}_{\varepsilon_{i\phi}}\\&\underbrace{-\frac{\partial\left(\overline{u_i'u_j'\phi'}\right)}{\partial x_j}-\frac{\partial}{\partial x_j}\left(\alpha\frac{\overline{u_i'\partial\phi'}}{\partial x_j}\right)-\frac{\partial}{\partial x_j}\left(\nu\frac{\overline{\phi'\partial u_i'}}{\partial x_j}\right)}_{D_{i\phi}}\end{aligned}\qquad\text{Eq. 3-28}$$

where

$C_{i\phi}$ = Convection of scalar flux term

$P_{i\phi}$ = Production of scalar flux term

$\Phi_{i\phi}$ = Pressure-Scalar Gradient Term

$\varepsilon_{i\phi}$ = Molecular Dissipation or Destruction of Scalar Fluxes

$D_{i\phi}$ = Turbulent and Molecular Diffusion of scalar flux term

The convection of scalar fluxes ($C_{i\phi}$) does not need modelling. The production of scalar flux term ($P_{i\phi}$) expresses the rate of creation due to the combined actions of mean velocity and mean scalar gradients. The former tend to increase the velocity fluctuations and the latter intend to increase the magnitude of the scalar fluctuations. The molecular dissipation or destruction term ($\varepsilon_{i\phi}$) is associated with small scales. The isotropic value of the scalar flux dissipation rate is zero and also negligible in non-isotropic flows when the turbulence Reynolds number is high. The turbulent and molecular diffusion ($D_{i\phi}$) rapidly remove small scale directional preferences, so at a high Reynolds number, the small scale motion is nearly isotropic. Also based on this consideration, the turbulent diffusion controls the rate of mixing, thus the molecular diffusion of the scalar flux term is usually neglected. The pressure scalar gradient term ($\Phi_{i\phi}$) is the counterpart of the pressure-strain term in the stress equation and of main relevance in the balance of this equation. With the direct dissipation negligible, it provides the mechanism which limits the growth of the fluxes.

The last three terms in Eq. 3-28 need to be modelled with the intention to close the turbulent scalar flux transport equation. Next some models to estimate the Pressure-Scalar term ($\Phi_{i\phi}$) and the Turbulent Diffusion Term ($D_{i\phi}$) are shown. The molecular dissipation or destruction term is sometimes included as a part of the turbulent diffusion term. However, in the present work it is neglected based on its low magnitude in comparison to the turbulent diffusion; thus, no model for this term is proposed.

3.2.2.1 Pressure-Scalar Term

After neglecting the influence of viscous transport and dissipative terms, only the pressure-scalar gradient term is responsible for counteracting the scalar fluxes production. Therefore, the accuracy of the pressure-scalar gradient term ($\Phi_{i\phi}$) model plays a determinant role. The approximation of this term is based on the Poisson equation for the fluctuating pressure multiplied by a concentration gradient. If buoyancy is neglected, the pressure-scalar term is usually decomposed into two parts:

$$\Phi_{i\phi} = \Phi_{i\phi 1} + \Phi_{i\phi 2} \qquad \text{Eq. 3-29}$$

where $\Phi_{i\phi 1}$ is the slow part and $\Phi_{i\phi 2}$ is the rapid part, and they are the analogue to the slow and rapid pressure-strain terms of Reynolds stress models (See Eq. 3-16). A general expression to include the different model proposals available in the literature can be written as [Shab97]:

$$\Phi_{i\phi} = -C_{0\phi}\frac{1}{\tau}\overline{u_i'\phi'} + C_{1\phi}\frac{\overline{u_i'u_j'}}{\tau}\frac{\partial\overline{\phi}}{\partial x_j} + C_{2\phi}\overline{u_j'\phi'}\frac{\partial\overline{u_i}}{\partial x_j} + C_{3\phi}\overline{u_j'\phi'}\frac{\partial\overline{u_j}}{\partial x_i} \qquad \text{Eq. 3-30}$$

where the first two terms correspond to the slow (turbulence) part and the last two correspond to the rapid (mean strain) part. Most of the first proposals for approximating the scalar-flux term include only the slow part. Nowadays, the importance of the rapid part effects on the pressure fluctuations is generally recognized, at least in approximating the pressure-strain correlation in the stress equation. However, there is not consensus in the literature on the value for the constants. Some of them are summarized in the next table.

Table 3-7. - Resume of different pressure-scalar gradient models coefficients.

Case	$C_{0\phi}$	$C_{1\phi}$	$C_{2\phi}$	$C_{3\phi}$
Basic (Rotta-Monin) [Rott51][Moni65]	3.0	0	0	0
Launder [Laun75b]	3.2	0	0.8	-0.2
Launder [Laum75c]	3.2	0	0.5	0
Gibson-Launder [Gibs78]	3.0	0	0.33	0
Donaldson [Laun78]	5.0	0	-	-
Owen [Laun78]	4.1	0	0	0
Meroney [Laun78]	2,5	0	0	0
Jones-Musonge[6] [Jaya69]	C_1^*	0.12	1.09	0.51
Launder [Laun89]	2,9	0	0.4	0
Craft [Craf93]	3.0	0	0.5	0
Durbin [Durb93]	2.5	0.45	0	0
Shabany-Durbin [Shab97]	2.89	0	0.41	0.21
Wikstrom [Wiks98][7]	3.2	0.7	0	-1.0
Hanjalic-Jakirlic [Hanj02]	3.5	0	0.55	0

In Table 3-7 an untidy disarray among the various proposals is presented, which reflects the fact that most of these suggestions are based on comparison with specific non-universal data and sometimes without any recourse to experimental data. All cited models include a model coefficient for the slow part first term, ($C_{0\phi}$ in the order of 3), which is usually recognized as the direct counterpart of the [Rott51] "return to isotropy" model from the momentum stress equations. Similarly used but less common appears in the third column the recommendation of the first term for the rapid part ($C_{2\phi}$ in the order of 0.5). Finally, only one from the 14 cited models includes the four model coefficients, and three and four models of the list include the use of the second slow part ($C_{1\phi}$) or second rapid part ($C_{3\phi}$) terms as an intention to accommodate effects of turbulent anisotropy.

In addition to these "basic" second moment models, some further advanced or complex models for the pressure-scalar gradient term can be found in literature. Some examples are the proposal given as the TLC model from Craft and Launder [Craf96] and some newer models such as [Wiks00] and [Lueb01]. However, the validation of these recent models is still limited to very few applications/cases.

---

[6] The first model coefficient is: $C_1^* = 3 / \left(1 + 3\sqrt{b_{ij}.b_{ij}}\right)$ where the anisotropy tensor is $b_{ij} = \frac{\overline{u_i'u_j'}}{2k} - \frac{1}{3}\delta_{ij}$;

[7] Wikstrom uses a different time scale based on the mixture of the dynamic (k/ε) and an analogue scalar (k_ϕ/ε_ϕ) time scale. Please see the cited reference for details.

3.2.2.2 Turbulent Diffusion Term

The turbulent diffusion term is usually neglected in homogeneous turbulent flow, but to calculate inhomogeneous flows, it is required. The estimation of the turbulent diffusion term is proposed as [Laun78]:

$$D_{i\phi} = \frac{\partial}{\partial x_j}\left(\overline{u'_i u'_j \phi'}\right) \approx \frac{\partial}{\partial x_j}\frac{k}{\varepsilon}\left(C_1\left(\overline{u'_i u'_l}\right)\frac{\partial \overline{u'_j \phi'}}{\partial x_l} + C_2\left(\overline{u'_j u'_l}\right)\frac{\partial \overline{u'_i \phi'}}{\partial x_l}\right) \qquad \text{Eq. 3-31}$$

where the constants C_1 and C_2 are a pair of model coefficients which vary according to the different authors' proposals as 0.15 and 0 by [Wyng74], 0.1 and 0.1 by [Laun78], 0.18 and 0 by [Craf93], 0.15 ± 0.04 and 0 by [Durb01] or 0.15 and 0 by [Hanj02].

As mentioned earlier, the majority of the model proposals for turbulent diffusion include only the first term of the general model correlation presented by Eq. 3-31. This assumption is equivalent to make use of a calibrated Generalized Gradient Diffusion Hypothesis (GGDH) model from [Daly70] taken from a severe truncation of the third-moment transport equations. This assumption is the most common method used to estimate the turbulent diffusion term ($D_{i\phi}$). Similar to the scalar-pressure gradient term, some more advanced and complex models for turbulent diffusion can be found in the literature (see e.g. [Wiks98], [Craf02b] and [Ilyu02]). In the present work, considering passive scalar without buoyancy effects, the GGDH model was employed with the coefficients C_1=0.15 and C_2=0.

3.3 Near Wall Modelling Approach

Turbulent flows are significantly affected by the presence of walls due to the imposition of the no-slip boundary condition in such regions. Very close to the walls, the viscous effects are significant and govern the fluid motion. However, the turbulence is rapidly augmented with the wall distance by the production of turbulent kinetic energy and the large gradients in mean velocities. The pollutant concentrations, as a passive scalar, are directly affected by the accuracy of these boundary fluid flow models.

The majority of turbulence models given in the previous chapters are suitable for completely developed turbulent flows. But the validity of these models is questionable in the regions where the viscous effects prevail over the turbulence. To solve this problem, the easy and favourable results of near-wall functions have been converted to a common practice for a turbulence modelling assumption. The inclusion of near-wall models can significantly impact the fidelity of numerical solutions.

Therefore, accurate representation of the flow in the near-wall region determines successful predictions of wall-bounded turbulent flows.

The derivation of the velocity profile in a boundary layer can be found in any fundamental fluid mechanic book. For modelling purposes, it is usually divided and approximated in several regions as in Figure 3-1. The first sub-layer beside the wall is the viscous sub-layer, which extends from the wall to the non-dimensional wall distance $z^+ \approx 5$. In this region the molecular viscosity plays a dominant role in momentum and species transport. The other important part, the turbulent or log-law region, extends from about $z^+ > 30$ to the first 30% of the complete boundary layer ($z/\delta < 0.3$, where δ is the boundary layer thickness). It is in this region where turbulence plays the major role. The buffer layer is the overlap or intermediate region between the viscous sub-layer and the log-law region where both phenomena, viscous and turbulence transport, have similar magnitude. Finally, in the top wake region, the constant free stream velocity is usually approached.

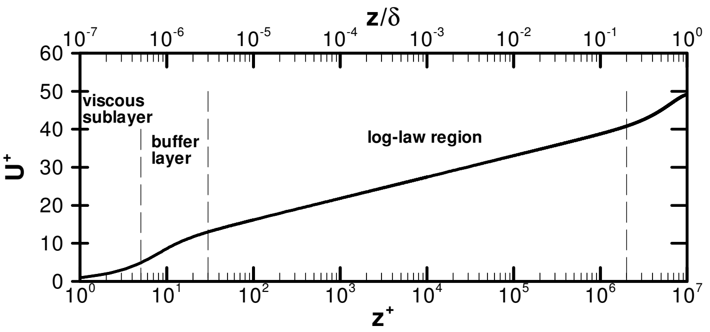

Figure 3-1. Boundary layer profile of non-dimensional velocity $u^+(=u\cdot z/u_\tau$, where $u_\tau=[\tau_w/\rho]^{1/2})$ as a function of the non-dimensional wall distance $(z^+ \equiv \rho\cdot u_\tau/\mu)$ and the non-dimensional wall distance z/δ.

Analytical wall functions have been developed to estimate the near wall flow field for velocities and species concentrations in every region of the boundary layer. Next, the formulation and implementation of the wall functions used in the software are presented and explained for each of the transport equations of interest.

3.3.1 Near-Wall Functions

The commercial software employed for the numerical simulation of pollutant dispersion uses by default (for all transport equations) the so-called standard wall functions. This is the most common approach to model the flow at the wall. Here the viscosity affected region close to walls is bridged by wall functions, removing the necessity to resolve the large velocity gradients near the walls. These functions are applied always in the first cell beside the wall with the purpose of bridging the numerical solution away from the wall to the analytical solution at the walls.

The employed standard wall functions are taken from the proposal of Launder and Spalding [Laun74]. The law-of-the-wall for mean velocity reads:

$$u^* = \frac{1}{\kappa}\ln\left(Ez^*\right) \qquad \text{Eq. 3-32}$$

where

$$u^* = \frac{\bar{u}_P C_\mu^{1/4} k_P^{1/2}}{\bar{\tau}_W / \rho} \qquad \text{and} \qquad z^* = \frac{\rho C_\mu^{1/4} k_P^{1/2} z_P}{\mu} \qquad \text{Eq. 3-33}$$

and κ(= 0.4187) is the von Karman constant, E(= 9.793) is an empirical constant, $\bar{u}_P$ is the mean velocity of the fluid at the evaluation point P, k_p is the turbulence kinetic energy at the same point, z_p is the perpendicular distance from point P to the wall, and μ is the dynamic viscosity of the fluid.

This logarithmic law for mean velocity is implemented in the first adjacent cell beside the wall when $z^* > 11.225$. When the near wall mesh is finer than this lower limit, i.e. $z^* < 11.225$ at the first wall-adjacent cell's centre, it is applied to the linear or laminar stress-strain relationship $u^* = z^*$.[8]

For flows over rough walls, the log-law is still valid but the velocity decreases due to the increased drag exerted by the roughness elements. The reduction of the velocity is taken into account by the inclusion of a roughness measure in the logarithmic velocity distribution. The roughness is expressed in terms of the sand-grain roughness k_s and the velocity change is taken into account inserting an additional parameter ΔB. Then, the log-law for flows over rough walls reads:

$$u^* = \frac{1}{\kappa}\ln\left(Ez^*\right) - \Delta B \qquad \text{Eq. 3-34}$$

The new inserted term ΔB is a function of the non-dimensional roughness height k_s^+ $(= u_\tau \cdot k_s/\nu)$. The influence of this roughness is divided into three regimes. For $k_s^+ \leq 2.25$ the wall is called hydrodynamically smooth because the roughness has no influence on the velocity distribution, i.e. $\Delta B = 0$. For $k_s^+ > 90$, the regime is called fully rough because the influence of the roughness is dominant. Between these values of k_s^+ the wall is transitionally rough.

---

[8] It should be noted that the laws-of-the-wall for mean velocity and species are based on the wall unit, z^*, rather than on the standard z^+ $(\equiv \rho u_\tau z/\mu)$. However, these quantities are approximately equal in equilibrium turbulent boundary layers.

Several empirical formulas have been proposed to describe the dependence of ΔB on k_s^+, (e.g., [Ligr86] and [Cebe77]). The proposal from [Cebe77] is implemented in the commercial code FLUENT 6.3. For a fully rough regime it is:

$$\Delta B = \frac{1}{\kappa}\ln\left(1 + C_r k_s^+\right) \qquad \text{Eq. 3-35}$$

where the constant $C_r \in [0,1]$ must be chosen by the user. A discussion of the equivalent z_0 roughness commonly used in meteorology is given by [Fran07b].

Similarly to the velocity, the law-of-the-wall for the mean species ($\bar{\phi}$) can be expressed as:

$$\phi^* = \frac{\left(\bar{\phi}_{i,w} - \bar{\phi}_i\right)\rho C_\mu^{1/4} k_p^{1/2}}{J_{i,w}} = \begin{cases} Sc \cdot z^* & , z^* < z_\phi^* \\ Sc_t\left[\frac{1}{\kappa} Ln\left(Ez^*\right) + P_\phi\right] & , z^* > z_\phi^* \end{cases} \qquad \text{Eq. 3-36}$$

where $\bar{\phi}_i$ is the species mass fraction in the cell adjacent to the wall, $\bar{\phi}_{i,w}$ is the species mass fraction at the wall, Sc and Sc_t are the molecular and turbulent Schmidt numbers, respectively, $J_{i,w}$ is the diffusion flux of species at the wall, and ρ is the density of fluid. The non-dimensional thickness of the viscous sub-layer for species, z_ϕ*, is computed as the z^* value at which the linear law and the logarithmic law intersect each other.

Finally, P_ϕ is computed by using the formula given by Jayatilleke [Jaya69]:

$$P_\phi = 9.24\left[\left(\frac{Sc}{Sc_t}\right)^{3/4} - 1\right]\left[1 + 0.28e^{-0.007Sc/Sc_t}\right] \qquad \text{Eq. 3-37}$$

The turbulent parameters are solved in different ways depending on the selected turbulence model. When the differential Reynolds stress turbulence model LRRIP is used, the transport equation for the Reynolds stresses $\overline{u_i' u_j'}$ and ε are not calculated at wall-adjacent cells centres, but their respective specific values are set for this region instead. The turbulent kinetic energy at the wall-adjacent cells is obtained by solving the following equation.

$$\frac{\partial\left(\rho k \bar{u}_i\right)}{\partial x_i} = \frac{\partial}{\partial x_j}\left[\left(\mu + \frac{\mu_t}{\sigma_k}\right)\frac{\partial k}{\partial x_j}\right] + \frac{1}{2}\left(P_{ii} + G_{ii}\right) - \rho\varepsilon \qquad \text{Eq. 3-38}$$

where σ_k=0.82. Eq. 3-38 can be obtained by contracting the modelled equation for the Reynolds stresses (Eq. 3-16). As one can expect, it is essentially the same equation used to estimate the turbulent kinetic energy in the SKE model.

The equation for the turbulent dissipation rate ε is not solved but instead is computed at the first node under the assumption of equilibrium between production and dissipation.

$$\varepsilon_P = \frac{C_\mu^{3/4} \cdot k_P^{3/2}}{\kappa \cdot z_P} \qquad \text{Eq. 3-39}$$

where the sub-index P makes reference again to the wall-adjacent cell's centre.

The Reynolds stresses also need to be specified at the wall-adjacent cells' centres. The near-wall values of the Reynolds stresses are calculated from the wall functions. Explicit wall boundary conditions for the Reynolds stresses are applied by using the log-law and the assumption of equilibrium, disregarding convection and diffusion in the transport equations for the stresses. With a local coordinate system with 1 as the stream wise direction and 3 as the perpendicular direction from the walls, see Figure 3-2, the near-wall values Reynolds stresses values are:

$$\frac{\overline{u_1'u_1'}}{k} = 1.098 \ , \ \frac{\overline{u_2'u_2'}}{k} = 0.655 \ , \ \frac{\overline{u_3'u_3'}}{k} = 0.247 \ , \ \frac{\overline{u_1'u_3'}}{k} = 0.255 \qquad \text{Eq. 3-40}$$

Similarly, when the k-ε turbulence model is used, the turbulent dissipation rate (ε) is solved by Eq. 3-39 and the turbulent kinetic energy (k) transport equation is solved in the whole domain including the wall-adjacent cells. The boundary condition for k imposed at the wall is:

$$\frac{\partial k}{\partial n} = 0 \qquad \text{Eq. 3-41}$$

where n is the local coordinate normal to the wall.

With these and previous assumptions, the turbulent parameters needed to solve the transport equations at the wall boundaries are completed.

3.3.2 Enhanced Wall Treatment

The enhanced wall treatment is a near-wall modelling method available in the used commercial software (FLUENT 6.3) that combines a two-layer model with enhanced wall functions [Flue06]. If the near-wall mesh is fine enough to be able to resolve the laminar sub layer (typically $y^+ \approx 1$), then the enhanced wall treatment will be identical to the two-layer zone model (explained below). This method is recommended by [Flue06] to skip the necessity of creating a very fine grid at the walls, which thus avoids the requirement of large computational resources in detailed near-wall flow simulations.

The two-layer near-wall model employed with the enhanced wall treatment consists of resolving the governing equations through the viscosity-affected near-wall region. The two-layer approach is used to specify the turbulent dissipation rate ε and the turbulent viscosity μ_t in the near-wall cells. Like in the standard approach, the domain is subdivided into a viscosity-affected region and a fully-turbulent region. The limit of these two regions is determined by a wall-distance-based turbulent Reynolds number, Re_z, defined as:

$$\mathrm{Re}_z \equiv \frac{\rho z \sqrt{k}}{\mu} \qquad \text{Eq. 3-42}$$

where z is the normal distance from the closest wall to the cell centres.

In the turbulent region ($\mathrm{Re}_z > \mathrm{Re}_z^*$, $\mathrm{Re}_z^* = 200$), the k-ε models or the LRRIP models are employed. In the viscosity-affected near-wall region ($\mathrm{Re}_z < \mathrm{Re}_z^*$), the one-equation model proposed by [Wolf69] is employed. In this one-equation model, the transport equation of momentum and turbulent kinetic energy k are calculated. However, the turbulent viscosity, μ_t, here is computed from:

$$\mu_{t,2layer} \equiv \rho C_\mu l_\mu \sqrt{k} \qquad \text{Eq. 3-43}$$

where the length scale l_μ is calculated by [Chen88]:

$$l_\mu = z C_l^* \left(1 - e^{-\mathrm{Re}_z / A_\mu}\right) \quad \text{where} \quad A_\mu = 70 \qquad \text{Eq. 3-44}$$

This two-layer definition is smoothly blended with the high-Reynolds-number formulation for the outer region, as proposed by [Jong92]:

$$\mu_{t,enh} = \lambda_\varepsilon \mu_t + (1 - \lambda_\varepsilon)\mu_{t,2layer} \qquad \text{Eq. 3-45}$$

where μ_t is the standard turbulent viscosity for high-Reynolds-number definition k-ε and LRRIP models. The blending function, λ_ε, is equal to unity far from walls and is zero very near to walls. The blending function chosen is:

$$\lambda_\varepsilon = \frac{1}{2}\left[1 + \tanh\left(\frac{\mathrm{Re}_z - \mathrm{Re}_z^*}{A}\right)\right], \quad \text{where} \quad A = \frac{|\Delta \mathrm{Re}_z|}{\tanh(0.98)} \qquad \text{Eq. 3-46}$$

When this model is chosen, the turbulent dissipation rate ε is computed from:

$$\varepsilon = \frac{k^{3/2}}{l_\varepsilon}, \quad \text{where} \quad l_\varepsilon = z C_l^* \left(1 - e^{-\mathrm{Re}_z / A_\varepsilon}\right) \qquad \text{Eq. 3-47}$$

and the additional constants are: $A_\varepsilon = 2 \cdot C_l^*$, and $C_l^* = \kappa C_\mu^{-3/4}$

Then, this law-of-the wall is expressed as a single equation for the entire wall region by blending linear (laminar) and logarithmic (turbulent) laws-of-the-wall using a function suggested by [Kade81]:

$$u^{+} = e^{\Gamma} u^{+}_{lam} + e^{\frac{1}{\Gamma}} u^{+}_{turb} \qquad \text{Eq. 3-48}$$

where the blending function Γ is given by:

$$\Gamma = \frac{-a\left(z^{+}\right)^{4}}{1+bz^{+}} \qquad \text{Eq. 3-49}$$

with $a = 0.01$ and $b = 5$.

Then, the enhanced wall functions are developed by smoothly blending an enhanced turbulent wall law with the laminar wall law. The enhanced turbulent law-of-the-wall for incompressible flow including pressure gradients and neglecting temperature and compressible effects was derived by [Flue06] from [Whit71] and [Huan06] proposals. It is calculated as:

$$\begin{gathered} \frac{du^{+}_{turb}}{dz^{+}} = \frac{1}{\kappa z^{+}}\left(S'\right)^{1/2} \\ S' = \begin{cases} 1+\alpha\, z^{+} & for \quad z^{+} < z^{+}_{s} \\ 1+\alpha\, z^{+}_{s} & for \quad z^{+} \geq z^{+}_{s} \end{cases} \end{gathered} \qquad \text{Eq. 3-50}$$

where

$$\alpha = \frac{\mu}{\rho^{2}\left(u^{*}\right)^{3}} \frac{\partial \overline{p}}{\partial x} \qquad \text{Eq. 3-51}$$

and z^{+}_{s} is the location at which the log-law slope will remain fixed. The default value in the software is $z^{+}_{s} = 60$. The α coefficient in Eq. 3-50 represents the influences of pressure gradients. As can be observed, when this coefficient is equal to zero, an analytical solution would lead to the classical turbulent logarithmic law-of-the-wall.

The enhanced wall functions for species follow the same approach developed for the profile of u^{+}. The unified wall species formulation blends the laminar and logarithmic profiles according to the method proposed again by [Kade81]:

$$\overline{\phi}^{+} = \frac{\left(\overline{\phi}_{w} - \overline{\phi}_{P}\right)\rho C_{P} u^{*}}{J_{\phi,w}} = e^{\Gamma_{b}} \overline{\phi}^{+}_{lam} + e^{\frac{1}{\Gamma_{b}}} \overline{\phi}^{+}_{turb} \qquad \text{Eq. 3-52}$$

where the notation for $\overline{\phi}_{P}$ and $J_{\phi,w}$ are the same as for standard species wall functions (see Eq. 3-36). Furthermore, the blending factor Γ_{b} is defined as:

$$\Gamma_b = \frac{a\left(Sc \cdot z^+\right)^4}{1 + b \cdot Sc^3 \cdot z^+} \qquad \text{Eq. 3-53}$$

where *Sc* is the molecular Schmidt number, and the coefficients *a* and *b* were defined in Eq. 3-49.

Apart from the formulation for ϕ^+ in Eq. 3-52, the enhanced wall functions for species follow the same logic as was shown for standard wall functions (see Section 3.3.1) and result in the following definition for turbulent and laminar wall functions:

$$\begin{aligned} \phi^+_{lam} &= Sc\left(u^+_{lam} \frac{\rho u^*}{2J_{\phi,w}} \bar{u}^2 \right) \\ \phi^+_{turb} &= Sc_t \bigg\{ u^+_{turb} + P + \frac{\rho u^*}{2J_{\phi,w}} \bigg[\bar{u}^2 - \left(\frac{Sc}{Sc_t} - 1 \right) \left(u_c^+\right)^2 \left(u^*\right)^2 \bigg]\bigg] \bigg\} \end{aligned} \qquad \text{Eq. 3-54}$$

where the quantity u_C^+ is the value of u^+ at the fictitious intersection between the laminar and turbulent region and the function P_ϕ is defined in the same way as for standard wall functions. For further details about this model, please refer to the original source of this section in the FLUENT 6.3 User's Guide [Flue06].

3.3.3 Derivation of Second Moment Boundary-Layer Flow Modelling

For the implementation of the algebraic scalar flux model, the mean species transport equation with a boundary condition of zero perpendicular flux of species from the wall must be specified. But special attention must be taken for the second moment models because there is a transport equation for every scalar flux, and therefore boundary conditions for every one of them must be set. A short analysis of the boundary condition for these equations is presented in this section.

Following the ideas from Prandtl in 1904 [Pran04], the boundary layer theory is applied to a plane surface with steady state, incompressible, viscous flow with the coordinates ‘x’ as the streamwise direction parallel to a flat plane with velocity ‘Uo’, and ‘z’ as the vertical direction normal to the plane with velocity ‘*w*’ (see Figure 3-2). The gravity is neglected, which is only important in boundary layers where fluid buoyancy is dominant.

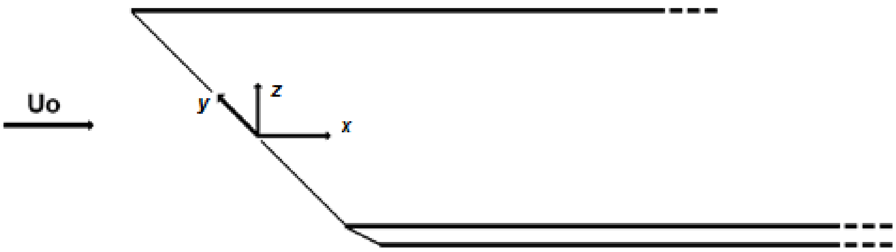

Figure 3-2. Flat Plane Boundary Layer coordinates

With the intention to analyse the wall boundary conditions for the scalar flux transport equations, the proposal from Hanjalic-Jakirlic [Hanj02] has been selected and analyzed. The general expression of this model for the scalar flux transport equation can be seen in 0:

At the walls, considering only the [Hanj02] proposal in the x-direction, the model transport equation for the $\overline{u'\phi'}$ scalar flux component would read:

$$
\begin{aligned}
&\overline{u}\frac{\partial \overline{u'\phi'}}{\partial x}+\overline{v}\frac{\partial \overline{u'\phi'}}{\partial y}+\overline{w}\frac{\partial \overline{u'\phi'}}{\partial z}=-\overline{u'u'}\frac{\partial \overline{\phi}}{\partial x}-\overline{u'v'}\frac{\partial \overline{\phi}}{\partial y}\\
&\quad-\left\{\overline{u'w'}\frac{\partial \overline{\phi}}{\partial z}\right\}-\overline{u'\phi'}\frac{\partial \overline{u}}{\partial x}-\overline{v'\phi'}\frac{\partial \overline{u}}{\partial y}-\left\{\overline{w'\phi'}\frac{\partial \overline{u}}{\partial z}\right\}\\
&\quad-\left\{C_{1\phi}\varepsilon\frac{\overline{u'\phi'}}{k}\right\}-C_{2\phi}\overline{u'\phi'}\frac{\partial \overline{u}}{\partial x}-C_{2\phi}\overline{v'\phi'}\frac{\partial \overline{u}}{\partial y}-\left\{C_{2\phi}\overline{w'\phi'}\frac{\partial \overline{u}}{\partial z}\right\}\\
&\quad+C_{4\phi}\frac{\partial}{\partial x}\left[\overline{u'u'}\frac{k}{\varepsilon}\frac{\partial \overline{u'\phi'}}{\partial x}+\overline{u'v'}\frac{k}{\varepsilon}\frac{\partial \overline{u'\phi'}}{\partial y}+\overline{u'w'}\frac{k}{\varepsilon}\frac{\partial \overline{u'\phi'}}{\partial z}\right]\\
&\quad+C_{4\phi}\frac{\partial}{\partial y}\left[\overline{v'u'}\frac{k}{\varepsilon}\frac{\partial \overline{u'\phi'}}{\partial x}+\overline{v'v'}\frac{k}{\varepsilon}\frac{\partial \overline{u'\phi'}}{\partial y}+\overline{v'w'}\frac{k}{\varepsilon}\frac{\partial \overline{u'\phi'}}{\partial z}\right]\\
&\quad+C_{4\phi}\frac{\partial}{\partial z}\left[\overline{w'u'}\frac{k}{\varepsilon}\frac{\partial \overline{u'\phi'}}{\partial x}+\overline{w'v'}\frac{k}{\varepsilon}\frac{\partial \overline{u'\phi'}}{\partial y}+\overline{w'w'}\frac{k}{\varepsilon}\frac{\partial \overline{u'\phi'}}{\partial z}\right]
\end{aligned}
\qquad \text{Eq. 3-55}
$$

Taking into account the boundary layer approximations for a fully developed flow with a large Reynolds number, $\overline{w}$ and $\partial/\partial x$ are zero. Additionally, considering that the flow is statistically independent in the *y*-direction, it is equal to a 2D flow for the presented coordinate system. Then, it can also be stated that $\overline{v}$ and $\partial/\partial y$ are zero. Finally, the diffusion transport through the wall boundaries is neglected because the diffusion transport of pollutants through the walls is not of current interest and therefore this case was not considered in the present study. With these simplifications, only the four terms between braces ({ }) need attention. After some algebra, the scalar flux for the streamwise direction (x) at the walls can be reduced to:

$$-\overline{u'\phi'}\Big|_w = \frac{1}{C_{1\phi}}\frac{k}{\varepsilon}\overline{u'w'}\frac{\partial\overline{\phi}}{\partial x} + \frac{k}{\varepsilon}\frac{(1-C_{2\phi})}{C_{1\phi}}\overline{w'\phi'}\frac{\partial\overline{u}}{\partial z} \qquad \text{Eq. 3-56}$$

and following an analogue procedure for the other two scalar flux components, the result is:

$$-\overline{v'\phi'}\Big|_w = 0.0 \qquad \text{Eq. 3-57}$$

$$-\overline{w'\phi'}\Big|_w = \frac{1}{C_{1\phi}}\frac{k}{\varepsilon}\overline{w'w'}\frac{\partial\overline{\phi}}{\partial z} \qquad \text{Eq. 3-58}$$

These results coincide with the well known second moment boundary layer model proposed by Gibson & Launder [Gibs78], neglecting buoyant terms. These three equations (Eq. 3-56, Eq. 3-57 and Eq. 3-58) must be used in the simulations as wall boundary conditions for the transport equations of scalar fluxes.

For the interest of this work, the simulation of pollution dispersion from a single pollutant source within a well defined urban area, there is not transport of pollutants from the solid walls (street or buildings) to the flow field. Therefore, the boundary condition at all wall boundaries for the transport equation of the mean species concentration is zero gradient in the direction perpendicular to the walls $(\partial\overline{\phi}/\partial z = 0)$. It is the equivalent setup to an adiabatic wall boundary condition if the scalar were the temperature. Including this new condition, the boundary conditions at walls for every one of the scalar flux transport equations is zero, i.e. $\overline{u'\phi'} = \overline{v'\phi'} = \overline{w'\phi'} = 0$.

The ratio of scalar fluxes for each of the implemented scalar flux models were calculated and compared using the analytic solution of the log-law. The scalar fluxes were evaluated at the first cell beside the walls because the near-wall treatment only takes place in those locations. These scalar flux ratios were compared with the values reported in the publication of the well known second moment scalar flux model of Gibson and Launder [Gibs78]. Comparing all presented models with their respective coefficients, the scalar flux ratios are:[9]

---

[9] The used turbulent kinetic energy and dissipation rate profiles have been calculated based on the log-law approximation of an equilibrium boundary layer over a rough wall from [Rich93].

Table 3-8. Comparison of scalar flux ratios using different models.

MODEL	***Scalar flux ratio*** $\overline{u'\phi'}/\overline{w'\phi'}$
SED (Sc_t=0.7)	0.0
GGDH [Daly70]	-1.03
Abe-Suga [Abe01]	-2.72
ABE [Abe06]	-1.89
WET [Laun89]	-2.03
Younis et al [Youn05]	-2.30
Hanjalic & Jakirlic [Hanj02]	-1.46
Gibson & Launder [Gibs78]	-2.1
Wyngaard et al. [Wyng71]	-4.0

The comparison of the models' behaviour at near-wall boundaries (Table 3-8) show that all the studied advanced anisotropic scalar flux models keep similar order of magnitude but within an appreciable range of differences. It can be seen that the SED model presents the worst predictions in comparison with those calculated by the old and well known second moment model from Gibson & Launder [Gibs78][10]. These results and their effects in the prediction of scalar fluxes in anisotropic flows (e.g. flows very close to walls) must produce appreciable differences for the calculation of pollution dispersion in atmospheric applications.

---

[10] [Gibs78] recognize that “the value of the near-wall heat-flux ratio in neutral conditions is the subject of considerable uncertainty” and justify his differences stating that “in this region the level of temperature fluctuations is necessarily very small and the signal contamination by velocity fluctuations may become significant”.

4 Numerical Procedure

The fundamental equations in fluid mechanics are partial differential equations and their analytical solutions are only possible under very simple geometry and fluid flow conditions. For a general fluid flow and geometry case, these equations can only be solved numerically through their transformation into algebraic equations by means of discretization in space and possibly in time. To perform this transformation, several numerical approaches can be employed, including the Finite Difference Method, Finite Element Method, Finite Volume Method and others. In the present chapter, only the Finite Volume Method (FVM) will be described because it is the method employed by FLUENT V6.3, which is the commercial software employed for the numerical simulations. Although most of the description of the FVM is based on the used capabilities of this software, many of the presented aspects can be directly transferred to other numerical approaches.

4.1 General Convection-Diffusion Transport Equation: Discretization and Solution

The conservative form of all governing equations in fluid mechanics and any other transport phenomenon of the convection-diffusion problem can be written in the following form:

$$\frac{\partial(\rho\phi)}{\partial t}+\nabla\cdot(\rho\phi\vec{u})=\nabla\cdot(\Gamma_\phi\nabla\phi)+S_\phi \qquad \text{Eq. 4-1}$$

where ϕ is a generic scalar variable. By setting ϕ equal to 1, u, v, w, h or c and setting appropriate values for the scalar diffusion coefficient Γ_ϕ and source terms S_ϕ, it is possible to obtain the continuity, the three momentum components, energy or species transport equations respectively. To solve Eq. 4-1 numerically, the flow field domain is first divided into discrete macroscopic control volumes (or cells) using a computational grid. The control volume technique consists of integrating the transport equation over each control volume, which yields a discrete equation that represents the conservation law on a control-volume basis. The discretization of the governing equations is illustrated by considering the integral of Eq. 4-1 over an arbitrary control volume *V*, as follows:

$$\int_V \frac{\partial(\rho\phi)}{\partial t}dV + \int_V \nabla\cdot(\rho\phi\vec{u})dV = \int_V \nabla\cdot(\Gamma_\phi\nabla\phi)dV + \int_V S_\phi dV \qquad \text{Eq. 4-2}$$

where ρ is the density and $\vec{u}$ is the velocity vector. The first term on the left side is easily recognized and signifies the rate of change of the total amount of fluid property ϕ in the control volume. In steady state problems, like in the present work, this first term is equal to zero. The convection and diffusion terms (second from the left side and first on the right side, respectively) can be rewritten as surface integrals by applying the Gauss divergence theorem. Integrating over a boundary surface *S* around the control volume *V* leads to:

$$\int_S \vec{n}\cdot(\rho\phi\vec{u})dS = \int_S \vec{n}\cdot(\Gamma_\phi\nabla\phi)dS + \int_V S_\phi dV \qquad \text{Eq. 4-3}$$

where $\vec{n}$ is the unitary vector in perpendicular direction to the surface *S*. The surface integrals are estimated with the second-order midpoint rule—i.e. the integral is approximated as the product of the integrand function evaluated at the surface centre, multiplied by the surface area:

$$\int_S FdA \approx F_{centre}.S \qquad \text{Eq. 4-4}$$

Similarly, the volume integral is also estimated with a second-order accurate approximation as the product of the source term S_P in the cell centre and the total volume:

$$\int_V S_\phi dV = \overline{S}_\phi V \approx S_{\phi,P}V \qquad \text{Eq. 4-5}$$

Considering the case of a general simple equidistant 2D mesh as appears in Figure 4-1, the integrals of Eq. 4-3 over each volume yield:

$$\underbrace{\sum_{i=n,s,e,w}^{N}\rho_i\vec{u}_i\phi_i\cdot\vec{A}_i}_{Convection} = \underbrace{\sum_{i=n,s,e,w}^{N}\Gamma_\phi\nabla\phi_i\cdot\vec{A}_i}_{Diffusion} + \underbrace{S_{\phi,P}V}_{Source} \qquad \text{Eq. 4-6}$$

where *N* is the number of faces enclosing the control volume. Here *N* = 4 for the 2-D case (*N* = 6 in 3-D), and the *i* indexes correspond to *n* = north, *s* = south, *e* = east, *w* = west. In this form, ϕ_i is the value of ϕ on the face *i*, $\rho_i\vec{u}_i\cdot\vec{A}_i$ is the mass flux through the face i, $\vec{A}_i$ is the area vector of the face i, $\nabla\phi_i$ is the gradient of ϕ at the face i, V is the cell volume, and $S_{\phi,P}$ is the value of the source in the cell centre. The calculated surface and volume integrals are second order accurate and the resulting equation is applied to each control volume in the entire computational domain.

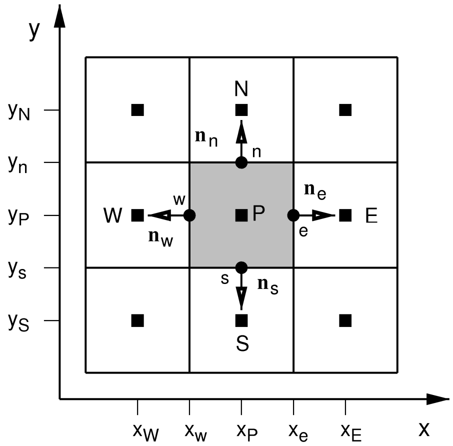

Figure 4-1. - Cartesian computational grid and definition of the volume V_P.

The convective and diffusive terms in Eq. 4-6 include the value of the variable ϕ and its gradient evaluated on the surfaces between two control volumes. The FVM estimates only the discrete value of the scalar ϕ at the cell centres; therefore, the face values ϕ_i must be approximated by an interpolation from the surrounding cells. There are different interpolation methods depending the respective term and they are explained next.

4.1.1 Approximation of Diffusion Terms

The discretization of the diffusion term is usually based on the simple linear profile assumption between the cell centres. At this level, the diffusion coefficient Γ_ϕ as well as any other fluid property are the assumed scalar constant quantity and are known in all locations. But the gradient on the face ($\nabla\phi_i$) must be estimated with the intention to calculate the diffusion transport through every face. The most common way to calculate the gradient of ϕ at the faces is using the central difference method. The standard central difference method evaluated at the east face (See Figure 4-1) would read:

$$\left(\frac{\partial\phi}{\partial x}\right)_e \approx \frac{\phi_E - \phi_P}{x_E - x_P} \qquad \text{Eq. 4-7}$$

where ϕ_E and ϕ_P are the cell centre values of ϕ and x_E and x_P are the corresponding coordinate positions at the east and middle cell centres. When the location of the face '*e*' is in the middle between *P* and *E* (e.g. on a uniform grid), the approximation is of second order accurate and first order otherwise.

Another possibility for the approximation of the derivatives in the face centres is to first approximate them in the cell centres and then interpolate these approximations to the face centres. This gradient is calculated based on the Green-Gauss theorem, as:

$$\nabla\phi \approx \frac{1}{V}\sum_{i=n,s,e,w}\phi_i\vec{A}_i \qquad \text{Eq. 4-8}$$

where ϕ_i is the value of ϕ at the cell face centred, computed from the simple arithmetic average of the values at the neighbouring cell centres. For boundary faces no interpolation is made, but the value of the gradient is derived from the boundary conditions, i.e. it is either fixed (Dirichlet) or extrapolated from the interior (von Neumann).

4.1.2 Approximation of Convective Term

With the intention to discretize the convective term, it is important to remember the fundamental definition of this phenomenon. Convection in the most general terms refers to the movement of fluid particles (parcels) within fluids. The convection, which is also called advection in meteorology, is the transport phenomenon of a substance or a conserved property with a moving fluid. Therefore, the convection transport must produce influence only in the direction of the flow instead of in the negative gradient directions like it occurs for the diffusion transport. Therefore, the discretization of this term is carried out in this work with the upwind schemes.

The upwind schemes mean that the main upstream transport direction is favoured. Two different options of upwind spatial discretization schemes available in the commercial software have been used during the simulations. They are:

1. The first-order upwind scheme considers that the cell-centre value of ϕ represents a cell-average and it remains constant through the entire cell. Therefore, the face value ϕ_i is set equal to the cell-centre value of ϕ in the

upstream cell. Using again the nomenclature from Figure 4-1 for the east face, it would be:

$$\phi_e = \begin{cases} \phi_P, \text{ if } \vec{u}_e \cdot \vec{n}_e > 0 \\ \phi_E, \text{ if } \vec{u}_e \cdot \vec{n}_e < 0 \end{cases} \qquad \text{Eq. 4-9}$$

where $\vec{u}_e$ corresponds to the face centre velocity vector. This result comes after retaining only the first term of the Taylor series expansion about *P* (for a cartesian grid and $(\vec{u} \cdot \hat{n})_e > 0$):

$$\phi_e = \phi_P + (x_e - x_P) \cdot \left.\frac{\partial \phi}{\partial x}\right|_P + \frac{(x_e - x_P)}{2} \left(\frac{\partial^2 \phi}{\partial x^2}\right)_P + H \qquad \text{Eq. 4-10}$$

where *H* denotes higher order terms. This method is very stable on computing iterative solutions but usually considerable numerical diffusion[11] is produced due to the truncation error.

2. The second-order upwind scheme consists of computing the cell face quantities (ϕ_i) using a linear interpolation approximation and the gradient limiting function factor of the multidimensional linear reconstruction approach proposed by [Bart89]. Thus, supposing a horizontal main flow direction ($(\vec{u} \cdot \vec{n})_e > 0$) and following the notation from Figure 4-1, the second-order upwind scheme computes the face value ϕ_e as:

$$\phi_e = \phi_P + (\nabla \phi)_P \cdot \vec{r}_e \cdot f \qquad \text{Eq. 4-11}$$

where ϕ_P and $(\nabla\phi)_P$ are the cell-centred values and its gradient in the upstream cell, and $\vec{r}$ is the displacement vector from the upstream cell centre to the face centre (in this case $\vec{r} = \vec{r}_e = (x_e - x_P,\ y_e - y_P)^T$). In comparison to the first-order interpolation scheme, this formulation approach allows higher-order accuracy at cell faces through the inclusion of an additional term from the Taylor series expansion (Eq. 4-10) of the cell-centred solution in the cell centroid. Also, the use of this approximation is usually recommended in best practice guidelines instead of the first-other upwind scheme. The second-order upwind scheme requires the implementation of good quality meshes and the determination of the gradients. The gradient term in Eq. 4-11 is computed using the divergence theorem as was written in Eq. 4-8.

---

[11] Numerical diffusion is a numerical error which appears after the discretization of the transport equations and depends on the spatial discretization scheme and numerical grid used [Ferz02].

Finally, the resultant value of the gradient ($\nabla\phi_P$) is limited by its multiplication with a function factor $f \in [0,1]$. This limiting function imposes the monotonic principle commanding that values of the linear reconstruction function must not exceed the minimum and maximum of neighbour centroid values (including the centroid value in *P*). Defining ϕ_{max}=max(ϕ_p, ϕ_{nb}) and ϕ_{min}=min(ϕ_p, ϕ_{nb}), it means:

$$\phi_P^{\min} \le \phi_P \le \phi_P^{\max} \qquad \text{Eq. 4-12}$$

Then, a function *f* is calculated as the minimum averaged function obtained over every neighbour cell

$$f = \min(\bar{f}_{Pn}, \bar{f}_{Ps}, \bar{f}_{Pe}, \bar{f}_{Pw}) \qquad \text{Eq. 4-13}$$

where

$$\bar{f}_{Pi} = \begin{cases} \min\left(1, \dfrac{\phi_P^{\max} - \phi_P}{\phi_i - \phi_P}\right), \text{if } \phi_i - \phi_P > 0 \\ \min\left(1, \dfrac{\phi_P^{\min} - \phi_P}{\phi_i - \phi_P}\right), \text{if } \phi_i - \phi_P < 0 \\ 1 \qquad\qquad\qquad , \text{if } \phi_i - \phi_P = 0 \end{cases} \qquad \text{Eq. 4-14}$$

and the sub-index *i* represents the face indices *n*, *s*, *e* and *w* from Figure 4-1.

The second-order upwind method was used in all simulation of this work except when it is specified otherwise.

It must be mentioned that a well known Best Practice Guideline [Case00] recognizes the possible improvement of results using the first-order spatial discretization scheme in special conditions. For example, [Case00] mentions that the first-order spatial discretization scheme can perform better than second-order when a characteristic wavy pattern with a wavelength of two cell sizes appears in the neighbourhood of steep gradients. Also, after some experience in simulation of pollution dispersion, the author of this book highlights the possible improvement of results of first-order over the second-order spatial discretization schemes when the selected combination of turbulent models underestimate the turbulence diffusion of scalar transport. Under these conditions the higher numerical diffusion of the first-order increases the transport and improves the accuracy of pollution dispersion. It is a typical case of compensation of errors or better known as “right for the wrong reason.”

4.1.3 Approximation of Source Terms

As shown in Eq. 4-5, the simplest approximation of the integrals, the mid-point rule, is applied to the sources. Here, the source term in the cell centre is approximated as the source integrand function evaluated at the cell centre. Following the notation from Figure 4-1, it would be:

$$\bar{S}_{\phi,P} V \approx S(\phi_P) V \qquad \text{Eq. 4-15}$$

where $S(\phi_P)$ is the original source function per unit volume evaluated at the middle cell centre. When there is considerable variation of S as a function of ϕ, a linearization of the source function is performed to improve the numerical solution of the equation. The linearization of the source function can then be written as:

$$S(\phi_P) = S_C + S_P \phi_P \qquad \text{Eq. 4-16}$$

where S_C represents the constant part of S and S_P is the coefficient of ϕ_P.

4.2 General Solution Procedure.

After making the substitution for the approximation of convective, diffusion and source terms, the discretized scalar transport equation (Eq. 4-6) contains only the unknown scalar variable ϕ at the cell centres from the middle (ϕ_P) and the surrounding neighbour (ϕ_N, ϕ_S, ϕ_E, ϕ_W, ϕ_{NN}, ϕ_{SS}, etc.) cells. Using any of the presented interpolation methods, reorganizing and grouping the coefficients for every cell centre value with the respective indexes (see Figure 4-1), the following equation is obtained:

$$a_P \phi_P = a_E \phi_E + a_W \phi_W + a_N \phi_N + a_S \phi_S + b \qquad \text{Eq. 4-17}$$

or in general form as:

$$a_p \phi_p = \sum a_{nb} \phi_{nb} + b \qquad \text{Eq. 4-18}$$

where the sub-index nb refers to each neighbour cell, a_P and a_{nb} are the linearized coefficients for ϕ_p and ϕ_{nb} respectively, and b represents the ϕ's non-dependent terms resulting from contributions of the constant part of the source term (S_C in Eq. 4-16) and the boundary conditions. The deduction of equation Eq. 4-18 was written for a 2D structured grid, but the number of neighbours would vary depending on the grid dimension and topology. In general, the number of neighbours will be equal to the number of faces enclosing the cell (boundary cells being the exception). The centred coefficient, a_P, in Eq. 4-18 is calculated as:

$$a_p = \sum_{nb} a_{nb} - S_P \qquad \text{Eq. 4-19}$$

Similar equations can be formulated for each cell in the entire computational domain, resulting in a closed algebraic system of equations of the form:

$$A_{ixi} \Phi_{ix1} = b_{ix1} \qquad \text{Eq. 4-20}$$

where A is the coefficient matrix of dimensions ixi, Φ is the vector solution of dimension ix1, and b is the independent terms' vector of dimension ix1. Here, i is equivalent to the number of unknowns or cells' centre values in the complete computational domain. Because every equation is formulated from a different control volume, the equations are independent of each other and the system has a unique solution. Due to the typical large size of the matrix A, this system of equations is usually solved using numerical methods.

There are two main families of methods available for the solution of an algebraic system of equations: direct and iterative methods. Direct methods are based on a finite number of arithmetic operations leading to an exact solution of a linear algebraic system. Unfortunately, the number of operations of the direct method can be very high and computationally too expensive, as they can increase up to N^3, where N is the number of unknowns. Furthermore, the discretization error is usually larger than the accuracy of computer arithmetic so there is no reason to solve the system of equations entirely accurately considering the final solution would never be better than the discretization error. In fact, direct methods are very seldom used and mostly limited to particular conditions.

On the other hand, the iterative methods consist of a succession of approximate solutions, leading to the exact solution after, in theory, an infinite number of iterations. In practice, a first initial solution is guessed and then the equations are used to systematically improve it until a tolerance error is reached. In CFD software, this is usually the method employed. The iterative point implicit Gauss-Seidel linear equation solver method is implemented and used for the simulations in the commercial software FLUENT 6.3 coupled to an Algebraic Multigrid (AMG) method. The AMG method uses a multigrid scheme to accelerate the convergence of the solver by computing corrections on a series of coarse grid levels, reducing the number of iterations and the CPU time required to obtain a converged solution [Flue06].

Considering the iterative solution methods, the system of equations presented by Eq. 4-20 would be modified to:

$$A\Phi^{(m)} - b^{(m)} = r^{(m)} \qquad \text{Eq. 4-21}$$

where $r^{(m)}$ is the residual vector and m is the iterations number. The residual vector is a very useful parameter because it allows monitoring the difference or imbalance between the current and the exact solutions. In a hypothetical case with an infinite computational precision, these residuals will go to zero as the solution converges. But on a real computer, the residuals reduce until some small value and then stop changing. The residual vector depends on the iteration number and it is usually monitored by its scaled norm. This "scaled" residual is defined as:

$$r^{(m)} = \frac{\sum_{All-Cells}\left(\sum a_{nb}\phi_{nb} + b - a_p\phi_p\right)}{\sum_{All-Cells}\left(a_p\phi_p\right)} \qquad \text{Eq. 4-22}$$

In the case of momentum equations, the denominator term $a_P\phi_P$ is replaced by $a_P v_P$, where v_P is the magnitude of the velocity at cell P. There is not a standard definition of residuals in all CFD software. As an example, in FLUENT v.6.3 uses a residual that is normalized with the maximum residual norm of the first five iterations for the continuity equation.

The iterative solution of Eq. 4-22 is limited by the user when a threshold value for the normalized residual is specified. This threshold value indicates the stopping criteria when the normalized residual for a solved variable drops below the corresponding convergence criteria. Overly high convergence criteria specified by the user may result in an incomplete iterative solution. Depending on the magnitude of the prescribed convergence criteria, the computed solution still contains appreciable errors from the incomplete iterative solution, as the computed solution does not fulfil Eq. 4-20. The magnitude of this incomplete iterative solution error should be analyzed by comparing the results obtained with different values for the convergence criteria.

4.3 Discretization of Continuity and Momentum Equation

As mentioned at the beginning of this chapter, the discretization principles of a generic conservation equation represented by Eq. 4-6 also apply to the momentum and continuity equations. Here, it is described how terms which differ between momentum equations and general conservation equations can be treated. The deduction and final formulation are always based on the considerations and simplifications needed for this work—i.e. for a Newtonian, steady and incompressible fluid flow.

The unsteady terms in the continuity and momentum transport equations are again neglected. After the corresponding substitutions, the convective and diffusion terms in both transport equations are very similar to their counterparts in the generic equation but, because the velocity is a vector, the substitution contributions become a bit more complex. Also, the momentum equations contain a pressure gradient term which is out of the form presented by the generic equation; thus, it is taken into account as a source term or as a surface force. The main complication of this discretization process is that since every velocity component appears in each of the momentum and continuity equations, all these equations are intricately linked. However, the most complex question to resolve is the role played by the pressure because it appears in each momentum equation and there is not an explicit (transport or other) equation for it.

The pressure field is solved by employing an algorithm for coupling the solution of the momentum and continuity equations. It is performed by a restriction in the solution of the flow field: if the correct pressure field is applied in the momentum equations then the resulting velocity field should satisfy continuity. With this in mind, a pressure equation is derived from the continuity and the momentum equations in such a way that the velocity field, corrected by the pressure, satisfies the continuity. Since the governing equations are nonlinear and coupled to one another, the solution process involves iterations wherein the entire set of governing equations is solved repeatedly until the solution converges. An additional problem arises because the pressure locations needed in the discretized equation do not coincide with the cell centres; therefore a spatial interpolation scheme of pressure must be implemented.

4.3.1 Discretization of the Momentum Equation

Following the discretization scheme described for the general scalar transport equation in Eq. 4-1 to the algebraic form given in Eq. 4-18, the discretization of each velocity component (e.g. the x-momentum equation) can be obtained by setting $\phi = u$, then:

$$a_p u_p = \sum a_{nb} u_{nb} + \sum p_f A \cdot \hat{i} + S_p \qquad \text{Eq. 4-23}$$

The y- and z-velocity momentum equations can be found analogously. Different from Eq. 4-18, the second and third terms on the right side of last equation correspond to the discretization of the pressure gradient term and any additional term from the viscous and turbulent stresses that cannot be represented by the diffusion term. These two terms are usually collected in the source term.

Nowadays, the most common way to solve Eq. 4-23 with CFD commercial software (including FLUENT 6.3) is by using a co-located scheme, which means that the pressure and velocity are both stored at cell centres. However, this equation requires the value of the pressure at the faces. If the pressure field at face locations is known, Eq. 4-23 can be solved in the manner outlined for the generic transport equation, and a velocity field obtained. Nevertheless, the pressure field is not known a priori and must be obtained as a part of the solution. Therefore, an interpolation scheme is required to compute the face values of pressure from the cell centre values.

One of the simplest schemes to interpolate pressure values at the faces is using the momentum equation coefficients. Following the notation from Figure 4-1, the east cell face pressure interpolation would read: ([Rhie83])

$$P_e = \frac{\dfrac{P_P}{a_P} + \dfrac{P_E}{a_E}}{\dfrac{1}{a_P} + \dfrac{1}{a_E}} \qquad \text{Eq. 4-24}$$

where a_P and a_E represent the momentum equation coefficients in the middle and east cells respectively.

This procedure works well as long as the pressure variation between cell centres is smooth. When there are jumps or large gradients in the momentum source terms between control volumes, the pressure profile has a high gradient at the cell face, and cannot be interpolated using this scheme.

Some alternate methods for cases in which the standard pressure interpolation scheme is not valid are:

- A linear scheme, which computes the face pressure as the average of the pressure values in the adjacent cells.
- A second-order scheme, which calculates the face pressure value in the manner used for second-order accurate convection terms (see Section 4.1.2). This scheme may provide some improvement over the standard and linear schemes, but it may have some trouble if it is used at the start of a calculation, with a bad mesh resolution or when the flows presents discontinuous pressure gradients, such as flow in porous media [Flue06].

All results reported in the present work are converged using the second-order scheme except when specified otherwise.

4.3.2 Discretization of the Continuity Equation

The continuity equation can be found after the substitution of $\phi = 1$ for the general transport equation (Eq. 4-1), together with the $\Gamma_\phi = S_\phi = 0$ for the diffusion coefficient and source terms. Finally, the corresponding integrated equation (Eq. 4-6) remains only with the convective term. Following the notation from the control volume in Figure 4-1 yields the discrete equation:

$$\sum_{i=n,s,e,w}^{N} \rho_i \vec{u}_i \cdot \vec{A}_i = 0 \qquad \text{Eq. 4-25}$$

where N is again the number of faces and $\rho_i \vec{u}_i \cdot \vec{A}_i$ is the mass flux through face A_i.

Next, the cell centre values of velocity (u_i) must be interpolated to the faces. To prevent checkerboard effect, the face value of the velocity is not averaged linearly; instead, momentum-weighted averaging—using weighting factors based on the a_P coefficient from the momentum equation—is performed. Using this procedure and the same notation as before, the total face flux J_e ($=\rho u_e$) going through the east face may be written as [Flue06]:

$$J_e = \rho_e \frac{a_p u_{P,n} + a_E u_{E,n}}{a_P + a_E} + d_e\left(\left(p_P + (\nabla p)_P \cdot \vec{r}_P\right) - \left(p_E + (\nabla p)_E \cdot \vec{r}_E\right)\right) = \hat{J}_e + d_e\left(p_P - p_E\right) \qquad \text{Eq. 4-26}$$

where p_P , p_E and $u_{P,n}$, $u_{E,n}$ are the pressures and normal velocities, respectively, within the two cells on either side of the east face, and the $\hat{J}_e$ term is a substitution which represents the influence of velocities in this cell. The term d_e is a function of the relation between the average face area perpendicular to the flux, and the a_P and a_E which are the coefficients from the momentum equation.

4.3.3 Pressure-Velocity Coupling

Pressure-velocity coupling is achieved by using Eq. 4-26 as an additional condition for pressure. Some of the most common algorithm options for pressure-velocity coupling are SIMPLE, SIMPLER, SIMPLEC, PISO, etc. The SIMPLE algorithm was selected for all simulations in the present work. The problems associated with the non-linearity of the momentum equations and the coupling between transport equations are tackled by adopting an iterative solution strategy. The majority of these schemes are based on the predictor-corrector approach, which consists of improving the calculated or guessed solution of the previous iteration.

The most popular solution algorithms for pressure and velocity calculations with the finite volume method possess the following common steps:

- Solve discretized momentum equation to yield intermediate velocity field.
- Calculate pressure or equivalent mass flux correction by solving the continuity equation in the form of an equation for pressure (Eq. 4-26).
- Correct pressure and velocities by adding the correction to the corresponding previous iteration result.
- Solve all other discretized transport equations (e.g. k, ε, ϕ).
- Repeat until p, u, v, w and any scalar ϕ fields have all converged.

4.3.4 Under-Relaxation of Variables

In an iterative solution of the algebraic equations or in the overall iterative scheme employed for handling nonlinearity, the calculation processes is often susceptible to divergence unless some under-relaxation is used. Additionally, over or under-relaxation are often useful to speed up or to slow down the changes, from iteration to iteration, in the values of the dependent variable. The under-relaxation of a variable ϕ consists of the reduction of the change produced during each iteration by limiting the influence of the previous iteration over the present one. If you choose a small value, it may prevent divergence or oscillations in residuum developing, but at the same time the solution may need more time to converge. In a simple form, the new value of the variable ϕ within a cell depends upon the old value, ϕ_{old}, the computed change in ϕ, $\Delta\phi(=\phi_{new}-\phi_{old})$, and the specified under-relaxation factor, α, as follows:

$$\phi = \phi_{old} + \alpha\Delta\phi \qquad \text{Eq. 4-27}$$

This expression is always used for any general variable ϕ.

5 Implementation of scalar flux modelling.

In Chapter 3, different advanced models that can be used to estimate the scalar flux term which appears after performing the Reynolds average of the transport equation of pollutant dispersion were presented. However, there is a problem in implementing these advanced scalar flux models because they cannot be represented with a simple scalar diffusion coefficient like the one used by the standard isotropic gradient diffusion model. Therefore, small changes in the discretization of the transport equation of pollution dispersion must be done to employ these models. These changes are explained in the present chapter.

5.1 Numerical Solution of Scalar Transport Equation

In addition to the fluid flow field equations calculated by the commercial software (FLUENT), it is possible to solve some extra equations (such as pollutant transport or any other arbitrary scalar quantity ϕ) using the same fluid flow domain. Solving these extra equations can be done in two ways: using the species transport equation or defining a User-Defined Scalar (UDS) equation. Under general steady state conditions, both equations are comparable and can be reduced to the form:

$$\frac{\partial}{\partial x_j}\left(\rho \bar{u}_j \bar{\phi} - \Gamma_\phi \frac{\partial \bar{\phi}}{\partial x_j}\right) = S(\bar{\phi}) \qquad \text{Eq. 5-1}$$

where Γ_ϕ is the diffusion coefficient and $S(\bar{\phi})$ is the source term of $\bar{\phi}$. This equation is equivalent to the equation of transport of pollutants (Eq. 2-16), just considering the source as the gradient of the scalar flux term. It is:

$$S(\bar{\phi}) = -\frac{\partial}{\partial x_j}\left(\rho \overline{u'_j \phi'}\right) \qquad \text{Eq. 5-2}$$

FLUENT solves the UDS and species equations (Eq. 5-1) in the same way as the continuity and Navier-Stokes equations, using the Finite Volume Method (FVM). The FVM transforms the differential transport equations into an algebraic form. This process is done by integrating the equation over every finite volume in the computational domain. In steady state flow conditions it will be:

$$\oint_S n_i \bullet \left(\rho \bar{u}_j \bar{\phi} - \Gamma_\phi \frac{\partial \bar{\phi}}{\partial x_j} \right) ds = \int_V S(\bar{\phi}) dV \qquad \text{Eq. 5-3}$$

The complete term on the left side of Eq. 5-3 is automatically discretized and resolved by FLUENT through the FVM following the procedure explained in the last chapter. The source term (S_ϕ) needs to be linearized and separated into two parts for the solution of the algebraic equation (See Eq. 4-16). This step is done because the nominally linear framework would allow only a formal linear dependence and because the incorporation of linear dependence is usually better than treating S_ϕ as a constant [Pata80]. However, the approximation of the source to a linearized form is not always possible.

From a simple examination of each of the scalar flux models considered in this work (presented in Table 3-6), it can be seen that there are no linear dependencies of the concentration ϕ with the scalar fluxes in any of the models. Therefore, there are only two possibilities to include them in Eq. 5-1, treating all models as the constant part source term (S_C) or as an anisotropic diffusivity coefficient tensor (Γ_{ij}). The descriptions and implementations of both methods are explained in the next sub-section.

5.1.1 Species or UDS Equation

As mentioned earlier, there are two ways to compute the pollution dispersion transport equation (Eq. 5-1) in FLUENT 6.3: using the species transport equation or defining a UDS equation. These two equations are the same and can be presented in the form of Eq. 5-1. However, there are some differences between the two methods to solve this equation. When the species transport equation is used, it is considered a mixture of different materials or “species” with a list of rules governing their interaction. They are:

- A list of mixing laws dictating how mixture properties (density, viscosity, specific heat, etc.) are to be derived from the properties of individual species, if composition dependent properties are desired.
- A direct specification of mixture properties if composition-independent properties are desired.
- Diffusion coefficients for individual species in the mixture.
- Other material properties, chemical reactions and other phenomena not considered in this work.

For the special case of interest of this work, all reaction source and thermal effects can be neglected, but the species transport equation does not allow setting up anisotropic (tensor) diffusion coefficients. As a result, in addition to the SED model (already available in the software), all scalar fluxes models should be treated in the species equation as a source. After some simulations with the anisotropic models implemented as a source term in the species transport equation, numerical instability that was too high was found. In accordance with the theory [Pata80], this high instability is due to the strong imbalance effects created by the implementation of the complete model terms in the constant part (S_C) of the source (see Eq. 4-16). All implemented scalar flux models are anisotropic and have a non-linear dependency on the concentrations, making it impossible to adapt them to the linear equation of the source term (Eq. 4-16). Therefore, it has been needed to discard the use of the species equation and change to the anisotropic diffusion facility of the UDS transport equation.

The UDS is a FLUENT feature that provides the possibility to calculate an additional differential transport equation to simulate pollutants' dispersion and set a customized anisotropic diffusion coefficient. In comparison to the species transport equation, the UDS equation does not have any pre-specified physical rules or mixing laws to set the variation of scalar properties. However, this lack in the software is not relevant when the pollutants are considered as a passive scalar. To measure the influence of the active/passive scalar transport simplification, both the simulation of pollution dispersion with the species transport equation and with the UDS transport equation were performed. The results of these two simulations appear in the results chapter of the two-dimensional street canyon. (see 7.4.3, page 104)

5.1.2 Anisotropic Diffusion Programming for UDS

The UDS transport equation of the commercial software FLUENT 6.3 was employed for the simulation of pollutants as a passive scalar with the implementation of advance turbulent scalar flux models in the anisotropic diffusion coefficient. This is a new software feature available since the FLUENT version 6.3, which includes the possibility to edit a tensor diffusion coefficient for each additional UDS transport equation. To understand it better, the diffusion term of this UDS transport equation (Eq. 5-1) can now be re-written in a general form as:

$$\frac{\partial}{\partial x_j}\left(\Gamma_{ij}\frac{\partial \bar{\phi}}{\partial x_i}\right) \qquad \text{Eq. 5-4}$$

where Γ_{ij} is the tensor diffusion coefficient. It is a second order tensor with six-components in case of bi-dimensional flow and nine components in case of three-dimensional flow. The software allows to specify in the simulation setup every one of the tensor diffusion components. They can be set as constant values or as a function of the flow variables through a "User-Defined Function" (UDS) subroutine called "DEFINE ANISOTROPIC DIFFUSIVITY" [Flue06]. All tensor diffusion components must be specified.

The programmed subroutines for the implementation of the anisotropic scalar flux models make use of flow field and turbulent parameters already calculated by the software, e.g. k (turbulent kinetic energy), ε (Turbulent dissipation rate), the velocity gradients ($\partial \bar{u}_i / \partial x_j$) and in some cases geometry information (wall distance), in conjunction with the respective model coefficients. When the LRRIP second moment Reynolds stress model is not used, the Reynolds stresses must be calculated for the implementation of the algebraic scalar flux models. This calculation was done using the Boussinesq relation (Eq. 3-1).

This general implementation procedure was applied for all algebraic isotropic and anisotropic scalar flux models. However, there were two exceptions: the WET model and the second moment models. Because the WET model's formulation is implicit, it makes use of its own results for scalar fluxes. Therefore, the implicit term was decoupled from the original model and inserted as a source of the mean pollutant transport equation.

The second moment models were implemented by calculating not only one additional transport equation for the mean concentration (as was done for the algebraic models), but also one additional transport equation for every one of the scalar fluxes. As a result, in addition to the flow field, one transport equation for mean concentrations and two additional transport equations in bidimensional flows or three transport equations in three-dimensional flows must be solved. Each of the scalar flux transport equations also includes an anisotropic diffusion term like the

GGDH with different model coefficient and some additional terms always included as sources.

For further details about the model implementation, the User-Defined Function from FLUENT's subroutines are included in the Appendix D (page191). In the next section, the boundary conditions employed for these simulations in the commercial software FLUENT 6.3 are described. Specific details for every simulation setup are given with each of the selected geometries.

5.2 Boundary Conditions

Boundary conditions are a set of restraints needed for the solution of partial differential equations. The most common boundary conditions in CFD applications are the Dirichlet (boundary value fixed), the Neumann (boundary gradient value fixed) or mixed (Dirichlet and Neumann). The commercial CFD packages usually employ aggregated boundary conditions for all flow variables with different names for easier understanding and application. The commercial names of boundary conditions used in the present work during the test cases are:

- Velocity Inlet
- Pressure Outlet
- Wall
- Symmetry
- Periodic
- Mass Flow Inlet

Next, a short description of these used boundary conditions is given. For further details please refer to FLUENT 6.3 User Manual.

5.2.1 Velocity Inlet

Velocity inlet boundary conditions are used to define the flow velocity and all relevant scalar properties of the flow, at flow entrances. At velocity inlet boundary conditions, the velocity magnitude and direction or velocity components, temperature (for energy calculations), turbulence parameters (for turbulent calculations) and chemical species mass fractions (for species calculations) must be set.

The velocity inlet boundary condition is normally used to specify a flow entering the computational domain. In this case, the software uses both the velocity components and the scalar quantities defined to compute the inlet mass flow rate, momentum fluxes, and fluxes of energy and chemical species. The mass flow rate entering a fluid cell adjacent to a velocity inlet boundary is computed as:

$$\dot{m} = \int \rho \vec{v} \cdot d\vec{A} \qquad \text{Eq. 5-5}$$

Note that only the velocity component normal to the control volume face contributes to the inlet mass flow rate.

5.2.2 Pressure Outlet Boundary Condition

Pressure outlet boundary conditions require the specification of a static (gauge) pressure at the outlet boundary. At pressure outlets, the used commercial software, FLUENT, uses the specified boundary condition pressure as input for the static pressure of the fluid at the outlet plane and extrapolates all other conditions from the interior of the domain (von Neumann boundary condition). When the pressure outlet BC is set, a fully developed flow is specified at the given boundary $(\partial/\partial x = 0)$ where x is the coordinate with direction perpendicular to the pressure outlet boundary condition.

5.2.3 Wall Boundary Condition

Wall boundary conditions are used to bound fluids with solid surfaces. By definition, no-slip boundary conditions are enforced at walls for viscous flows. The shear stress and heat transfer between the fluid and the wall are computed based on the flow details in the local flow field.

When a wall boundary is specified, the boundary conditions for turbulent quantities are directly specified by the software. These expressions are explained in detail under the Near Wall Modelling Approach section in Chapter 3.3.

5.2.4 Symmetry Boundary Conditions

The symmetry boundary conditions are used when the physical geometry of interest and the expected pattern of the flow solution have mirror symmetry. They can also be used to model zero-shear slip walls in viscous flows. It is unnecessary to set any additional information at symmetry boundaries due to the fact that all variables are equally set at this kind of boundary condition. This process is accomplished by neglecting the derivatives for each variable in perpendicular direction to this boundary.

5.2.5 Periodic Boundary Condition

FLUENT 6.3 provides the ability to calculate fully-developed (so-called periodic) fluid flow. This boundary condition is originally designed to simulate flows in compact heat exchanger channels and flows across tube banks. However, other applications include fully-developed flow in pipes and ducts. In such flow configurations, the geometry varies in a repeating manner along with the direction of the flow, leading to a periodic fully-developed flow regime in which the flow pattern repeats in successive cycles. These periodic conditions are achieved after a sufficient entrance length, which depends on the flow Reynolds number and geometric configuration. The periodic flow conditions exist when the flow pattern repeats over some length L, with a constant pressure drop across each repeating module in the streamwise direction. Additionally, some limitations apply for the use of this kind of boundary condition in the commercial software including that the flow must be steady state and incompressible, and that additional net mass through extra inlets/exits and multiphase modelling are not allowed.

This boundary condition was used to create a fully developed atmospheric boundary layer in the 2D street canyon exercise.

5.2.6 Mass Flow Inlet Boundary Conditions

Mass flow boundary conditions can be used in FLUENT to provide a prescribed mass flow rate or mass flux distribution at an inlet. Physically, specifying the mass flux permits the total pressure to vary in response to the interior solution. This is in contrast to the pressure inlet boundary condition where the total pressure is fixed while the mass flux varies.

It is possible to specify the mass flow rate through the inlet zone and make FLUENT convert this value to mass flux or specify the mass flux directly. For cases where the mass flux varies across the boundary, you can also specify an average mass flux. If the mass flow rate is set, it will be converted internally to a uniform mass flux over the zone by dividing the flow rate by the area of the zone.

6 Model validation

The evaluation of the turbulence models has been performed with special emphasis on the prediction capabilities of the variable C^*, which is the normalized concentration defined as:

$$C^* = \left(C \cdot U_{ref} \cdot L^2\right) / Q_S \qquad \text{Eq. 6-1}$$

where C is the actual measured concentration (ppm), U_{ref} is the reference velocity (m/s), L is a characteristic length (m) and Q_S is the pollutant flow rate introduced in the computational domain (m^3/s). The parameters U_{ref} and L are defined in a different way for every test case.

6.1 Statistical Evaluation Parameters

6.1.1 Metrics

In general, any model can be evaluated in at least three ways [Chan05]: statistically (e.g., [Hann93]), scientifically (e.g., [Nappo98]), and operationally (e.g., [Chan98]). Statistical evaluation mainly consists of comparing model predictions with observations (sometimes called validation). Scientific evaluation examines model algorithms, physics, and assumptions in detail for their accuracy, efficiency, and sensitivity, and requires in-depth knowledge of the model's scientific basis. Operational evaluation mainly considers issues related to the user-friendliness of the model, such as the user's guide, the user interface, error checking of input data, internal model diagnostics, output display, and consistency of application by multiple users.

Statistical evaluations describe the comparison of model predictions with certain reference states, which in most cases are simply "observations." Observations can be directly measured by instruments, or can be themselves products of other models or analysis procedures. Statistical evaluations provide general information on model performance, but it is possible to have a situation where the model produces the right answers but for wrong reasons (i.e. compensating errors). On the other hand, the reliability or accuracy of these reference "observations" is not estimated in this model evaluation.

Quantitative statistical measures for evaluating air dispersion models have already been recommended by [Hann91] and [Hann93], and the procedure were implemented in a computational software package called BOOT. Nowadays, these evaluation metrics have been commonly used by many researchers in this application area. For example, it has been adopted as a common model evaluation framework by the European Initiative on "Harmonisation within Atmospheric Dispersion Modelling for Regulatory Purposes" [Oles01] and as a validation metric for model evaluation within the European Cooperation in Science and Technology (COST) Action 732: Quality Assurance and improvement of microscale meteorological models" [Brit07] [Scha10].

In order to evaluate model performance for turbulent numerical simulations, the statistical model evaluation parameters described by Chang and Hanna [Chan04] and implemented in the BOOT software [Chan05] have been employed in the present work. They propose the use of the fractional bias (FB), geometric mean bias (MG), the normalized mean square error (NMSE), geometric variance (VG) and the fraction of predictions within a factor of two of observations (FAC2) given by:

$$
\begin{aligned}
&\mathrm{FB} = \frac{\langle C_o^* \rangle - \langle C_p^* \rangle}{0.5\left(\langle C_o^* \rangle + \langle C_p^* \rangle\right)}, && \left|\mathrm{FB}\right| < 0.3 \\
&\mathrm{MG} = \exp\left(\langle \ln(C_o^*) \rangle - \langle \ln(C_p^*) \rangle\right) && 0.7 < \mathrm{MG} < 1.3 \\
&\mathrm{NMSE} = \frac{\langle \left(C_o^* - C_p^*\right)^2 \rangle}{\langle C_o^* \rangle \cdot \langle C_p^* \rangle}, && \mathrm{NMSE} < 4 \\
&\mathrm{VG} = \exp\left[\langle \left(\ln C_o^* - \ln C_p^*\right)^2 \rangle\right] && \mathrm{VG} < 1.6 \\
&\mathrm{FAC2} = \frac{N}{n} = \frac{1}{n}\sum_{i=1}^{n} N_i,\ \mathrm{N_i} = \begin{cases} 1 \text{ for } 0.5 \le \dfrac{P_i}{O_i} \le 2.0 \\ 1 \text{ for } O_i \le W \text{ and } P_i \le W \\ 0 \text{ else} \end{cases} && \mathrm{FAC2} > 0.5
\end{aligned}
\tag{Eq. 6-2}
$$

where C_o^*, C_p^* and $\langle C^* \rangle$ are observations, model predictions and the average over the data, respectively. Different to the BOOT software, the FAC2 was implemented here with a case differentiation based on the threshold *W*, also used in the hit rate. If the observation is below the threshold *W* then it is counted as within a factor of two (see [Scha10]). A perfect model would have MG, VG, and FAC2 equal to 1.0, and FB and

NMSE equal to 0.0. Additionally, [Chan04] gives a range of typical values for an 'acceptable' model performance, as appears beside each parameter in Eq. 6-2. The acceptable model performance detailed in Eq. 6-2 was originally proposed by [Hann04], based on research-grade field experiments. Acceptable model performance means that the fraction of predictions within a factor of two of observations is higher than 50%, the mean bias is within ± 30% of the mean, and the random scatter is lower than approximately a factor of two of the mean [Scha10]. The translation of these values to a particular test case is not straightforward but based on the idea that [Hann04] uses these values for comparisons of maximum concentrations on arcs—i.e. unpaired in space. As the present exercise is based on a point by point comparison, which is more stringent, less strict criteria might be used. The values of metrics can differ widely depending on the data that the metrics actually represent [Scha10].

It is necessary to consider multiple performance measures, as each measure has advantages and disadvantages and there is not a single measure that is universally applicable to all conditions [Chan05]. The relative advantages of each performance measure are partly determined by the distribution of the variable of interest. The distribution resembles a log-normal distribution for atmospheric pollutant concentrations. The linear measures FB and NMSE are strongly influenced by infrequently occurring high observed and predicted concentrations, whereas logarithmic measures MG and VG provide a more balanced treatment of extremely high and low values. Therefore, for a dataset where both predicted and observed concentrations vary by many orders of magnitude, MG and VG are more appropriate. However, [Chan04] mention that MG and VG are also known to be strongly influenced by extremely low values, and are undefined for zero values. These low and zero values are not uncommon in dispersion modelling, where a low concentration value might be at a receptor that the plume has missed. Therefore, when calculating MG and VG, it is useful to impose a minimum threshold for data values. The FAC2, which sometimes includes a threshold, is the most robust measure because it is not overly influenced by high and low outliers.

FB and MG are measures of mean bias and indicate only systematic errors, whereas NMSE and VG are measures of scatter and reflect both systematic and unsystematic (random) errors. For FB, which is based on a linear scale, the systematic bias refers to the arithmetic difference between C^*_p and C^*_o. For MG, which is based on a logarithmic scale, the systematic bias refers to the ratio of C^*_p to C^*_o. Because FB and MG are based on the mean bias, it is possible for a model whose predictions are completely out of phase with observations to still have an FB = 0 or MG = 1. As solution to this problem, a modified version of these parameters can be calculated [Chan05]. The error can be separately considered in two components, the over-prediction part (FB_{FP}) and the under-prediction part (FB_{FN}) where $FB = FB_{FN} - FB_{FP}$. These two and their analogues MG_{FP} and MG_{FN} are also available from the BOOT software with $MG = MG_{FN} / MG_{FP}$. These error metrics are calculated as:

$$\mathrm{FB_{FN}} = \frac{\sum\limits_i \left[\left| C^*_{o_i} - C^*_{p_i} \right| + \left(C^*_{o_i} - C^*_{p_i} \right) \right]}{\sum\limits_i \left(C^*_{o_i} + C^*_{p_i} \right)}$$

$$\mathrm{FB_{FP}} = \frac{\sum\limits_i \left[\left| C^*_{o_i} - C^*_{p_i} \right| + \left(C^*_{p_i} - C^*_{o_i} \right) \right]}{\sum\limits_i \left(C^*_{o_i} + C^*_{p_i} \right)} \qquad \text{Eq. 6-3}$$

$$\mathrm{MG_{FN}} = \exp\left[\frac{1}{2N} \sum_i \left[\left| \ln C^*_{o_i} - \ln C^*_{p_i} \right| + \left(\ln C^*_{o_i} - \ln C^*_{p_i} \right) \right] \right]$$

$$\mathrm{MG_{FP}} = \exp\left[\frac{1}{2N} \sum_i \left[\left| \ln C^*_{o_i} - \ln C^*_{p_i} \right| + \left(\ln C^*_{p_i} - \ln C^*_{o_i} \right) \right] \right]$$

where N is the total number of measurements.

Additionally, some general statistical parameters are given from the BOOT software. For example, the correlation coefficient, R, reflects the linear relationship between the predicted and observed concentrations and is thus insensitive to either an additive or a multiplicative factor. That is, if $C^*_p = \alpha + \beta C^*_o$, where α and β (>0) are arbitrary constants, R will always equal 1.0 between C^*_p and C^*_o. Therefore, a perfect correlation coefficient is necessary, but not in itself sufficient to create conditions for a perfect model [Chan04]. Similar conditions may occur with other reported general evaluation parameters such as the MEAN (arithmetic average), the SIGMA (standard deviation) and the BIAS (absolute difference of means). They are calculated as:

$$\mathrm{R} = \frac{\langle (C^*_o - \langle C^*_o \rangle)(C^*_p - \langle C^*_p \rangle) \rangle}{\sigma_o \sigma_p}$$

$$\mathrm{MEAN}\left(\langle C^*_{o,p} \rangle \right) = \frac{1}{N} \sum_{i=1}^{N} C^*_{o_i,p_i}$$

$$\mathrm{SIGMA}\,(\sigma_{o,p}) = \sqrt{\frac{1}{N} \sum_{i=1}^{N} \left(C^*_{o_i,p_i} - \langle C^*_{o,p} \rangle \right)^2} \qquad \text{Eq. 6-4}$$

$$\mathrm{BIAS} = \frac{1}{N} \left(\sum_{i=1}^{N} C^*_{o_i} - \sum_{i=1}^{N} C^*_{p_i} \right)$$

All of the presented statistical parameters together with the HIGH (highest prediction/observation) and the second HIGH (second highest prediction/observation) complete the results output file from the BOOT software. However, due to the intrinsically overly general or partial information in the definition of most of the presented statistical parameters, those from Eq. 6-2 have been taken into account for the error analysis and the rest are used as complementary information.

In summary, the BOOT software reports all the aforementioned statistical metrics and the ideal values for a full agreement with the experiments. The complete list of the statistical metrics are: MEAN (mean average), SIGMA (Standard Deviation), BIAS (Difference in the means), NMSE (Normalized-Mean-Square-Error), CORR (Correlation Coefficient R), FA2 (Factor of Two), FB (Fraction Bias), FB_{FN} (Fraction Bias False Negative), FB_{FP} (Fraction Bias False Positive), VG (Geometric Variance), MG (Geometric Mean-bias), MG_{FN} (Geometric Mean-bias False Negative), MG_{FP} (Geometric Mean-bias False Positive), HIGH (highest prediction/measurement), 2^{nd}.HIGH (2^{nd}. Highest prediction/measurement). For further details please refers to [Chan05]. For illustrative proposes, an example of the BOOT software output file is included in the Appendix C (page 183).

6.1.2 Hit-Rate

In addition to the metrics, the concept of Hit-Rate from the German VDI Guideline as an evaluation of prognostic wind-field models [VDI05] has been also employed for the model evaluation. On the basis of the normalised model results P_i and the normalised comparison values O_i, the Hit-Rate q indicates the proportion of the total correctly predicted values (i_n) in the total number of comparison values (N):

$$q = \frac{1}{N}\sum_{n=1}^{N} i_n$$

$$i_n = \begin{cases} 1 & \text{if } \left|(O_n - P_n)/O_n\right| \le D \text{ or } \left|O_n - P_n\right| \le W \\ 0 & \text{otherwise} \end{cases} \qquad \text{Eq. 6-5}$$

where D is the allowed relative difference and W is the allowed absolute difference specified for every variable. For successful validation, the [VDI05] recommends an equivalent “acceptance criterion” of $q \geq 0.66\%$ in comparisons with the measurements or observations. A new utility from the BOOT software package also computes the Hit-Rate and it has been employed in the present work. A graphic explanation of this metrics is given by [Scha10].

6.2 Discretization Error Estimation

The grid dependency of the results has been calculated through the use of the generalized Richardson Extrapolation technique at all the measurement point locations. The Richardson extrapolation is a postprocessor error estimation technique independent of the numerical method used to obtain the numerical solutions. It can be applied to each fluid flow variable as well as to derived quantities. This error estimator comes from the statement that the discretized equations represent a truncated approximation of the differential equation. After a general CFD simulation, the exact solution of a variable (f_{ex}) and the numerical simulation results on a specific mesh (f_i) can be related by a Taylor series.

$$f_i - f_{ex} = g_p h_i^p + g_{p+1} h_i^{p+1} + g_{p+2} h_i^{p+2} + \ldots \qquad \text{Eq. 6-6}$$

where h_i is a (linear) measure of the grid i, p is the order of accuracy and g_i are their coefficients [Fran07]. In the asymptotic convergence range, all terms of higher order than p can be neglected. From this assumption, the remaining variables f_{ex}, g_p and p can be estimated with the solution obtained on three different grids. If i = 1, 2 and 3 denote the fine, medium and coarse grids, then two grid refinement ratios $r_{21} = h_2/h_1$ and $r_{32} = h_3/h_2$ can be calculated. With these ratios, the truncated series can be written as:

$$\begin{array}{lllll} f_1 & = & f_{ex} + g_p h_1^p & = & f_{ex} + g_p h_1^p \\ f_2 & = & f_{ex} + g_p h_2^p & = & f_{ex} + g_p (r_{21} h_1)^p \\ f_3 & = & f_{ex} + g_p h_3^p & = & f_{ex} + g_p (r_{21} r_{32} h_1)^p \end{array} \qquad \text{Eq. 6-7}$$

The applicability of generalised Richardson extrapolation with solutions from three well-refined meshes is accurate when the solution displays monotonic convergence [Ferz02]. From the ratio of the solution changes, $R = (f_2 - f_1)/(f_3 - f_2)$, three different behaviours can be discerned.

$$\begin{array}{lll} (i) & 0 < R < 1 & : \text{monotonic convergence} \\ (ii) & -1 < R < 0 & : \text{oscillatory convergence} \\ (iii) & |R| > 1 & : \text{divergence} \end{array} \qquad \text{Eq. 6-8}$$

For divergence, no error estimation can be obtained, and for oscillatory convergence, the use of more solutions than three to compute the error is generally required [Fran07]. To calculate the solution changes it is necessary that all solutions are available in the same positions. In the case of always doubling the number of cells in each coordinate direction (i.e. $r = r_{21} = r_{32} = 2$) without moving the nodes of the coarse grid, this requirement is fulfilled. Another option is interpolation of the results from the medium and fine grid onto the nodes of the coarse grid. Then the order of the interpolation must be at least as high as the formal order of the numerical approximations. In this work a similar approach was used. The results of all grids were linearly interpolated onto the measurement positions, where all numerical error estimates were performed.

Assuming a general case where all solutions are available on the coarse grid and monotonic convergence according to Eq. 6-8 is fulfilled, the order of accuracy can be calculated from Eq. 6-7 by solving the transcendental equation

$$p = \frac{\ln[(f_3 - f_2)/(f_2 - f_1)]}{\ln(r_{21})} - \frac{1}{\ln(r_{21})}\left[\ln\left(r_{32}^{p} - 1\right) - \ln\left(r_{21}^{p} - 1\right)\right] \tag{Eq. 6-9}$$

with an iterative method. After the elimination of g_p in Eq. 6-7, an estimation of the exact solution is obtained as:

$$f_{ex} = f_1 + \frac{f_1 - f_2}{r_{21}^{p} - 1} \tag{Eq. 6-10}$$

The second term on the right side of Eq. 6-10 defines a correction of the fine grid solution f_1. This correction is only available at the positions of the variable on the coarse grid. The (spatial) discretization error DE_1 of the fine grid solution, i.e. the difference between the solution on the fine grid and the extrapolated solution used to estimate the unknown exact solution after truncation of the Taylor series expansion, can be calculated from Eq. 6-10 as:

$$DE_1 = f_1 - f_{ex} = \frac{f_2 - f_1}{r_{21}^{p} - 1} \tag{Eq. 6-11}$$

In similar way, the discretization errors for the medium and coarse grid are calculated as:

$$\begin{aligned} DE_2 &= f_2 - f_{ex} = \frac{r_{21}^{p}(f_2 - f_1)}{r_{21}^{p} - 1} = r_{21}^{p} DE_1 \\ DE_3 &= f_3 - f_{ex} = \frac{r_{32}^{p} r_{21}^{p}(f_2 - f_1)}{r_{21}^{p} - 1} = (r_{32} r_{21})^{p} DE_1 \end{aligned} \tag{Eq. 6-12}$$

If the computed order of accuracy p is larger than the theoretical order (considered in the present work between one and two), the relation for the error estimation DE_1' is solved with the grid triplet [Roy05]:

$$\begin{aligned} DE_1' &= f_1 - f_{ex} \approx g_1 h_1 + g_2 h_1^2 \\ DE_2' &= f_2 - f_{ex} \approx g_1 h_2 + g_2 h_2^2 \\ DE_3' &= f_3 - f_{ex} \approx g_1 h_3 + g_2 h_3^2 \end{aligned} \tag{Eq. 6-13}$$

Finally, the estimation of numerical uncertainty U_1 used in the present work employ the GCI method originally proposed by [Roac94] but with the improvements proposed by [Eca04] and recommended by [Fran06] and [Fran08b] in wind engineering applications. [Eca04] mention that when the three grid solutions are diverging no uncertainty estimation can be made. But for any other case, at least four categories to calculate the numerical uncertainty can be specified. For cases of monotonic convergence and oscillatory convergence (using Eq. 6-8), the performed estimation of U_1 depends on p following the next Table 6-1:

Table 6-1.-Grid Convergence Index (GCI) for uncertainty estimation.

Case	*Condition*	*Uncertainty Estimation*
(I)	Monotonic convergence with $0.5 < p < 2$	$U_1 = 1.25 \cdot DE_1$
(II)	Monotonic convergence with $2 < p < 3$	$U_1 = 1.25 \cdot Max(DE_1, DE_1')$
(III)	Monotonic convergence with $p < 0.5$ or $p > 3$	$U_1 = 3 \cdot Max(\lvert f_3 - f_2 \rvert, \lvert f_2 - f_1 \rvert)$
(IV)	Oscillatory convergence	$U_1 = 3 \cdot Max(\lvert f_3 - f_2 \rvert, \lvert f_2 - f_1 \rvert)$
(V)	Divergence	No uncertainty estimation.

7 Flow and Dispersion in a 2D Street Canyon

The first test case selected to study the performance of the advanced turbulent scalar flux models in urban environment applications is the data set published by Pavageau and Schatzmann [Pava99]. It is a wind tunnel experiment of a bi-dimensional street canyon performed at the Meteorological Institute of the University of Hamburg, Germany. The main reasons for this selection were the simplicity of its 2D characteristics (ideal condition for a first test), the well detailed measurements and description of the experiments, and the already large amount of work available in this or similar geometries which allow for the comparison of results.

In this chapter, the wind tunnel experiment is briefly explained, emphasizing the relevant information used for the construction and definition of the computational domain and boundary conditions. Subsequently, the grid dependence of the results for the normalized concentrations is analysed by means of the Richardson Extrapolation technique. Finally, the wind tunnel measurements and other published LES results are used to discuss and evaluate the numerical simulations of the concentrations and the most relevant variables affecting the implemented passive scalar flux models and pollutant predictions.

7.1 Experiment Description

The selected wind tunnel measurement published by [Pava99] is an idealized model of a street canyon inserted within an urban area, consisting of 26 equally spaced bars of rectangular cross section located in perpendicular direction to the main flow direction. The 20th canyon (formed by the 20th and 21st bar) was considered as a fully developed flow and was selected to represent an urban 2D street canyon. In the centre-bottom of this canyon a constant mass flow of ethane was introduced and subsequently measured in 70 locations across the canyon. The detection of tracer concentrations was achieved with a fast Flame Ionisation Detector (FID). The experiment is sketched in Figure 7-1.

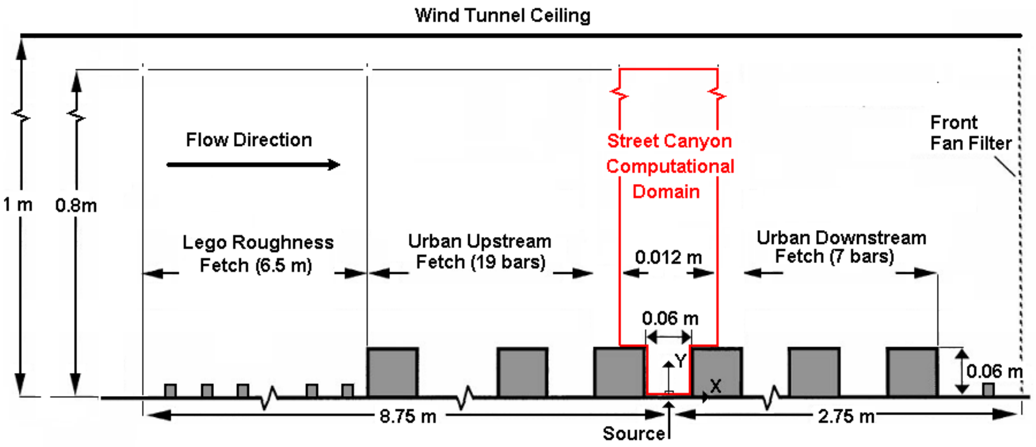

Figure 7-1. Wind tunnel setup of street canyon from Pavageau and Schatzmann [Pava99]. Red lines represent the flow field area selected as computational domain of the numerical simulations.

The wind tunnel experiment reproduces the atmospheric boundary layer. The velocity profile of the flow approaching the modelled urban area was reported in the experiments using an approximation of the power law equation. It is:

$$\frac{\bar{u}(z)}{U_{ref}} = \left(\frac{z - d_0}{z_{ref} - d_0} \right)^{\alpha} \qquad \text{Eq. 7-1}$$

where d_0 is the displacement height, $\bar{u}(z)$ is the mean velocity at elevation z, and U_{ref} is the mean velocity at the reference height z_{ref}(=0.65m). The vertical wind profile exponent α and the displacement height d_0 reported from the wind tunnel experiments were 0.28 and 2 mm, respectively.

In the same way, the wind tunnel experiments reported the measurements of pollution concentration based on a similar definition of the previously mentioned normalized concentration C^* (see Chapter 6). It is:

$$C^* = \left(C \cdot U_{ref} \cdot H \cdot L \right) / Q_S \qquad \text{Eq. 7-2}$$

where C is the actual measured concentration (ppm), U_{ref} is the x-velocity at the reference point $P_{\mathrm{ref}}(x,y)$=(0,0.65) in (m/s), H is the height of the buildings in the street canyon (0.06m), L is the length of the source line of pollutants (0.91 m in the experiments but 1 m for the 2D simulation case), and Q_S is the pollutant flow rate ($1.23 \cdot 10^{-6}$ m^3/s).

7.2 Computational Domain and Boundary Conditions

Figure 7-2(a) shows a general view of the fluid flow domain and boundary conditions used for the simulation of the street canyon. The geometry dimensions were taken from the wind tunnel setup detailed in [Pava99] and the pollutants' source design from [Mero96]. As can be seen in this figure, a pollutant source was located at the bottom of the selected canyon with a small "roof" to remove any vertical momentum effects. Although this small pollutant roof appears to be a solid block inserted within the flow field (or computational domain), it is usually neglected in previous simulations of this experiment. The dimensions of this pollutant roof appear in Figure 7-2(b) in addition to the graphical distribution of measurement locations where the pollution dispersion models are evaluated.

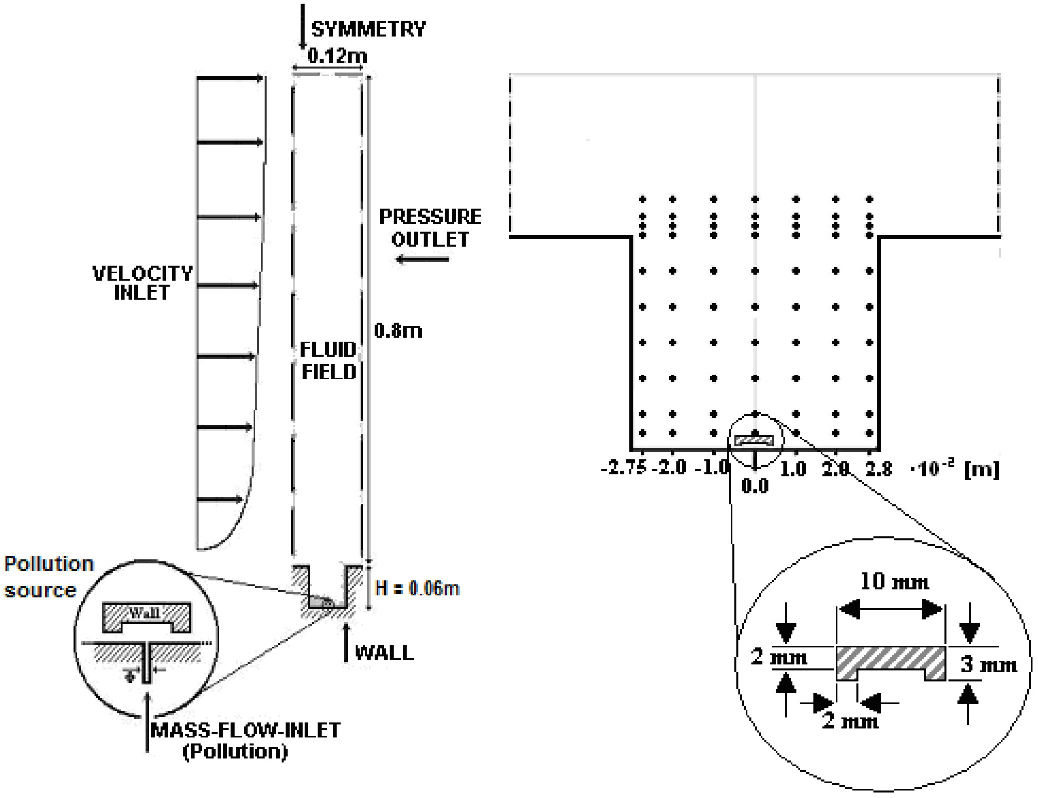

a) b)

Figure 7-2. - (a) Computational Domain and boundary conditions. (b) Measurement point locations and pollution source dimension details.

The boundary condition at the main flow entrance was fixed with a previously generated fully developed flow profile (explained below) with a velocity-inlet condition of pure air and zero pollutant concentration. Similarly, symmetry condition at the top and constant pressure-outlet condition on the exit of the flow were set. The wall boundary condition was specified in all other borders except at the entrance of the pollutants (i.e. mixture of air and ethane), where a mass-flow-inlet boundary condition with mass flow rate of $5.26 \cdot 10^{-05}$ $\mathrm{Kg \cdot s^{-1}}$ and ethane mass fraction of 2.9643% was specified. Except in cases where a different specification is explicitly given, the pollutant transport was always treated as a passive scalar.

The near wall treatment used was always the Enhanced Wall Treatment [Flue06] (see Chapter 3.3.2 for a short description of this method). This near wall treatment is recommend by [Flue06] for grids where the y^+ of the first cell beside the grid is within the laminar sub-layer. In the studied canyon, all y^+ values were around 5 for all simulations using the middle grid.

The fully developed flow profile prescribed at the flow entrance for each of the simulations were generated in FLUENT 6.3 using the software feature of periodic boundary conditions and the finest available grid (shown later). This type of boundary condition allows a pressure drop to occur across translational periodic boundaries, enabling the modelling of "fully-developed" periodic flow (see Chapter 5.2.5 for more details). It was set by specifying the equivalent mass flow rate obtained from the integral of the power law but using the velocity profile above the bars as recommended by the experiments—the same Eq. 7-1 with α=0.28 and d_0=60mm. The seven developed flow profiles, which include the velocity components and turbulent parameters for each turbulence model, were individually generated using the same numerical parameters and boundary conditions of the final simulations but setting zero mass flow at the pollutant entrance. At the end, the generated profiles were used as constant velocity and turbulence parameters at the main flow entrance in every corresponding simulation.

Figure 7-3 shows the velocity profiles and turbulence parameters used as boundary conditions for the simulation of the atmospheric boundary layer. The velocity profiles for each turbulence model in the main flow direction are compared with the analytical solution of the power-law (Eq. 7-1 with α and d_0 equal to 0.28 and 60mm respectively) and the log-law equation based on equilibrium boundary layer profiles [Rich93]. The analytic profiles for the time-averaged velocity component in the x-direction ($\overline{u}$), the turbulent kinetic energy (k), and its dissipation (ε) are calculated as:

$$\overline{u}(z) = \frac{u_*}{\kappa} \ln\left(\frac{z + z_0}{z_0}\right) \qquad \text{Eq. 7-3}$$

$$k(z)=\frac{u_*^2}{\sqrt{C_\mu}} \qquad \text{Eq. 7-4}$$

$$\varepsilon(z)=\frac{C_\mu^{1/4}k^{1/2}}{\kappa(z+z_0)} \qquad \text{Eq. 7-5}$$

where u^* is the friction velocity derived from Eq. 7-3 with z_0 = 0.5mm and U_{ref} = 3.07m/s at (x,y) = (0.0, 0.65)m; κ = 0.4187, the von Karman constant; C_μ = 0.09, a constant from the standard k-ε model. The y-velocity component, based on the equilibrium boundary condition assumption, must be equal to zero.

As can be seen in Figure 7-3, the main flow direction in the atmospheric boundary layer (x-velocity) presents a similar behaviour between all models and the described analytical solutions. However, the x-velocity maintains a general over-prediction for all models at low y-coordinates levels, which exceeds the analytical results by up to 20% when the SKW model is used. The reason for these results is the smooth wall boundary conditions set at the walls for all simulations. If the analytical approximations (power-law or logarithmic profile) accurately represent the wind-tunnel experiment, higher velocities around or within the canyon may be expected in the numerical simulations. The y-velocity profiles present values very close to zero for most of the domain with some small variations at the bottom. This behaviour of the y-velocity component may be expected as a product of the mass and momentum exchange between the main flow field over the street canyon and the recirculations within it.

Figure 7-3 also reports the turbulence parameters (k and ε) for some of the used turbulence models, together with their respective profiles for the equilibrium boundary layer. As expected, the strongest velocity gradients and thus production of turbulent kinetic energy (k) accompanied by the highest turbulent dissipation rate (ε) take place close to the walls. Farther from the walls, the production of turbulent kinetic energy is reduced. However, the predicted turbulent kinetic energy of all models is two or three times higher than in an equilibrium boundary layer. The highest turbulent kinetic energy predictions are obtained by the k-ω based models. On the other hand, the LRRIP model leads to the lowest k predictions. The different predictions reported for the turbulent kinetic energy are especially relevant in this work because of its explicit (using k) and implicit (through the Reynolds stresses) effects in the formulation of the scalar flux models.

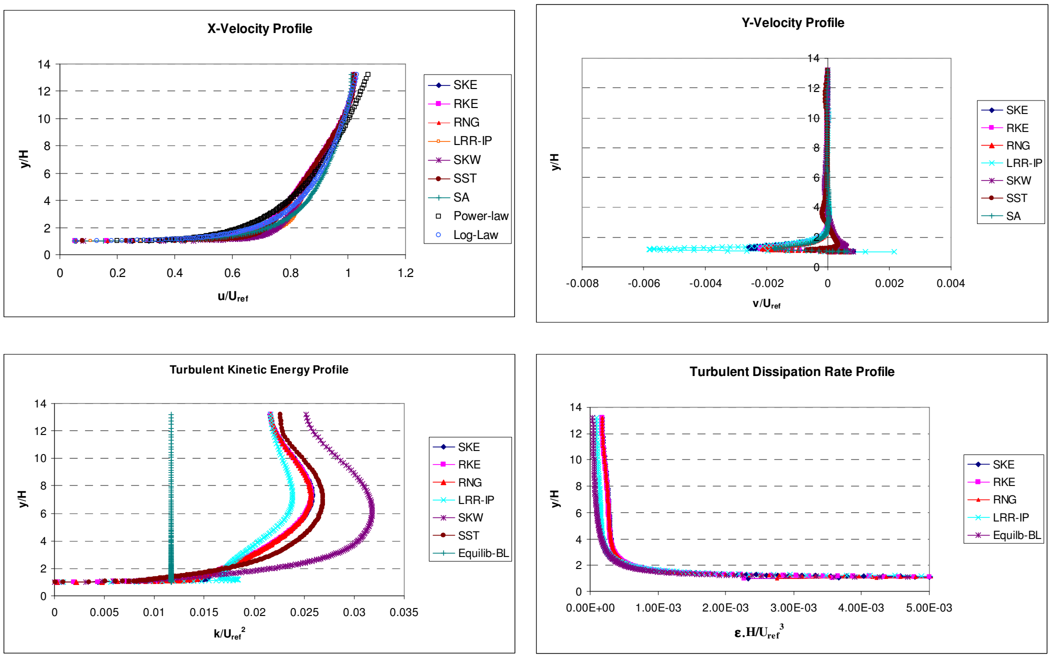

Figure 7-3. - Plots of inflow profiles developed for every turbulent model.

In addition to the previously mentioned numerical and computational considerations, an important change in the geometry was needed to perform the numerical simulations of the canyon. This geometrical change was needed due to the translation of the real 3D experiments to a simplified 2D test case. In the real experiments, the pollution is introduced in the fluid field through a row of 302 small pipes (diameter Φ_0=2.50·10^{-4}m) located along the width of the wind tunnel test section. The two-dimensional simulations used an equivalent two-dimensional source channel with width Φ (=1.62·10^{-5}m) calculated from the summation of the total pipes' areas, distributed in the same distance as the wind tunnel width. To examine the influence of the selected 2D channel size, additional simulations were performed using the new 2D-source-channel of width Φ and another 2D-source-channel with width of the original pipe's diameter Φ_0. For both sizes, the same mass flow rate was prescribed as a boundary condition, resulting in flow velocity variations of around one order of magnitude (0.2 m/s vs. 2.8 m/s). The results showed differences in the computed concentrations at the measurement locations with a maximum of only 1.1%. Therefore, it has been considered that the choice of a different inlet size has almost no influence on the results.

7.3 Discretization Error Estimates

Three systematically refined meshes have been used to estimate the spatial discretization error of results. The first created mesh was the middle one, consisting of 16484 quadrilaterals with a cell height of $8.3 \bullet 10^{-3}$ H and $1 \bullet 10^{-5}$ H on the buildings and bottom of the canyon, where $H = 6 \bullet 10^{-2}$m is the height of the buildings. Doubling and halving the number of elements in each coordinate direction, the fine and coarse meshes were generated with 65936 and 4121 quadrilateral cells, respectively. All meshes were completed keeping the maximum expansion ratio below 1.1.

Figure 7-4 shows a detail of the fine, middle and coarse grids used to perform the generalized Richardson Extrapolation analysis. After the discretization error estimate, the middle size mesh was selected to carry out all simulations comparing the performance of the models.

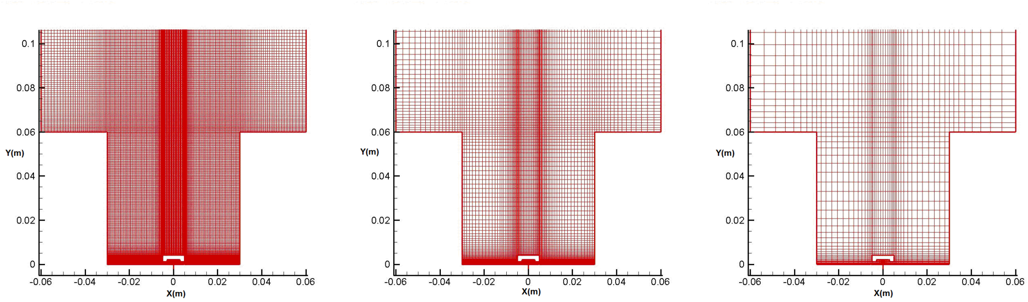

a) Fine Mesh **b) Middle Mesh** **c) Coarse Mesh**

Figure 7-4.- Detail of the three used grids for the 2D street canyon geometry.

The Richardson extrapolation technique was implemented to estimate the spatial discretization error in the 2D street canyon at all measurement locations. Table 7-1 and Table 7-2 present the uncertainty results on the fine mesh for the normalized concentrations, using the fine, middle and coarse mesh in the specified geometry for some of the possible combinations of turbulence models. Columns *I*, *II*, *III*, *IV* and *V* are the percentages of measurement locations separated in categories according to Table 6-1 (p.82). $<p>$ is the arithmetic mean order of accuracy for monotonic convergence of cases *I*, *II* and *III*. $<R>$ is the mean arithmetic ratio of solution changes for cases *I* to *IV*. Finally, $<U_1>$ is the mean absolute uncertainty in the finest grid for cases *I* to *IV* and it represents the final output of the method. The local uncertainty values U_1 in each specific location can be used as error bars (where available) to represent the spatial discretization error or grid uncertainty.

The results obtained in Table 7-1 from the application of Richardson Extrapolation show that the numerical error from the finest grid can be calculated in the majority of points where the concentrations were compared with the experiments. For example, the first line of Table 7-1 shows that the RKE model for Reynolds stresses in combination with the SED model for scalar fluxes has more than 94% of the total measurement points where the grid uncertainty can be estimated. This result means that under this combination, more than 47% of the points fulfil the monotonic convergence conditions for cases *I*, *II* and *III,* and approximately 47% of the points fulfil it for the oscillatory convergence condition of case *IV*. Only in 5.74% of the points does one find that the spatial grid uncertainty cannot be estimated. The last columns show the average absolute uncertainty of *C** in the finest grid, which means that 10.47 units of *C** is the spatial grid uncertainty for this specific case. The <p> of 1.87 (larger than 1) means that the order of accuracy of this grid is on average slightly below second order. Please refer to Chapter 6.2 for further details about the estimation of spatial discretization error using the Richardson Extrapolation technique.

Table 7-1. - Grid uncertainty estimation on the finest grid (U_1) of normalized concentrations C* at the measurement locations for the combination of some turbulent momentum and scalar flux models.

Predicted C* using	***Monotonic convergence (Cases I,II and III [%])***	***Oscillatory convergence (Case IV [%])***	***Divergence (Case V[%])***	***<p>***	***<R>***	***<U_1>***
RKE and SED	47.14	47.14	5.71	1.876	0.154	10.47
LRRIP and SED	31.43	34.29	34.29	1.197	-0.28	3.10
LRRIP and GGDH	61.34	21.43	17.14	1.221	-0.65	5.45
LRRIP and ABE-SUGA	60.00	20.00	20.00	1.474	0.846	12.07
LRRIP and ABE	57.06	32.86	10.00	1.998	0.04	19.51

In a general view of Table 7-1, one can see that monotonic convergence occurs in a high percentage of the measurement points for the majority of the presented cases. Also the oscillatory convergence occurs in a lower but appreciable amount of these points, and the lowest percentages were usually found with divergence. The values reported for the first two cases (monotonic and oscillatory convergence) imply that the points where the estimation of spatial discretization error is possible are always more than those where this uncertainty is unknown.

Another interesting illustration in the previous table is that fixing the turbulence model for Reynolds stresses (e.g. LRRIP from the second to the fifth model combination), the grid uncertainty increases with the complexity of the scalar flux models. This tendency of increase in grid uncertainty may be due to an accumulative spatial grid error as a consequence of the inclusion of additional terms in the more complex scalar flux models. In general, it can be said that the Richardson Extrapolation technique presents reasonable values of numerical uncertainties and it is a very useful technique to quantify the quality of a grid in view of specific parameters of interest.

Table 7-2. - Grid uncertainty estimation of normalized concentration C^* for the combination of some turbulent momentum and scalar flux models. All reported grids uncertainties are calculated only for cases I, II and III (see Table 6-1).

Predicted C using*	*Monotonic convergence (Cases I and II [%])*	*Monotonic convergence (Case III [%])*	$\langle U_1 \rangle$	$\langle U_2 \rangle$	$\langle U_3 \rangle$
RKE and SED	34.29	12.86	1.14	1.81	3.35
LRRIP and SED	24.29	7.14	1.23	1.96	3.99
LRRIP and GGDH	47.14	14.29	1.01	1.72	2.98
LRRIP and ABE-SUGA	42.86	17.14	0.37	1.06	5.10
LRRIP and ABE	22.86	34.29	0.19	0.89	9.34

The grid uncertainty of results for the other two grids may be partially estimated by applying the generalized Richardson extrapolation. In this way, Table 7-2 presents the grid uncertainty calculated for all three grids but only taking into account the points with convergence tendency corresponding to cases I, II and III. In this table, one can observe that the grid uncertainty reported from this fraction of the data shows similar values for the finest and middle grid. These results are relevant and valuable parameters for the selection of the middle grid to study the performance of different turbulence model combinations in this work.

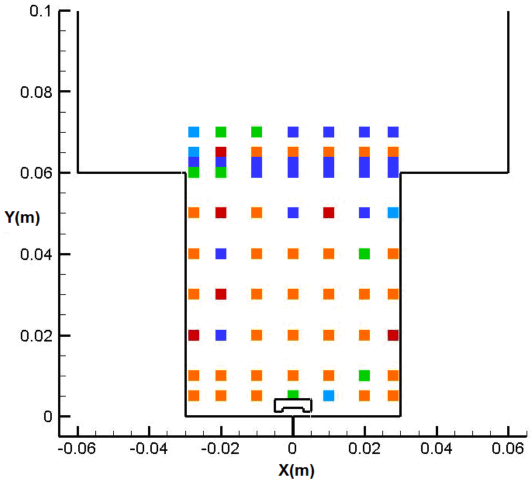

Figure 7-5.- Example of grid uncertainty distribution according to the five cases used for Richardson Extrapolation in Table 6-1. Simulation carried out using RKE and SED models. The colours (cases) are: (I) Dark Blue, (II) Light Blue, (III) Green, (IV) Orange, (V) Red.

Figure 7-5 shows the spatial distribution of convergence behaviour for concentrations using the turbulence model combination RKE and SED. The five cases are identified by colours to show a geographical distribution of the discretization error estimate. The absolute uncertainty calculated for every point has been included in the next sub-section as error bar for the comparison of predicted and measured concentrations in the 2D street canyon.

7.4 Analysis of Results

7.4.1 Concentration Prediction Using Different Turbulence Models for Reynolds Stresses

The street canyons contain some peculiar flow characteristics, and depending on the selection of turbulence model for Reynolds stresses, considerable important flow field variations can be obtained. As a consequence, important variations may also occur in the pollutant field. Figure 7-6 presents some details of the streamlines obtained with seven turbulence models (SKE, RNG, RKE, LRRIP, SKW, SST, SA) and the LES results of the same street canyon reported from [Liu02] (see section 1.3). Please note that the y-coordinate in this work corresponds to the z coordinate in the LES.

The flow field presented in each case consists of three main recirculation areas using any of the turbulent models, but substantial changes in size and shape can be distinguished. In all studied cases, a big recirculation located close to the centre of the canyon has been found (see Figure 7-6), with a diameter of circulation around the height of the canyon. It covers the majority of the flow field within the canyon and governs the predominant fluid motion. In the second level of details, there are two other vortices located at every bottom corner of the canyon rotating in the opposite direction of the big recirculation. These two secondary vortices also show small changes in size and shape for every model but always keep similar dimensional proportions between them. A fourth small recirculation was also found on the top-leeward corner for the turbulence models SA, SKW and SST.

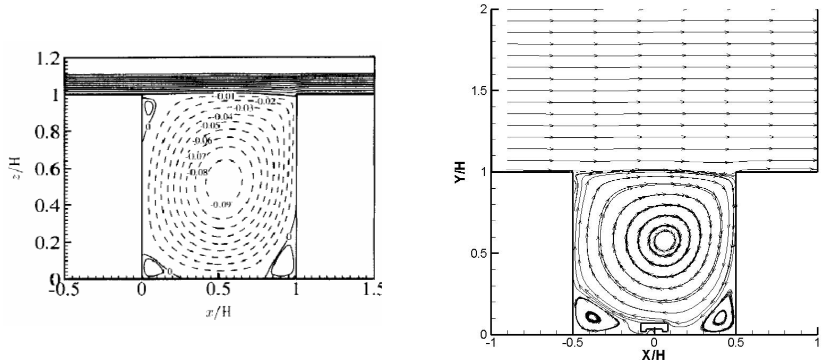

LES [Liu02] **SKE**

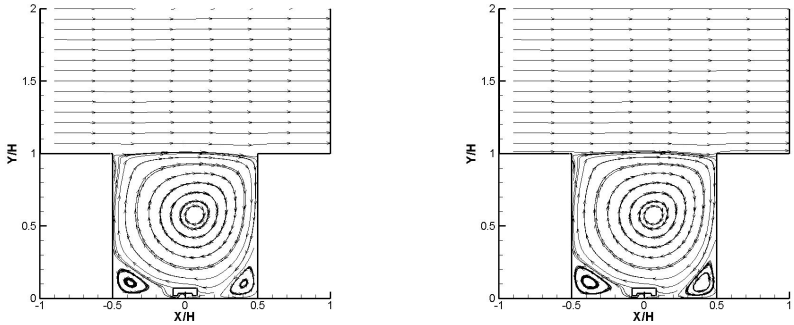

RNG **RKE**

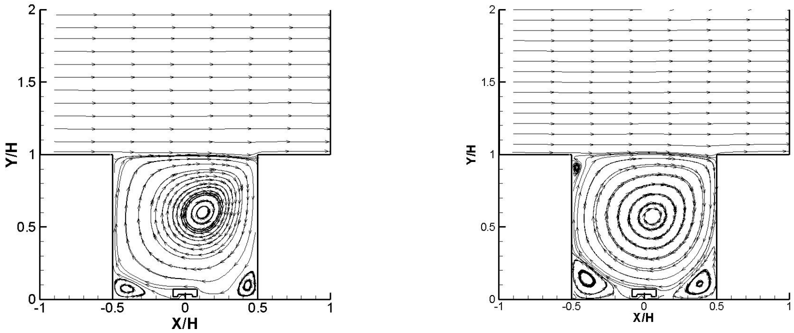

LRRIP **SA**

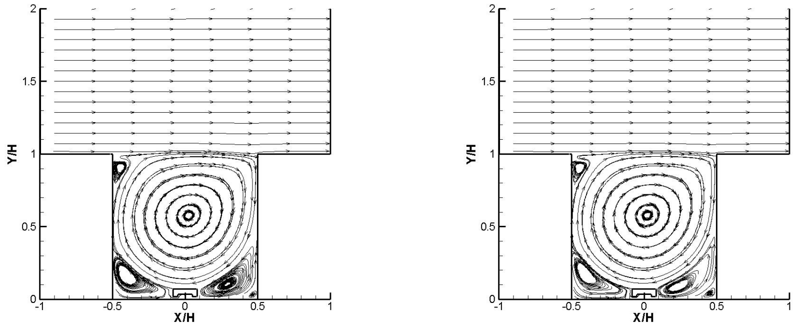

KW-SST **SKW**

Figure 7-6.-Streamlines numerically predicted for each of the used turbulence models for Reynolds stresses and LES predictions from [Liu02].

The direction and magnitude of all recirculation regions are produced and maintained by the transport of momentum taken by the big recirculation from the free flow area above the top of the canyon. Inside the canyon, this momentum is transported to the smaller vortices and then dissipated.

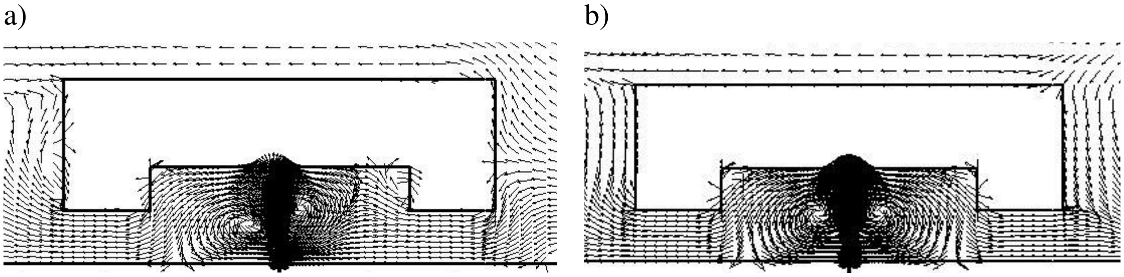

Figure 7-7.-Velocity field under pollution source roof in the centre bottom of the canyon. Details for (a) LRRIP and (b) SKW

Figure 7-7 presents a detail of two kinds of flow fields observed at the entrance of the pollutant to the canyon. Figure 7-7 (a) represents the model performance of a group (a), composed of the models SKE, RKE, RNG, LRRIP and S-A, and Figure 7-7 (b) represents the second kind of model performance of a group (b), composed of the SKW and SST models. The important aspect to take into account from the velocity fields (Figure 7-6) and the pollutant entrance performance (Figure 7-7) is how the recirculation sizes and entrance conditions affect the pollutant distribution. The flow field predicted by the models (a) presents two small recirculations at the bottom corners of the canyon. However, in the case of group (b), larger recirculations are formed in the same locations allowing flow contact between the windward bottom corners with the pollutant's source entrance. As a result, the pollutant in the first group enters at the bottom of the canyon and disperses following the main direction of the flow, from right to left. However, the second group performs very differently. The big recirculations at the bottom corners of the canyon, produced by the smaller prediction of turbulent viscosity in the *k-ω* based models (see comparison of turbulent viscosity in Appendix B (page 178), generate a flow movement with almost symmetrical flow direction (left and right) at the pollutant's entrance (see Figure 7-7 b).

Figure 7-8 shows how the different flow fields at the entrance of the pollutant using the *k-ω* based models generate a completely different dispersion of pollutants within the street canyon.

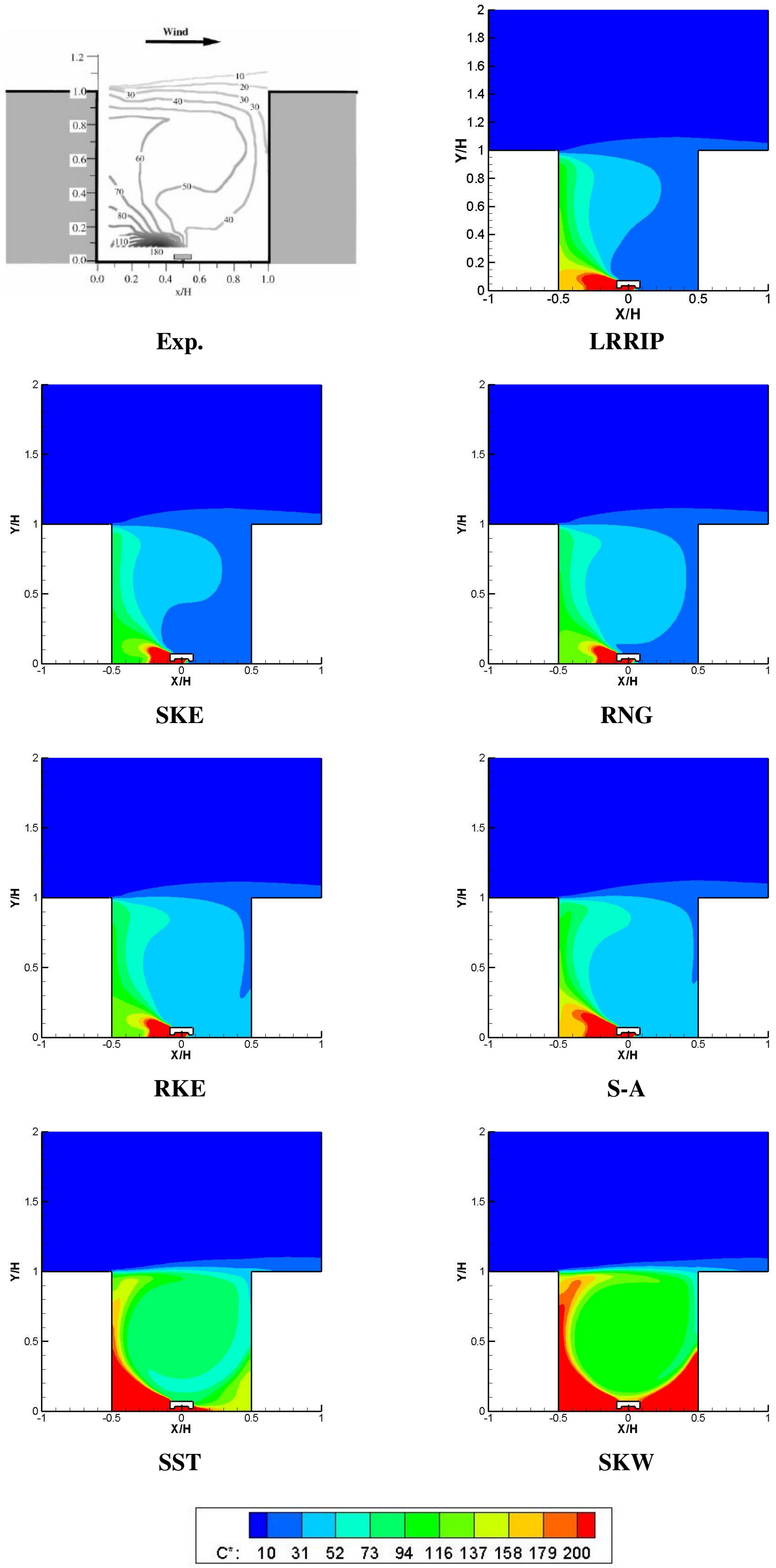

Exp.

LRRIP

SKE

RNG

RKE

S-A

SST

SKW

Figure 7-8. - Prediction of normalized concentration (*C) for all turbulence models for Reynolds stresses with the SED model. Experiments from [Pava99].**

The analysis of the two different behaviours of the flow at the pollutant entrance are not present in the LES results because this simulation neglects the flow effects produced for the pollution source roof, meaning the "roof" body located in front of the pollution source was not included in the simulations. However, looking at the small size of the bottom corner recirculations in the LES, it can be inferred that the LES results also behave as the flow field represented by group (a) in Figure 7-7.

Figure 7-9 shows the concentration comparison in the street canyon between the seven turbulence models for Reynolds stresses with the SED model and the experiments. The results have been separated into seven vertical lines (at constant x-coordinate) to cover all 70 measurement locations. This figure also includes the error bars from the spatial discretization error U_2 calculated from the Richardson extrapolation method in the simulation of the LRRIP model (see Table 7-2).

The evaluation of model performance has been based on the prediction of the normalized concentration C^* (see Eq. 7-2). The numerical predictions show a qualitatively fixed overestimation of concentrations within the entire canyon for the k-ω based models (SKW and SST). The rest of the models (SKE, RNG, RKE, SA and LRRIP) maintain similar predictions of concentration and in many cases, their differences are smaller than the mesh uncertainty (plotted only as example for the LRRIP). Again, in general it is possible to confirm that the SKW model presented the worst predictions for the concentrations C^*. Previous works like [Liu02] mention the predominance of the turbulence diffusion phenomenon for the transport and expulsion of pollutants outside of the canyon. Those results also coincide with the very high concentrations of pollutants observed in the k-ω based models as a consequence of their always lower turbulent viscosity predictions.

Another observation is that all models present the biggest errors and highest over-predicted concentrations at the first evaluation point located on the left side after the pollutant source entrance (see LINE X=-1.0E-02m of Figure 7-9), and it coincides with the area of the largest concentration gradient. In the second level of errors, some high concentration errors can be seen in the middle and right side of the canyon, which is probably due to the wrong prediction of diffusion coefficients. The specific locations of bad concentration predictions for all used turbulence models appear to be a common lack of RANS. The most probable reasons of these modelling limitations are due to the application of isotropic models.

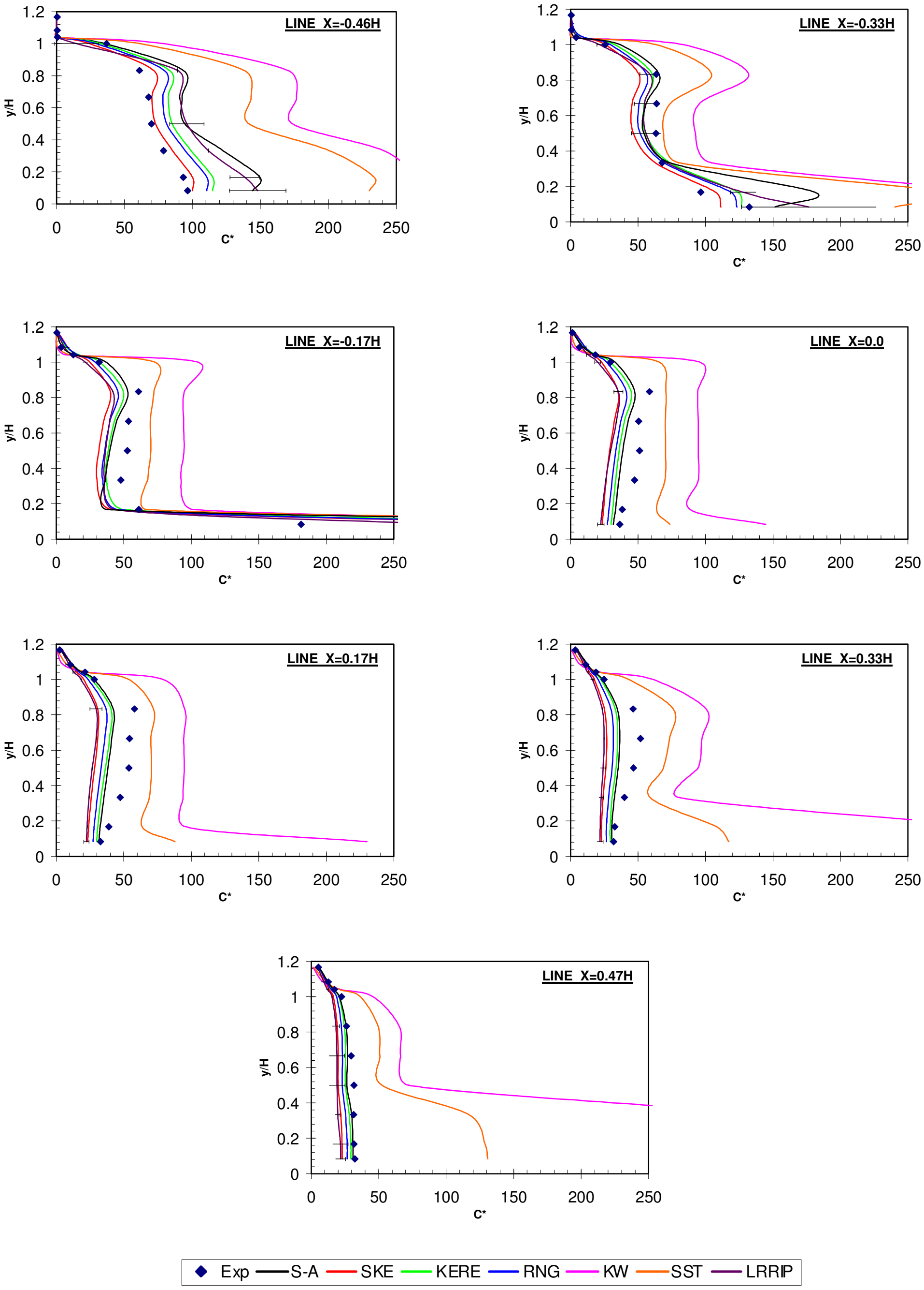

Figure 7-9. - Normalized concentration predictions for the seven turbulence models for Reynolds stresses with SED model for passive scalar concentration. Error bars for LRRIP show uncertainty U_2.

Finally, the numerical simulations have been quantitatively compared with the experiments through statistical metrics commonly used for the evaluation of model performance. Please refer to Chapter 6.1.1 for details about their calculation or directly to its original source at [Chan04]. These implemented statistical evaluation parameters have been used to compare the prediction capabilities of the seven turbulence models for Reynolds stresses in combination with the Simple Eddy Diffusivity (SED) model (with Sc_t=0.7) for the species transport equation at the 70 measurement points. The BOOT software [Chan05] was used to compute the evaluation metrics. The results are presented in Table 7-3 and Table 7-4. The software's authors recommend a rage for "acceptable" model prediction (see Chapter 6.1). The given ranges for each metric are FAC2 > 0.5, $|FB| < 0.3$, NMSE < 4, 0.7 < MG < 1.3 and VG < 1.6. The gray coloured cells in Table 7-3 are those where the results fulfil these conditions.

Table 7-3. - Reynolds stress model comparison using SED scalar flux model (Part I).

Model	*VG*	*MG*	MG_{FN}	MG_{FP}	*NMSE*	*FAC2*	*FB*	FB_{FN}	FB_{FP}	*q*
Exp	1.0	1.0	1.0	1.0	0.0	1.0	0.0	0.0	0.0	1.0
SKE	3.13	1.4	1.58	1.12	0.62	0.86	0.13	0.24	0.11	0.46
RKE	2.72	1.22	1.36	1.12	0.75	0.89	-0.05	0.11	0.16	0.77
KW	65.4	0.94	1.87	2.00	3.34	0.36	-0.95	0.01	0.95	0.29
SST	24.8	1.1	1.70	1.54	2.1	0.57	-0.65	0.01	0.65	0.40
RNG	3.01	1.28	1.44	1.13	0.61	0.87	0.02	0.16	0.14	0.67
LRRIP	4.18	1.53	1.68	1.10	0.33	0.89	0.08	0.23	0.15	0.31
S-A	7.5	1.36	1.50	1.11	2	0.93	-0.19	0.09	0.28	0.79

Table 7-4.-Reynolds stress model comparison using SED scalar flux model (Part II).

Model	*Mean*	*Sigma*	*Bias*	*High*	*2nd High*	*R*
Exp	39.52	32.07	0.0	181.34	132.5	1.0
SKE	34.64	50.85	4.87	400.03	111.37	0.86
RKE	41.47	58.66	-1.96	462.43	126.68	0.86
KW	110.44	117.8	-70.92	615.09	387.29	0.71
SST	77.21	97.23	-37.69	705.57	278.32	0.88
RNG	38.63	53.95	0.89	420.28	123.23	0.87
LRRIP	36.43	47.45	3.09	288.1	176.55	0.93
S-A	48.03	84.41	-8.51	676.2	180.88	0.82

The first line in Table 7-3 and Table 7-4 are the experimental values which represent the ideal values at which a model would give a perfect numerical prediction. The FAC2 in Table 7-3 is probably the easiest metric to fulfil the acceptance criteria recommended by [Chan05] because it allows a high percentage of error with the prescribed tolerance of 50%. The results show very good FAC2 values for most of the models with the anticipated exception of SST and KW. The SST model is included inside of the minimum tolerance with lower ranking, but the SKW model already falls out. The Fractional Bias (FB), which is a measure of the arithmetic difference between observed and predicted concentrations, is well predicted by all models except again the k-ω based models, but this time both SKW and SST fail. The FB_{FP} and FB_{FN} ($FB= FB_{FN}-FB_{FP}$) confirm the obvious over-prediction using these two models. A smaller over-prediction occurs for RKE and S-A. Under-prediction predominance is found for the SKE model in coincidence with previous works like [Walt02] and in lower proportion for the RNG and LRRIP model. Similar conditions to FB occur for the Normalized Mean Square Error (NMSE) parameter. This factor measures the scatter and reflects both, systematic and unsystematic (random) errors, and again excludes the same models as FB from the "acceptable" range, but adds S-A.

The VG and MG metrics may be seen as analogues to FB and NMSE but in logarithmic scale. This scale has the advantage to provide a more balanced treatment for extremely high and low values. However, the dependency of logarithmic functions at low concentrations makes them unstable. In this case, the considerable high amount of points with very low pollution concentrations (mostly located at the top of the canyon) cause the VG and MG parameters to report some incongruence with the other metrics for the best model selection. This behaviour occurs because the logarithmic values of the concentrations close to zero are not mathematically defined. Therefore, when calculating MG and VG, it is usually recommended to impose a minimum threshold for data values. The typical solution to overcome this problem is to set the instrument detection limit as the lower bound for both observed and predicted concentrations. In this case, the measurement uncertainty of 10ppm was used as the limit for full agreement for negligible pollutant concentrations. The MG_{FN} and MG_{FP} are mathematically analogous to the FB_{FN} and FB_{FP} in logarithmic scale and therefore suffer from the same problems as MG and VG.

Another important parameter presented in Table 7-4 is the Hit Rate "*q*" (see Chapter 6.1.2). It is a metric similar to FAC2 but it employs a lower relative tolerance W(=2) and the absolute tolerance or threshold from the measurements' uncertainty D(=25%), which is very useful for low concentration areas. The original Hit Rate acceptance criterion of 66% proposed by [VDI05] was used. The Hit Rate results show two interesting aspects. The first is that it confirms that the S-A, RKE and RNG models are in good agreement as was earlier reported by the FAC2. The second interesting observation is that the SKE and the most complex Reynolds stress model LRRIP got considerably worse marks than for the conservative FAC2. The most apparent reason for this change in the best model selection used by the Hit Rate is that the SKE and LRRIP models have a considerably high percentage of measurement points with a relative concentration error between 25% and 50%.

The additional reported parameters also corroborate the previously mentioned results. For example, the high values in the MEAN, SIGMA and BIAS help to observe the general large over-prediction of the data and their errors when these parameters from the k-ω based models are compared with the experiments. These results, in addition to those reported from the HIGH and second HIGH parameters, are useful to understand the differences between the systematic (FB and MG) and unsystematic (NMSE and VG) parameters when highly disperse error distributions are obtained. Finally, the correlation R close to one is a pre-requirement for a good model prediction, but in this case it does not present considerable differences to report relevant information for a best model selection.

Unfortunately, the wind tunnel experiment [Pava99] selected to validate these numerical simulations does not report any details about the velocity field or turbulence parameters. Therefore, the evaluation of turbulence models can only be performed based on the predicted concentration accuracy. It must be mentioned that this assumption only makes it possible to evaluate the model combination (for stresses and scalar fluxes). It does not necessarily mean that the best model combination coincides with the best prediction of velocity field or pollutant dispersion.

7.4.2 Reynolds Stress Tensor Prediction

The Reynolds stresses are very important parameters to take into account for anisotropic scalar flux modelling. They are inserted in most of the scalar flux models (see Table 3-6), and therefore an analysis of them must be done. The Reynolds stresses are calculated explicitly by the LRRIP model. For the two-equation models, the stress components have been calculated using the predicted turbulent kinetic energy, turbulent viscosity and velocity gradients with the Boussinesq hypothesis (Eq. 3-1). All implemented turbulence models for Reynolds stresses were computed and compared in this way except for the S-A model, because this approach does not incorporate an explicit estimation of turbulent kinetic energy (see section 3.1.1 for more details).

A qualitative comparison of Reynolds stresses was carried out contrasting the computed Reynolds stresses with the LES results from [Liu02]. The root-mean-square for u (u_{rms}) and v (v_{rms}) velocity fluctuations, non-dimensionalized with the reference velocity (U_{ref}) are shown in Figure 7-10 and Figure 7-11. From the results, general similarities can be seen between most of the RANS models with LES. The LES presented two very clear locations of maximum values of the u_{rms} and v_{rms} parameters. However, these local maximums are not always so clearly observed in the RANS results.

The root-mean-square of the streamwise turbulent normal stress (u_{rms}) presents the highest maximum along the top and top-windward corner of the canyon, and a second local maximum is located at the bottom leeward corner of the canyon. Similarly, the v_{rms} predictions present again the highest values at the top and second highest at the bottom windward corner of the canyon. The reason for these locations is due to the formation of a flapping shear layer at the top of the street canyon due to the continuous exchange of mass and momentum with the atmospheric boundary flow above. It also causes strong velocity variations close to the windward wall in which the flow impinges. The other two local maximums at the two bottom corners are due to the presence of the secondary recirculations. These corner eddies should be very unstable and change their form and local velocity directions continuously.

The RANS models present a comparable order of magnitude for the u_{rms} results but the locations of the maximum normal stresses are more dispersed and not as high and clearly defined as reported from the LES results. As can be seen in the graphics, the u_{rms} values were always under-predicted in comparison to the LES. Between the RANS models, the three k-ε based models (SKE, RNG and RKE) present close similarity and some few bigger differences were found using the LRRIP model. The simulations using the LRRIP model report lower u_{rms} in comparison to the k-ε models at the leeward bottom recirculation area but they also report higher values at the general maximum located at the top of the canyon.

The RANS predictions of v_{rms} for the same four models (SKE, RNG, RKE and LRRIP) agree with the location of the general maximum along the top of the canyon with extension through the windward wall and its bottom corner. The magnitude of the v_{rms} reported for all RANS models is also under-predicted in the entire canyon compared to the LES.

The results for the k-ω based models (SKW and SST) have been also included in the figures and they show much lower Reynolds stress predictions in the entire canyon. Thus, the lower predictions of turbulent viscosity from these two-equation models do not produce sufficiently high normal stresses. To observe some qualitative comparison of these model predictions please refer to Figure B- 5.

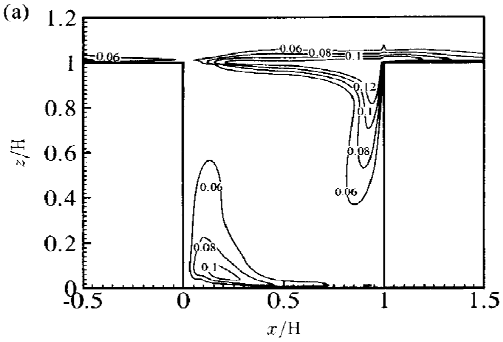

u_{rms} /U_{ref} for LES [Liu02]

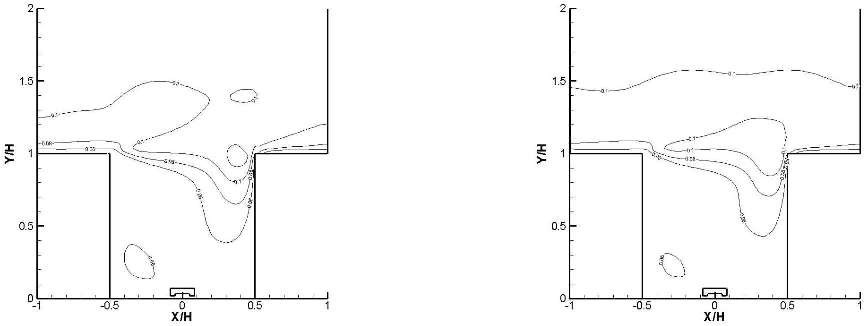

u_{rms} /U_{ref} for SKE

u_{rms} /U_{ref} for RNG

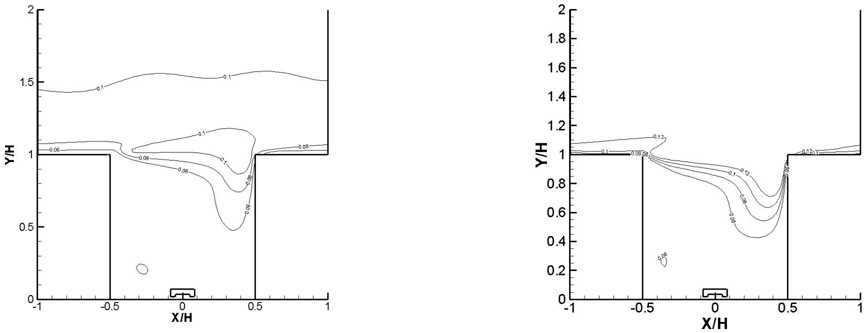

u_{rms} /U_{ref} for RKE

u_{rms} /U_{ref} for LRRIP

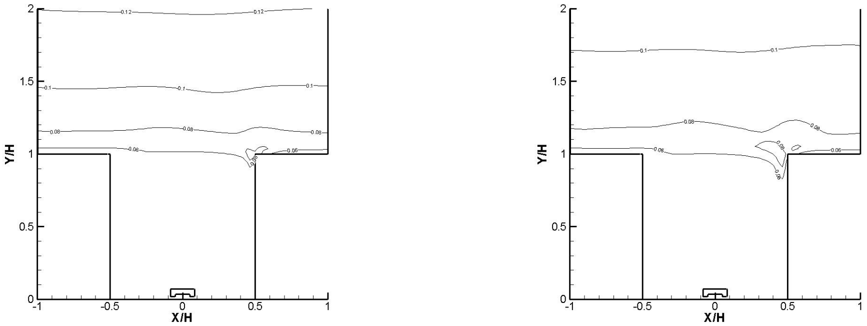

u_{rms} /U_{ref} for KW

u_{rms} /U_{ref} for SST

Figure 7-10.- Contour plots of normalized Reynolds stresses (u_{rms} /U_{ref}) for LES [Liu02] and SKE, RKE, RNG, LRRIP, KW, SST.

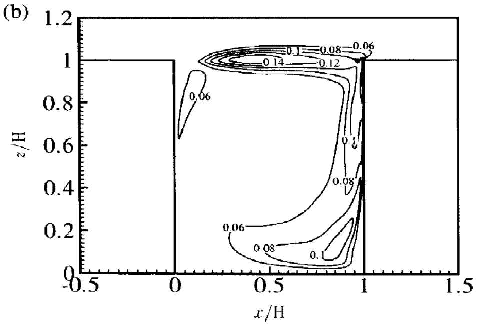

v_{rms}/U_{ref} **for LES [Liu02]**

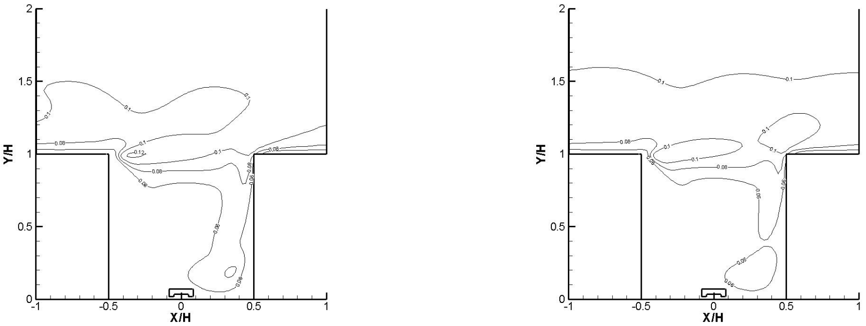

v_{rms}/U_{ref} **for SKE**

v_{rms}/U_{ref} **for RNG**

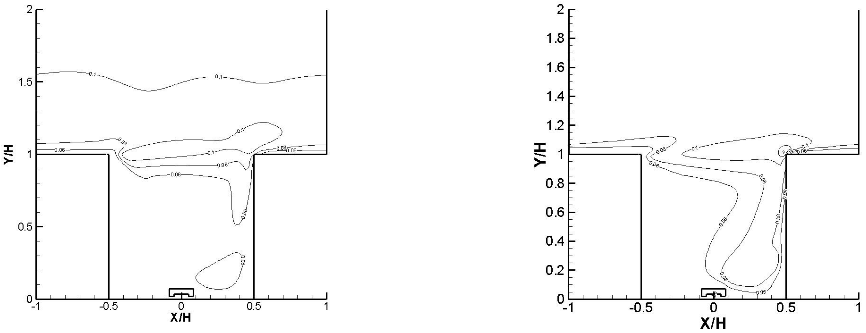

v_{rms}/U_{ref} **for RKE**

v_{rms}/U_{ref} **for LRRIP**

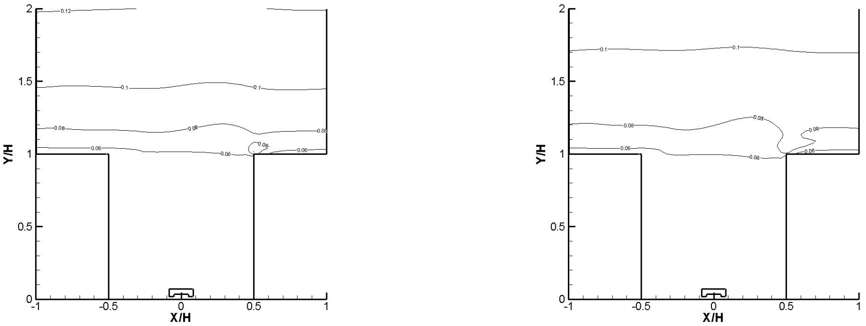

v_{rms}/U_{ref} **for KW**

v_{rms}/U_{ref} **for SST**

Figure 7-11.- Contour plots of normalized Reynolds stresses (v_{rms}/U_{ref}) for LES [Liu02] and SKE, RKE, RNG, LRRIP, KW, SST.

7.4.3 Active and Passive Pollutant Simulation

As explained in Chapter 5.1.1, an additional study was performed to compare the pollutant dispersion in the canyon considering the pollutants either as a passive or an active scalar. This possible influence is analysed here.

The active scalar transport equation is simply the Reynolds averaged species transport equation (Eq. 2-4) which was introduced as one of the governing equations in fluid mechanics but with some additional source terms. The active scalar transport considered in this work takes into account buoyant effects and fluid property variations due to the inclusion of a different fluid in the flow field. When a passive scalar is considered, it is an inert species, meaning that the species transport equation is reduced to a simple convective-diffusion transport equation without buoyancy or property variations. In this case, the transported scalar quantity does not affect the flow field.

The general setup conditions for these simulations are separated in two cases:

- **Case 1.** Simulation of pollutants as an active scalar: This simulation has been done through the calculation of the species transport equation considering the inclusion of a different fluid (ethane) in the main fluid flow (air). It is theoretically the most accurate calculation without taking into account chemical reactions and heat transfer between the two different fluids. These other transport phenomena were also neglected in the experiments.
- **Case 2.** Simulation of pollutants as a passive scalar: This simulation has been accomplished through the calculation of a UDS transport equation and a subroutine to implement the same scalar flux model (SED). The same computational domain, grid and setup conditions used for the Case 1 were maintained but all fluid properties were changed from the pollutant (ethane) equal to the main fluid (air).

Figure 7-12 shows the concentration profiles for the simulation of pollutant dispersion as an active and passive scalar in contrast with the experiments. The used turbulence models were the LRRIP for Reynolds stresses and the Simple Eddy Diffusivity (Sc_t=0.7) for scalar fluxes. The two simulation results are plotted along seven vertical lines to cover all the measurement points within the canyon. In general, the active and passive scalar computations predict very similar species concentrations for most of the domain. As expected, the point with biggest absolute concentration difference between both simulations is where the highest measured concentration is found, which can be seen at the bottom part of the line $X=-1.0\cdot 10^{-2}$m. However, the average relative difference in C^* between both cases was under 4% and in most cases, these differences were smaller than the mesh uncertainty.

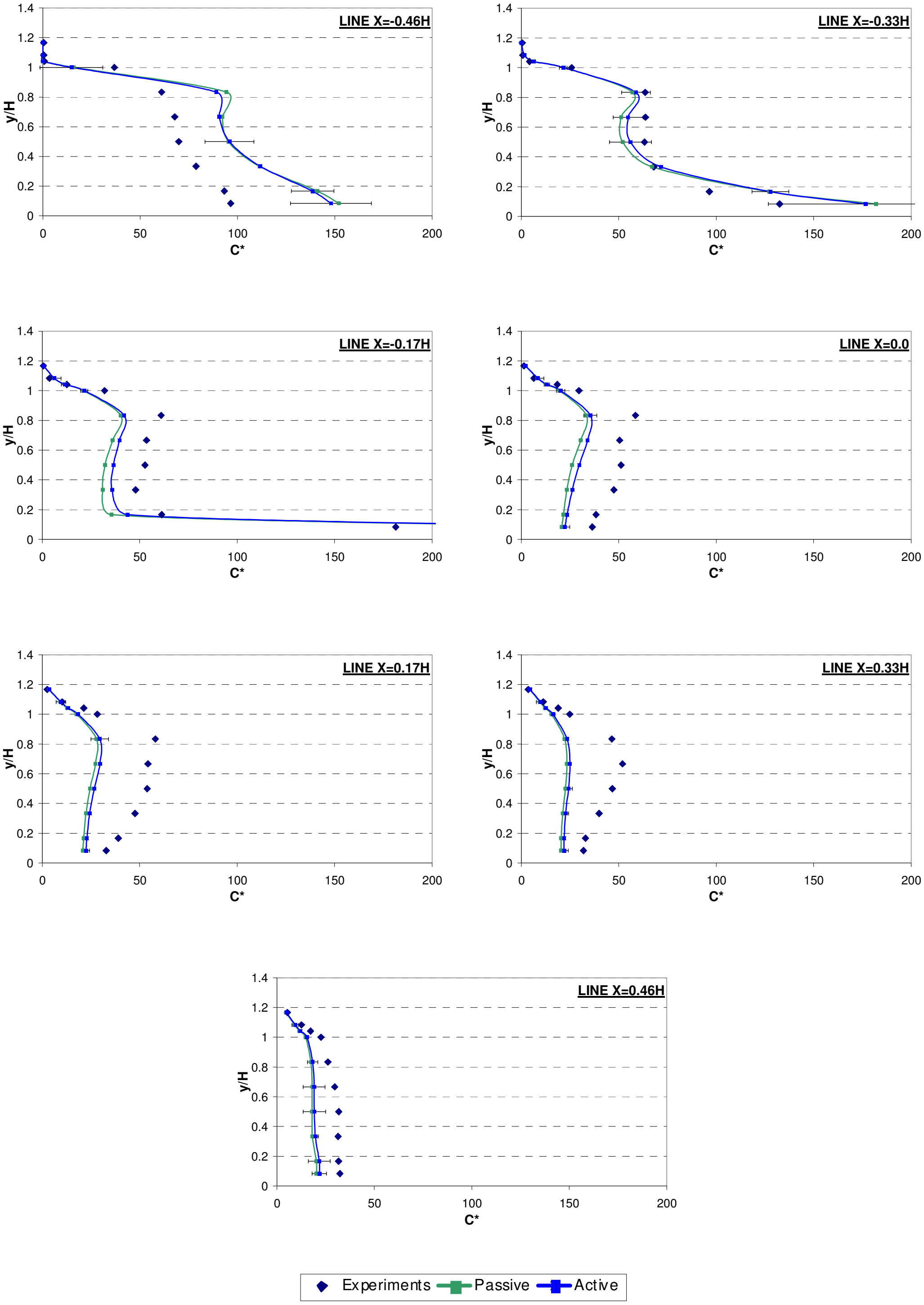

Figure 7-12.- Passive/active scalar dispersion and experiment. Error bars from passive LRRIP and SED model combination behaviour.

The previous observations can be corroborated with statistical metrics analysis. To quantify the differences between passive and active pollutant simulations, statistical metrics have been included in Table 7-5 and Table 7-6. The ideal metric values for a perfect model agreement are presented in the line Exp (it means here that there is a perfect agreement of the experiments with itself). The results show again very high similarity between the two studied cases in most evaluation parameters, with some very small improvement for the full species (active scalar) transport equation. With these results, it has been shown that the small property differences between air and ethane at this low concentration do not produce considerable changes in the flow. Under these conditions, ethane can be perfectly considered as a passive scalar pollutant.

Table 7-5. – Metrics of *Cfor active and passive scalar treatment. (Part I)**

Model	*VG*	*MG*	*MG_{FN}*	*MG_{FP}*	*NMSE*	*FAC2*	*FB*	*FB_{FN}*	*FB_{FP}*	*q*
Exp	1	1	1.00	1.00	0.0	1.0	0.0	0.0	0.0	1
Passive	4.57	1.61	1.77	1.10	0.36	0.81	0.11	0.26	0.16	0.31
Active	4.18	1.53	1.68	1.10	0.33	0.88	0.08	0.23	0.15	0.31

Table 7-6. - Metrics of *Cfor active and passive scalar treatment. (Part II)**

Model	*Mean*	*Sigma*	*Bias*	*High*	*2^{nd} High*	*R*
Exp	39.52	32.07	0.0	181.34	132.5	1.0
Passive	35.35	47.45	4.17	279.92	182.04	0.92
Active	36.43	47.45	3.09	288.10	176.55	0.93

7.4.4 First and Second Order Spatial Discretization Schemes

The comparison between first (1^{st}) and second (2^{nd}) order spatial discretization schemes was also performed. This study was carried out with the intention to take into account as many parameters as possible which can influence a pollution dispersion prediction of a CFD simulation. Some published studies about CFD good practices or technical recommendations ([Case00] and [Flue06], for example), suggest the selection of second order spatial discretization schemes to obtain results with lower numerical errors.

To analyse the first and second order influence in pollution dispersion, the numerical simulation of three different cases has been performed. They are: (a) 1^{st} order (all variables), (b) 2^{nd} order (all variables), (c) 1^{st}order2 (1^{st}order for species and 2^{nd}order for any other variable). The results are shown in Figure 7-13 where experimental measurements are always included.

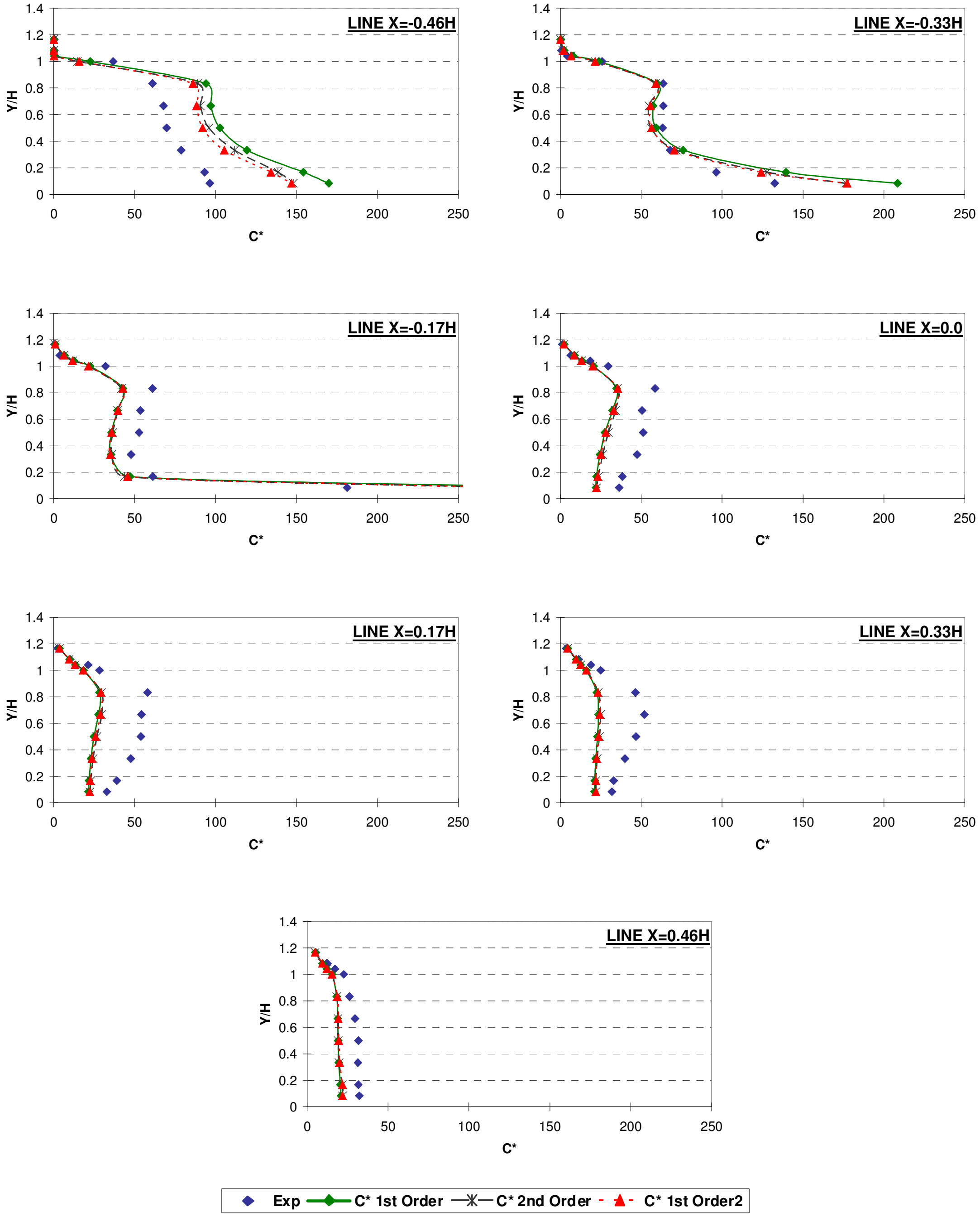

Figure 7-13. - Comparison of 1st and 2nd order spatial discretization schemes. The three simulations are: 1storder (all variables), 2nd order (all variables), 1st order2 (1st order for species and 2nd order for any other variable).

The pollution dispersion for the first and second order spatial discretization schemes was calculated using the LRRIP and SED models with the middle size mesh. The results show a similar prediction between all cases with average relative error of 7.63% (1storder – 2ndorder), 2.66% (2ndorder – 1storder2) and 6.38% (1storder – 1storder2), with respect to the experiments, i.e.:

$$Percentage = \left\langle \frac{Sim_A - Sim_B}{Exp} \right\rangle_P \qquad \text{Eq. 7-6}$$

where Sim_A and Sim_B are the two different predicted concentrations from simulations *A* and *B* respectively, and *Exp* is the corresponding experimental measurement. All three parameters were evaluated at the same location *P*.

The biggest relative error was found between the full 1st and 2nd order simulations (up to 100% with absolute error $C^* \approx 0.77$) and is located in a point situated at the top leeward corner. The second highest prediction difference (up to 24% with absolute error $C^* \approx 43$) is located at the first measurement point after the pollutant entrance. Both cases coincide with points where high concentration gradients exist.

Table 7-7 and Table 7-8 present the computed metrics of the three studied cases. Similar to the graphical plots, it can be observed that the concentration predictions are very similar between the three simulations. An interesting observation from these tables is that the presented metrics show non-uniform behaviour in making a clear "best model" selection. The best model performance changes depending on the selected statistical evaluation parameter.

For example, an ideal model (see line Exp) would have a NMSE equal to zero, thus NMSE report the best agreement for the C* from 1^{st}order2, followed closely by the C* from 2^{nd}order and the worst predictions are for the C* from 1^{st}order. If the ideal FB must be equal to zero and FAC2, VG and MG equal to one, the best model agreement is always different. This case is a good example of the BOOT software recommendation of taking into account more than one statistical metric. Other authors (e.g. [Oles08]) also suggest looking at the graphical representation of results in conjunction with the metrics.

Table 7-7. – Metrics of *Cfor 1^{st} and 2^{nd} order spatial discretization schemes (Part I)**

Model	*VG*	*MG*	MG_{FN}	MG_{FP}	*NMSE*	*FAC2*	*FB*	FB_{FN}	FB_{FP}	*q*
Exp	1	1	1.00	1.00	0	1	0	0.00	0.00	1
C*1^{st}ord	1.95	1.34	1.52	1.13	0.52	0.84	0.02	0.23	0.21	0.34
C*2^{nd}ord	4.18	1.53	1.68	1.10	0.33	0.89	0.08	0.23	0.15	0.31
C*1^{st}ord2	2.13	1.42	1.56	1.10	0.30	0.86	0.09	0.24	0.14	0.31

Table 7-8. - Metrics of *Cfor 1^{st} and 2^{nd} order spatial discretization schemes (Part II)**

Model	*Mean*	*Sigma*	*Bias*	*High*	*2^{nd} High*	*R*
Exp	39.52	32.07	0	181.34	132.5	1
C*1^{st}ord	38.67	54.23	0.84	331.58	208.44	0.92
C*2^{nd}ord	36.43	47.45	3.09	288.1	176.55	0.93
C*1^{st}ord2	35.92	46.4	3.6	281.07	177.38	0.93

In conclusion, no significant differences were seen for the selection of 1st or 2nd order spatial discretization schemes for better performance of the numerical simulation of pollutant dispersion. However, a different analysis of results would be possible depending on the relevance of these reported "insignificant" differences. For example, small increases of toxic or radioactive pollutants in an urban area may represent a significant health risk for the inhabitants in the surroundings. Therefore, the neglection of these small variations in the numerical predictions may represent an important issue in specific applications.

All simulations performed in the present work have been carried out following the cited theoretical recommendations. Therefore, the second order spatial discretization scheme was selected for the evaluation of all turbulence models.

7.4.5 Concentration Predictions Using Different Turbulence Models for Scalar Fluxes

Analogous to the Reynolds stress models, it was expected that the scalar flux models would also produce major differences in the prediction of pollution dispersion. In total, nine scalar flux models were employed in this work. They can be classified into three groups (see Chapter 3.2). The first group has two versions of the isotropic Simple Eddy Diffusivity model with Sc_t=0.7 (SED1) and Sc_t=0.9 (SED2). The second group has five different algebraic anisotropic models—the Generalized Gradient Diffusion Hypothesis (GGDH), the ABE-SUGA model, the ABE model, the WET model, and the YOUNIS model. Finally, the third group has two second moment models represented by the S-M DURBIN model and the S-M HANJALIC model. Similar to the previous studies, the normalized concentration C^* has been used to compare the combined performance of each of the implemented scalar flux models together with the LRRIP Reynolds stress model.

Figure 7-14 shows the scalar predictions of each scalar flux turbulence model plotted along the seven vertical lines to cover the 70 measurement points. From this figure, several important observations can be mentioned. The most evident is probably the expected better behaviour in a high percentage of the measurement points when using the second moment models. In general, the algebraic scalar flux models present a similar performance with the usual under-predicted concentrations in the centre and on the right side of the canyon. The region on the left side of the canyon presents similar over- and under-prediction behaviour for most models. All models fail as they consistently over-predict the concentration of the passive scalar at the highest measured concentration (C^*=181) located on the left side of the pollutant's entrance (see bottom point in LINE X=-017H, Figure 7-14). The highest absolute error for all models and the highest relative error for several models occur at this location. These values are:

Table 7-9. – Maximum absolute and relative error at the point with highest measured concentration, which is the closest point to the pollutant source.

	SED1	*SED2*	*GGDH*	*ABE-SUGA*	*ABE*	*WET*	*YOUNIS*	*S-M DURBIN*	*S-M HANJALIC*
Absolute error (C^*)	98.57	109.82	96.48	111.44	47.61	156.89	259.92	246.95	259.88
Relative. error (%)	54.36	60.56	53.21	61.45	26.25	86.52	143.33	136.18	143.31

As can be seen in Table 7-9, both second moment models (S-M DURBIN and S-M HANJALIC) together with the YOUNIS model have the highest over-prediction. The same tendency also occurs for a few more points with high concentrations. Therefore, although general improvement can be seen for the second moment models' behaviour, their prediction close to the source is still problematic. The highest relative error for all algebraic models is located at the top of the canyon where the concentration values are generally small. From Table 7-9, one may conclude that the RANS models usually over-predict concentrations in locations with very high concentration gradients.

These results have also been analysed by means of statistical evaluation metrics (see Table 7-10 and Table 7-11). The FAC2 and q (Hit-Rate), which are commonly known as very stable statistical metrics, report considerable differences between them. The FAC2 presents relatively good and comparable results between most of the models (within ±6%), with special outstanding behaviour for the SED2 and GGDH model and the two second moment models with values for FAC2 over 90%. However, the q (Hit-Rate) results only promote the use of the second moment models. The differences between these two metrics may be produced due to the more strict conditions of the allowed relative difference (D=25%) and the inclusion of a very small allowed absolute tolerance of C^*(W=2) in the Hit-Rate calculation. On the other hand, the WET model fails in being always out of the recommended range of an "acceptable" model, and presents the worst agreement with the experiments. As can be observed in Table 7-10 and Table 7-11, there is an appreciable change between the SED models due to a simple variation of the turbulent Schmidt number (Sc_t), meaning that the selection of this parameter must be done with special care (see discussion in Chapter 3.2.1.1). The Sc_t is usually set at a value between 0.7 and 0.9 (see e.g. [Durb01] and [Tomi07]), and for that reason these two limits were selected to represent the SED1 and SED2 models, respectively.

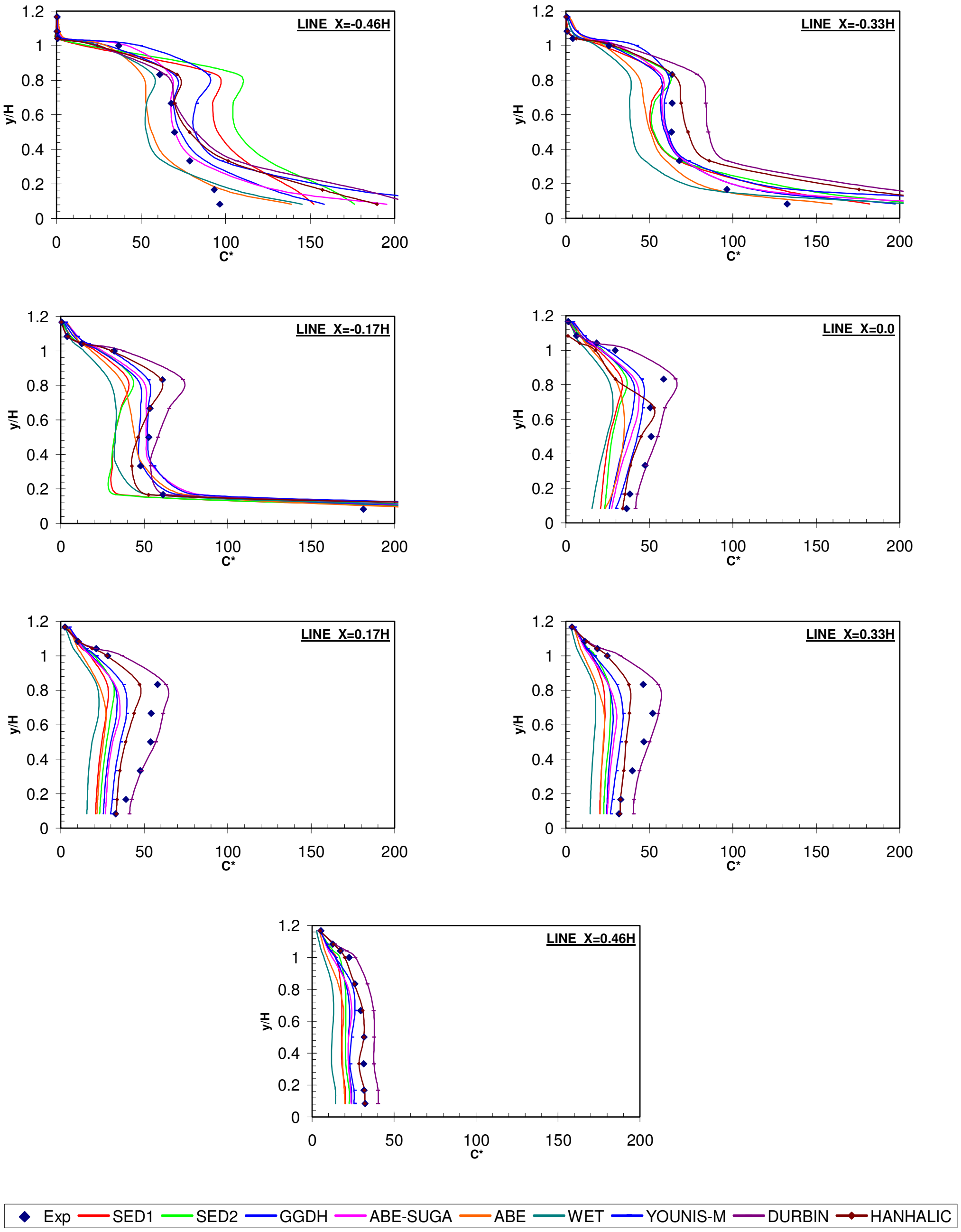

Figure 7-14. - Comparison of normalized concentration *C for several turbulent models for scalar fluxes in combination with the LRRIP model for Reynolds stresses.**

The NMSE metric shows that all the models' performance is inside of the recommended range. The best performance was found for the ABE and GGDH model and the worst for the YOUNIS model. Similar to the NMSE, the FB includes almost all models inside of the recommended range, but with the FB the selection of the best models should be analysed in conjunction with their over-prediction (FB_{FP}) and under-prediction (FB_{FN}) parts. The SED2, GGDH and ABE-SUGA models present the best FB factor under 0.05. However, the FB metric of SED2 results come from the difference of a much higher absolute value for under- and over-predictions, which means that this good FB factor is more a result of error compensation than a genuine accurate prediction. Table 7-10 also confirms the high over-prediction (large FB_{FP} and negative FB) of the second moment models (S-M DURBIN and S-M HANJALIC) and the YOUNIS model. Therefore, the GGDH and ABE-SUGA can be mentioned as the best performers for the metric FB.

The VG and MG parameters, with acceptance criteria of VG<1.6 and 0.7<MG<1.3, perform similarly to their analogues NMSE and FB. However, VG and MG errors are larger and their acceptance criteria exclude the WET and SED models as well as the ABE and the two Second Moment models (S-M DURBIN and S-M HANJALIC) for VG. The GGDH model performs best for these two factors and the S-M DURBIN model also presents good agreement for MG. This general lower ranking in the VG parameter is a reflection of an unsystematic error distribution within the data.

Table 7-10.- Scalar flux model predictions using LRRIP model(Part I).

Model	*VG*	*MG*	MG_{FN}	MG_{FP}	*NMSE*	*FAC2*	*FB*	FB_{FN}	FB_{FP}	*q*
Exp	1	1	1.00	1.00	0	1	0	0.00	0.00	1
SED1	4.57	1.61	1.77	1.10	0.36	0.81	0.11	0.27	0.16	0.31
SED2	8.39	1.6	1.76	1.10	0.45	0.94	0.02	0.22	0.20	0.39
GGDH	1.3	1.12	1.28	1.15	0.25	0.91	0.05	0.17	0.12	0.57
ABE-SUGA	1.46	0.96	1.22	1.27	0.36	0.86	-0.02	0.15	0.17	0.57
ABE	1.68	1.15	1.43	1.24	0.21	0.70	0.22	0.29	0.07	0.40
WET	1.78	1.61	1.78	1.11	0.69	0.44	0.30	0.42	0.13	0.31
YOUNIS	1.39	0.89	1.16	1.30	1.14	0.84	-0.21	0.10	0.30	0.63
S-M HANJALIC	3.26	1.23	1.29	1.19	0.81	0.94	-0.18	0.06	0.24	0.83
S-M DURBIN	1.86	0.98	1.18	1.20	0.79	0.90	-0.32	0.01	0.32	0.73

Table 7-11.- Scalar flux model predictions using LRRIP model (Part II)

Model	*Mean*	*Sigma*	*Bias*	*High*	*2nd High*
Exp	39.52	32.07	0	181.34	132.5
SED1	35.35	47.45	4.17	279.92	182.04
SED2	38.87	52.18	0.64	291.17	210.58
GGDH	37.71	45.71	1.81	277.83	197.37
ABE-SUGA	40.15	49.85	-0.63	292.79	228.26
ABE	31.62	37.48	7.9	228.96	159.42
WET	29.3	49.58	10.21	338.24	205.96
YOUNIS	48.55	72.08	-9.03	441.27	344.21
S-M HANJALIC	47.08	65.21	-7.56	441.23	257.49
S-M DURBIN	54.53	67.14	-15.01	428.30	286.46

In addition to the mentioned metrics, some general statistical parameters are given in Table 7-11. They are the MEAN, SIGMA, BIAS, R, HIGH and 2nd HIGH.

These additional parameters have been taken into account as secondary or complementary information for the error analysis. The MEAN (arithmetic mean average), SIGMA (standard deviation) and BIAS (Difference in the means) are very general parameters and therefore must be taken into account with careful consideration. From these three parameters one can note the pronounced under-prediction by the WET model and the predominant over-predictions of both second moment models. All these parameters together with the HIGH and 2^{nd} HIGH are also useful for understanding the systematic and unsystematic distribution characteristics of the data, and for avoiding possible incongruence from the average-based metrics. For example, the reported HIGH and 2^{nd} HIGH values express an idea of the large range of concentrations and the unsystematic distribution of errors of the second moment models. The HIGH and 2^{nd} HIGH over-predictions explain the reported high values in the MEAN, SIGMA or BIAS, although the second moment models have very good FAC2 and Hit-Rate.

It is important to refer to the good FAC2 ranking of the SED based models under the special flow case which occurs within the street canyon. A possible reason for this high ranking may be due to an alignment of the scalar gradient direction coinciding with the main fluid flow direction at the pollutant entrance. This condition is one of the most well known and important limitations of this model, but it looks like the SED model was applied in a favourable condition. Also, previous works like [Tomi07] mention that the convection transport inside a street canyon is the predominant transport phenomenon of pollutants. Therefore, it can be expected that this model should achieve similar results like the other models.

Next, Figure 7-15 shows the contours of the normalized concentration C^* corresponding to the results of Table 7-10 and Table 7-11. This figure presents the contour plot for the two isotropic algebraic scalar flux models (SED1 and SED2), all the anisotropic algebraic scalar flux models (GGDH, ABE-SUGA, ABE, WET and YOUNIS), the two implemented second moment models (S-M DURBIN and S-M HANJALIC), and the experimental measurements plotted in a coarse distribution of 70 measurement points inside the canyon. The comparison of scalar flux models in the contour plots presents good agreement with the previously reported statistical metrics. In general, all concentration predictions show similar behaviour with some variation in the shape of the pollutant dispersion. Based on the qualitative description presented by the contour plot and the reported statistical metrics, the two versions of second moment models (S-M DURBIN and S-M HANJALIC) present the closest agreement with the experimental measurements.

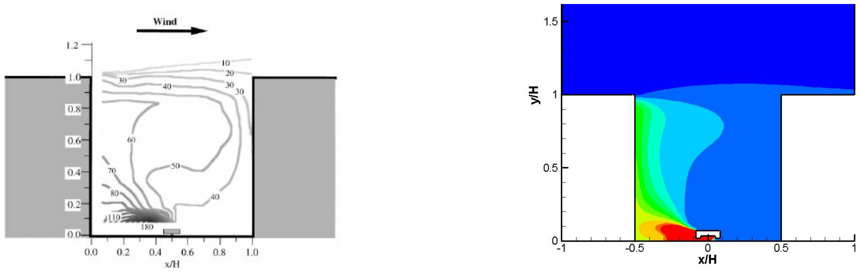

Experiments [Pava99] **Model SED1**

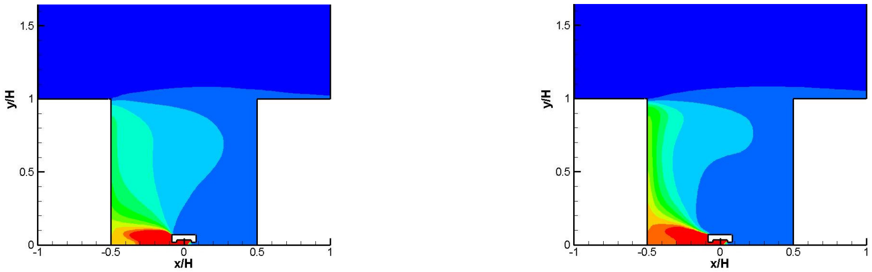

Model GGDH **Model SED2**

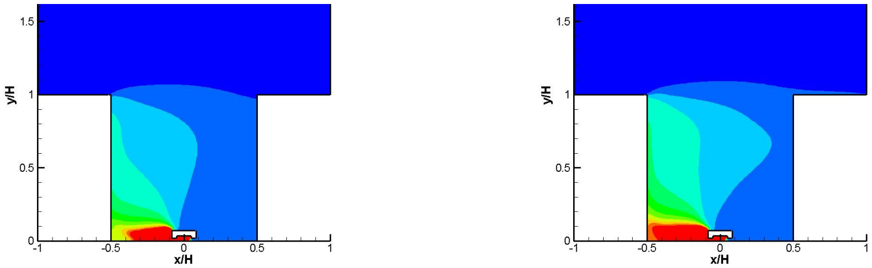

Model ABE **Model ABE-SUGA**

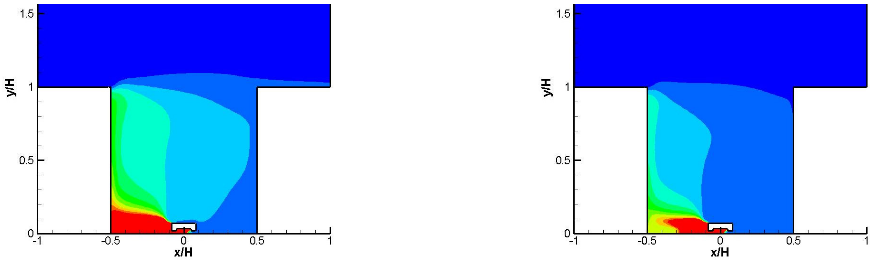

Model YOUNIS **Model WET**

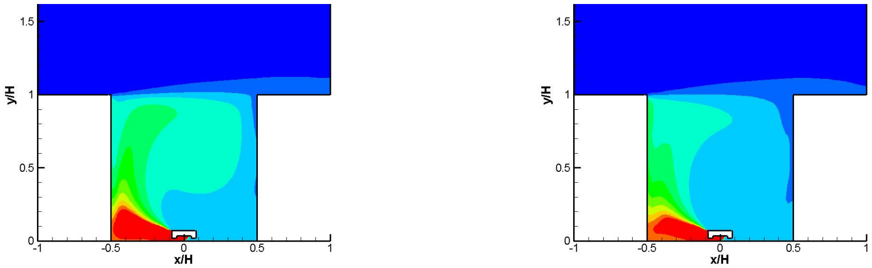

Model S-M DURBIN **Model S-M HANJALIC**

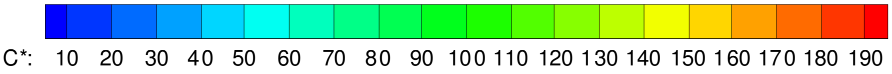

Figure 7-15.- Normalized concentration *C from computed scalar flux models and experiments.**

7.4.6 Comparison of Turbulent Scalar Flux Predictions

Turbulent scalar fluxes are the inter-medium results for the calculation of the pollutant distribution because they represent the value of one term within the complete average pollutant transport equation. They are, however, the final result for each of the scalar flux models studied in this work. Therefore, they are analysed in this separate section.

The first inconvenience of a scalar flux study is that the numerical quantities cannot easily be measured in the experiments and therefore are usually not reported[12]. Unfortunately, the wind tunnel experiment used in the present work to validate the numerical results ([Pava99]) did not report the scalar fluxes. Therefore, no quantitative error evaluation like statistical metrics or Hit-Rate can be done. Thus, only the qualitative comparison of contours with the further advanced LES [Liu02] results may be used for the analysis of scalar flux predictions.

Figure 7-16 and Figure 7-17 show the contour plots of the calculated scalar fluxes $\overline{u'\phi'}$ and $\overline{v'\phi'}$ respectively. The LES results from [Liu02] were also included in each of these figures for qualitative comparison purposes. The normalization of scalar fluxes was done with the factor (HL/Q) where H [m] is the building height, L [m] is the bi-dimensional pollutant source line length and Q [m^3/s] is the pollutant volume flow rate. The Reynolds stress model selected for this analysis is the LRRIP model because this model should help to maximize the anisotropic effects of these advanced turbulent scalar flux models.

To understand the behaviour of scalar fluxes, a preliminary physical description is needed. Scalar fluxes are turbulent parameters used to measure the fluctuating convective transport of pollutants. They are formed by time averaged products of fluctuating velocity components and fluctuating concentrations. Due to the physical definition of the concentrations, their value cannot be negative and therefore the sign of these parameters is exclusively dependent on the direction of the fluctuating velocities. Thus, the absolute value of the scalar fluxes is the actual magnitude of these fluctuating convective transports and the sign represents the direction in which the transport takes place.

The highest scalar flux magnitudes calculated for both $\overline{u'\phi'}$ and $\overline{v'\phi'}$ were found at the bottom leeward corner of the canyon. Similarly, an important local minimum for the streamwise scalar flux and almost general maximum for the vertical scalar flux was found at the top level of the canyon. In general, the results from the

---

[12] See e.g. [Pfad08] for a description of a method to measure the analoguous heat fluxes.

RANS simulations are congruent with the reported LES from [Liu02], but include some variations in contour shapes, their magnitudes, and differences in the location of maximum/minimum scalar fluxes.

The distributions of the scalar fluxes have a clear reason. The scalar fluxes are formed by the multiplication of a velocity fluctuation and a scalar fluctuation. Therefore, the only possibility to have a local/general maximum or minimum in the scalar fluxes is when either the velocity and/or scalar fluctuations are large. Examining the u_{rms} distribution within the canyon (Figure 7-10) and the scalar fluctuation reported from the experiments (Figure B- 4, Appendix B, p.178) one can understand the location of the high scalar flux values. For example, the large local minimum of the streamwise scalar flux and the local maximum of the vertical scalar flux both located at the top of the canyon are the result of the high velocity fluctuation in the shear layer (see Figure 7-10 and Figure 7-11). As mentioned before, the sign of the scalar fluxes are only a consequence of the direction of the velocity fluctuation. The location of the maximum at the bottom leeward corner of the canyon has a different reason because it is produced by the combined effect of high u_{rms} and very high scalar fluctuations.

The highest $\overline{u'\phi'}$ maximum situated at the bottom leeward corner is captured by all the models but with some differences in size and shape. These differences are directly dependent on the parameters affecting the calculation of the Reynolds stresses. The lowest and spatially extended local minimum (situated along the top of the canyon) was only reported for the anisotropic models with considerable shape differences. The isotropic models (SED1 and SED2) do not show the local minimum at all.

As evident in Figure 7-16, the highest scalar flux magnitude is obtained by the WET model, and then in a second group with similar order of magnitude, the ABE, YOUNIS, LES, ABE-SUGA, GGDH, S-M DURBIN and S-M HANJALIC appear. Finally, in the third and lowest level of streamwise scalar flux predictions are the SED models. In a general qualitative view, it looks like the two second moment models present the best scalar flux prediction agreement with the LES simulations.

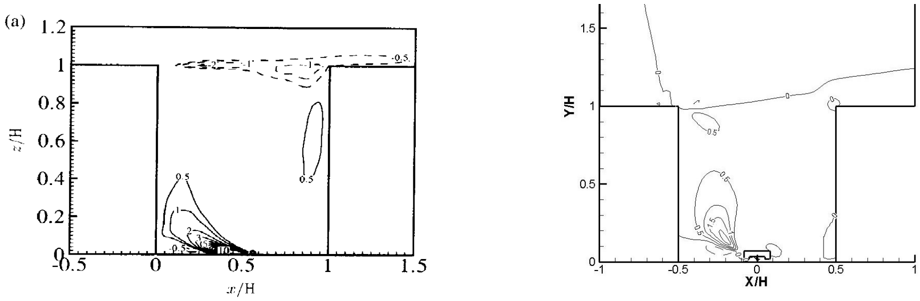

Model LES [Liu02]

Model SED1

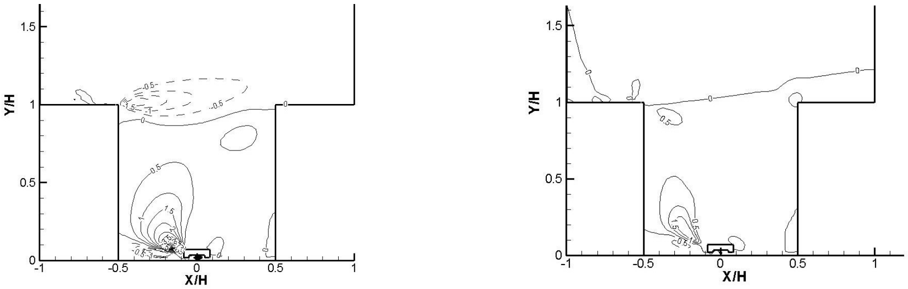

Model GGDH

Model SED2

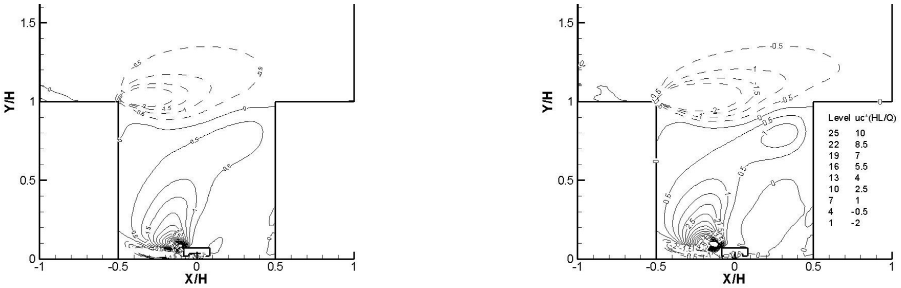

Model ABE

Model ABE-SUGA

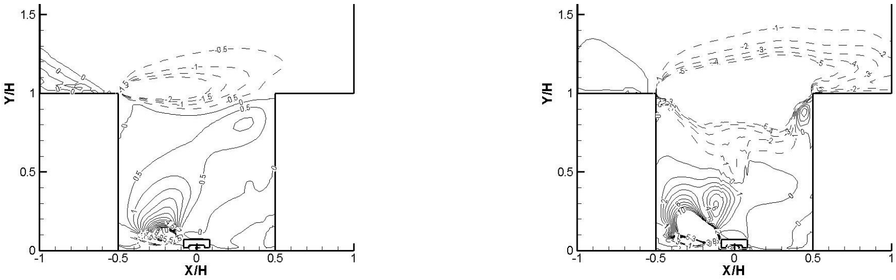

Model YOUNIS

Model WET

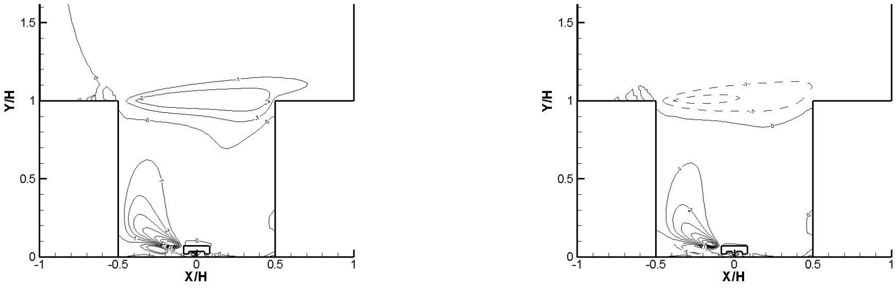

Model S-M DURBIN

Model S-M HANJALIC

Figure 7-16. - Comparison of normalized turbulent scalar flux component $\left(\overline{u'\phi'}\right)\cdot\left(HL/Q\right)$.

The range of the predicted vertical scalar flux component ($\overline{v'\phi'}$) presents a considerably lower magnitude (up to four to five times lower) than the streamwise component. This flux component shows two local maximums, one situated in the leeward bottom corner and the other one situated along the top of the canyon. Both highest local concentrations of vertical scalar fluxes have a similar order of magnitude and were similarly predicted for almost all models. Only the WET model presents some negative areas in addition to the mentioned common behaviour.

The gradient of scalar fluxes is the exact term that participates in the differential equation of pollutant transport. Therefore this gradient is one of the most relevant terms to be taken into account, and the shape of the scalar flux distribution becomes very important. Some examples of relevant differences based on this term are that the LES results show thinner and longer shapes in comparison to the majority of the RANS models in both scalar flux components. The small areas with high concentrations of scalar fluxes imply high and concentrated areas of scalar flux gradients, and therefore different turbulent diffusion of pollutants take place. This analysis is congruent with the larger extent of pollutant dispersion and the general under-prediction of concentration typically seen in the RANS scalar flux models.

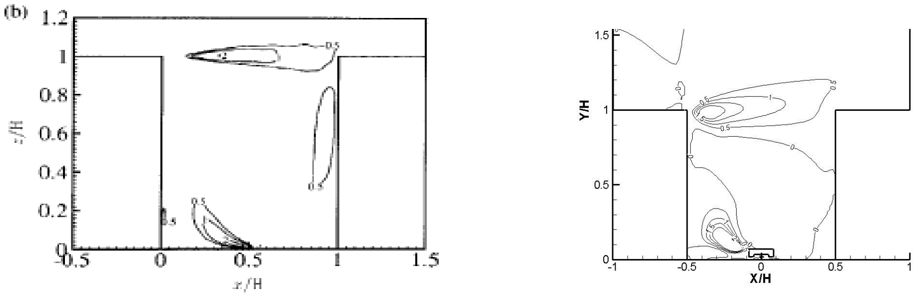

Model LES [Liu02]

Model SED1

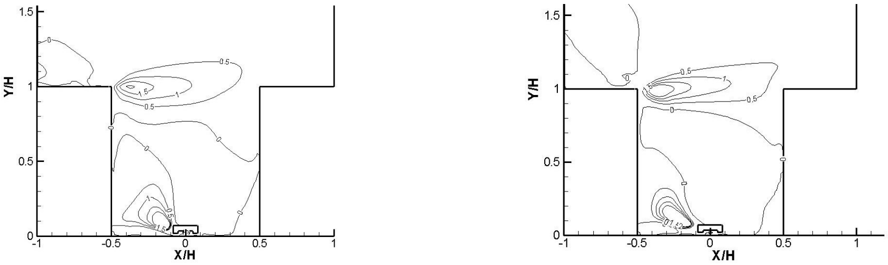

Model GGDH

Model SED2

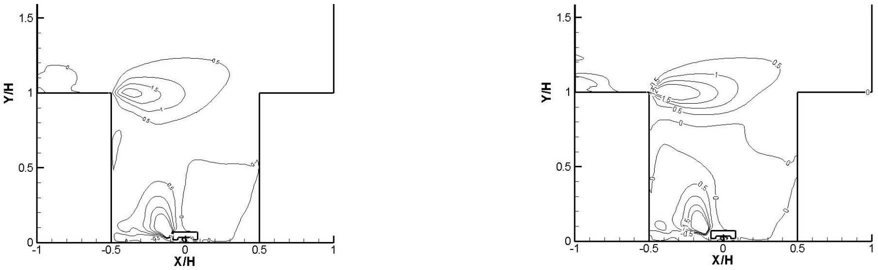

Model ABE

Model ABE-SUGA

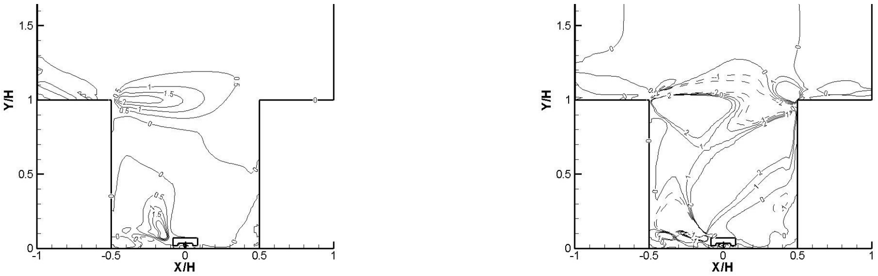

Model YOUNIS

Model WET

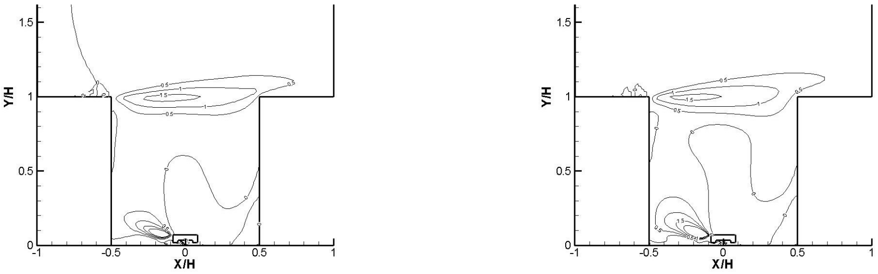

Model S-M DURBIN

Model S-M HANJALIC

Figure 7-17. - Comparison of normalized scalar flux component $\left(\overline{v'\phi'}\right)\cdot\left(HL/Q\right)$.

8 Flow and Dispersions in the MUST Urban Model Experiment

The Mock Urban Setting Test (MUST) is the three-dimensional wind-tunnel experiment selected in this work for the evaluation and comparison of the advanced scalar flux models. The simulations of the MUST experiment presented in this chapter (and probably also those presented for the two-dimensional test case) represent first time in which this geometry is simulated using anisotropic scalar flux models for pollution dispersion. Different from the street canyon, the MUST experiment is a relatively new study and the use of its experimental data was provided to this dissertation under agreement and cooperation with the COST action 732[13]. Thus, this experiment has been selected not only for its detailed description of the experimental setup and measurements, but also because many research groups have recently been working with the MUST geometry, providing EXCEL evaluation tools and a constructive comparison of results.

Following a similar procedure of the previous two-dimensional exercise, this chapter first presents a brief description of the MUST wind tunnel experiment, emphasizing the necessary information for the setup of simulations and grid description. Then, the simulation results are presented in two parts. The first part shows the study of the flow field including a qualitative and quantitative discussion of prediction accuracy for the velocities and turbulence parameters. The second part presents a similar analysis but for normalized pollution concentrations, using several

---

[13] COST Action 732 is an European Cooperation in Scientific and Technical research group entitled “Quality Assurance and Improvement of Micro-scale Meteorological Models.” The wind tunnel data used are now available on the internet. See address in reference [Cost732].

combinations of turbulence models for Reynolds stresses (LRRIP and RKE) and scalar fluxes (GGDH, ABE-SUGA, ABE, S-M HANJALIC).

8.1 MUST Experiment

The MUST experiment was a scaled urban dispersion experiment conducted for the Defence Threat Reduction Agency (DTRA) at the U.S. Army Dugway Proving Ground (DPG) Horizontal Grid test site, in cooperation with many international institutions. Its objective was to acquire meteorological and dispersion data sets at near full-scale to provide a better understanding of how plume structure dispersion is affected by a large array of obstacles, and to help develop and validate urban toxic hazard assessment models.

Another objective of MUST was to overcome the scaling and measurement limitations of laboratory experiments, and to characterize the main flow field parameters to overcome difficulties presented in real urban area studies. Real urban areas create their own roughness boundary layers, also called roughness sub-layers (RSL), that affect the dispersion of pollutants in ways that are not well defined. Many research efforts are still under development to test urban dispersion models. Nowadays, there are data sets available from wind tunnel experiments or measurements conducted in real urban settings, and both are used for model validation. However, it is not easy to achieve the proper scaling in the experiments and obtain detailed RSL measurements in laboratory settings because of the size and complexity of real cities. Consequently, there are few adequately scaled and thoroughly documented urban dispersion data sets that meet the needs of urban dispersion model developers. The need for an intermediate case where both the abovementioned limitations are overcome was one of the main motivations in designing and studying the MUST experiment.

The field measurement of the MUST experiment was carried out in September 2001 in a flat area in the Great Basin desert of western Utah, USA. The experiment consisted of an array of 120 obstacles placed in an aligned configuration consisting of 12 rows of 10 obstacles each. The array contains 119 shipping containers (12.2 m long, 2.4 m wide and 2.54 m high) and one so called VIP building located roughly in the centre of the array. The obstacles were placed with gaps between them intentionally spaced to produce a flow regime that connects the wake interference and isolated flow regime [Oke87]. The array was sufficiently large to create its own internal roughness sub-layer, but sufficiently small to be adequately characterized using available instrumentation. For further details please refer to [Yee04].

This experiment was simulated in 2005 in the large boundary layer wind tunnel “WOTAN” by Bezpalcová [Bezp07] from Hamburg University (see Figure 8-1). Bezpalcová did measurements of the flow fields (shear stress profiles, development of the flow within the canopy, dependence on wind direction, etc.) and concentrations for several wind directions. She made her flow velocity measurements using a two-dimensional Laser Doppler Anemometer (LDA) with a spatial resolution of 1mm. The dispersion experiment was carried out using ethane (C_2H_6) as a neutral buoyant tracer gas. It was measured using a slow Flame Ionization Detector (SFID) for the background concentrations and a fast Flame Ionization Detector (FFID) for the concentrations within the model. The MUST field geometry, including the small irregularities in the containers’ sizes and locations, was modelled at a scale of 1:75. These wind tunnel measurements are well suited for the evaluation of RANS simulations due to their statistically steady boundary conditions. In addition they are reproducible with known uncertainties.

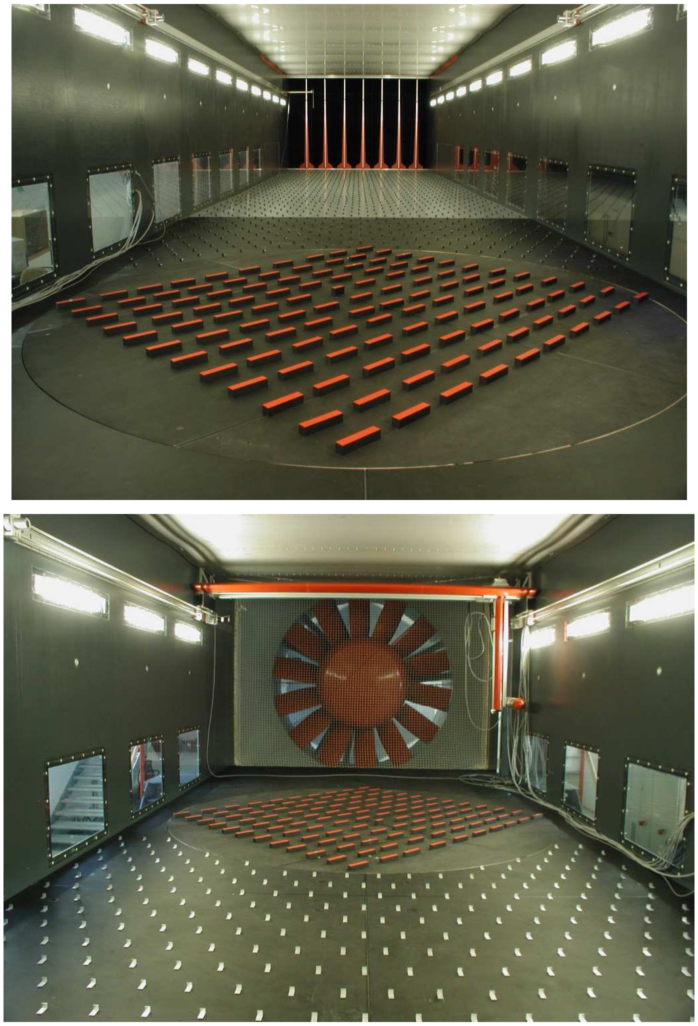

Figure 8-1.- The -45 degree setup of the MUST experiment in the boundary layer wind tunnel “WOTAN” of Hamburg University [Bezp07].

The measurement accuracy was also reported. The maximum positioning error in the model setup was 1mm. The instrumentation for the flow and dispersion measurement (LDA and FFID) had to be located in agreement with the model coordinate system. Each instrumentation setup reports an accuracy error of 1mm. The turn table used to change the approach flow direction includes an imprecision lower than 0.5º. The flow measurement equipment (LDA) presents a velocity exactness of 0.05 ms^{-1}. The concentration measurement equipment reports a 3% error for the FFID and 1% error for the SFID from the measurements, with a minimum detection of 2 ppm. The pollutant volume flow introduced in the model also presents an accuracy error of 1%.

The instrument uncertainties are very important data because they are commonly used to specify the total uncertainty of the measurements. Although these measurement uncertainties are very well specified from the wind tunnel experiments, to define the final thresholds for the statistical metrics (FAC2 and Hit-Rate), only the repeatability uncertainty of the wind tunnel measurements were taken into account in this work, under agreement with COST action 732 [Cost732].

8.2 Computational Domain

Two different computational domains were used for the simulations of MUST. The two computational domains are shown in Figure 8-2 with their distances between boundaries and obstacles. In both cases, the flow is in the positive x direction (from left to right). The two implemented computational domains and their respective grids were provided to this work after collaboration with its main creator [Fran09].

(a)ROTDOM (b)STDDOM

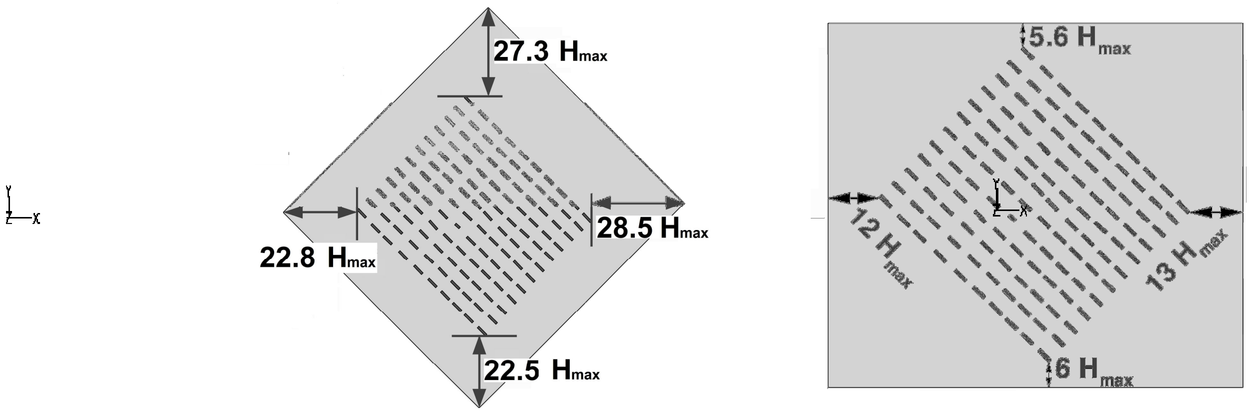

Figure 8-2. Computational domains for the simulations. (a) Rotated domain (ROTDOM) and (b) Standard wind tunnel setup domain (STDDOM). The wind blows from left to right.

The first computational domain, shown in Figure 8-2(a), is called ROTDOM from "rotated domain." Its name relates to the fact that it was obtained by a rotation of -45° around the centre from the original and simplest MUST case 0 degree, where the approach flow was perpendicular to the main street canyons (not shown here). This -45° rotated domain ROTDOM was used for the simulation of pollutants because there were not wind tunnel concentration measurements reported for the 0° case.[14] The second domain, shown in Figure 8-2(b), was generated by using the same grid distribution between the obstacles as ROTDOM, but it extended the computational domain up to the wind tunnel walls. This domain is referred to as STDDOM (from "standard domain"), and it includes the side walls and boundaries as they appear in the wind tunnel experiment. The reason that two different domains were implemented was because the first domain was already available from the 0° MUST simulation, and the second domain was developed with the intention to study the possible influence of the wind-tunnel walls that were not included in the previous computational domain.

The height of both computational domains is $6H_{max}$, where H_{max} = 3.51 m, which is the height of the highest obstacle located in the middle of the domain. It is called the VIP building from the field's nomenclature. The standard container height is 2.54m. Although the wind tunnel measurements were used for the comparison of numerical predictions, the computational domain size used was based on the full scale.

8.3 Boundary Conditions

The type of boundary conditions employed for all simulations in both computational domains are summarized in Figure 8-3. A velocity-inlet boundary condition was set with a fully developed flow profile at the entrance of the flow, using a mixture between analytical relations and experimental measurements.

---

[14] The 0 degree MUST experiment was not studied in this work.

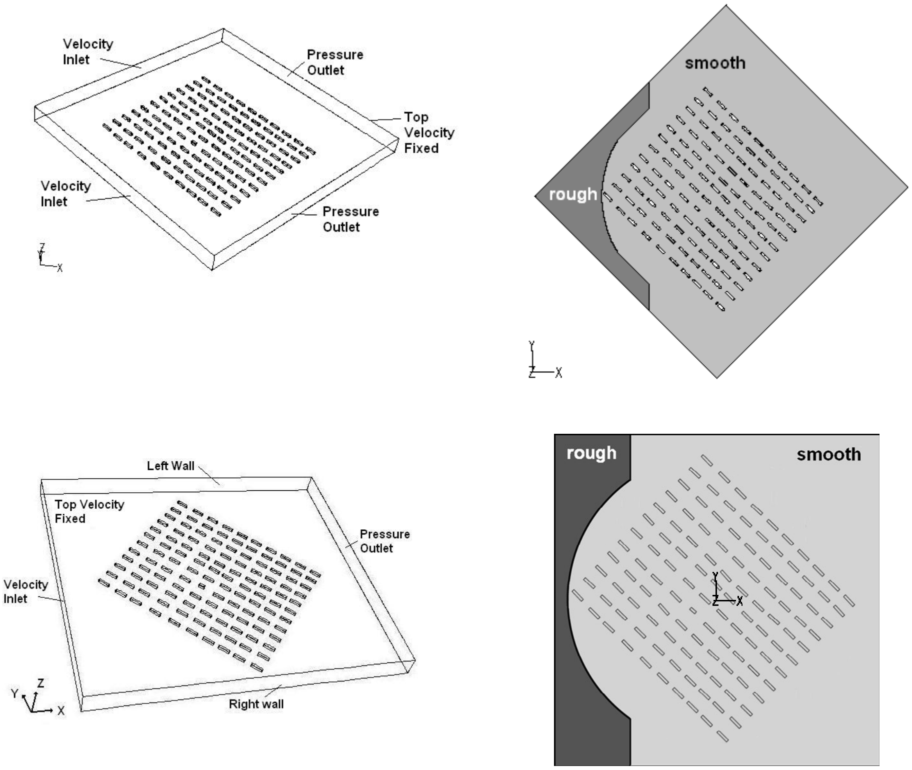

Figure 8-3. Boundary conditions details for computational domains.

The velocity profile in the wind tunnel experiment was described by using the logarithmic law equation. With the Reynolds averaged velocity vector defined as $\overline{u}_i = (\overline{u}, \overline{v}, \overline{w})$ [m/s], the *x*-direction mean velocity components specified for the numerical simulation are given by the expression:

$$\overline{u}(z) = \frac{u_*}{\kappa} \ln\left(\frac{z + z_0}{z_0}\right) \qquad \text{Eq. 8-1}$$

where the friction velocity $u_* = 0.07$ m/s (from $U_{ref} = 1$m/s at the point $P_{ref} = (-144, -2.25, 7.29)$m), the roughness height z_0=0.0165m, and the Von Karman constant κ=0.4187. The other two perpendicular velocity components at the main flow entrance were set to zero ($\overline{v} = \overline{w} = 0$ m/s). The components of the inlet approaching Reynolds stresses were approximated by constant values taken from the measurements above the container height, and are summarized in Table 8-1.

Also at the main flow entrance, *k* (only in two equations models) and ε (in all cases) must be specified. The turbulent kinetic energy (*k*) was calculated from the three normal Reynolds stress components. The turbulent dissipation rate (ε) at the inlet was calculated from the turbulent kinetic energy under the assumption of local equilibrium ([Rich93]).

$$k = \frac{1}{2}\left(\overline{u'u'} + \overline{v'v'} + \overline{w'w'}\right) \quad \text{Eq. 8-2}$$

$$\varepsilon = \frac{k}{C_\mu^{0.75}\kappa\left(z + z_0\right)} \quad \text{Eq. 8-3}$$

These velocity and turbulence parameter profiles were also used to specify the flow field at the top boundary, using the corresponding value from the flow inlet profiles at the top boundary height 6 H_{max}. Figure 8-4 presents the profiles of the velocities and turbulence parameters specified for all simulations at the main flow entrance in comparison to the values predicted and measured at the approach flow location, which does not coincide with the inlet boundaries of the computational domains. This location is situated at 6.4*H* upwind the containers and 10.2*H* downwind from the inlet boundary of case STDDOM (see Figure 8-8). The results presented in Figure 8-4 correspond to the predictions using STDDOM and the LRRIP turbulence model. As can be observed, these graphics show satisfactorily good agreement between the three presented cases—measured (Exp), specified (at Inlet BC) and predicted (at approach flow measurement location) — for most of the fluid flow parameters. The most relevant exception is the *y*-direction velocity component "*v*", where the calculated profile deviates from the measured and specified values due to the occurrence of transversal pressure gradients ($\partial\overline{p}/\partial y \neq 0$). This calculated profile is presented and discussed in section 8.5.1. For further details about the implementation of these boundary conditions in the commercial software, please refer to the source code attached in Appendix D (page 191).

A constant pressure was prescribed at the exit of the flow with a pressure outlet boundary condition. The floor was partly treated as a rough wall in the upwind side of the obstacles (see Figure 8-3), corresponding to the simulated area located outside the turn table in the wind tunnel (Figure 8-1). In this region, the hydrodynamic roughness height used (z_0= 0.0165m) was converted to a sand grain roughness (k_s ≈0.1616m) as explained by [Fran07] and [Fran09], because the CFD software FLUENT uses wall functions based on sand grain roughness. Any other walls—such as all of the containers and the two lateral walls in case of the STDDOM domain—were treated as smooth walls.

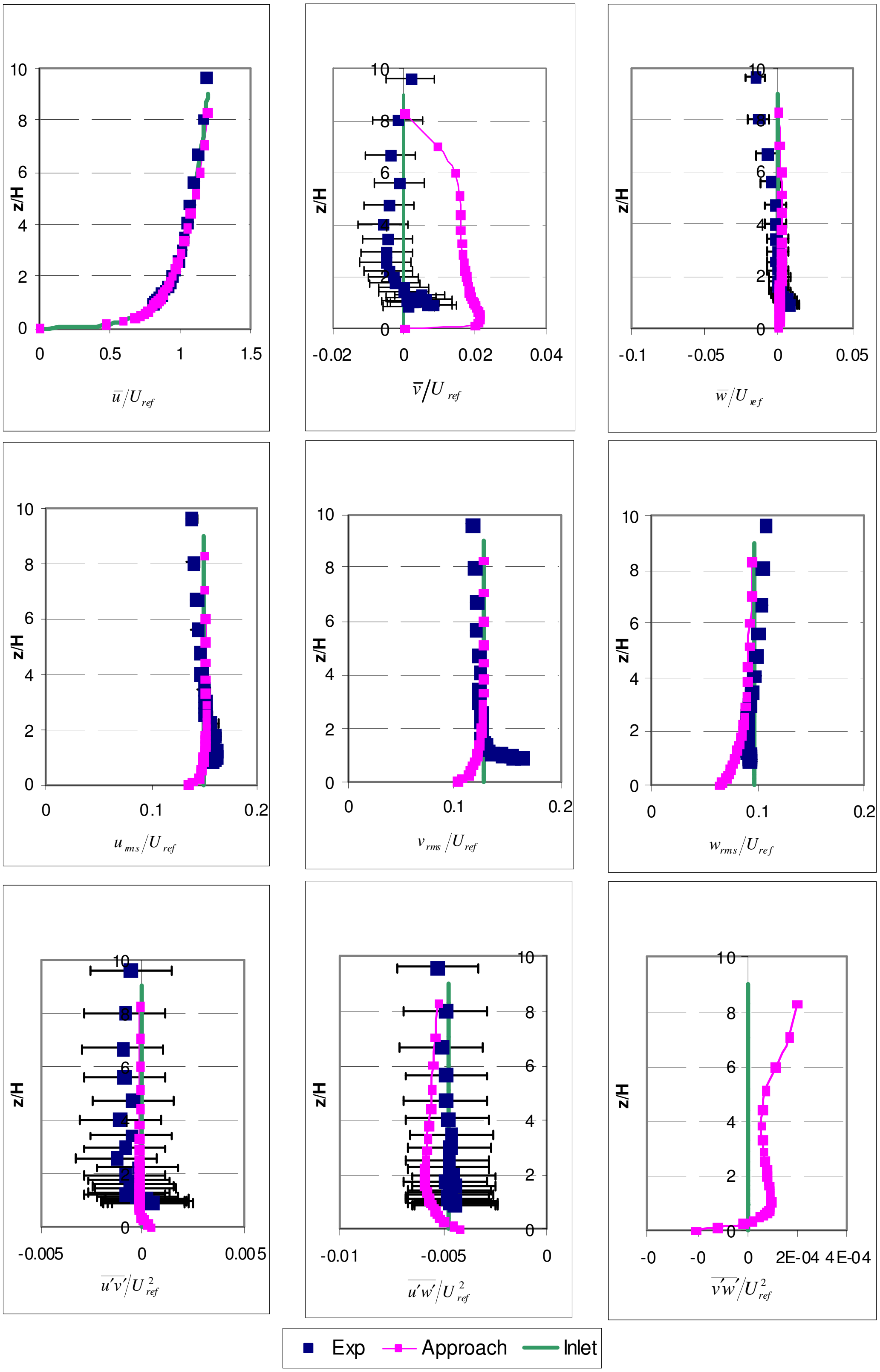

Figure 8-4.-Comparison of the specified boundary condition at the flow inlet with the measured and predicted velocity and turbulence parameters at the approach profile location in front of the obstacles. All measurements include its measurement error.

Table 8-1. - Boundary Conditions for MUST Simulation

Boundary Name	***Type***	***Setup Details***
Bottom	Wall	Roughness Height(m): udf bottom_ks.c Roughness Constant: 1 Mean dispersion: Specified Flux=0 Scalar Fluxes (2^{nd} Moment): Specified Flux=0
Inlet	Velocity Inlet	Velocity components: $\overline{u}$: udf profile.c $\overline{v}$: 0.0 m/s $\overline{w}$: 0.0 m/s Reynolds stresses: $\overline{u'u'} = 0.0225\, m^2/s$ $\overline{v'v'} = 0.016384\, m^2/s$ $\overline{w'w'} = 0.009216\, m^2/s$ $\overline{u'w'} = 0.004722\, m^2/s$ $\overline{u'v'} = 0.0\, m^2/s$ $\overline{v'w'} = 0.0\, m^2/s$ Turbulent kinetic energy (*k*): udf profile.c Turbulent dissipation rate (ε):udf profile.c Mean dispersion: Specified Value=0 Scalar Fluxes (2^{nd} Moment): Specified Value=0
Left and Right	Wall	Roughness Height(m): 0 Roughness Constant: 1 Mean Dispersion: Specified Flux=0 Scalar Fluxes (2^{nd} Moment): Specified Flux=0
Live	Fluid	A source term for the passive scalar was defined in the cell containing the centre of the experimental source with $\dot{m}$ =$1.872 \cdot 10^{-5}$kg/s.
Outlet	Pressure Outlet	Mean Dispersion: Specified Flux=0 Scalar Fluxes (2^{nd} Moment): Specified Flux=0
Top	Velocity Inlet	Velocity components: $\overline{u}$: udf profile.c $\overline{v}$: 0.0 m/s $\overline{w}$: 0.0 m/s Reynolds stresses: $\overline{u'u'} = 0.0225\, m^2/s$ $\overline{v'v'} = 0.016384\, m^2/s$ $\overline{w'w'} = 0.009216\, m^2/s$ $\overline{u'w'} = 0.004722\, m^2/s$ $\overline{u'v'} = 0.0\, m^2/s$ $\overline{v'w'} = 0.0\, m^2/s$ Turbulent kinetic energy (*k*): udf profile.c Turbulent dissipation rate (ε):udf profile.c Mean Dispersion: Specified Value=0 Scalar Fluxes (2^{nd} Moment): Specified Flux=0

Note: The User-Define Function (UDF) files *bottom_ks.c* and *profile.c* can be found in Appendix D.

Finally, for the concentration, a value of zero at the inflow boundaries and a vanishing normal gradient at all other boundaries was set. The source was implemented as a volumetric source term in the cell that contained the centre of the experimental ground source location (x=-102.48, y=-7.06, z=0.0). Some differences must be expected from this assumption because in the wind tunnel experiment, the pollutants were inserted at the ground level through a circular area (pipe) with diameter equivalent to 0.6m. A summary of the boundary conditions implemented in the MUST numerical simulations appear in Table 8-1.

8.4 Discretization Error Estimates

A total of four block-structured hexahedral grids were employed, which are presented in Figure 8-5. Three systematically refined grids were used to assess the influence of the grid resolution on the results for the ROTDOM geometry. These three grids are grid #1 (for the finest), grid #2 (for the middle) and grid #3 (for the coarsest), consisting of 3,208,752 cells, 1,552,792 cells and 751,194 cells, respectively. The numbers of cells between each grid were increased by a factor of 2, approximately. The expansion ratios of these three grids never exceeded a factor of 1.3. However, grid #3 has 1.61% cells with an expansion ratio above 1.3 but below 1.45. All implemented grids were created by Franke [Fran09].

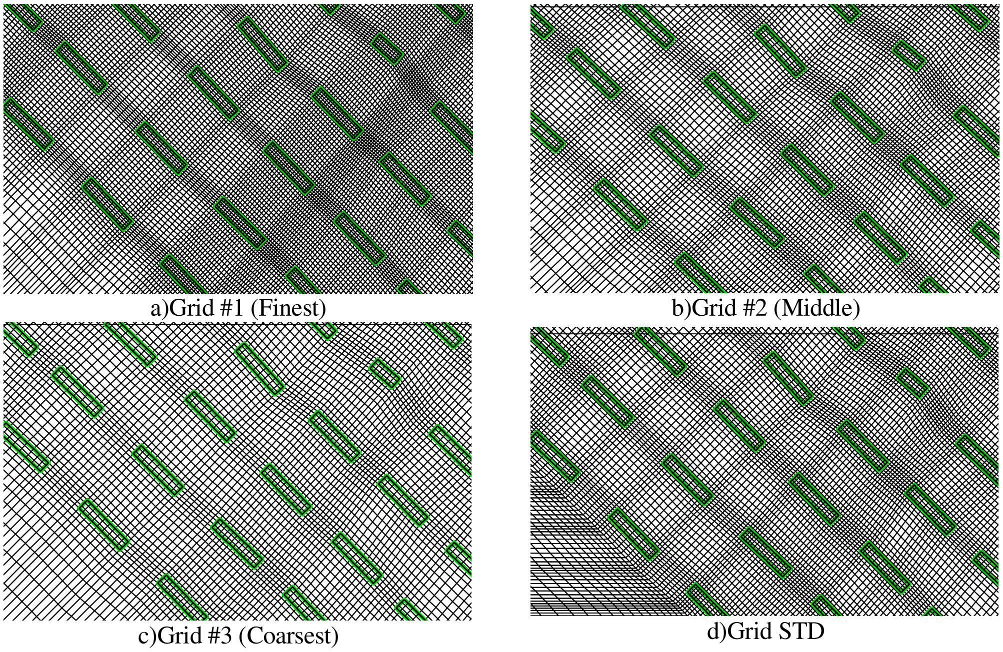
a)Grid #1 (Finest)
b)Grid #2 (Middle)
c)Grid #3 (Coarsest)
d)Grid STD

Figure 8-5.Detail of the four grids implemented for the MUST experiment.

The numerical simulations of the STDDOM computational domain were performed using only one hexahedral grid. This grid has the same resolution between the obstacles as the middle grid of ROTDOM, but gridlines approaching the walls and in/out flow boundaries are perpendicular. A comparison of the middle grid of ROTDOM and the STDDOM's grid is shown in Appendix C (p.183). The STDDOM has a maximum expansion ratio that is always below 1.3, and the vertical resolution is identical to the ROTDOM grids. The final number of cells for the STDDOM grid is 1,675,712.

The numerical uncertainty of the finest grid was quantified through the Richardson Extrapolation technique, as explained in Chapter 6.2. The predictions of the three grids for ROTDOM were analysed in the 1742 measurement points for the flow field and 256 measurement points for concentrations. Their locations are shown in Figure 8-8 and Figure 8-11, respectively.

Table 8-2 and Table 8-3 present the application of RE for flow and concentration predictions for the finest grid in the MUST exercise, using the LRRIP turbulence model. The column for monotonic convergence includes the total percentage of cases I, II and III according to Table 6-1. The monotonic and oscillatory convergence cases (I, II, III and IV) are the grid points where spatial uncertainty estimation is possible. Symbol <p> is the mean observed order of accuracy and <R> is the mean ratio of solution changes, and both reported averages are for the monotonic convergence cases I to III. $<U_l>$ is the mean absolute uncertainty for cases monotonic and oscillatory convergence (I to IV). The refinement ratio is a relation between a characteristic size of every grid ($r_{ij}=r_i/r_j=(V/N_i)/(V/N_j)=N_j/N_i$, where V is the total volume and N_i is the total amount of cells in grid i). As the refinement ratios r_{21} and r_{32} differ in the present work only by 10^{-5}, a constant $r = (r_{21}+r_{32})/2$ was used in the Richardson extrapolation.

Compared to the street canyon exercise, the application of the Richardson Extrapolation technique in the MUST experiment shows that the numerical uncertainty of the grid can be calculated in a much lower percentage of the points. The most probable reason of these results is that these three are not fine enough to be in the asymptotic range, which is a requirement to apply the Richardson Extrapolation. The spatial discretization analysis for the flow field shows that the two main velocity components, $\overline{u}$ and $\overline{v}$, cannot be estimated in more than the half of the studied points. Slightly better results were found for the $\overline{w}$ velocity component and for the root-mean-square of the turbulent normal stresses (u_{rms}, v_{rms} and w_{rms}), which show convergence in approximately 60% of the points. Similarly, this table shows that for all variables, the mean ratio of solution changes <R> is always around 0.5 and the mean calculated order of accuracy <p> is around 1.6. However, the calculated mean uncertainty $<U_l>$ is as expected different for every velocity component because the main velocities have mean uncertainties one order of magnitude higher than the uncertainties for the fluctuating velocities.

The concentration predictions for the combination of different scalar flux models and the LRRIP turbulent model (Table 8-3) presents a much lower percentage of points where the grid uncertainty can be estimated. In this case, oscillatory convergence characteristics were found in more cases than monotonic convergence. Other studies carried out with the same implemented computational grids [Scha10] have shown that the Richardson Extrapolation analysis of these three grids is affected by the wrong treatment of the source. As the source was always specified for only one cell, the source volume changed from grid to grid. In conclusion, the divergence case is therefore the most common tendency for all concentration predictions. Another difference from the Richardson Extrapolation table of the flow field is that this table shows the mean ratio of solution changes for the concentrations <*R*> lower and closer to the limit of oscillatory convergence (0), which coincides with the higher percentage of points with this tendency. The mean calculated order of accuracy <*p*> is again lower than 2 and there are some considerable differences between the models. The maximum <*p*> was reported for SED1 and ABE-SUGA models, and the minimum was reported for the S-M HANJALIC model. Reviewing the results of concentration uncertainties <U_1> from a different combination of models presented in this table, one can compare values for the absolute value of <U_1> and observe that the S-M HANJALIC model is by far the model with the largest uncertainty.

In general, a similar amount of uncertainty and tendencies were found for the flow and concentrations in previous works [Scha10], but with a slightly lower number of locations where the grid uncertainties could not be measured. The possible source of these differences may come from the specified simulation setup like turbulence models and boundary conditions.

Table 8-2. - Richardson extrapolation grid analysis for flow field (using LRRIP model for Reynolds stresses).

Model	*Monotonic convergence*	*Oscillatory convergence*	*Divergence*	*<R>* *(E-01)*	*<p>*	*<U_1>* *(E-02)*
$\overline{u}$	34.67%	12.92%	52.41%	4.96	1.64	7.83
$\overline{v}$	29.91%	11.19%	58.90%	5.02	1.59	5.35
$\overline{w}$	40.36%	12.69%	46.96%	5.58	1.49	4.65
u_{rms}	38.23%	16.82%	44.95%	4.89	1.69	0.545
v_{rms}	45.58%	19.23%	35.19%	4.38	1.72	0.479
w_{rms}	42.19%	13.66%	44.14%	5.24	1.63	0.301
Average:	38.49%	14.42%	47.09%			

Table 8-3. - Richardson extrapolation grid analysis for C^* (using LRRIP model for Reynolds stresses).

Model	*Monotonic convergence*	*Oscillatory convergence*	*Divergence*	*<R>* (E-01)	*<p>*	*$<U_1>$* (E-02)
SED1	11.24%	20.60%	68.16%	3.20	1.87	1.83
SED2	13.11%	25.84%	61.05%	3.83	1.68	2.01
GGDH1	12.73%	31.46%	55.81%	2.87	1.49	1.57
GGDH2	12.73%	31.09%	56.18%	3.02	1.45	1.57
ABE-SUGA	10.86%	36.70%	52.43%	3.89	1.84	1.57
ABE	14.23%	26.59%	59.18%	4.48	1.55	1.10
S-M HANJALIC	7.12%	14.23%	78.65%	5.32	1.42	2.62
Average:	12.48%	28.71%	58.80%			

As mentioned earlier, the flow field accuracy has a significant influence on the pollutant dispersion. To quantify the flow uncertainty at different levels between the containers, an RE analysis (included in Appendix C) was performed separately for four planes located at different heights, including the plane where concentrations were measured. The numerical simulations show a similar convergence tendency and an average uncertainty in comparison to the total flow field. The maximum uncertainties of all parameters are around one order of magnitude above the reported average uncertainty in each case.

8.5 Results

8.5.1 General Description of Flow Field

The results obtained from the numerical simulations of the MUST flow field show congruent prediction with the wind tunnel and field measurements reported in literature [Bezp07]. The simulation shows that the flow approaches the containers in a positive x direction (from left to right in Figure 8-6), which strongly affects the velocity field. When the flow reaches the first line of containers, the lower part of the velocity profile is deformed and the flow changes its direction bordering the containers, which produces boundary layer separation, recirculation, and stagnation areas around them (see in Figure 8-6a). The same fluid behaviour also occurs for the internal blocks but with lower flow impact because the previous ground obstructions retard the movement of the air moving close to the ground. This reduction of wind speed produces a change in the boundary layer profile which includes the flow effects of these obstacles

Due to the position and shape of the containers, at low flow levels in the area between the containers, the main velocity changes from the initial positive *x*-direction at the inlet and tends to follow the direction parallel to the principal street canyons (see in Figure 8-6b). This change of the main velocity direction only occurs close to the containers, and it progressively vanishes in the vertical direction at a farther distance from the bottom. Thus, the resulting velocity profile is a good example of a three-dimensional flow field. Figure C- 2 (Appendix C, page 183) presents contour and vector plots of velocity magnitude for better understanding of the flow field approaching the obstacles.

Some important aspects should be mentioned about the flow field. When the simulation of one block or array of blocks is performed, special attention must be paid to the flow field around or between the obstacles, because this region presents highly non-uniform and non-homogenous flow directions. This region also contains the largest velocity and pressure gradients, and the ground obstacles are the largest source of turbulent kinetic energy within this computational domain. For these reasons, it is especially important to employ a very high refinement of the grid close to the walls and around the containers.

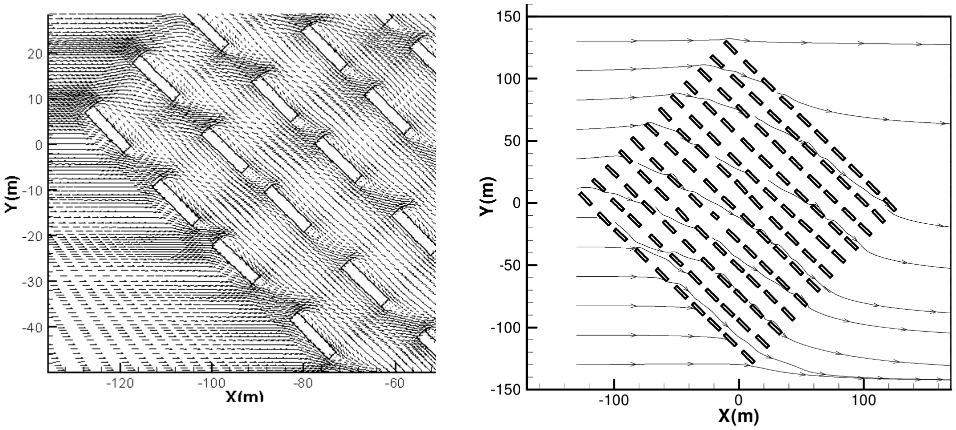

Figure 8-6. (a) Detail of velocity vectors and (b) streamlines at the horizontal plane at half height of the containers (z=H/2).

A qualitative analysis of the pressure field also shows interesting results. Figure 8-7 shows the geographical distribution of the pressure variation in comparison to the reference pressure level set at the exit of the flow. Around each container it can be seen that the highest pressure levels are always located in the container's side situated in front of the flow direction (windward side) and the lowest pressure levels are located on the opposite side of the containers (leeward side). Between the windward sides, higher pressures occur always on the longer windward sides than on the shorter windward sides. Similarly, the longer leeward sides have lower pressures than the shorter sides. This pressure distribution repeated for a group of obstacles like MUST produces a large pressure increase in the region of the approaching flow towards the longer windward walls (y < 0) and the asymmetric pressure field observed in the figure.

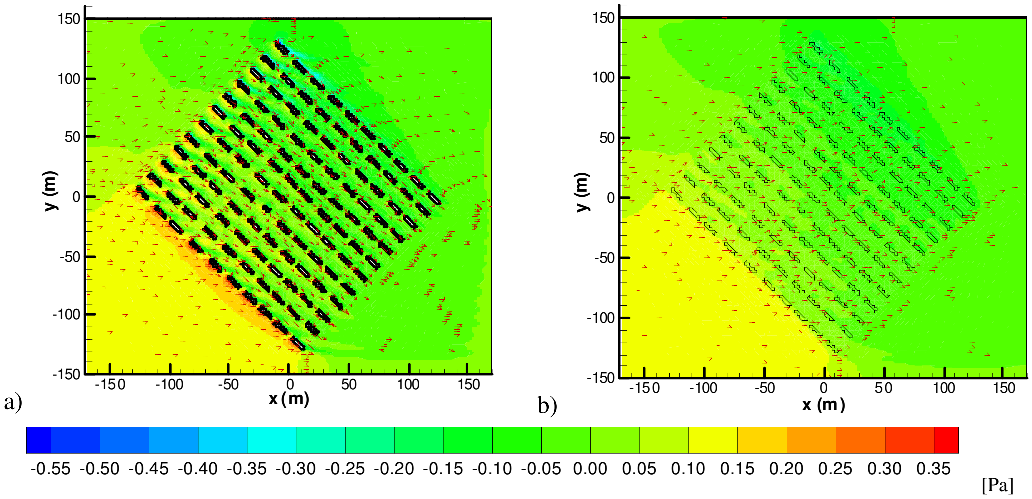

Figure 8-7. Contour plots of pressure variation in the STDDOM computational domain with some vectors showing the flow direction. Two different heights are plotted: (a) for z=H and (b) for z=3H.

The lowest pressures within the container's array are located at the corner with highest *y*-coordinate values and their location is also consequence of the asymmetric pressure field in the upwind side of the containers. Another interesting observation from these pressure plots is that the pressure distribution does not have significant changes at different heights as can be seen by the velocity magnitude contours. The most likely reason for this difference between the velocity and pressure fields is due to the square-linear relation between these two parameters (see e.g. Bernoulli equation). Linear changes in the pressure at a given height within a streamline are compensated with the square change in the velocity field. In addition, it is well known that the pressure field in a boundary layer wind tunnel is relatively constant and essentially governed by the main flow where the downwind pressure gradient is usually negligible.

Unfortunately, no pressure measurements were reported from the wind tunnel experiments, so it is not possible to have a quantitative comparison. The only relevant value to mention is the global pressure difference. The simulations reported a very small pressure difference (less than 1 Pa) for the complete domain. This result is a congruent flow characteristic after the fully developed incompressible flow field condition imposed for the simulation setup and the zero horizontal pressure gradients imposed in the wind tunnel experiments.

The contour plot of pressure variation with an asymmetric increase of pressure in the upwind side of the containers may represent a problem. This local pressure increase is a problem because it occurs before the flow enters the studied flow field, meaning outside the computational domain. This non-constant pressure distribution in the boundary condition is affected by the specified velocity imposed at the entrance of the flow. Also, a wrong pressure prediction modifies the velocity field and may produce a wrong velocity profile in front of the containers. Neither condition creates accurate results because a wrong (and probably non-real) flow could be arriving to the containers' array. A zero pressure gradient in the y-direction is a prerequisite to set a fully developed flow condition, which is not fulfilled here. A good signal to show the absence of a fully developed flow can be observed in the y-velocity approach flow profile presented in Figure 8-4. At this location, the y-velocity is not zero as it was set at the inlet, and therefore it does not fulfil the “horizontal homogeneity” condition which means that an unstable and non-fully developed velocity profile was set. The term “horizontal homogeneity” refers to the absence of stream-wise gradients in the vertical profiles of both the mean wind speed and of the turbulence quantities. These profiles must be maintained with downstream distance. This flow type occurs when the vertical mean wind speed and turbulence profiles are in equilibrium with the roughness characteristics of the ground surface [Bloc07].[15]

In summary, to improve the two previously mentioned weaknesses in the performed simulations, the grid refinement and the size of the computational domain must be increased. These two computational settings are opposite to each other because the number of finite volume elements to solve in CFD simulations is limited by the available computational resources. Similarly, to increase the computational domain without losing the previously prescribed flow discretization would increase the number of cells. Therefore, a compromise between both parameters always exists for a CFD practitioner. At the moment of development of this thesis, the available computational resources did not allow the author to do substantial refinement or increase of computational domain. Therefore, further modifications of the grid or computational domains have been left for future studies. As final advice, with the

---

[15] At this point is also important to mention that the data obtained from the wind tunnel measurements fulfil the horizontal homogeneity condition.

very low reported values of pressure variation in the simulations, for future improvements, the author would suggest testing the higher grid refinement within the containers area and then, when possible, increasing the size of the computational domain.

8.5.2 Flow Field at Measurements Positions

Two different turbulence models for Reynolds stresses have been used to calculate the flow field. They are the two-equation Realizable k-ε (RKE) model and the Reynolds Stress Transport model (LRRIP). See Chapter 3.1 for their details. Here two simulations are shown using the computational domain STDDOM with both turbulence models. The Reynolds numbers predicted in the simulations were compared with those reported in the experiments (approximately $2.4\cdot10^5$) with the velocities at the reference point and as characteristic length the maximum obstacle height (H_{max}). The calculated Reynolds numbers were predominantly under-predicted (with exception of the coarse grid), with a small variation of a Reynolds number always below 2.3%. The flow field results in the rest of the domain were studied using some of the statistical evaluation parameters recommended in the literature to assess the model performances for pollution dispersion.

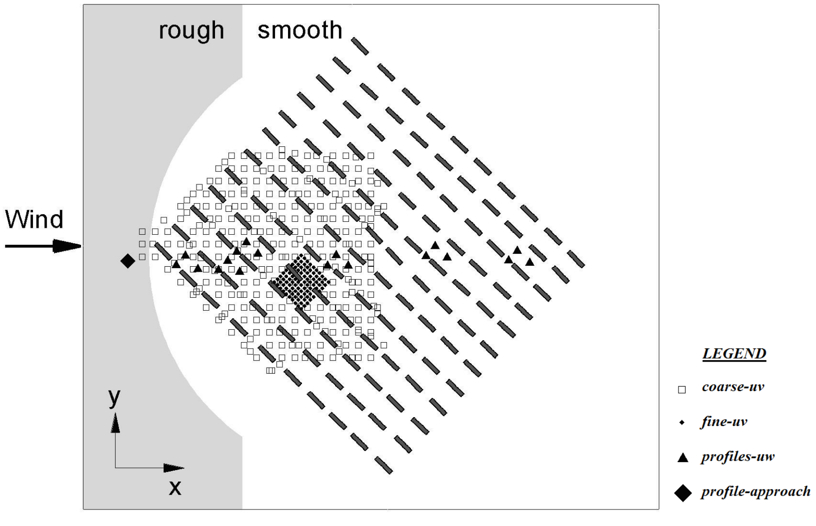

Figure 8-8. MUST flow field measurement zones used for model validation.

A total of 1742 measurement points from the wind tunnel experiment were studied and grouped into four major zones. They are the two horizontal zones "coarse-uv" and "fine-uv," the vertical "profiles-uw," and the vertical "profile-approach". These zones are shown in Figure 8-8. The coarse-uv and fine-uv zones contain measurements at three and four different heights, respectively. The coarse-uv measurement planes are located at z = 1.275, 2.55, and 5.1 m and the fine-uv measurements planes are located at z = 0.9, 1.275, 1.575 and 2.55 m. The vertical profiles-uw contain different measurement locations with height in the range of z = 0.45 m to z = 13.5 m. Similarly, the approach-profile includes measurements at the fixed location of (-144 m, -2.25 m, z), with z in the range of 2.25 to 21.6 m.

Table 8-4 to Table 8-6 present the statistical metrics of Hit-Rate and FAC2 (explained in Chapter 6.1) used to quantitatively compare the numerical predictions with the experiments[16]. For the flow field only these two evaluation parameters were calculated because the velocities may have positive and negative signs, therefore the parameters FB, MG NMSE and VG are mathematically undefined or senseless. All results presented in these tables have been calculated and corroborated with the BOOT software [Chan05] for the Hit-Rate in Table 8-4 and Table 8-5, or with the EXCEL tool [Cost732] for FAC2 in Table 8-6. Table 8-7 provides the allowed tolerances used for both metrics.

Table 8-4. Hit-Rate for LRRIP model predictions.

Model LRRIP						
z [m]	$\overline{u}/U_{ref}$	$\overline{v}/U_{ref}$	$\overline{w}/U_{ref}$	u_{rms}/U_{ref}	v_{rms}/U_{ref}	w_{rms}/U_{ref}
Hit-Rate for planes coarse-uv						
1.275	0.82	0.73	—	0.79	0.77	—
2.55	0.97	0.42	—	0.87	0.81	—
5.1	1.00	0.14	—	1.00	0.98	—
Hit-Rate for planes fine-uv						
0.9	0.81	0.66	—	0.73	0.72	—
1.275	0.89	0.74	—	0.74	0.86	—
1.575	0.87	0.73	—	0.79	0.82	—
2.55	0.93	0.34	—	0.84	0.81	—
Hit-Rate for all planes-uv						
—	0.91	0.50	—	0.85	0.83	—
Hit-Rate for profile-uw						
0.45-13.5	0.87	—	0.20	0.98	—	0.70
Hit-Rate for approach-profile						
2.25-21.6	1.00	0.05	0.86	1.00	0.95	1.00
All						
—	0.90	0.49	0.23	0.89	0.83	0.72

---

[16] The velocity measurements were carried out with 2D Laser Doppler Anemometry (LDA). Therefore, only two velocity components and three Reynolds stress components are available at each measurement position.

Table 8-5. Hit-Rate for RKE model predictions.

Model RKE						
z [m]	$\overline{u}/U_{ref}$	$\overline{v}/U_{ref}$	$\overline{w}/U_{ref}$	u_{rms}/U_{ref}	v_{rms}/U_{ref}	w_{rms}/U_{ref}
Hit-Rate for planes coarse-uv						
1.275	0.88	0.43	—	0.72	0.69	—
2.55	0.97	0.38	—	0.85	0.87	—
5.1	1.00	0.15	—	0.94	1.00	—
Hit-Rate for planes fine-uv						
0.9	0.84	0.36	—	0.72	0.68	—
1.275	0.85	0.31	—	0.78	0.79	—
1.575	0.79	0.32	—	0.82	0.80	—
2.55	0.95	0.22	—	0.86	0.88	—
Hit-Rate for all planes-uv						
—	0.92	0.32	—	0.82	0.82	—
Hit-Rate for profile-uw						
0.45-13.5	0.92	—	0.18	0.92	—	0.68
Hit-Rate for approach-profile						
2.25-21.6	1.00	0.05	0.91	1.00	0.95	0.09
All						
—	0.92	0.32	0.21	0.85	0.83	0.65

Table 8-6. FAC2 for LRRIP and RKE model predictions.

FAC2			
		LRRIP	***RKE***
Horizontal Planes-uv	$\overline{u}_{uv}$	0.99	0.99
	$\overline{v}_{uv}$	0.64	0.63
	k_{uv}	0.85	0.92
Vertical Planes-uw	$\overline{u}_{uw}$	0.97	0.99
	$\overline{w}_{uw}$	0.43	0.29
	k_{uw}	0.99	0.99

Table 8-7. Allowed tolerance used in the calculation of the Hit-Rate and FAC2 for RKE and LRRIP model predictions.

$\overline{u}/U_{ref}$	$\overline{v}/U_{ref}$	$\overline{w}/U_{ref}$	u_{rms}/U_{ref}	v_{rms}/U_{ref}	w_{rms}/U_{ref}
0.008	0.007	0.007	0.006	0.005	0.005

As mentioned earlier, statistical metrics are very useful parameters to estimate the quality of a model prediction. However, these parameters show only part of the information and therefore they do not always represent the complete model performance [Oles08], [Fran08], [Scha10]. To complete the possible information missing for the flow analysis, Figure 8-9 and Figure 8-10 present scatter plots of these results made with the COST Action Excel tool [Cost732].

In general, the Hit-Rate analysis shows very good agreement between the simulation and measurements for the main velocity component $\bar{u}$. Also good Hit-Rate performance can be seen for the three normal Reynolds stresses, which are represented by their root-mean-square values (u_{rms}, v_{rms} and w_{rms}). Slightly better Hit-Rates were found for the flow field predicted with the LRRIP model, the more complex model, than with the RKE turbulence model.

In a more detailed analysis of the horizontal planes, one can observe that there are better predictions for all flow field variables when distance from the bottom is increased. Only the $\bar{v}$ velocity component does not show this tendency. The better agreement at higher planes could be expected because the absence of obstacles allows for homogenization of the flow direction, reduction of velocity gradients, and neglect of near-wall function effects. The main velocity component $\bar{u}$ definitively has the best Hit-Rates at almost every zone, and it gives perfect, congruent agreement between the graphics and metrics. On the other hand, the $\bar{v}$ velocity component has the worst results and a completely reversed Hit-Rate tendency within the horizontal planes (meaning a lower Hit-Rate at higher planes). This general behaviour of the flow field variables was also found by [Fran09] for simulations performed with a different turbulence models.

In addition to the aforementioned errors inserted into the *y*-velocity component at the approach flow, there are other reasons to understand the different Hit-Rate behaviour, which can be explained by looking at the allowed tolerances and the graphic analysis of results. The Hit-Rate evaluation parameter represents a fraction of the total amount of locations where a tolerance condition is fulfilled. This is the case when the difference between measurements and predictions is lower than a specific relative or absolute tolerance. From the scatter plots, where a generally good prediction of the *y*-velocity component is shown, one can see that it changes from negative to positive. Additionally, in contrast to the behaviour of the *x*-velocity component, at higher planes the *y*-velocity component reduces its magnitude to a level where the relative allowed tolerance loses its effects. Under these conditions, only the absolute tolerance is in charge of the Hit-Rate achievement, and it appears that the range of differences for the *y*-velocity component is not low enough to be within the absolute tolerance.

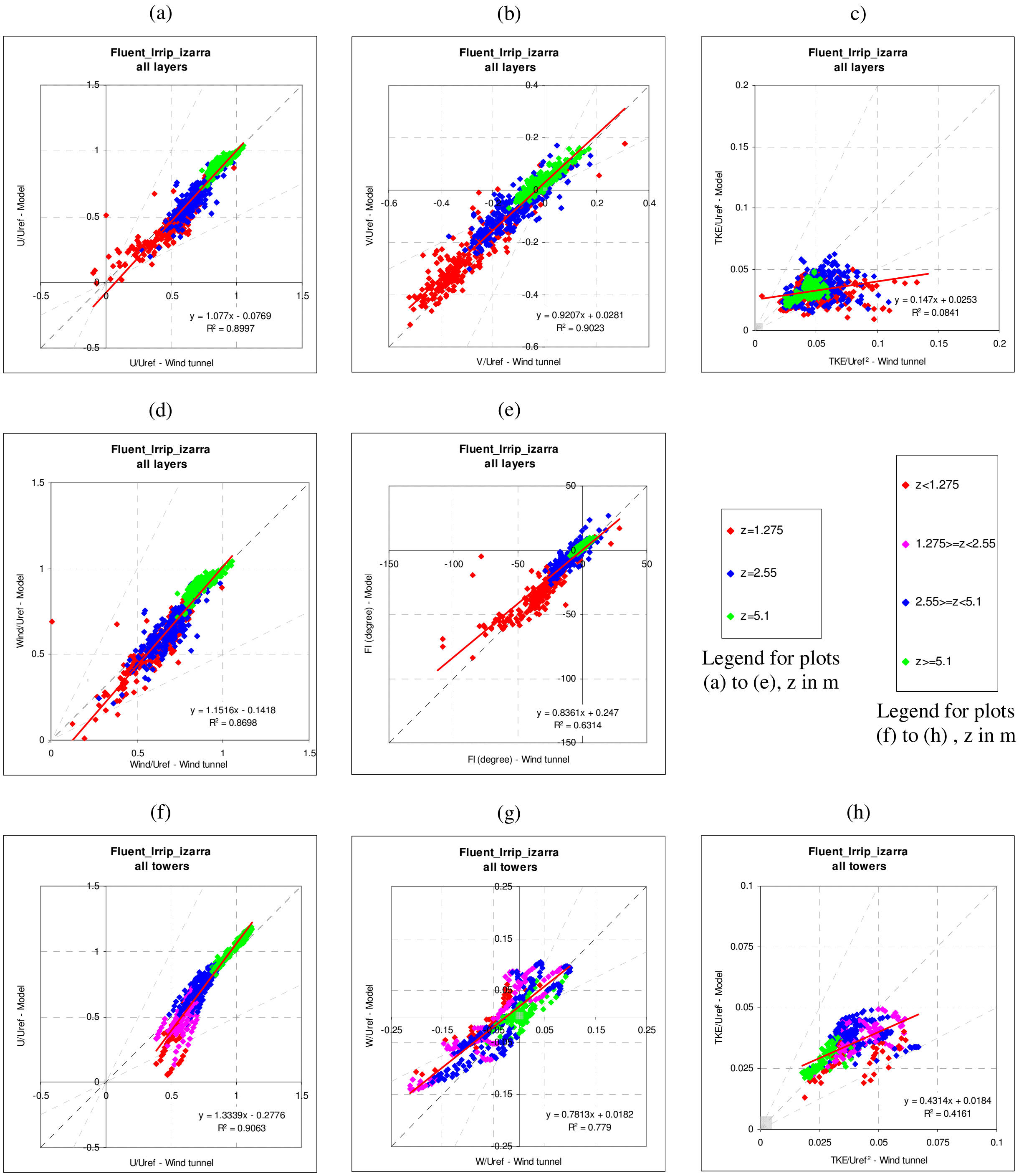

Figure 8-9. Flow field measurements vs. LRRIP model predictions in the MUST flow field measurement points. The segmented lines are the limits of FAC2 and the red segmented line represents the correlation coefficient R (see Chapter 6.1.1). The U/Uref, V/Uref, W/Uref, TKE/Uref^2, Wind/Uref and Fi are the normalized results for the three mean velocities, turbulent kinetic energy, wind velocity magnitude and velocity vector direction, respectively.

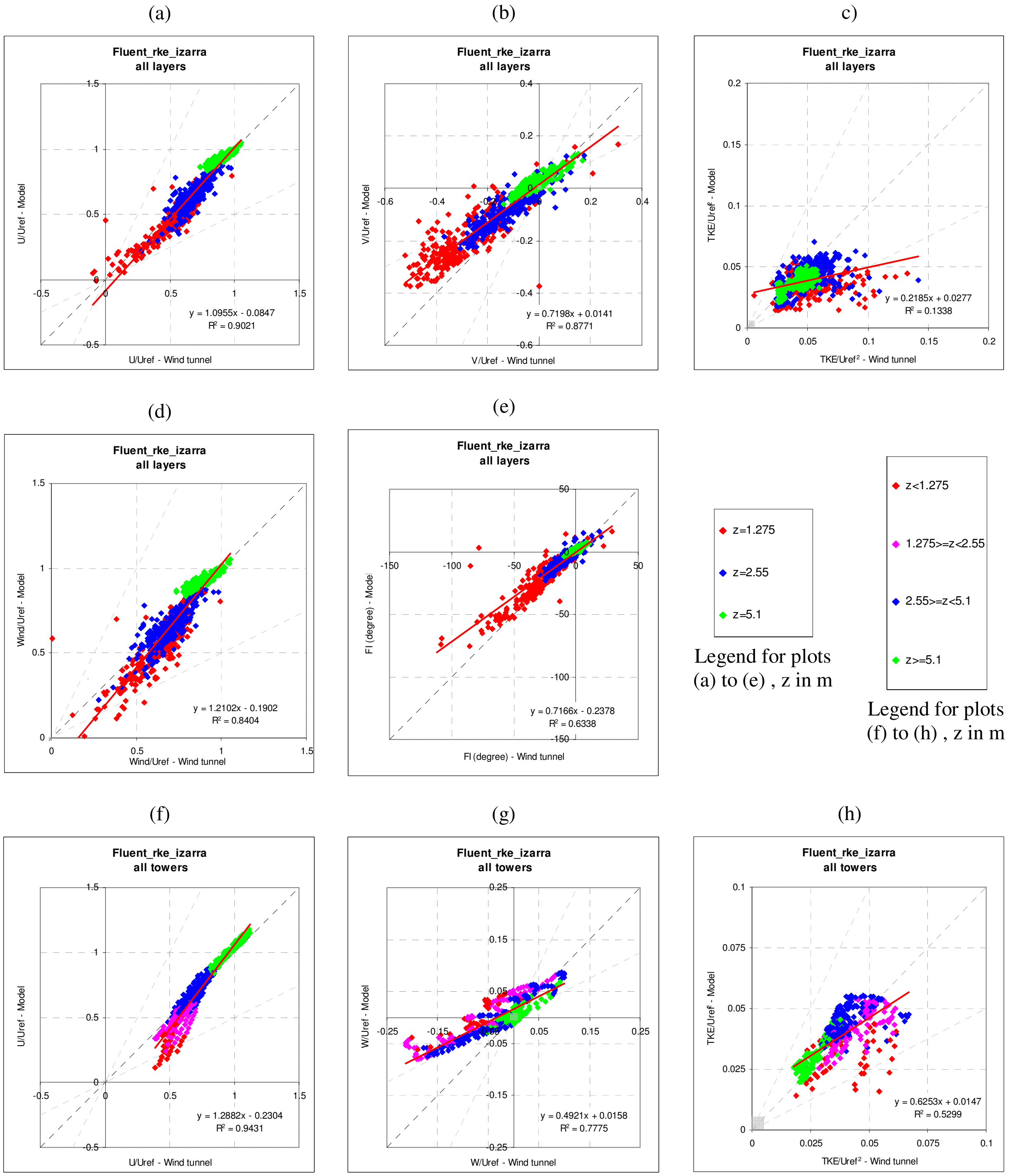

Figure 8-10. Flow field measurements vs. RKE model predictions in the MUST flow field measurement points. The segmented lines are the limits of FAC2 and the red segmented line represents the correlation coefficient R (see Chapter 6.1.1). See variable definitions in Figure 8-9.

Contrary to the y-velocity component, the scatter plots of the turbulent kinetic energy (TKE) do not show agreement as good as expected from the high Hit-Rates of the root-mean-square normal stresses. The reason is the comparison of different parameters. On one hand, three normal velocity fluctuations were not measured in the experiments for technical reasons. Therefore, these model predictions are compared with an approximation of two perpendicular velocity fluctuations under the assumption of $\overline{v'v'} = \overline{w'w'}$. See comparison of $\overline{v'v'}$ and $\overline{w'w'}$ in Figure 8-12. Other studies has shown that the main source of differences are because the root-mean-square fluctuations enter the turbulent kinetic energy quadratic. If the variances of the fluctuations are evaluated with the Hit-Rate, lower results are obtained.[Fran09]

Table 8-6 shows the results for the FAC2 statistical metric. As can be observed, this metric presents similar results to the Hit-Rate but with higher values. Based on the equations presented in Chapter 6.1 and using the full agreement condition over the data below the measurement and absolute tolerance, the only difference between both metrics is the larger relative tolerance used for the FAC2. The relative tolerance of the FAC2 is calculated from the difference between the predictions and wind-tunnel measurements within an error of 50% to 200%, but the Hit-Rate only allows a difference of ±25%. In general, these FAC2 values confirm the results from the Hit-Rate with considerably good agreement for the predictions of the x-velocity component and normal stresses (represented by the high values for the turbulent kinetic energy), and lower agreement for the other two ($\overline{v}$ and $\overline{w}$) velocities.

In addition to the normalized parameters of $\overline{u}$, $\overline{v}$ and $\overline{w}$ velocities and k turbulent kinetic energy, mentioned earlier, Figure 8-9 and Figure 8-10 present the scatter plots of Wind/U_{ref} for the normalized wind magnitude and the angle FI of the velocity vector direction using the Excel tool recommended from [Cost732]. These two parameters present very good agreement between numerical predictions and wind tunnel measurements. Again, they show the best behaviour at a larger distance from the bottom and some accuracy improvements when the LRRIP model is used instead of RKE.

8.5.3 Concentration Field

The normalized concentration C^* is a common way to report concentration distribution of experiments and numerical simulations. It has been also implemented in the present work and it is defined here as:

$$C^{*}=\frac{C\cdot U_{ref}\cdot H^{2}}{Q_{source}} \qquad \text{Eq. 8-4}$$

where C[ppm] is the actual concentration, U_{ref} [ms^{-1}] is the reference velocity in x-direction at the reference point $P_{ref}(x,y,z)$ = (-144,-2.25,7.29)m, H(=2.54 m) is the height of the containers, and Q_{source} (= $1.527\cdot10^{-5}$ m^3s^{-1}) is the volumetric flow rate of the concentration source. As can be seen, the reference point is located within the vertical zone called the profile approach.

The source and measurement locations for the concentrations are shown in Figure 8-11. The concentration measurements are all located at constant height z = 1.275 m. The exact source location in the wind-tunnel experiment is P_{source}(x,y,z) = (-102.48, -7.064, 0)m. The source of concentration is introduced as volume source in the computational domain of the numerical simulations in the cell centre of the computational grid cell which contains the point P_{source}.

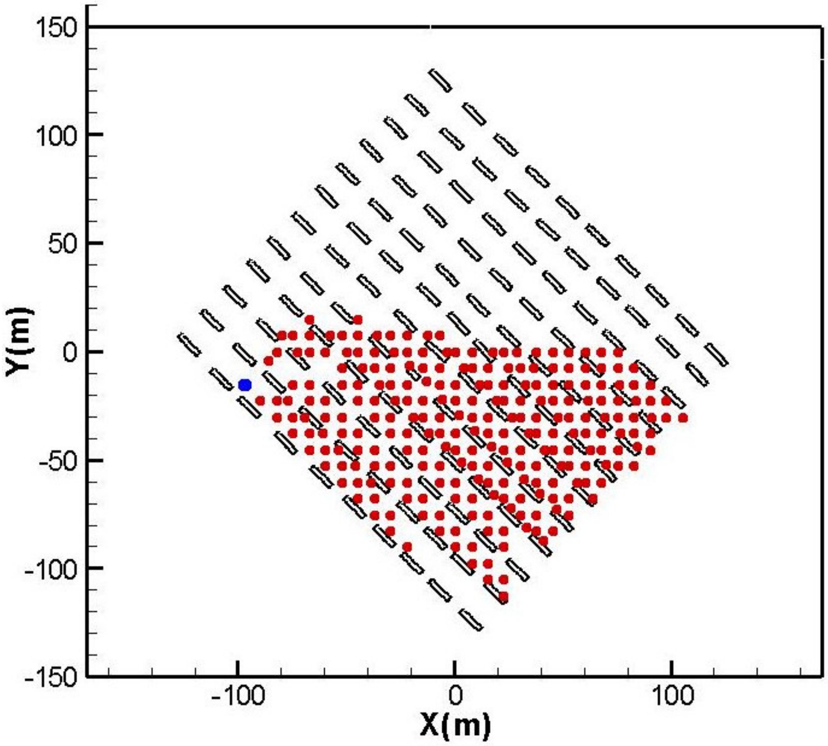

Figure 8-11. Ground source location (blue point) and concentration measurement positions (red points) at z=1.275m for the MUST experiment.

Table 8-8 presents eight of the evaluation parameters (defined in Chapter 6.1) used to compare and quantify the error of results for each of the seven scalar flux models implemented in this test case. The results of five simulations from different combinations of turbulence models and computational/grid domains are compared with the experimental measurements. Table 8-8 shows the numerical predictions of concentrations using the STDDOM domain together with the LRRIP or RKE turbulence models (Cases 1 and 5), and the numerical predictions of concentrations for three different grid refinements necessary to access the grid dependency of results of the ROTDOM domain with the LRRIP turbulence model (Cases 2 to 4). The scalar flux models implemented for this test case were the SED1, SED2 (with Sc_t of 0.7 and 0.9, respectively), GGDH1, GGDH2 (without and with wall damping functions, respectively), ABE-SUGA, ABE, and S-M HANJALIC (see Chapter 3.2 for details).

Table 8-8. Metrics for the six scalar flux models in a total of five different simulations

Simulation Case	***Model***	FB_{FN}	FB_{FP}	***FB***	***NMSE***	***MG***	***VG***	***FA2***	***Q***
1) STDDOM-LRRIP	SED1	0.16	0.12	0.04	1.46	1.05	1.12	0.92	0.84
	SED2	0.29	0.04	0.25	1.55	1.2	1.17	0.90	0.73
	GGDH1	0.12	0.34	-0.22	2.52	0.89	1.18	0.93	0.81
	GGDH2	0.12	0.34	-0.22	2.52	0.89	1.18	0.94	0.81
	ABE-SUGA	0.18	0.49	-0.31	4.96	0.88	1.51	0.81	0.66
	ABE	0.22	0.28	-0.06	4.02	1.02	1.24	0.92	0.79
	S-M HANH	0.10	0.64	-0.54	6.32	0.74	1.42	0.85	0.50
2) ROTDOM Fine-LRRIP	SED1	0.18	0.50	-0.32	4.39	0.83	1.54	0.80	0.53
	SED2	0.21	0.57	-0.36	5.22	0.83	1.82	0.68	0.5
	GGDH1	0.26	0.58	-0.33	7.24	0.84	2.04	0.72	0.5
	GGDH2	0.25	0.58	-0.33	7.24	0.84	2.03	0.73	0.5
	ABE-SUGA	0.34	0.68	-0.34	13.2	0.87	3.04	0.67	0.49
	ABE	0.27	0.52	-0.25	11.09	0.89	1.74	0.77	0.67
	S-M HANH	0.28	0.50	-0.22	9.23	0.98	1.68	0.79	0.62
3) ROTDOM Middle-LRRIP	SED1	0.17	0.46	-0.32	3.52	0.83	1.35	0.86	0.61
	SED2	0.16	0.51	-0.34	4.19	0.84	1.51	0.79	0.53
	GGDH1	0.22	0.51	-0.29	5.58	0.85	1.72	0.75	0.52
	GGDH2	0.22	0.51	-0.29	5.57	0.85	1.71	0.75	0.52
	ABE-SUGA	0.34	0.59	-0.24	10.45	0.90	2.39	0.70	0.53
	ABE	0.24	0.47	-0.23	8.35	0.88	1.57	0.82	0.72
	S-M HANH	0.19	0.77	-0.59	9.31	0.71	2.5	0.56	0.44
4) ROTDOM Coarse-LRRIP	SED1	0.17	0.53	-0.35	4.84	0.84	1.53	0.81	0.55
	SED2	0.20	0.59	-0.39	5.73	0.84	1.82	0.70	0.48
	GGDH1	0.25	0.62	-0.37	8.16	0.83	2.1	0.70	0.46
	GGDH2	0.25	0.62	-0.37	8.14	0.83	2.09	0.70	0.46
	ABE-SUGA	0.35	0.70	-0.35	12.68	0.86	3.34	0.66	0.46
	ABE	0.26	0.55	-0.29	10.7	0.86	1.78	0.78	0.67
	S-M HANH	0.20	0.87	-0.68	13.06	0.69	3.27	0.52	0.42
5) STDDOM-RKE	SED1	0.12	0.18	-0.06	0.67	0.97	1.13	0.95	0.74
	SED2	0.09	0.29	-0.20	1.27	0.89	1.12	0.97	0.69
	GGDH1	0.26	0.09	0.16	0.86	1.11	1.27	0.82	0.70
	GGDH2	0.26	0.09	0.17	0.86	1.11	1.27	0.82	0.70
	ABE-SUGA	0.32	0.09	0.23	1.26	1.18	1.35	0.79	0.69
	ABE	0.57	0.07	0.51	2.85	1.39	1.75	0.68	0.60
	S-M HANH	0.05	0.78	-0.74	7.92	0.59	1.56	0.54	0.36
Exp. Meas.	-	0	0	0	0	1	1	1	1

It is necessary to consider multiple performance measures because each measure has its own advantages and disadvantages and there is not a single measure that is universally applicable to all conditions. The ideal metric values are given at the bottom of Table 8-8 and they represent the values at which the prediction would present perfect agreement with the experimental measurements. To analyse these results, the recommended acceptance criterion or range of tolerance proposed by [Chan04] and [VDI05] was employed. The grey colour cells represent the results that fulfil the respective acceptance criterion, which are FAC2 > 0.5, $|FB| < 0.3$, NMSE < 4, $0.7 < MG < 1.3$ $VG < 1.6$ and $q>0.66$. The absolute and relative threshold of q (Hit-Rate) was fixed at 0.003 and 25%, respectively. As complementary information to Table 8-8, Figure 8-14 and Figure 8-15 present these same results plotted in the form of concentration profiles for each scalar flux model at a different distance from the pollutant source.

A first overall view of the Table 8-8 shows that most of the metrics reported an oscillatory behaviour with grid resolution. This trend means that the results are likely to change with further grid refinements and this is the reason why the three grid results are included at this point. The fine, middle and coarse grid implemented in the ROTDOM computational domain to assess the grid sensitivity of the results shows that the numerical predictions are not always in the asymptotic range. For example, the Hit-Rates obtained from the ROTDOM-middle grid are higher than for the ROTDOM-fine grid. This performance is also consistent with the low percentage of points where the calculation of grid uncertainty was possible, because reaching the asymptotic range is necessary to quantify the numerical grid uncertainty applying the Richardson extrapolation technique. However, the Richardson Extrapolation is also adversely affected by the inconsistent definition of the volumetric source, as explained in Chapter 8.4.

The concentration results show that the calculated values of the metric FAC2 are for all cases inside the recommended acceptance criteria (FAC2>0.5). The high agreement of this metric is given due to its appreciable large relative tolerance. A similar condition to FAC2 also occurs for the metric MG where only three simulated cases (two of S-M HANJALIC and one of ABE model) fail the recommended acceptance criterion. The MG measures systematic errors and it shows a relatively good systematic agreement for the majority of the models. However, this information may not be relevant because this case contains one of the well-known limitations of MG where large fractions of measurements have very low concentrations [Chan05]. The other evaluation parameters provide a different selection of models that fulfil the recommended acceptance criteria. With a few exceptions, the metrics NMSE, FB, VG and q show the best agreement when using algebraic anisotropic models with the STDDOM domain. The FB metric ($FB=FB_{FN}-FB_{FP}$) also shows some good results for the three cases of ROTDOM, but they can be easily neglected because of their very high over-prediction value reported by FB_{FP}. Another clear interesting result from the table is that the S-M HANJALIC model often fails the acceptance criteria and generally performs worse than the algebraic models.

Between the algebraic models, one may observe that in a rather complex case—pollution release within an array of obstacles—the most simple and well known model SED1 (with Sc_t=0.7) performed best for most of the evaluation parameters considered here. However, when using the LRRIP Reynolds stress turbulence model, the anisotropic models ABE and GGDH also performed as well as or sometimes better than the SED1 model. From the two GGDH model variations, it could be observed that the large size of the cells employed close to the walls (which is common practice in micro-scale meteorology simulations), supersedes the necessity of wall damping functions in urban scale pollution dispersion applications. A more interesting output from these results is the considerably good agreement obtained for the recently published ABE model. While its results are sometimes even better than any other of the models studied here, the ABE model is not in common use yet. The worst predictions of the ABE model were obtained when it was combined with the RKE turbulence model for the Reynolds stresses. A probable reason for this worse behaviour could be the less accurate calculation of Reynolds stresses using k-ε based models.

From Table 8-8, it can be observed that the usage of the STDDOM computational domain best replicates the experimental set up. This computational domain together with the LRRIP model yields the best prediction of concentrations, which is very clear in the comparison between Cases 1 and 3. Although both computational domains present exactly the same grid refinement between the obstacles, the metrics NMSE, VG and FB perform very differently. Both domains have the same grid resolution in the centre of the domain, which corresponds to the area where the concentration measurements took place. Therefore, the different concentrations can only be due to changes in boundary conditions and the subsequent flow predictions in the surrounding array of blocks. Some of the most important differences in the boundary conditions between both domains are the altered approach velocity profile generated by the STDDOM domain (see discussion in Chapter 8.5.1) and the neglect of wall effects in the ROTDOM computational domain.

When using the RKE turbulence model for the Reynolds stresses, the concentration results show a noticeable change. With exception of NMSE, all metrics are slightly worse for RKE than when using the LRRIP model. Another exception is evident for the SED models, which improve in the FAC2 and are not considerably affected in the majority of the metrics, as the other scalar flux models are. Comparing only the algebraic model performance within the same computational domain and grid (for example, Case 1 STDDOM-LRRIP and Case 5 STDDOM-RKE), there is an exact change of sign of the FB metric. The SED models changed from predominant under-prediction (positive sign) to predominant over-prediction (negative sign), and the reverse for the opposite case. Within the RKE turbulence model, the worst model prediction was found again for the S-M HANJALIC model and within the algebraic models, the ABE model presents the worst results. The most likely reason for the worse results of concentrations when using the RKE is because the worse prediction of Reynolds stresses with the k-ε based formulation. Therefore, it could be considered that the SED models were not as strongly affected by this change because the Reynolds stresses have no direct influence on the turbulent scalar fluxes, as is the case for all the anisotropic scalar flux models presented here.

The predictions of the anisotropic algebraic flux models ABE, ABE-SUGA and GGDH are fundamentally related because all of them are based on different combinations of the Reynolds stresses, and therefore they suffer the same kind of problems. Looking at their derivation, the ABE and ABE-SUGA were developed with the intention to overcome the limitations of the GGDH at near-wall regions. In this work as well as in most microscale meteorological studies, the first off-wall calculation points are located at a large distance from the walls well in the logarithmic region. Some improvements were achieved for the ABE model when Reynolds stresses were calculated more accurately. However, further tests and validation of these models with different applications must be done before stating final conclusions.

Based on the high dependence of the anisotropic algebraic scalar flux models on the Reynolds stresses, each Reynolds stress component (3 normal and 3 shear stresses) must be analyzed to understand the anisotropic model behaviour. Figure 8-12 presents the six Reynolds stress components plotted at half the height of the containers, which is where the concentration measurement took place.

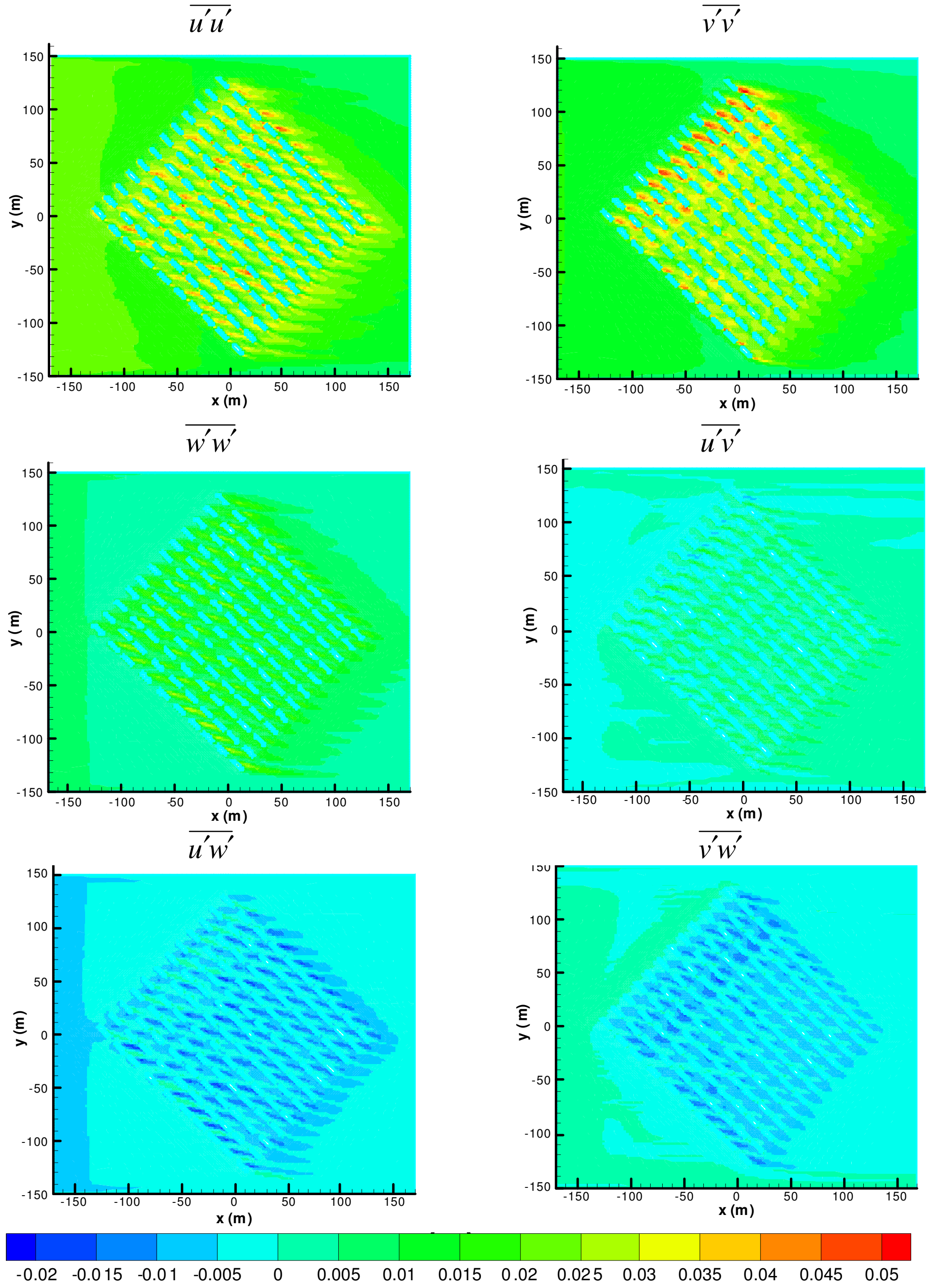

Figure 8-12. Contour plots of Reynolds stresses [$m^2 \cdot s^{-2}$] calculated using LRRIP model in MUST experiment. Plane z=H/2.

As mentioned earlier in the two-dimensional test case, the values of the Reynolds stresses represent the main source of differences between the isotropic and anisotropic scalar flux models. The comparison of these models may be observed by their turbulent diffusion coefficients (i.e. Γ_{ij} in Eq. 5-4). In tensor notation, the diffusion coefficient for the isotropic turbulence model (SED) is a scalar multiplied by the identity matrix. Thus, if the turbulent diffusion coefficient of an anisotropic model is equal to the Reynolds stress tensor (e.g. GGDH), the differences between these two models (i.e. SED vs. GGDH) are exclusively concentrated in the variation of each respective value of the tensor Γ_{ij}. Figure 8-12 shows that the usual higher values of the normal stresses over the shear Reynolds stresses reflect the similar behaviour between the isotropic and anisotropic models. However, the three normal stresses located in the main diagonal of the anisotropic diffusion coefficient (Γ_{ij}) are not equal, as occurs for the isotropic models. The contour plots of Reynolds stresses (Figure 8-12) show that the $\overline{u'u'}$ and $\overline{v'v'}$ components are the highest terms and therefore they represent the predominant direction of the scalar transport by turbulent diffusion. From this analysis, one can conclude that the main difference between the isotropic and anisotropic algebraic models is that the last one provides higher diffusion in the horizontal direction and lower in the vertical direction. These results are consistent with the higher concentrations reported by the isotropic models at larger vertical distance from the MUST experiment (see Figure 8-13).

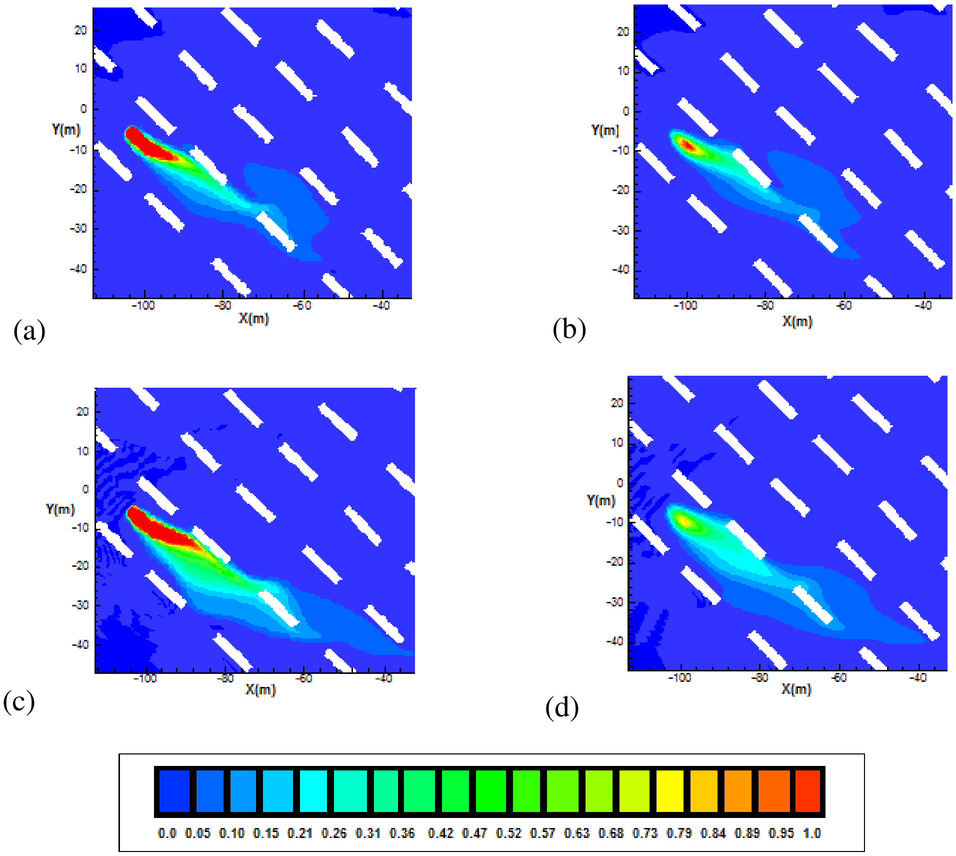

Figure 8-13. Contour plot of *C concentration for SED1 [(a) and (b)] and GGDH1 [(c) and (d)] scalar flux models in the MUST experiment. Two different heights are plotted: Plane 1 [(a) and (c)] at 0.175m (≈H/14) and Plane 2 [(b) and (d)] at 1.275m(≈H/2).**

The qualitative analysis of the results presented in Table 8-8 is completed by concentration profiles presented in Figure 8-14 and Figure 8-15. The first noticeable result from these plots is that all the models present similar behaviour at large distances from the source, which is usually with differences smaller than the measurement uncertainty of $C^*(=3 \cdot 10^{-3})$. The biggest variations of model predictions are concentrated in the few evaluation points located close to the pollution source, which is why the metrics report only a few quantitative differences. The shape of concentration profiles (typically of Gaussian curve shape) also changes according to the selection of the Reynolds stress turbulence model. In comparison to the LRRIP, the RKE model produces an evident reduction of lateral dispersion for all models and an increase of over-prediction tendency in the case of S-M HANJALIC and SED models. This tendency can be also observed from the negative sign of FB for RKE simulations reported in Table 8-8. These results are a consequence of the worst predictions of anisotropic effects when the RKE is used, the typical over-prediction of turbulence viscosity obtained from k-ε based turbulence models (See comparison of turbulent viscosities in Appendix C) and the lack of calibration of each term of the second moment model formulation. Other observations of profiles in Figure 8-14 and Figure 8-15 include a higher disparity of the concentration predictions using the LRRIP models, and the general tendency of lateral displacement of the dispersion puff away from the Gaussian shape, presented by the too coarse positioning of the measurement points. These graphics do not present clear enough behaviour to state the best Reynolds stress and scalar flux model combination.

Finally, from an engineer's point of view, the concluding goal of this work must be to define a ranking for the best general model performance. It is not an easy task based on the qualitative comparison of results of concentration profiles, but it can be relatively well done based on the results for the FAC2 and the Hit-Rate records presented in Table 8-8. These two metrics are very robust measures for the agreement between measurement and numerical predictions. They report the worst predictions for the LRRIP runs using the S-M HANJALIC model, mainly due to a persistent over-prediction of concentrations. For the RKE model, the worst predictions were found for the ABE and S-M HANJALIC model. In general, a decrease in almost all marks was observed with these two models in comparison to LRRIP runs. Other model combinations present better and similar results with agreements inside of the recommended acceptance criteria of FAC>0.5 and q>0.66. Of all scalar flux models, the best agreement with the experimental measurements of the MUST exercise was found for the SED1 and GGDH models using both LRRIP and RKE. Further discussion of model improvements and analysis of the MUST results, together with the previous two-dimensional street canyon exercise, is done in Chapter 9.

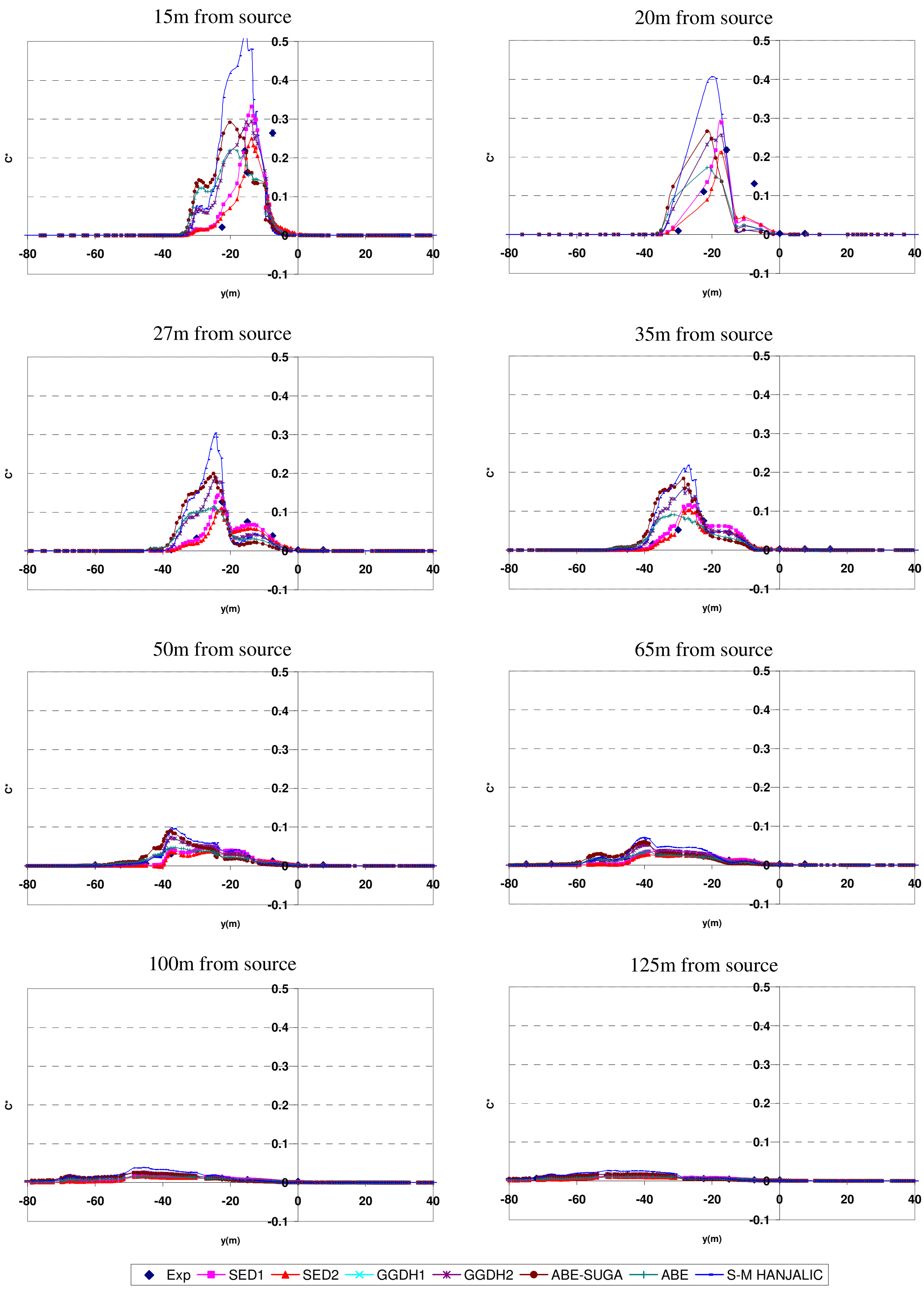

15m from source

20m from source

27m from source

35m from source

50m from source

65m from source

100m from source

125m from source

Figure 8-14.- Comparison of concentration model performance for LRRIP at different distances from the source location

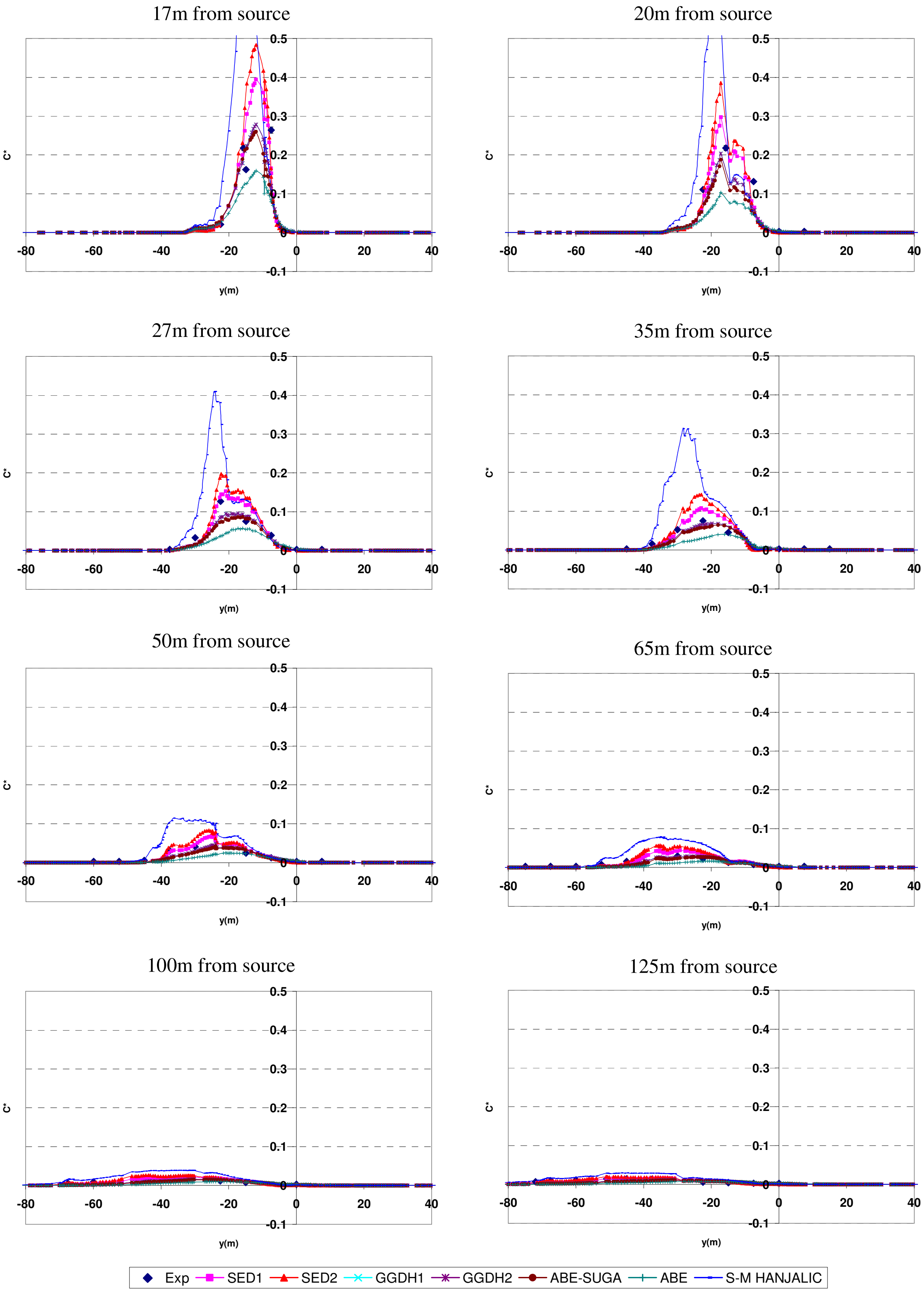
17m from source

20m from source

27m from source

35m from source

50m from source

65m from source

100m from source

125m from source

Figure 8-15.- Comparison of concentration model performance for RKE at different distances from the source location

9 Analysis of Results

In this dissertation, two different test cases were examined (a 2D street canyon and a 3D urban area) to study pollution dispersion in urban environments. Different turbulence models for Reynolds stresses (SA, SKE, RKE, RNG, SKW, SST, LRRIP) and scalar fluxes (SED, GGDH, ABE, ABE-SUGA, YOUNIS, S-M HANJALIC, S-M DURBIN) were used in these simulations and have been quantitatively evaluated by means of statistical metrics, and qualitatively analyzed with scatter and contour plots of velocities and concentration profiles. However, different conclusions may be extracted from each case. Here, three important arguments are presented to explain the different results and the intrinsic considerations which make them possible.

1) First, two different conclusions from the Simple Eddy Diffusivity (SED) models were obtained. From the MUST exercise, one may conclude that the SED2 model (with Sc_t = 0.9) does lead to worse results than the SED1 model (with Sc_t = 0.7). However, in the street canyon exercise, the SED2 model performs better than the SED1 model[17]. These statements are not true for all considered metrics, but they show a trend, which is at least part of the reason why many authors recommend a range [0.7 to 0.9] (e.g. [Durb01]) instead of one value for Sc_t. Other authors have even recommended lower values than 0.7 (e.g. [Tomi07] [Disa07]) or higher values than 0.9 (e.g. [Tang06]), usually based on a specific simulation exercise. Therefore, if a detailed analysis is carried out with more than one diffusion coefficient, the final recommendation for the best model prediction may yield different result.

The considerable improvement obtained in this work after the change of Sc_t in the simplest isotropic SED model is not an isolated case. Another example of modelling improvements by modification of the diffusion model coefficient can be observed with the different value recommendation for the turbulent Prandtl number

---

[17] The increase/reduction of the constant Sc_t is equivalent to set a lower/higher diffusion coefficient for the scalar. The best model coefficient depends on a number of reasons. Please refer to Chapter 3.2.1.1 for a discussion of different recommended values of Sc_t.

(Pr_t=0.85)[18] and turbulent Schmidt number (Sc_t=0.7) in the employed commercial software [Flue06]. Similarly, the GGDH model is also used with a different model coefficient for the turbulent diffusion term in the differential models for momentum and scalar. Thus, the calculation of the appropriate diffusion coefficient is not a simple task and its value is definitely related to the final engineering application. Therefore, because momentum, heat and species transport are different physical phenomena, the influence of the diffusion terms in these transport equations are different. In addition, the different predictions of Reynolds stresses obtained from the variation of turbulence models produce variations of the concentration field. As a consequence, the anisotropic model employed to simulate the diffusion transport must be also calibrated according to the specific case of interest.

The sensitivity of Sc_t in the SED model and the GGDH model coefficients were analysed in the MUST experiment for a discrete range of values and for several turbulent models of Reynolds stresses. These results are presented in Figure 9-1. As expected, the variation of the model coefficient for both models (SED and GGDH) produces a wide range of results. These results are sometimes better than those obtained with the respective standard (recommended) model coefficients. As a preliminary analysis, it appears that there is an optimum value of model diffusion coefficients different for each scalar flux model, each turbulence model and each computational domain. These results may modify the reported ranking order given for the best scalar flux model selection. For example, the optimum value of Sc_t in the MUST experiment using the SED-LRRIP simulation case is a value between 0.7 and 0.5, and it is different for the SED-RKE and for any other combinations of turbulence models. Similarly, the GGDH-LRRIP simulations show the best agreement with the measurements for a model coefficient value between 0.4 and 0.5 (when its standard value is 0.3), but changing for any other simulation conditions. Preliminary studies of model coefficient sensitivity for the second moment models have also shown a possible prediction improvement. Behind this analysis there is a large theory and list of scientific publications about the physical and experimental considerations used to develop each scalar flux model and/or propose new scalar flux model coefficients. Due to the complexity of these physical and mathematical parameters in each of the implemented scalar flux models, it is not possible to present a final conclusion for the optimum model coefficients in this work. Thus, further analysis of sensitivity of model coefficients is proposed for a future study.

---

[18] Pr_t is the analogue of Sc_t in the energy equation.

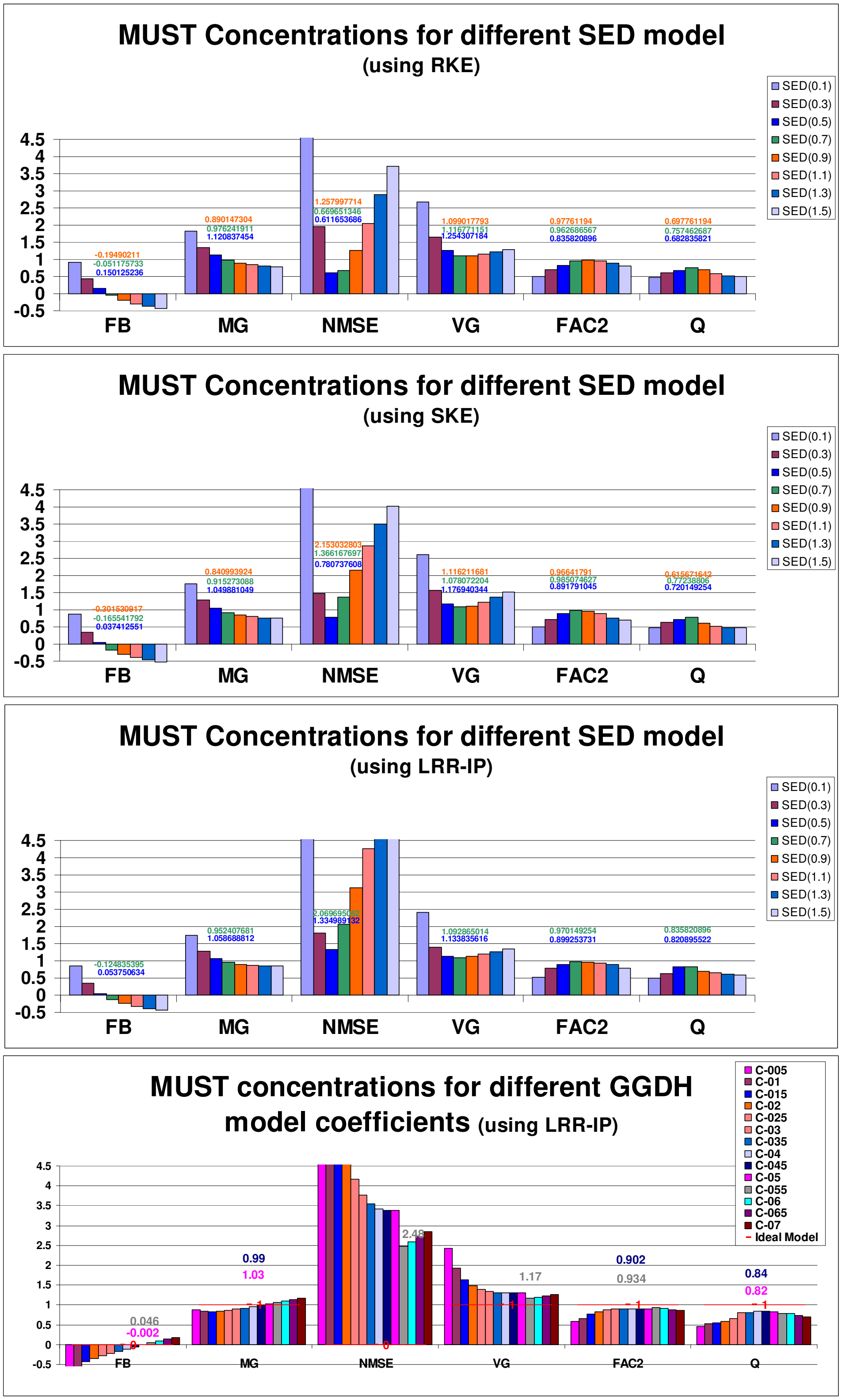

Figure 9-1.- Sensitivity analysis of MUST experiment for different Sc_t in SED and GGDH model coefficients with different turbulence models for Reynolds stresses.

2) The second observation and probably one of the most relevant findings of this work is that although some improvements may be obtained from a more exhaustive analysis of model coefficients, the implemented advanced anisotropic models presented only small improvements over the simple isotropic gradient based models. This observation confirms that there are some applications where the simple SED model can perform almost as well as theoretically more advanced models. To understand these unanticipated results, the flow field and the Reynolds stresses were analysed carefully. In free turbulent flow (far from the walls), the scalar transport is dominated by convection and therefore diffusion processes play no dominant role. However, close to the wall the transport budget of the scalar changes. Within the thin diffusive sub-layer part of the boundary layer, lower flow velocities exist and hence the diffusion transport becomes the predominant transport phenomenon. Farther from the wall, these phenomena become rapidly negligible. Thus, it is in this region close to the wall where an accurate formulation of the turbulent diffusion of scalar fluxes must be used. Also close to the walls, the maximum anisotropic behaviour of the flow occurs and consequently the anisotropic models deviate more from the isotropic model behaviour. At high Reynolds numbers and a relatively high molecular Schmidt numbers (like the air flow in the atmosphere) the thickness of the diffusive sub-layer is very small. Due to the large cell sizes near walls usually used in micro-scale obstacle resolving simulations, the calculated concentration profile in these locations is mainly determined by the scalar near-wall function, where the diffusive sub-layer is usually not resolved. As a result, the anisotropic effects inserted by the implemented anisotropic turbulence models have practically only a weak influence on the complete dispersion field.

3) The third and final argument is the lack of three-dimensional measurements in both wind tunnel experiments. The first test case is a street canyon which was intentionally defined and measured considering a two-dimensional flow field. Therefore, no three-dimensional information could be obtained from it. The second test case is the 12x10 array of obstacles called the MUST experiment. Although it was carried out in complete three-dimensional flow field conditions and without any plane of symmetry, all of its concentration measurements are located in a horizontal plane with a constant distance from the floor.

To understand this situation better, one must remember the intrinsic characteristic of anisotropic flows. Anisotropic flows deal with directional preference or predominance of transport—in this case, the transport of a scalar or pollutant. As in any other transport phenomenon in turbulence conditions, the anisotropic characteristic of a flow is highly related to the convection transport, and hence to the convection of velocity fluctuations known as Reynolds stresses. The well-known high anisotropy effects close to walls actually result from the variations of each of the normal and shear stresses as a function of the wall distance. Thus, in comparison to the standard isotropic scalar flux model, an anisotropic model is able to predict the directional preference of dispersion according to the turbulence characteristics of the flow. Therefore, although one selected isotropic model may replicate better the measurements than the anisotropic models in a specific plane, the constant value of Sc_t may not adapt to the changes in the scalar transport at different heights from the floor.

Furthermore, if an exhaustive study is presented for the calibration of the scalar flux model coefficients using the MUST experiment, the best model coefficient would be limited to the best prediction of dispersion in a single plane. Thus, the optimal model coefficient will always depend on the number of planes and the amount of measurements used for the validation of simulation results.

10 Conclusions

The numerical simulation of passive pollutant dispersion in urban environments under different setup conditions has been realized satisfactorily. The main objective of this dissertation —the application of advanced anisotropic scalar flux models for the solution of the transport equation of averaged concentrations— was performed and their behaviours were contrasted with the generally used standard isotropic scalar flux model and wind-tunnel experimental measurements. The implemented anisotropic scalar flux models were originally developed and applied to other engineering applications with analogue diffusion transport phenomena. Their performance in pollution dispersion is evaluated here, based on the comparison between numerical predictions and experimental concentration measurements of the two-dimensional street canyon model from [Pava99] and the three-dimensional urban area model, MUST, from [Bezp07]. The results were qualitatively and quantitatively analysed using different plots and statistical metrics recommended in the literature to assess the predictive capability of pollution dispersion models [Chan04].

Complex physical phenomena are involved in turbulent pollution dispersion in urban environments. Therefore, a good simulation of atmospheric flows in urban environments is necessarily related to the good simulation capabilities of the applied software. Recent progress of commercial CFD codes with advanced and attractive features, up-to-date computational models, validated for different flow conditions and with well documented technical support included, has caused many institutions to shift from their local software to commercial CFD codes. Nevertheless, the local codes are usually well specialized in specific engineering applications and have completely accessible source code in comparison to the general propose commercial CFD codes. These differences are very important because before performing any CFD simulation one must take care of the current capabilities and limitations of the available commercial code and its effects on the predominant physical phenomena of interest. For example, in this work the anisotropic characteristics of the flow are expected to be a very important physical phenomenon in understanding the behaviour of passive pollutant dispersions. The reliable and accurate prediction of the pollutant field demands the accurate prediction of the velocity field. Therefore, these simulations also required the analysis of turbulent momentum shear stress (Reynolds stress) models.

Several turbulence models for Reynolds stresses were briefly explained and discussed in this work as a function of their different calculation approaches with the intention of studying how their predictions influence the passive scalar dispersion in urban environments. Some of the most commonly used Reynolds stress models were tested and the results corroborated that the main velocities and turbulent parameters can be estimated quite well. However, an accurate estimation of the flow field requires high numerical efforts, such as the set-up of a well detailed geometry, an extended computational domain, a sufficiently refined grid, the utilization of more complex turbulence models and others. The predicted dispersions in atmospheric turbulent flows confirmed its strong dependence on the right flow field and therefore on the selected Reynolds stress model. The comparison of simulation results for the studied two-dimensional test case shows that the three k-ε based models (Standard, RNG and Realizable), the Reynolds stress transport model (LRRIP), and the Spalart-Allmaras (S-A) model, combined with the Simple Eddy diffusivity model for scalar fluxes, performs relatively well and considerably better than when using the k-ω based models (Standard and SST) for Reynolds stresses. From this exercise, it was also observed that qualitatively small variations in the movement of the flow (such as changes in the size or shape of flow recirculations within the canyon) may produce a completely different pollution dispersion field with a Hit-Rate reduction for concentrations in up to 50% points (See Chapter 7.4.1).

The comparison of the three-dimensional simulations with their respective experimental measurements revealed that within the flow field and Reynolds stress model predictions there is still an area of possible improvement. This range of improvement can be observed from the low Hit-Rate values reported for the y-velocity component which were on ocations only 14% to 15% using the LRRIP or RKE turbulence model (see Chapter 8.5.2).

As shown in this work, the accurate calculation of atmospheric flow fields is not a simple task. Some better results may be obtained with future improvements in computational speed, which would allow overcoming the aforementioned numerical and computational limitations, and applying the new generation of turbulence models (such as LES) in atmospheric pollution dispersion.

The turbulent scalar flux models were also classified and discussed in light of their ability to reproduce experimental measurements of pollutant dispersion. Based on the evidence of the already present errors and uncertainties in the computed turbulent flow field, an ideal or perfect scalar flux model would produce wrong results. Thus, the analysis and discussion presented here is only valid for the specific combination of turbulent momentum and scalar flux transport models.

The combination of turbulence models is a common flaw in most commercial codes because these codes (like FLUENT) usually present many options and highly sophisticated models of turbulent Reynolds stresses (including large numbers of transport equations and turbulence quantities) but for scalar transport, the algebraic Simple Eddy Diffusivity (SED) model is the only one available. This model assumes the Reynolds analogy between momentum and scalar transport where the proportionality factor is the inverse of the usually assumed constant parameter, the turbulent Schmidt number. Most code users are aware of this problem, but unfortunately they usually apply the constant default value given in the code which may change due to many reasons (see discussion in Chapter 3.2.1.1).

In addition to this "standard" option represented by the SED model, five algebraic scalar flux models were implemented in this study (the Generalized Gradient Diffusion Hypothesis so-called GGDH from [Daly70] and the proposals ABE-SUGA [Abe01], ABE [Abe06], WET [Laun88] and YOUNIS [Youn05]), as well as two second moment scalar flux models (S-M HANJALIC [Hanj02] and S-M DURBIN [Durb93]) for the simulation of pollution dispersion using the commercial software FLUENT v6.3. From these scalar flux models, the SED and GGDH models were arbitrarily selected for a sensitivity study of model coefficients within a discrete range of values. All the employed models showed congruent and similar pollution distribution. The simplest and most well-known SED model, which has proved to fail in simple heat transfer applications in many previous works, presented satisfactory results in the present work (up to 84% Hit-Rate in MUST experiment and 79% in the street canyon), and was comparable to the advanced models for most of the statistical evaluation parameters. Nevertheless, no single constant optimum value for the Sc_t was found.

The formulation of the turbulent anisotropic scalar flux models shows that the results from these models are highly related not only to the value of concentration gradients (like expressed by SED) but also to the correct prediction of each of the Reynolds stresses. Therefore, the anisotropic scalar flux models are expected to perform better when the differential Reynolds stress turbulence models for the flow field are used. This analysis is congruent with the results obtained in this work. In general, the results revealed a lack of calibration for most of the scalar flux model coefficients for their application to the simulation of atmospheric pollution dispersion. The most straightforward method to overcome this problem may be following an analogous procedure to estimate the model coefficients of heat transfer, but by using a “passive” mass transport. This process is usually completed by comparing numerical predictions with experimental measurements at different boundaries or flow conditions. It may also be accomplished by extracting each term of interest from LES/DNS or by carrying on a statistical/mathematical genetic algorithm procedure for optimization of the coefficients (e.g. [Jani07]).

Other relevant simulation results should also be mentioned. The grid uncertainties of results in both geometries were estimated through the application of generalized Richardson Extrapolation. This grid post-processing procedure presented reasonable numerical uncertainty values and turned out to be a very useful technique for quantifying grid quality in view of each specific variable of interest. Additionally, other parameters needed for the simulation of pollution dispersion were studied. Small differences were found after the assumption of ethane as an active or passive scalar (less than 4%) and from the use of first or second order spatial discretization schemes (less than 24%). The model evaluation of all of these parameters—the different grids, passive/active scalar transport, and spatial discretization schemes—were also performed using the statistical metrics recommended by [Chan04] and [VDI05]. These metrics proved to be a very useful measurement tool, but they do not abandon the necessity of carefully reviewing data by alternative post-processing techniques, like simple graphical comparisons.

Furthermore, one of the most relevant findings of this work is that the implemented advanced anisotropic models hardly presented any improvement over the simple isotropic gradient based model (SED). The improvement measured is so small that its advantage may be judged against the extra work needed for its complex implementation and resolution. With these results, the well-known SED model (the oldest and simplest scalar flux model) showed why it is still commonly used in advanced engineering applications and in up-to-date CFD software. This work confirms that there are some applications where the simple SED model can still perform as well as other advanced models. However, it must be highlighted that in the present study the fluid properties were not changed: only air was used at isothermal conditions because this work is concentrated in the specific case of passive pollution dispersion within the atmosphere. Thus, direct inference to other fluids is only possible based on the theory of fluid dynamics similarity, paying special attention to possible changes in the boundary layer thickness and fluid properties.

The anisotropic scalar flux models results showed superior performance to the isotropic model in at least one or more of the utilized statistical evaluation parameters. The algebraic anisotropic models demonstrated a strong potential for further improvement with a relatively small amount of work. From the algebraic anisotropic models, the GGDH model may be highlighted and recommended for all pollution dispersion simulations due to its easy implementation and usual good predictions obtained within the suggested acceptance criteria. On the other hand, the second moment models confirm their unquestionable position as the most complete models because their formulation takes into account the majority of effects incorporated in turbulent flow modelling. However, similar to other scalar flux models, the second moment models showed reasonably strong agreement in the two-dimensional experiment but worse performance in the three-dimensional experiment. The results demonstrate that the better capabilities to predict scalar fluxes by using second moment models are highly related to the accurate calculation of each physical phenomenon and the precise calibration and validation of each term inserted in their formulation. Therefore, the complete implementation of second moment models for pollution dispersion would mean considerably more work compared to the algebraic models. Although in different proportion, the general worst performance was always observed in the three-dimension exercise for all of the studied scalar flux models. The most likely reason is a lack of previous applications and the calibration of the additional terms included in the three-dimensional formulation.

Finally, similar to other first time works of research groups in new application areas, this dissertation has raised many questions about further model improvements. Due the finite time to develop a doctoral dissertation, these questions were left as recommendations for future works. Some of these recommendations for future works are:

- Perform LES of a three-dimensional test case with the intention to obtain a much more accurate prediction of the mean velocities and Reynolds stresses.
- Perform the solution of the presented turbulent scalar flux (RANS) models with the fixed LES results for the flow field. This process would allow for a more real and complete assessment of these model predictive capabilities.
- Perform a model coefficient calibration of a selected group of algebraic anisotropic scalar flux models.
- Concerning the heat transfer experiences, study of model improvements using combined effects of the turbulent time scale of momentum (k/ε) and their scalar transport analogue (k_ϕ/ε_ϕ) may also be of interest.
- Toward the real pollution dispersion phenomena in the atmosphere, the final goal must be to study the transport of different kinds of active pollutant dispersions, taking into account chemical reactions and strong buoyancy effects.

11 References

[Abe01] Abe, K., and Suga, K., 2001. Towards the development of Reynolds-averaged algebraic turbulent scalar-flux model, International Journal of Heat and Fluid Flow, 22, pp.19-29.

[Abe06] Abe, K., 2006. Performance of Reynolds-averaged turbulence and scalar-flux models in complex turbulence with flow impingement, Prog. in Computational Fluid Dynamics, 6, pp.79-88.

[Abe95] Abe, K., Kondoh, T., and Nagano, Y., 1995. A new turbulence model for predicting fluid flow and heat transfer in separating and reattaching flows-II. Thermal field calculations, Int. J. Heat Mass Transfer, 38, 8, pp. 1467-1481.

[Abe96] Abe, K., Kondoh, T. and Nagano, Y., 1996. A two-equation heat transfer model reflecting second-moment closures for wall and free turbulent flows, Int. J. Heat and Fluid Flow, 17, pp.228-237.

[Amic08] Amicarelli, A., Leuzzi, G., Monti, P. and Thomson, D.J., 2008. A stationary 3D Lagrangian stochastic numerical model for concentration fluctuations, in Proceedings of the 12th International Conference on Harmonization within Atmospheric Dispersion Modelling for Regulatory Purposes, Cavtat, Croatia, pp. 387-391.

[Baik03] Baik, J.J., Kim, J.J., and Fernando, H.J.S., 2003. A CFD model for simulating urban flow and dispersion, Journal of Applied Meteorology, 42, pp. 1636–1648.

[Barm08] Barmpas, F., Ossanlis, I., and Moussiopoulos N., 2008. The effect of source treatment on pollutant dispersion in an idealised urban roughness in numerical simulation using the standard k-ε turbulence closure model, in Proceedings of the 12th International Conference on Harmonization within Atmospheric Dispersion Modelling for Regulatory Purposes, Cavtat, Croatia, pp. 680-684.

[Bart89] Barth, T. J. and Jespersen, D., 1989. The design and application of upwind schemes on unstructured meshes, Technical Report AIAA-89-0366, AIAA 27th Aerospace Sciences Meeting, Reno, Nevada, USA.

[Batc49] Batchelor, G. K., 1949. Diffusion in a field of homogeneous turbulence, Australian Journal of Scientific Research A 2, 4, pp.437-450.

[Baum08] Baumann-Stanzer, K., Piringer, M., Polreich, E., Hirtl, M., Petz, E. and Bügelmayer, M., 2008. User experience with model validation exercises, in Proceedings of the 12th International Conference on Harmonization within Atmospheric Dispersion Modelling for Regulatory Purposes, Cavtat, Croatia, pp. 52-56.

[Bern86] Bernard, P., 1986. Limitations of the near-wall k-ε turbulence model, AIAA Journal, 24, pp. 619-622.

[Bezp07] Bezpalcová, K., 2007. Physical Modelling of Flow and Dispersion in an Urban Canopy, PhD thesis, Faculty of Mathematics and Physics, Charles University, Prague. Czech Republic.

[Bloc07] Blocken, B., Stathopoulos, T., and Carmeliet, J., 2007. CFD simulation of the atmospheric boundary layer: wall function problems, Atmospheric Environment, 41, 2, Pages 238-252.

[Bloc08] Blocken, B., Stathopoulos, T., Saathoff, P., and Wang, X., 2008. Numerical evaluation of pollutant dispersion in the built environment: Comparisons between models and experiments, Journal of Wind Engineering and Industrial Aerodynamics, 96, pp. 1817–1831.

[Bous77] Boussinesq, J., 1877. Theorie de l' Ecoulemen Tourbillant. Mem. Presentes par Divers Savants Acad. Sci. Inst. Fr., 23, pp. 46-50.

[Brit07] Bitter, R., and Schatzmann, M., 2007. Background and justification document to support the model evaluation guidance and protocol, COST Action 732: Quality assurance and improvement if musicale meteorological models, Hamburg, Germany.

[Camb08] Cambridge Advanced Learner's Dictionary, 2008. Cambridge University Press; 3 edition, ISBN-10: 0521885418.

[Came05] Camelli, F.E., Lohner, R., and Hanna, S.R., 2005. VLES study of MUST experiment, 43rd AIAA Aerospace Meeting and Exhibit, paper 1279, Reno, Nevada, USA.

[Came06] Camelli, F., Coirier, W.J., Hansen, O.R., Huber, A., Kim, S., Hanna, S., and Brown, M., 2006. An inter-comparison of four computational fluid dynamics models: transport and dispersion around Madison Square Garden, American Meteorological Society, 6th Symposium on the Urban Environment. Atlanta GA, USA.

[Case00] Casey, M., and Wintergerste, T., 2000. Best Practice Guideline, ERCOFTAC Special Interest Group on: Quality and Trust in Industrial CFD, Published by ERCOFTAC.

[Cebe02] Cebeci, T., 2002. Convective Heat Transfer, Second Edition. Springer.

[Cebe77] Cebeci, T., and Bradshaw, P., 1977. Momentum Transfer in Boundary Layers, Hemisphere Publishing Corporation, New York.

[Chan01] Chang, Ch-H., and Meroney, R.N., 2001. Numerical and physical modelling of bluff body flow and dispersion in urban street canyons, Journal of Wind Engineering and Industrial Aerodynamics, 89, pp.1325–1334.

[Chan02] Chan, T.L., Dong, G., Leung, C.W., Cheung, C.S., and Hung W.T., 2002. Validation of a two-dimensional pollutant dispersion model in an isolated street canyon, Atmos. Environ. 36, pp.861–872.

[Chan04] Chang, J., and Hanna, S., 2004. Air quality performance evaluation, Meteorology and Atmospheric Physics, 87, pp.167-196.

[Chan05] Chang, J., and Hanna, S., 2005. Technical Descriptions and User's Guide for the BOOT Statistical Model Evaluation Software Package, Version 2.0. http://www.harmo.org/kit/BOOT_details.asp

[Chan98] Chang, J.C., Fernau, M.E., Scire, J.S., and Strimaitis, D.G., 1998. A Critical Review of Four Types of Air Quality Models Pertinent to MMS Regulatory and Environmental Assessment Missions, U.S. Department of the Interior, Minerals Management Service, Gulf of Mexico OCS Region, 1201

Elmwood Park Blvd., New Orleans, LA 70123, by Earth Tech, Inc., 196 Baker Avenue, Concord, MA 01742. USA.

[Chen05] Cheng, X., and Hu, F., 2005. Numerical Studies on Flow Fields Around Buildings in an Urban Street Canyon and Cross-Road, Avances in Amospheric Siences, 22, pp. 290–299.

[Chen88] Chen, H. C., and Patel, V. C., 1988. Near-Wall Turbulence Models for Complex Flows Including Separation, AIAA Journal, 26, 6, pp.641-648.

[Chua05] Chua, A.K.M., Kwok, R.C.W., and Yu, K.N., 2005. Study of pollution dispersion in urban areas using Computational Fluid Dynamics (CFD) and Geographic Information System (GIS), Environmental Modelling & Software, 20, pp.273–277.

[Coir06] Coirier, W.J., and and Kim, S., 2006. CFD Modelling for Urban Area Contaminant Transport and Dispersion: Model Description and Data Requirements, Sixth Symposium on the Urban Environment, The 86th AMS annual meeting, Atlanta, USA.

[Coir06b] Coirier, W.J., and Kim, S., 2006. Summary of CFD Urban Results in Support of the Madison Square Garden and Urban Dispersion Program Field Tests, American Meteorological Society, 6th Symposium on the Urban Environment. Atlanta, GA, USA.

[Cost732] URL 1: COST Action 732: European Cooperation in Scientific and Technical research group titled as: Quality Assurance and Improvement of Micro-scale Meteorological Models.
http://www.cost.esf.org/index.php?id=400,
http://www.mi.uni-hamburg.de/index.php?id=464

[Craf02] Craft, T.J., and Launder, B.E., 2002. Closure Modelling Near the Two-Component Limit, pp. 102-126, in Launder, B. and Sandham, N., (eds.), Closure Strategies for Turbulent and Transitional Flows, Cambridge University Press. ISBN-13: 9780521792080.

[Craf02b] Craft, T.J., and Launder, B.E., 2002. Application of TCL Modelling to Stratified Flows, pp. 407-423, in Launder, B., and Sandham, N., (eds.), Closure Strategies for Turbulent and Transitional Flows, Cambridge University Press. ISBN-13: 9780521792080.

[Craf93] Craft, T.J., 1993 Impinging jet studies for turbulence model assessment – II. An examination of the performance of four turbulence models, Int. J. Heat Mass Transfer, 36, 10, pp.2685-2697.

[Craf96] Craft, T.J., and Launder, B.E., 1996 Recent developments in second-moment closure for buoyancy-affected flows, Dynamics of Atmospheres and Oceans, 23, pp.99-114.

[Daly70] Daly, B., Harlow, F., 1970. Transport Equations in Turbulence, Phys. Fluids 13, 2634-2649.

[Defr10] Defraeye, T., Blocken, B., and Carmeliet, J., 2010. CFD analysis of convective heat transfer at the surfaces of a cube immersed in a turbulent boundary layer, International Journal of Heat and Mass Transfer, 53, 1-3, 297-308.

[Dejo09] Dejoan, A., Santiago, J. L., Pinelli, A., and Martilli, A., 2007. Comparison between LES and RANS computations for the study of contaminant dispersion in the MUST field experiment, American Meteorological Society, Submitted.

[Diet07] Dietz, Ch., Neumann, O., Weigand, B., 2007. A Comparative study of the performance of explicit algebraic models for the turbulent heat flux, Numerical Heat Transfer, Part A, 52: pp.101-126.

[Disa07] Di Sabatino, S., Buccolieri, R., Pulvirenti, B., Britter, R.E., 2007. Flow and Pollutant Dispersion in Street Canyons using FLUENT and ADMS-Urban, Environ. Model. Assess. 13, pp. 369-381.

[Disa08] Di Sabatino, S., Olesen, H., Berkowicz, R., Franke, J., Schatzmann, M., Britter, R., Schlünzen, H., Martilli, A. and Carissimo, B., 2008. A model evaluation protocol for urban scale flow and dispersion models, in Proceedings of the 12th International Conference on Harmonization within Atmospheric Dispersion Modelling for Regulatory Purposes, Cavtat, Croatia, pp. 409-413.

[Durb01] Durbin, P.A., Pettersson, B.A., 2001. Statistical Theory and Modelling for Turbulent Flows, Wiley & Sons, Chichester.

[Durb93] Durbin, P.A., 1993. A Reynolds stress model for near-wall turbulence, J. Fluid Mech., 249, pp.465-498.

[Eca04] Eça, L., and Hoekstra, M., 2004. A verification exercise for two 2-D steady incompressible turbulent flows, in: Neittaanmäki, P., Rossi, T., Majava, K., Pironneau, O. (Eds.), Proceedings of the ECCOMAS 2004, Jyväskylä.

[EEA08] European Environment Agency, report bulletin 171, September, 2008. www.transportenvironment.org.

[Efth08] Efthimiou, G.C., Bartzis, J.G., Andronopoulos, S., and Sfetsos, T., 2008. Modelling the concentration fluctuation and individual exposure in complex urban environments, in Proceedings of the 12th International Conference on Harmonization within Atmospheric Dispersion Modelling for Regulatory Purposes, Cavtat, Croatia, pp. 392-395.

[Eich08] Eichhorn, J., and Balczó, M., 2008. Flow, dispersal simulations of the Mock Urban Setting Test, in Proceedings of the 12th International Conference on Harmonization within Atmospheric Dispersion Modelling for Regulatory Purposes, Cavtat, Croatia, pp. 67-72.

[Feng98] Fenger, J., and Hertel, O., Palmgren, F., 1998. Urban Air Pollution – European Aspects, Kluwer Academic Publishers, Dordrecht – The Netherlands. ISBN 0792355024.

[Ferz02] Ferziger, J. H., and Peric, M., 2002. Computational Methods for Fluid Dynamics, Springer, Third edition.

[Fles02] Flesch, T.K., 2002. Turbulent Schmidt number from a tracer experiment. Agricultural and Forest Meteorology, 111, pp. 299–307.

[Flue06] Fluent V6.3, 2006. User’s Guide. FLUENT Inc., Lebanon, New Hampshire, USA.

[Fran05] Franke, J., and Frank, W., 2005. Numerical simulation of the flow across an asymmetric street intersection, EACWE4 — The Fourth European & African Conference on Wind Engineering, J. N´aprstek & C. Fischer (eds); ITAM AS CR, Paper #138, Prague.

[Fran06] Franke, J., and Frank, W., 2006. Application of Richardson extrapolation to the prediction of the flow field around building models, Fourth International Symposium on Computational Wind Engineering – CWE2006, Yokohama.

[Fran07] Franke, J., Hellsten, A., Schlünzen, H., and Carissimo, B., 2007. Best Practice Guideline for the CFD Simulation of Flows in Urban Environment, COST Action 732, Hamburg, Germany.

[Fran07b] Franke, J., 2007. Introduction to the Prediction of Wind Loads on Buildings by Computational Wind Engineering (CWE), in Baniotopoulos C.C. and Stathopoulos T., editors, Wind Effects on Buildings and Design of Wind-

Sensitive Structures, number 493 in CISM Internatinal Centre of Mechanical Sciences, chapter 3, Springer Verlag, Berlin Heidelberg New York. ISBN 978-3-211-73075-1.

[Fran08] Franke, J., Bartzis, J., Barmpas, F., Berkowicz, R., Brzozowski, K., Buccolieri, R., Carissimo, B., Costa, A., Di Sabatino, S., Efthimiou, G., Goricsan, I., Hellsten, A., Ketze, M., Leitl, B., Nuterman, R., Olesen, H., Polreich, E., Santiago, J., and Tavares, R., 2008. The MUST model evaluation exercise: statistical analysis of modelling results, in Proceedings of the 12th International Conference on Harmonization within Atmospheric Dispersion Modelling for Regulatory Purposes, Cavtat, Croatia, pp. 414-418.

[Fran08b] Franke, J., and Frank, W., 2008. Application of generalized Richardson extrapolation to the computation of the flow across an asymmetric street intersection, Journal of Wind Engineering and Industrial Aerodynamics, 96: pp. 1616 - 1628.

[Fran09] Franke, J., 2009. Validation of a CFD model for the prediction of flow and dispersion in the urban environment, Proceedings of the 4th International Building Physics Conference, Istanbul, Turkey, pp.969-976.

[Fu87] Fu, S., Launder, B.E., and Tselepidakis, D.P., 1987. Accommodating the effects of high strain rates in modelling the pressure-strain correlation, Thermo-fluids report TFD/87/5, UMIST, Manchester.

[Gail06] Gailis, R.M., and Hill, A., 2006. A wind-tunnel simulation of plume dispersion within a large array of obstacles, Boundary-Layer Meteorology, 119, pp.289–338.

[Gibs78] Gibson, M.M., and Launder, B.E., 1978. Ground effects on pressure fluctuations in the atmospheric boundary layer, J. Fluid Mech., 86, pp.491-511.

[Grom07] Gromke, C., Denev, J., and Ruck, B., 2007. Dispersion of traffic exhausts in urban street canyons with tree plantings – Experimental and numerical investigations, in Proceedings of Physmod 2007 – International Workshop on Physical Modelling of Flow and Dispersion Phenomena, University of Orléans, France. ISBN 2-913454-32-1.

[Grom08] Gromke, C., Buccolieri, R., Di Sabatino, S., and Ruck, B., 2008 Dispersion study in a street canyon with tree planting by means of wind tunnel and numerical investigations – Evaluation of CFD data with experimental data, Atmospheric Environment, 42, pp. 8640-8650.

[Hanj02] Hanjalic, K., Jakirlic, S., 2002. Second-Moment Turbulence Closure Modelling, in Launder, B., Sandham, N., (eds.), Closure Strategies for Turbulent and Transitional Flows. Cambridge University Press, Cambridge.

[Hann04] Hanna, S. R., Hansen, O. R. and Dharmavaram, S., 2004. FLACS CFD air quality model performance evaluation with Kit Fox, MUST, Prairie Grass, and EMU observations. Atmospheric Environment 38, pp.4675-4687

[Hann91] Hanna, S.R., Strimaitis, D.G., and Chang, J.C., 1991. Hazard Response Modelling Uncertainty (A Quantitative Method), Volume I: User's Guide for Software for Evaluating Hazardous Gas Dispersion Models; Volume II: Evaluation of Commonly-Used Hazardous Gas Dispersion Models; Volume III: Components of Uncertainty in Hazardous Gas Dispersion Models. Report no. A119/A120, prepared by Earth Tech, Inc., Concord, MA, for Engineering and Services Laboratory, Air Force Engineering and Services Centre, Tyndall Air Force Base, FL 32403; and for American Petroleum

Institute, Washington, D.C., USA.

[Hann93] Hanna, S.R., Chang, J.C., and Strimaitis, D.G., 1993. Hazardous gas model evaluation with field observations, Atmos. Environ., 27A, pp. 2265-2285.

[Hass98] Hassan, A.A., Crowther, J.M., 1998. Modelling of fluid flow and pollutant dispersion in a street canyon, Environ. Monit. Assess., 52, pp. 281–297.

[Hov94] Hov, O., Hjollo, B.A., Eliassen, A. 1994. Transport distance of ammonia and ammonium in Northen Europe I. Model description. J. Geophys. Res. 99, 18, pp.735-748.

[Hsie07] Hsieha, K.-J., Liena, F.-S. and Yee, E., 2007. Numerical modelling of passive scalar dispersion in an urban canopy layer, Journal of Wind Engineering and Industrial Aerodynamics, 95, pp. 1611–1636.

[Huan06] Huang, H., Ooka, R., Kato, S., Chen, H., Takahashi, T., and Watanabe, T., 2006. CFD Analysis on Traffic-Induced Air Pollutant Dispersion with Non Isothermal Condition in a Complex Urban Area in Winter, 4th Intl Symposium on Computational Wind Engineering (CWE2006) Japan.

[Huan93] Huang, P., Bradshaw, P., and Coakley, T., 1993. Skin Friction and Velocity Prole Family for Compressible Turbulent Boundary Layers. AIAA Journal, 31, 9, pp.1600-1604.

[Ilyu02] Ilyushin, B.B., 2002. Higher Moment Diffusion in Stable Stratification. Launder, B., and Sandham, N., (eds.), Closure Strategies for Turbulent and Transitional Flows, Cambridge University Press.

[Izar07a] Izarra-Garcia, R., Franke, J. and Frank, W., 2007. CFD simulation of pollution dispersion in a 2D Street canyon, in Proceedings of MicroCAD 2007. Miskolc, Hungary.

[Izar07b] Izarra-Garcia, R., Franke, J., and Frank, W., 2007. Evaluation of Pollution Dispersion Prediction Using RANS and Turbulence Models Available in FLUENT 6.3, in Proceedings of Physmod 2007 – International Workshop on Physical Modelling of Flow and Dispersion Phenomena, 29 - 31 August, University of Orléans, France. ISBN 2-913454-32-1.

[Izar08] Izarra-Garcia, R., Franke, J., and Frank, W., 2008. Pollution dispersion prediction for the MUST wind tunnel experiment with anisotropic algebraic models for turbulent scalar fluxes, in Proceedings of the 12th International Conference on Harmonization within Atmospheric Dispersion Modelling for Regulatory Purposes, Cavtat, Croatia, pp. 380-384.

[Jani07] Janiga, G., 2007. Optimization of the Model Parameters of the Spalart-Allmaras Turbulence Model, in Proceedings of MicroCAD 2007. Miskolc, Hungary.

[Jaya69] Jayatilleke, C., 1969. The influence of Prandtl number and surface roughness on the resistance of the laminar sublayer to momentum and heat transfer, Prog. Heat Mass Transfer, 1, pp.193-321.

[Jones88] Jones W.P. and Musonge P. 1988. Closure of the Reynolds stress and scalar flux equations, Physics & Fluids, 31, 12.pp. pp.3389-3604.

[Jong92] Jongen, T., 1992. Simulation and Modeling of Turbulent Incompressible Flows, PhD thesis, EPF Lausanne, Lausanne, Switzerland.

[Kade81] Kader, B., 1981. Temperature and Concentration Proles in Fully Turbulent Boundary Layers, Int. J. Heat Mass Transfer, 24, 9, pp.1541-1544.

[Kast99] Kastner-Klein, P. and Plate, E.J., 1999. Wind-tunnel study of concentration fields in street canyons, Journal of Atmospheric Environment, 33, pp.3973-3979.

[Ketz02] Ketzel, M., Louka, P., Sahm, P., Guilloteau, E., Sini, J.-F. and

Moussiopoulos, N., 2002. Inter-comparison of numerical urban dispersion models – part II: street canyon in Hannover, Germany, Water, Air, and Soil Pollution: Focus 2: pp.603–613.

[Kim03] Kim, J-J. and Baik, J-J., 2003. Effects of inflow turbulence intensity on flow and pollutant dispersion in an urban street canyon, Journal of Wind Engineering and Industrial Aerodynamics, 91, pp. 309–329.

[Kim89] Kim, J., and Moin, P., 1989. Transport of passive scalar in a turbulent channel flows, Turbulent Shear Flows, 6 Springer, Berlin, pp.85-96.

[Koel00] Koeltzsch, K., 2000. The height dependence of the turbulen Schmidt number within the boundary layer, Atmospheric Environment 34, pp.1147–1151.

[Kolm41] Kolmogorov, A.N., 1941. The local structure of turbulence in incompressible viscous fluid for very large Reynolds numbers, Proceedings of the USSR Academy of Sciences 30, pp.299–303, (Russian), translated into English and published at the Proceedings of the Royal Society of London, Series A: Mathematical and Physical Sciences 43, 4, pp.9–13.

[Laum75c] Launder, B.E., 1975. On the effects of a gravitational field on the turbulent transport of heat and momentum, J. Fluid Mech. 67, pp. 569-581.

[Laun72] Launder, B. E., and Spalding, D. B., 1972. Lectures in mathematical models of turbulence, Academic Press, London, England.

[Laun74] Launder, B.E., and Spalding, D.B. 1974. The numerical computation of turbulent flows, Computer Methods in Applied Mechanics and Engineering, 3, pp.269-289.

[Laun75] Launder, B. E., Reece, G. J., and Rodi, W. 1975. Progress in the development of a Reynolds-stress turbulence closure, J. Fluid Mech., 68, 3, pp.537-566.

[Laun75b] Launder, B.E., 1975. Lecture Series No. 76, Von Karman Inst., Rhode St. Genese, Belgium.

[Laun78] Launder, B.E., 1978. Heat and Mass Transport, Bradshaw P. Topics in Applied Physics. 12. Springer-Verlag. 1978.

[Laun88] Launder, B. E. 1988. On the computation of convective heat transfer in complex turbulent flows, Journal of Heat Transfer. 110. pp. 1112–1118.

[Laun89] Launder, B.E., 1989. Second-moment closure: present and future?, Inter. J. Heat Fluid Flow, 10, 4, pp.282-300.

[Leit02] Leitl, B., Schatzmann, M., Thielen, H., and Martens, R., 2002. A new validation data set for pollutant dispersion models, in proceedings from the 8th International Conference on Harmonisation within Atmospheric Dispersion Modelling for Regulatory Purposes, Sofia.

[Leit97] Leitl, B.M., and Meroney, R.N., 1997. Car exhaust dispersion in a street canyon. Numerical critique of a wind tunnel experiment, J. Wind Ind. Aerodyn. 67–68, pp.293–304.

[Lien06] Lien, F.S., Yee, E., Ji, H., Keats, A. and Hsieh, K.J., 2006. Progress and challenges in the development of physically based numerical models for prediction of flow and contaminant dispersion in the urban environment, International Journal of Computational Fluid Dynamics, 20, pp. 323–337.

[Ligr86] Ligrani, P.M., and Moffat, R.J., 1986. Structure of transitionally rough and fully rough turbulent boundary layers, J. Fluid Mech. 162, pp.69-98.

[Lill84] Lilley, D.G., and Abujelala, M.T., 1984. Limitations and empirical extensions of the k-epsilon model as applied to turbulent confined swirling flows, American Institute of Aeronautics and Astronautics, Aerospace

Sciences Meeting, Reno, NV, USA.

[Liu02] Liu, Ch.-H., and Barth, M., 2002. Large-Eddy Simulation of Flow and Scalar Transport in a Modelled Street Canyon, American Meteorological Society. 41, pp.660-673.

[Louk01] Louka, P., Ketzel, M., Sahm, P., Guilloteau, E., Moussiopoulos, N., Sini, J.-F., Mestayer, P.G., and Berkowicz, R., 2001. CFD inter-comparison exercise within TRAPOS European research network, 7th International Conference on Environmental Science and Technology, Syros, Greece

[Lueb01] Luebcke, H.M., 2001. Entwicklung expliziter Darstellungen zweiter statistischer Momente zur numerischen Simulation turbulenter Stroemungen. PhD Thesis. T.U. Berlin.

[Ment94] Menter, F.R., 1994. Two-equation eddy-viscosity turbulence models for engineering applications, AIAA Journal, 32, 8, pp.1598-1605.

[Mero96] Meroney, R.N., Pavageau, M., Rafailidis, S., and Schatzmann, M., 1996. Study of line source characteristics for 2-D physical modelling of pollutant dispersion in street canyons, J. Wind Engineering an Industrial Aerodynamics 62, pp.37-56.

[Mero99] Meroney, R., 1999. Perspectives on air pollution aerodynamics, 10th International Wind Engineering Conference, Copenhagen, Denmark.

[Mill06] Milliez, M., 2006. Modelisation micro-meteorologique en milieu urban: dispersion des pollutants et prise en compte des effets radiatifs, PhD thesis, Ecole Nationale Des Ponts Et Chaussees. France.

[Mill07] Milliez, M., and Carissimo, B., 2007. Numerical simulations of pollutant dispersion in an idealized urban area, for different meteorological conditions, Boundary-Layer Meteorology 122, pp.321–342.

[Mill08] Milliez, M.,·Carissimo, B., 2008. Computational Fluid Dynamical Modelling of Concentration Fluctuations in an Idealized Urban Area, Boundary-Layer Meteorology, 127, pp.241–259.

[Mill95] Miller, G., 1995. Environmental science: working with the Earth (5th ed.). California: ITP. ISBN 0-534-21588-2.

[Moni65] Monin, A.S., 1965. On the symmetry properties of turbulence in the surface layer of air, Atmos. Oceanic Phys. 1, 1, pp.45-54.

[Mora96] Moran, M.D., and Pielke, R.A., 1996. Evaluation of mesoscale atmospheric dispersion modelling system with observations from 1980 Great Plains Meso-scale tracer field experiment, Part II: Dispersion simulations. J. Appl. Meteorol., 35, pp.308-329.

[Mosc98] Mosca, S., Graziani, G., Klug, W., Bellasio, R., and Bianconi, R., 1998. A statistical methodology for the evaluation of long-range dispersion models: an application to the ETEX exercise, Atmos. Environ., 24, pp.4307-4324.

[Nappo98] Nappo, C.J., Eckman, R.M., Rao, K.S., Herwehe, J.A., and Gunter, R.L., 1998. Second Order Closure Integrated Puff (SCIPUFF) model verification and evaluation study, NOAA Technical Memorandum ERL ARL-227, Air Resources Laboratory, National Oceanic and Atmospheric Administration, Silver Spring, MD. USA.

[Nasa-url] NASA web site. URL: http://www.nasa.gov

[Nazr06] Nazridoust, K., and Ahmadi, G., 2006. Airflow and pollutant transport in street canyons, J. Wind Engineering and Industrial Aerodynamics, 94, pp.491-522.

[Oke87] Oke, T.R., 1987 Boundary Layer Climates, Routledge, London. ISBN 0-20340721-0, [Oles01] Olesen, H.R., 2001. Ten years of harmonization activities: past, present, and future, 7th International conference on Harmonisation within Atmospheric Dispersion Modelling for Regulatory Purposes, Belgirate, Italy. National Environmental Research Institute, Roskilde, Denmark.

[Oles08] Olesen, H.R., Baklanov, A., Bartzis, J., Barmpas, F., Berkowicz, R., Brzozowski, K., Buccolieri, R., Carissimo, B., Costa, A., Di Sabatino, S., Efthimiou, G., Franke, J., Goricsan, I., Hellsten, A., Ketzel, M., Leitl, B., Nuterman, R., Polreich, E., Santiago, J. and Tavares, R., 2008. The MUST model evaluation exercise: Patterns in model performance, in Proceedings of the 12th International Conference on Harmonization within Atmospheric Dispersion Modelling for Regulatory Purposes, Cavtat, Croatia, pp. 403-408.

[Pasq61] Pasquill, F., 1961. The estimation of the dispersion of windborne material, Meteorol. Mag. 90, 33-49.

[Pasq74] Pasquill, F., 1974. Atmospheric Diffusion, Ellis Horwood Ltd, Chichester, England. ISBN 0-85312 015-3

[Pata80] Patankar, S., 1980. Numerical Heat Transfer and Fluid Flow, Series in computational methods in mechanics and thermal sciences, Hemisphere Publishing Corporation.

[Pava99] Pavageau, M., and Schatzmann, M., 1999. Wind tunnel measurements of concentration fluctuations in an urban street canyon, Atmospheric Environment 33, pp. 3961-3971.

[Pfad08] Pfadler, S., Leipertz, A., and Dinkelacker, F., 2008. Systematic experiments on turbulent premixed Bunsen flames including turbulent flux measurements, Combustion and Flame 152, pp.616–631.

[Pope00] Pope, S., 2000. Turbulent Flows, Cambridge University Press, United Kingdom.

[Pran04] Prandtl, L., 1904. “Motion of Fluids with Very Little Viscosity”, English translation of “Über Flüssigkeitsbewegug bei sehr kleiner Reibung”, Third International Congress of Mathematicians at Heidelberg, 1904, from “Vier Abhandlungen zur Hydrodynamik und Aerodynamik”, pp. 1-8, Göttingen, 1927, NACA TM-452, 1928.

[Reyn75] Reynolds, A.J., 1975. The prediction of turbulent Prandtl and Schmidt numbers, International Journal of Heat Mass Transfer 18, pp.1055–1069.

[Rhie83] Rhie, C.M. and Chow, W.L., 1983. Numerical study of the turbulent flow past an airfoil with trailing edge separation, AIAA Journal, 21, 11, pp.1525-1532.

[Rich93] Richards, P.J., Hoxey, R.P., 1993. Appropriate boundary conditions for computational wind engineering models using the k-ε turbulence model, J. Wind Eng. Ind. Aerodyn. 46&47, pp.145-153.

[Ridd04] Riddle, A., Carruthers, D., Sharpe, A., McHugh, C., and Stocker, J., 2004. Comparisons between FLUENT and ADMS for atmospheric dispersion modelling, Atmospheric Environment, 38, pp. 1029–1038.

[Roac94] Roache, P.J., 1994. Perspective: a method for uniform reporting of grid refinement studies, J. Fluids Eng., 116, pp.405-413.

[Roge89] Rogers, M., Mansour, N., Reynolds, W., 1989. An algebraic model for the turbulent flux of a passive scalar, J. Fluid Mechanics, 203. pp.77-101.

[Ross09a] Rossi, R., Philips, D.A., and Iaccarino, G., 2009. Numerical simulation of scalar dispersion in separated flows using algebraic flux models, in Proceedings of the 6th Symposium on Turbulence, Heat and Mass, Rome, Italy.

[Ross09b] Rossi, R., and G., Iaccarino, 2009. Numerical simulation of scalar dispersion downstream of a square obstacle using gradient-transport type models, Atmospheric Environment, 43, pp.2518–2531.

[Ross10a] Rossi, R., Philips, D.A., and Iaccarino, G., 2010. A numerical study of scalar dispersion downstream of a wall-mounted cube using direct simulations and algebraic flux models, International Journal of Heat and Fluid Flow 31, pp.805–819.

[Ross10b] Rossi, R., 2010. A numerical study of algebraic flux models for heat and mass transport simulation in complex flows, International Journal of Heat and Mass Transfer 53, pp.4511–4524.

[Rott51] Rotta, J., 1951. Statistische Theorie nichthomogener Turbulenz, Mitteilung. Zeitschrift für Physik, 129, pp.547-572.

[Roy05] Roy, C.J., 2005. Review of code and solution verification procedures for computational simulation, J. Comp. Phys., 205, pp.131-156.

[Rubi91] Rubinstein, R., and Barton, J.M., 1991. Renormalization Group Analysis of Anisotropic Diffusion in Turbulent Shear Flows, Phys. Fluids A, 3, pp.415–421.

[Sahm02] Sahm, P., Louka, P., Ketzel, M., Guilloteau, E. and Sini, J.-F., 2002. Intercomparison of Numerical Urban Dispersion Models – Part I: Street Canyon and Single Building Configurations, Water, Air and Soil Pollution: Focus 2, pp.587-601.

[Salo07] Saloranta, J., and Hellsten, A., 2007. Evaluation of general CFD-solver for a micro-scale urban flow, in Proceedings of the 11th International Conference on Harmonization within Atmospheric Dispersion Modelling for Regulatory Purposes Cambridge, United Kingdom.

[Sant07] Santiago, J.L., Dejoan, A., Martilli, A., Martín, F., and Pinelli, A., 2007. LES and RANS simulations of the MUST experiments, Study of incident wind direction effects on the flow and plume dispersion, 7th International Conference on Urban Climate, June 29-July 3, Yokohama, Japan.

[Scha10] Schatzmann, M., Olesen, H. and Franke, J. (eds.), 2010. COST 732 model evaluation case studies: approach and results, COST Office, Brussels.

[Scir96] Scire, J.S., Strimaitis, D.G., and Fernau, M.E., 1996. New developments in the CALPUFF non-steady state modelling system, Air pollution modelling and its application. Edited by S-E Gryding and F. Schiermeier, Plenum Press, New York. ISBN 0-306-45381-9. 709.

[Shab97] Shabany, Y., Durbin, P.A., 1997. Explicit Algebraic Scalar Flux Approximation, AIAA Journal, 35, 6. pp. 985-989.

[Shih95] Shih, T.-H., Liou, W.W., Shabbir, A., Yang, Z., and Zhu, J., 1995. A new k-ε eddy-viscosity model for high reynolds number turbulent flows – model development and validation. Computers Fluids, 24, 3, pp.227-238,

[Sini96] Sini, J.-F., Anquetin, S., and Mestayer, P.G., 1996. Pollutant dispersion and thermal effects in urban street canyons, Atmospheric Environment 30, 15, pp. 2659 2677.

[Smag70] Smagorinsky, J., 1970. Numerical simulation of the global atmosphere, in The Global Circulation of the Atmosphere, G. A. Corby, Editor, London, UK, Royal Meteorological Society, 24-41.

[Spal94] Spalart, P.R., 1994. Allmaras S.R.: A one-equation turbulence model for aerodynamic flows. Recherche Aerospatiale 1, pp.5-21.

[Stul88] Stull, R., 1988. An Introduction to Boundary Layer Meteorology, Springer.

[Sutt32] Sutton, O.G., 1932. A Theory of Eddy Diffusion in the Atmosphere, in Proceedings of the Royal Society of London. Series A, 135, 826, pp. 143-165.

[Tang06] Tang, W., Huber, A., Bell, B., and Schwarz, W., 2006. Application of CFD simulations for short-range atmospheric dispersion over open fields and within arrays of buildings, in AMS 14th Joint Conference on the Applications of Air Pollution Meteorology with the A&WMA, Atlanta, USA.

[Tomi07] Tominaga, Y., Stathopoulos, T., 2007. Turbulent Schmidt numbers for CFD analysis with various flow fields. Atmospheric Environment, 41, 37, pp.8091-8099.

[Trem93] Tremback, C.J., Lyons, W.A., Thorson, W.P., and Walko, R.L., 1993. An emergency response and local weather forecasting software system, in Proceedings of the 20th ITM on air Pollution and its Application, Valencia, Spain, pp.423-429.

[Turn94] Turner, D.B., 1994. Workbook of Atmospheric Dispersion Estimates: An Introduction to Dispersion Modelling, (2nd Edition ed.), CRC Press, ISBN 1-56670-023-X.

[Urba08] Urban, J., Warner, S., Platt, N., and Heagy, F., 2008. Evaluation of atmospheric transport and dispersion models using data from the joint Urban 2003 filed experiment, in Proceedings of the 12th International Conference on Harmonization within Atmospheric Dispersion Modelling for Regulatory Purposes, Cavtat, Croatia, pp. 19-23.

[US-EPA] United States Environmental Protection Agency (USEPA), URL: www.epa.gov/

[VDI05] VDI, 2005. Environmental meteorology – Prognostic microscale windfield models – Evaluation for flow around buildings and obstacles, VDI guideline 3783, Part 9, VDI, Düsseldorf, Germany.

[Vers07] Versteeg, H.K., and Malalasekera, W., 2007. An introduction to computational Fluid Dynamics, The Finite Volume Method, Second Edition, Pearson Prentice Hall.

[Walt02] Walton, A., and Cheng, A.Y.S., 2002. Large-Eddy Simulation of Pollution Dispersion in Urban Street Canyon. – Part II. Idealized Canyon Simulation, Atmospheric Environment 36, pp.3615-3627.

[Wang06] Wang, X., and McNamara, K.F. 2006. Evaluation of CFD simulation using RANS turbulence models for building effects on pollutant dispersion, Environmental Fluid Mechanics, 6, pp. 181–202.

[Wang09] Wanga, B.-Ch., Yee, E., Lien, F.-S., 2009. Numerical study of dispersing pollutant clouds in a built-up environment. International Journal of Heat and Fluid Flow 30, pp.3–19.

[Warn06] Warner, S., Platt, N., Heagy, J.F., Jordan, J.E., and Bieberbach, G., 2006. Comparisons of Transport and Dispersion Model Predictions of the Mock Urban Setting Test Field Experiment, Journal of Applied Meteorology and Climatology, 45, 10, pp.1414-1428.

[West02] Westbury, P., 2002. CFD application on the evaluation of pedestrian-level winds, in Proceedings of the Workshop Impact of Wind and Storm on City life and Built Environment, Nantes, France, pp. 172-181.

[Whit71] White, F., and Christoph, G., 1971. A Simple New Analysis of Compressible Turbulent Skin Friction Under Arbitrary Conditions, technical report AFFDL-TR-70-133.

[Wik-ADM] http://en.wikipedia.org/wiki/Atmospheric_dispersion_modeling

[Wiks00] Wikström, P.M., Wallin, S., and Johansson, A.V., 2000. Derivation and investigation of a new explicit algebraic model for the passive scalar flux, Phys. Fluids 12, pp.688-702.

[Wiks98] Wikstrom, P., Hallbäck, M., and Johansson, A., 1998. Measurements and heat-flux transport modelling in a heated cylinder wake. Int. Journal of Heat and Fluid Flow. 19, pp.556-562.

[Wilc98] Wilcox, D.C., 1998. Turbulence Modelling for CFD, DCW Industries, Inc., La Canada, California, USA.

[Wils01] Wilson, J., Flesch, T., and Harper, L., 2001. Micro-meteorological methods for estimating surface exchange with a disturbed windflow, Agricultural and Forest Meteorology, 107, pp. 207–225.

[Wolf69] Wolfstein, M., 1969. The velocity and temperature distribution of one-dimensional flow with turbulence augmentation and pressure gradient. Int. J. Heat Mass Transfer, 12, pp.301-318.

[Wood89] Wood, C., 1989. Planning Pollution Prevention, Heinemann Newnes, Oxford – UK. ISBN: 0434922749.

[Wyng71] Wyngaard, J.C., Coté, O.R., and Izumi, Y., 1971. Local free convection, similarity and the budgets of shear stress and heat flux, J. Atmos. Sci. 28, pp.1171-1182.

[Wyng74] Wyngaard, J.C., and Coté, O.R., 1974. The evolution of a convective planetary boundary layer — A higher-order-closure model study, Boundary-Layer Meteorology. 7, 3, pp.289-308.

[Xi06] Xi, X., Liu, Ch., Leung, D., and Lam, K.M., 2006. Recent progress in CFD modelling of wind field and pollutant transport in street canyons, Atmospheric Environment, 40, pp.5640-5658.

[Xian06] Xian-Xiang, L., Liub, Ch.-H., Leunga, D.Y.C., and Lam, K.M., 2006. Recent progress in CFD modelling of wind field and pollutant transport in street canyons, Atmospheric Environment 40, pp.5640–5658.

[Yakh86] Yakhot, V., and S.A., Orszag, 1986. Renormalization group analysis of turbulence I. Basic theory, Journal of Scientific Computing, 1, 1, pp.1-51.

[Yass08] Yassin, M.F., Kellnerová, R., and Jaňour, Z., 2008. Impact of street intersections on air quality in an urban environment, Atmospheric Environment, 42, pp. 4948–4963.

[Yee04] Yee, E., and Biltoft, C.A., 2004. Concentration fluctuation measurements in a plume dispersing through a regular array of obstacles, Boundary-Layer Meteorol 111, pp.363–415.

[Yee06] Yee, E., Gailis, R.M., Hill, A., Hilderman, T., and Kiel, D., 2006. Comparison of wind-tunnel and water channel simulations of plume dispersion through a large array of obstacles with a scaled field experiment, Boundary-Layer Meteorology 121, pp.389–432.

[Youn05] Younis, B., Speziale, Ch., Clark, T., 2005. A rational model for the turbulent scalar fluxes, Proceedings of the Royal Society A 461, pp.575-594.

[Youn07] Younis, B., Weigang, B., Spring, S., 2007. An explicit algebraic model for turbulent heat transfer in wall bounded flow with streamline curvature, Journal Heat transfer, 129, pp.425-433.

Appendix A. Additional Model Description

A.1 Second Moment Model from Hanjalic-Jakirlic [Hanj02]

$$\frac{D\overline{u_i\phi}}{Dt} = -\overline{u_i u_k}\,\frac{\partial\phi}{\partial x_k} - \overline{u_k\phi}\,\frac{\partial\bar{u}_i}{\partial x_k} - C_{0\phi}\varepsilon\,\frac{\overline{u_i\phi}}{k} + C_{1\phi'}\overline{u_k\phi}\,\frac{\partial\bar{u}_i}{\partial x_k} + C_{4\phi}\,\frac{\partial}{\partial x_k}\left[\overline{u_i u_k}\,\frac{k}{\varepsilon}\,\frac{\partial\overline{u_i\phi}}{\partial x_l}\right]$$

$$\frac{D\overline{\phi^2}}{Dt} = -2\overline{u_k\phi}\,\frac{\partial\phi}{\partial x_k} - \frac{1}{2R}\,\frac{\overline{\phi^2}}{2k}\,\varepsilon + C_{\phi\phi}\,\frac{\partial}{\partial x_j}\left(\overline{u_i u_k}\,\frac{k}{\varepsilon}\,\frac{\partial\overline{\phi^2}}{\partial x_i}\right)$$

where:

$C_{\phi 0} = 0{,}35$ $C_{\phi 1'} = 0{,}55$ $C_{\phi 4} = 0{,}15$ $C_{\phi\phi} = 0{,}2$ R=0,5

A.2 Second Moment Model from Durbin [Durb93]

$$\frac{D\overline{u_i\phi}}{Dt} = -\overline{u_i u_k}\,\frac{\partial\phi}{\partial x_k} - \overline{u_k\phi}\,\frac{\partial\bar{u}_i}{\partial x_k} - C_{1\phi}\varepsilon\,\frac{\overline{u_i\phi}}{k} - C_{2\phi}\overline{u_k\phi}\,\frac{\partial\bar{u}_i}{\partial x_k} + C_c\,\frac{\partial}{\partial x_k}\left[\overline{u_i u_k}\,\frac{k}{\varepsilon}\,\frac{\partial\overline{u_i\phi}}{\partial x_l}\right]$$

where:

$C_{\phi 1} = 2{,}5$ $C_{\phi 2} = 0{,}45$ $C_c = 0{,}15$

A.3 Model coefficients and functions of Standard k-ω model

For the computation of the turbulent viscosity

$$\alpha^* = \alpha_\infty^* \left(\frac{\alpha_0^* + \mathrm{Re}_t / R_k}{1 + \mathrm{Re}_t / R_k} \right), \text{ where } \mathrm{Re}_t = \frac{\rho k}{\mu \omega}, \qquad R_k = 6, \qquad \alpha_0^* = \frac{\beta_i}{3} \text{ and } \beta_i = 0.072$$

In the turbulent production, G_ω term, α is calculated by:

$$\alpha = \frac{\alpha_\infty}{\alpha^*} \left(\frac{\alpha_0 + \mathrm{Re}_t / R_\omega}{1 + \mathrm{Re}_t / R_\omega} \right), \text{ where } R_\omega\text{=2.95.}$$

In the turbulent dissipation of k, term Y_k:

$$f_\beta = \begin{cases} 1 & \chi_k \le 0 \\ \dfrac{1 + 680\chi_k^2}{1 + 400\chi_k^2} & \chi > 0 \end{cases} \text{ where } \chi_k \equiv \frac{1}{\omega^3} \frac{\partial k}{\partial x_j} \frac{\partial \omega}{\partial x_j}$$

and

$$\beta^* = \beta_i^* \left[1 + \varsigma^* F(M_t) \right]$$

$$\beta_i^* = \beta_\infty^* \left(\frac{4/15 + (\mathrm{Re}_t / R_\beta)^4}{1 + (\mathrm{Re}_t / R_\beta)^4} \right)$$

$$\varsigma^* = 1.5 \qquad R_\beta = 8 \qquad \beta_\infty^* = 0.09$$

In the dissipation of ω, Y_ω:

$$f_\beta = \frac{1 + 70\chi_\omega}{1 + 80\chi_\omega} \qquad \text{where} \qquad \chi_\omega = \left| \frac{\Omega_{ij}\Omega_{jk}S_{ki}}{(\beta_\infty^* \omega)^3} \right|$$

and

$$\beta = \beta_i \left[1 - \frac{\beta_i^*}{\beta_i} \varsigma^* F(M_t) \right] \qquad \textit{with} \qquad F(M_t) = \begin{cases} 0 & M_t \le M_{t0} \\ M_t^2 - M_{t0}^2 & M_t > M_{t0} \end{cases},$$

Other model constants and functions are:

$$M_t^0 \equiv \frac{2k}{a^2}, \qquad M_{t0} = 0.25, \qquad a = \sqrt{\gamma R T}, \qquad \alpha_\infty^* = 1, \qquad \alpha_\infty = 0.52, \qquad \alpha_0 = \frac{1}{9},$$

$$\beta_\infty^* = 0.09, \qquad \beta_i = 0.072, \qquad R_\beta = 8 \qquad R_k = 6, \qquad R_\omega = 2.95, \qquad \varsigma^* = 1.5,$$

$$\sigma_k = 2.0, \qquad \sigma_\omega = 2.0$$

A.4 Model coefficients and functions of k-ω SST model

The turbulent Prandtl numbers are calculated from:

$$\sigma_k = \frac{1}{F_1/\sigma_{k,1} + (1-F_1)/\sigma_{k,2}} \qquad \text{and} \qquad \sigma_\omega = \frac{1}{F_1/\sigma_{\omega,1} + (1-F_1)/\sigma_{\omega,2}}$$

where

$$F_1 = \tanh\left(\Phi_1^4\right)$$

$$\Phi_1 = \min\left[\max\left(\frac{\sqrt{k}}{0.09\omega y}, \frac{500\mu}{\rho y^2 \omega}\right), \frac{4\rho k}{\sigma_{\omega,2} D_\omega^+ y^2}\right]$$

$$D_\omega^+ = \max\left[2\rho \frac{1}{\sigma_{\omega,2}} \frac{1}{\omega} \frac{\partial k}{\partial x_j} \frac{\partial \omega}{\partial x_j}, 10^{-10}\right]$$

And for the turbulent viscosity (μ_t):

$$F_2 = \tanh\left(\Phi_2^2\right), \qquad \text{with} \qquad \Phi_2 = \max\left[2\frac{\sqrt{k}}{0.09\omega y}, \frac{500\mu}{\rho y^2 \omega}\right]$$

where y is the distance to the next surface and D_ω^+ is the positive portion of the cross-diffusion term D_ω presented in Table 3-5.

In the turbulent production of ω (term G_ω), α_∞ is calculated from:

$$\alpha_\infty = F_1 \alpha_{\infty,1} + (1-F_1)\alpha_{\infty,2}$$

where

$$\alpha_{\infty,1} = \frac{\beta_{i,1}}{\beta_\infty^*} - \frac{\kappa^2}{\sigma_{\omega,1}\sqrt{\beta_\infty^*}}, \qquad \alpha_{\infty,2} = \frac{\beta_{i,2}}{\beta_\infty^*} - \frac{\kappa^2}{\sigma_{\omega,2}\sqrt{\beta_\infty^*}} \qquad \text{and} \qquad \kappa = 0.41$$

In the dissipation of k (term Y_k), f_i=1.

In the dissipation of ω (term Y_ω), f_β=1 and $\beta=\beta_i=F_1\beta_{i,1}+(1-F_1)\beta_{i,2}$.

Other constants are $\sigma_{k,1}$=1.176, $\sigma_{w,1}$=2.0, $\sigma_{k,2}$=1.0, $\sigma_{w,2}$=1.168, α_1=0.31, $\beta_{i,1}$=0.075, $\beta_{i,2}$=0.0828. All additional model constants and functions $\left(\alpha_\infty^*, \alpha_\infty, \alpha_0, \beta^*, \beta_\infty^+, R_\beta, R_k, R_\omega, \varsigma^* \text{ and } \mathrm{M}_{t0})\right)$ have the same values as for the standard k-ω model.

Appendix B. Additional Figures from the Simulation of the 2D Street Canyon

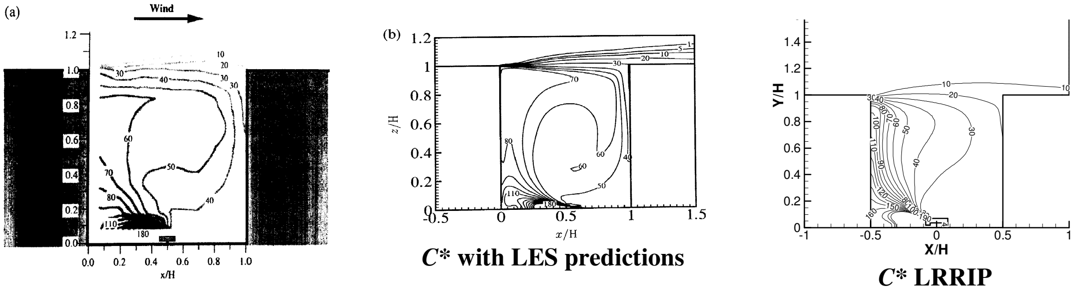

*C** Measurements [Pava99]

*C** with LES predictions from [Liu02]

*C** LRRIP

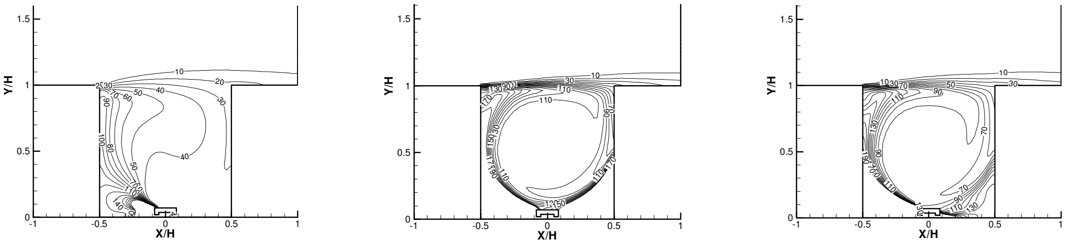

*C** RKE

*C** SKW

*C** SST

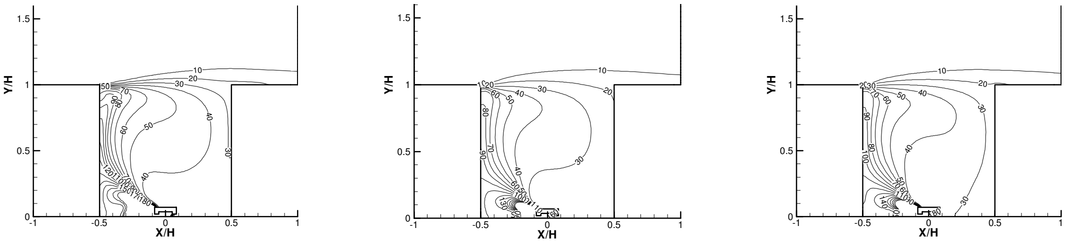

*C** SA

*C** SKE

*C** RNG

Figure B- 1. - Prediction of *C dispersion using different turbulence model for Reynolds stresses and SED1 for scalar fluxes. Experiments from [Pava99].**

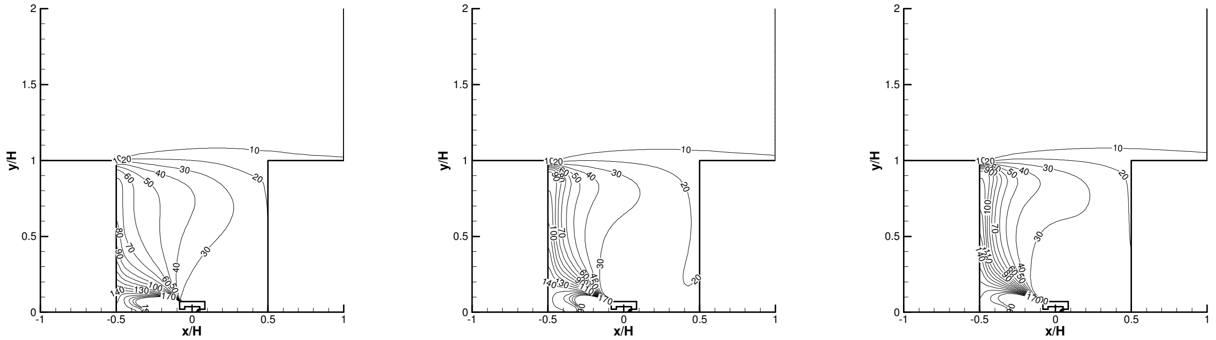

C* Model GGDH

C* Model SED1

C* Model SED2

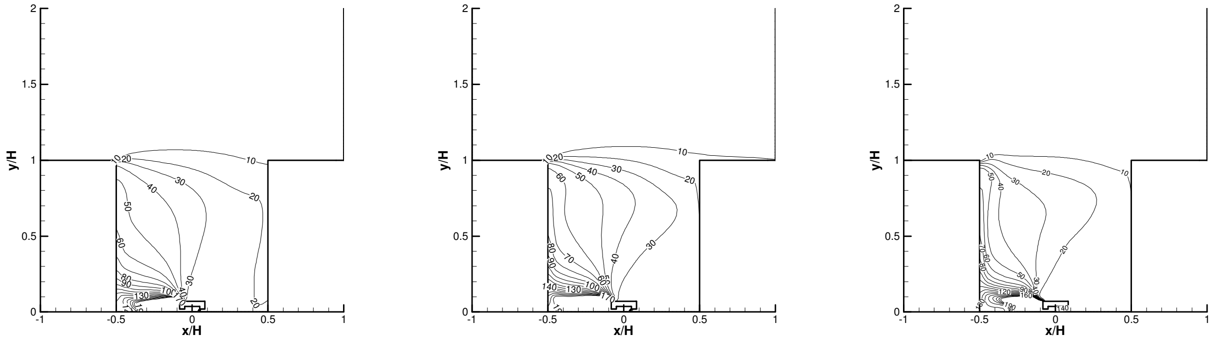

C* Model ABE

C* Model ABE-SUGA

C* Model WET

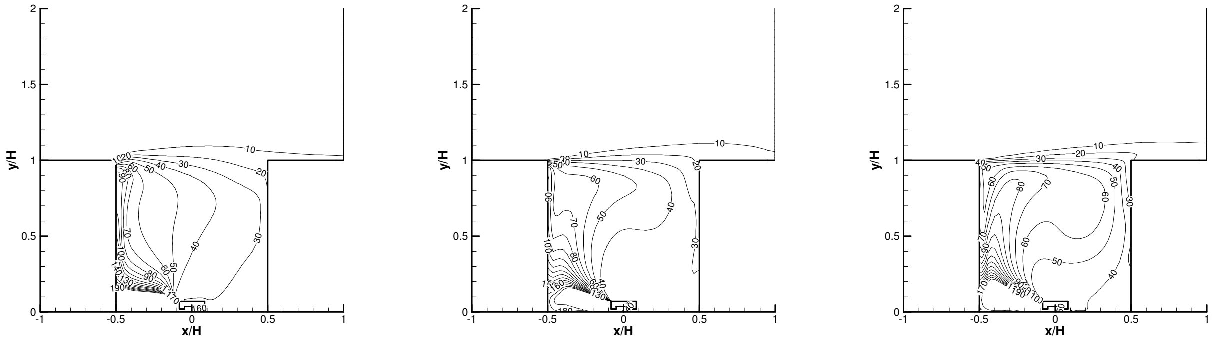

C* Model YOUNIS

C* S-M HANJALIC

C* S-M DURBIN

Figure B- 2.- Contour plot of normalized concentration *C for all implemented scalar flux models.**

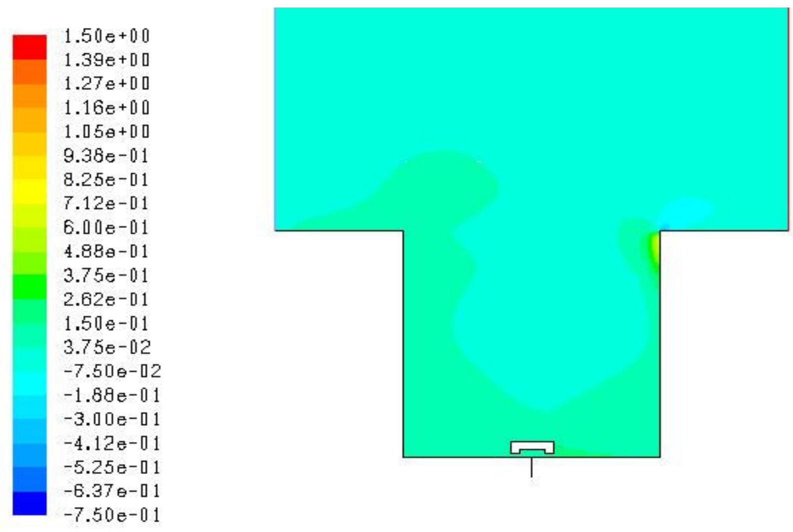

Figure B- 3.- Contour plot of pressure variation in the street canyon [Pa]. Predictions obtained using middle grid with LRR-IP and SED turbulence models.

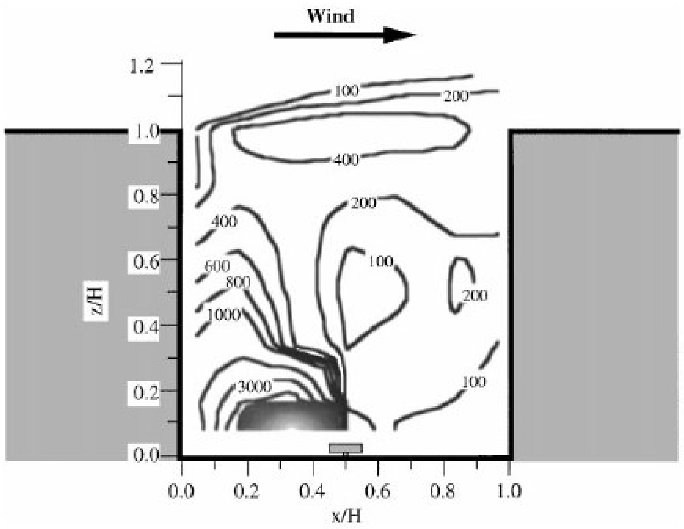

Figure B- 4. - Spatial Distribution of the concentration variance in the street canyon [Pava99].

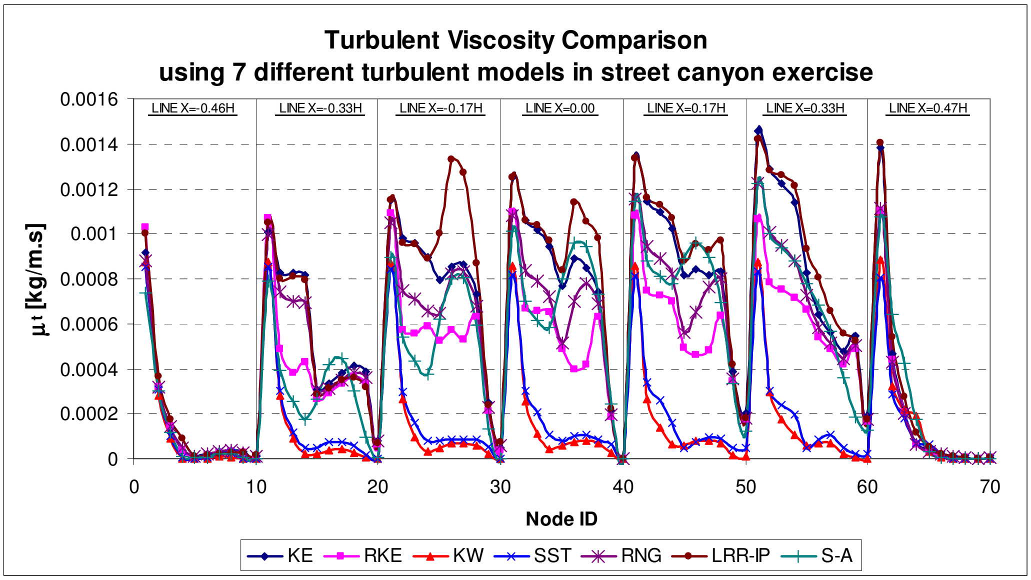

Figure B- 5.- Comparison of turbulent viscosity predictions (μ_t) using seven turbulence models for Reynolds stresses in the street canyon test case (see Figure 7-2-b). There are 10 nodes per line (7 lines=70 nodes) and they are plotted within each line in ascendant direction, i.e. from left (bottom of the canyon, y=0) to right (top of canyon, y=H).

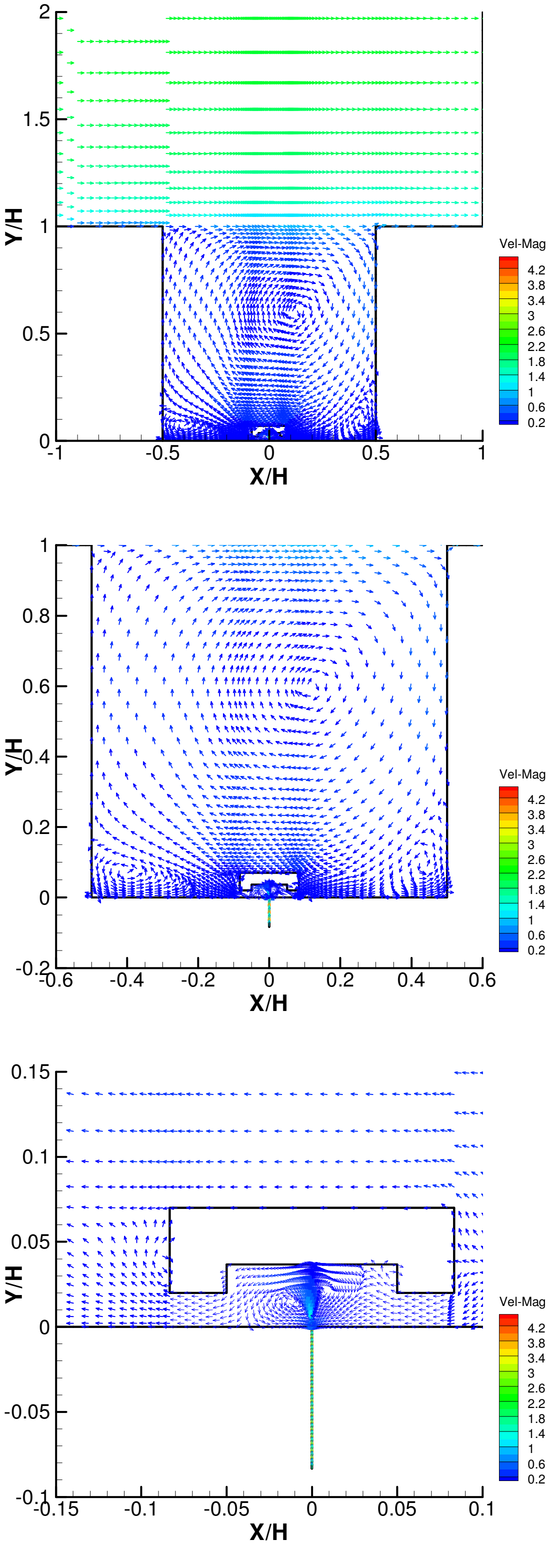

Figure B- 6.- Velocity vector predictions obtained using middle grid and LRRIP turbulence model. Vectors are colored by velocity magnitude [m/s]

Appendix C. Additional Figures from the Simulations of the MUST Experiment

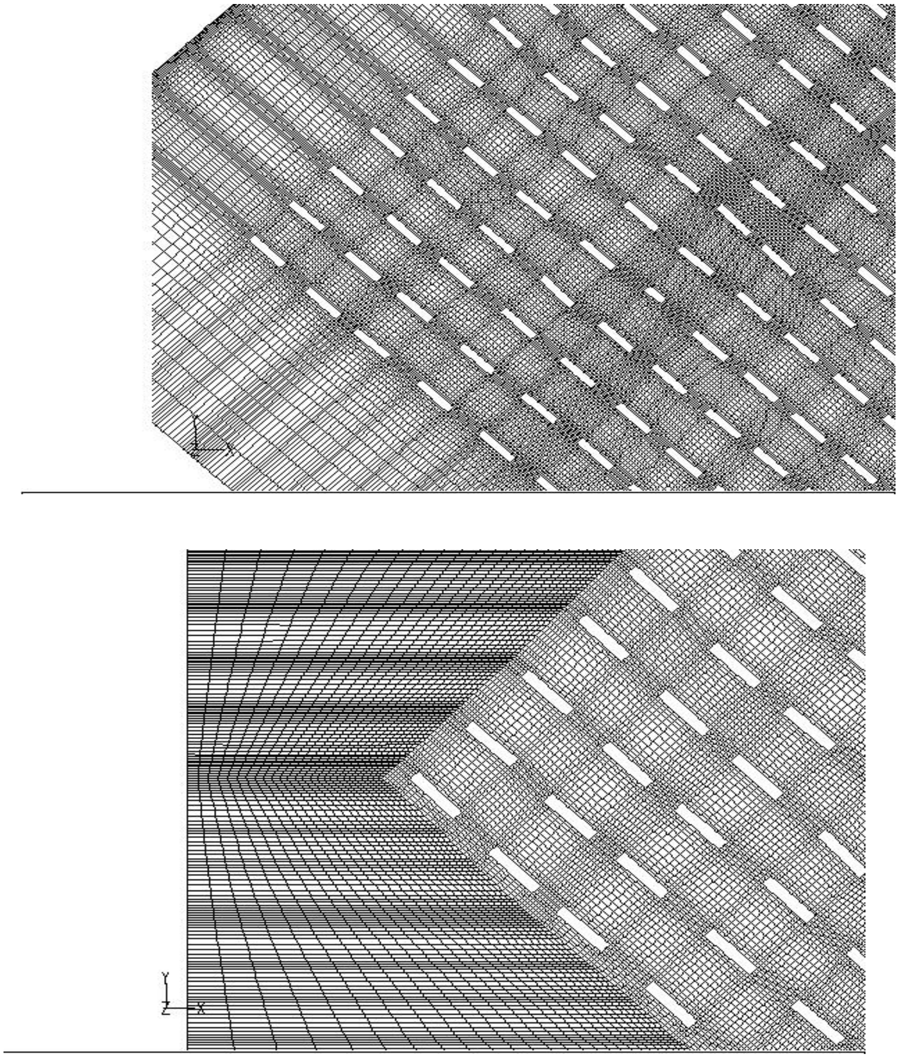

Figure C- 1. Detail of middle size grid of ROTDOM (a) and STDDOM(b).

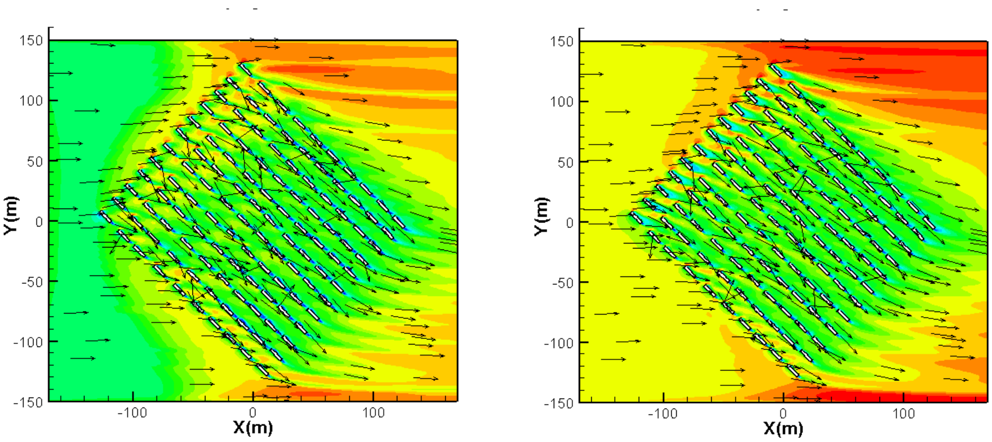

Plane Z=H/14 (≈0.18m) **Plane Z=H/2 (1.27m)**

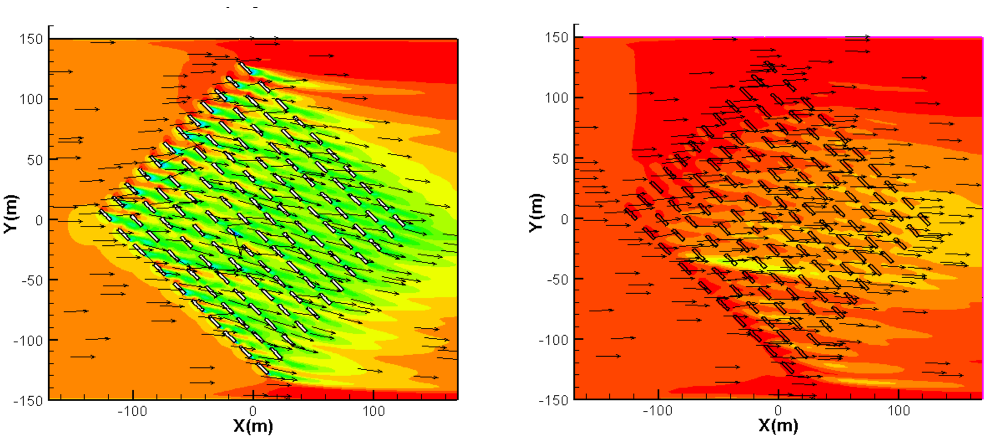

Plane Z=H (2.54m) **Plane Z=2H (5.08m)**

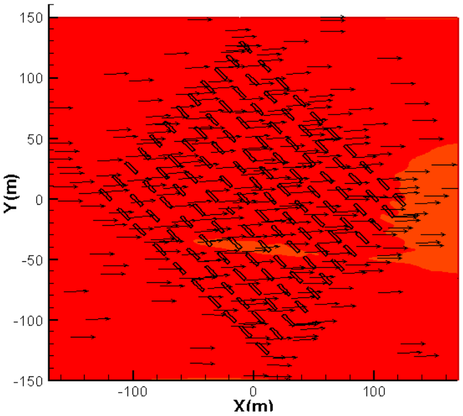

Plane Z=3H (7.62m)

Figure C- 2. Contour plots of velocity magnitude at different heights and vectors showing the flow direction of MUST test case. Results from computational domain STDDOM using LRRIP turbulence model.

Table C- 1.- Grid analysis by Richardson extrapolation for MUST flow field at z=1.275 m (considering only coarse-uv plane and using LRRIP model for Reynolds stresses).

Model	*Monotonic convergence*	*Oscillatory convergence*	*Divergence*	*<R> (E-01)*	*<p>*	*$U_{1\text{-}max}$ (E-01)*	*$<U_1>$ (E-02)*
U	35.58%	18.73%	45.69%	4.45	4.84	3.84	5.92
V	36.33%	19.48%	44.19%	4.86	4.29	5.25	7.62
w	38.20%	14.23%	47.57%	4.94	4.12	2.74	5.00
u_{rms}	30.34%	17.98%	51.69%	4.80	3.74	0.216	0.515
v_{rms}	32.58%	30.34%	37.08%	4.24	4.94	0.268	0.615
w_{rms}	42.32%	15.73%	41.95%	5.42	3.48	0.239	0.411
Average:	35.89%	19.41%	44.69%				

.

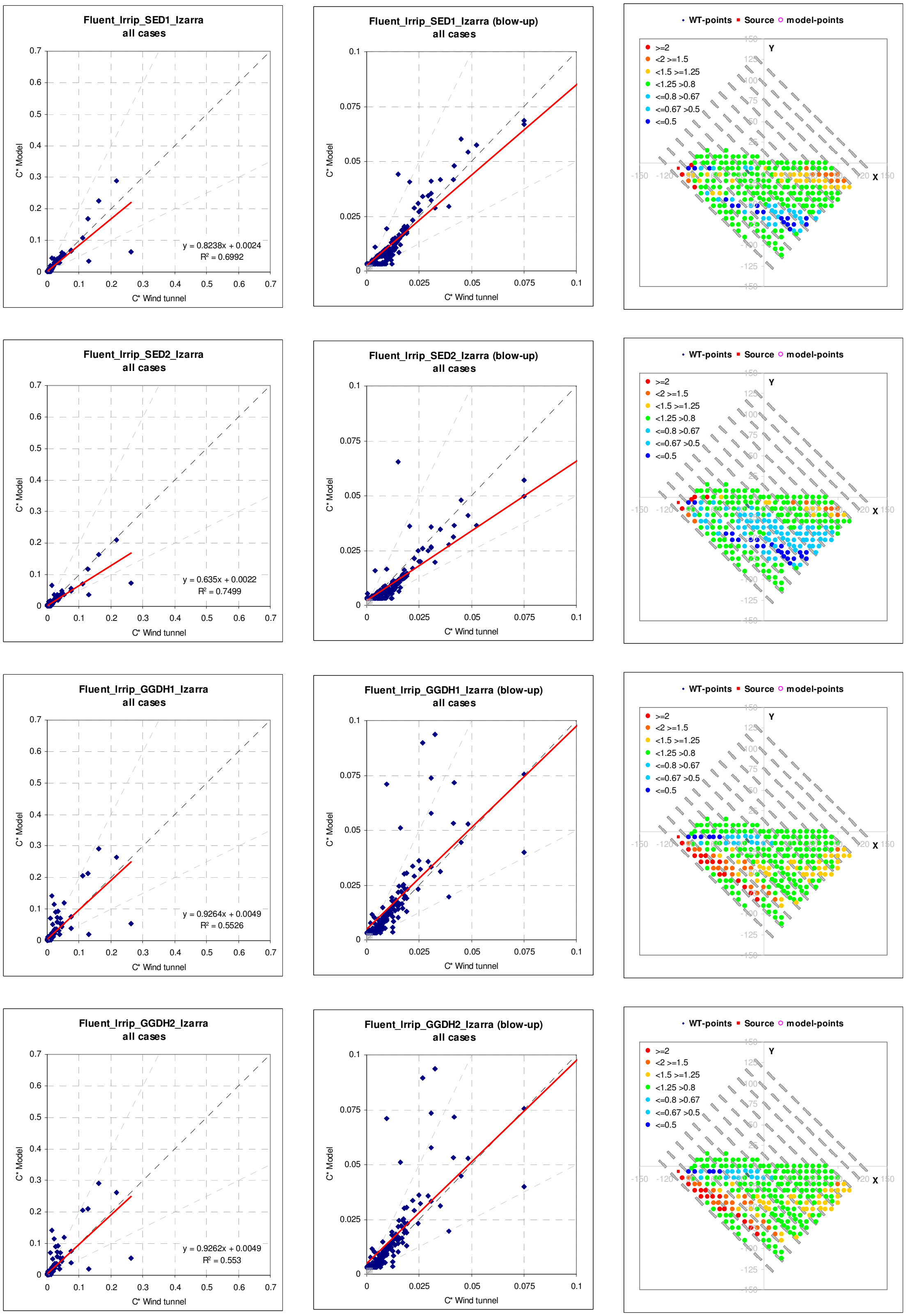

Figure C- 3. Scatter plots (1st and 2nd columns) and FAC2 plot (3rd column) of scalar flux models employed in MUST experiment using the Excel tool from the research group COST Action 732. Part I.

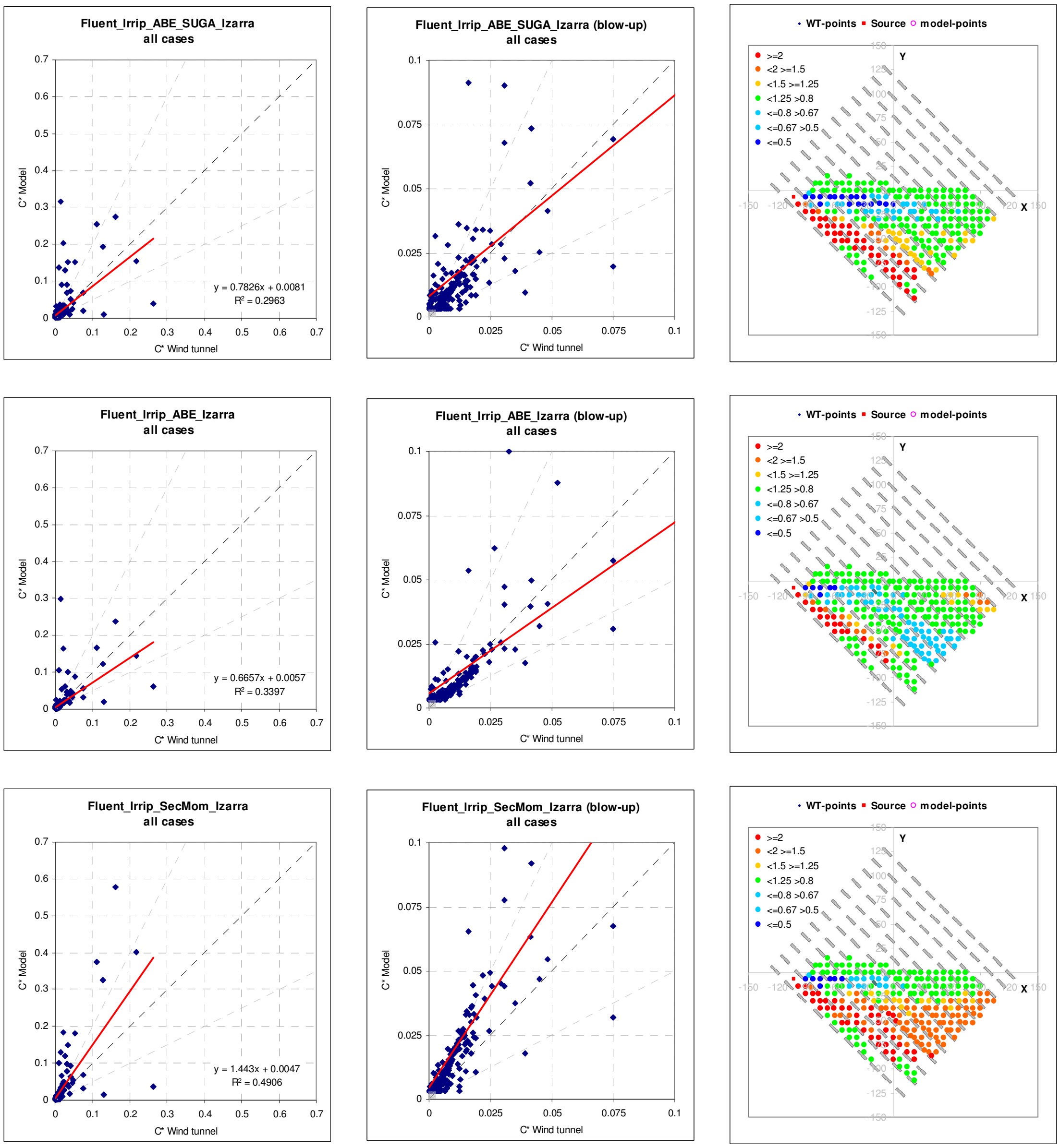

Figure C- 4. Scatter plots (1^{st} and 2^{nd} columns) and FAC2 plot (3^{rd} column) of scalar flux models employed in MUST experiment using the Excel tool from the research group COST Action 732. Part II.

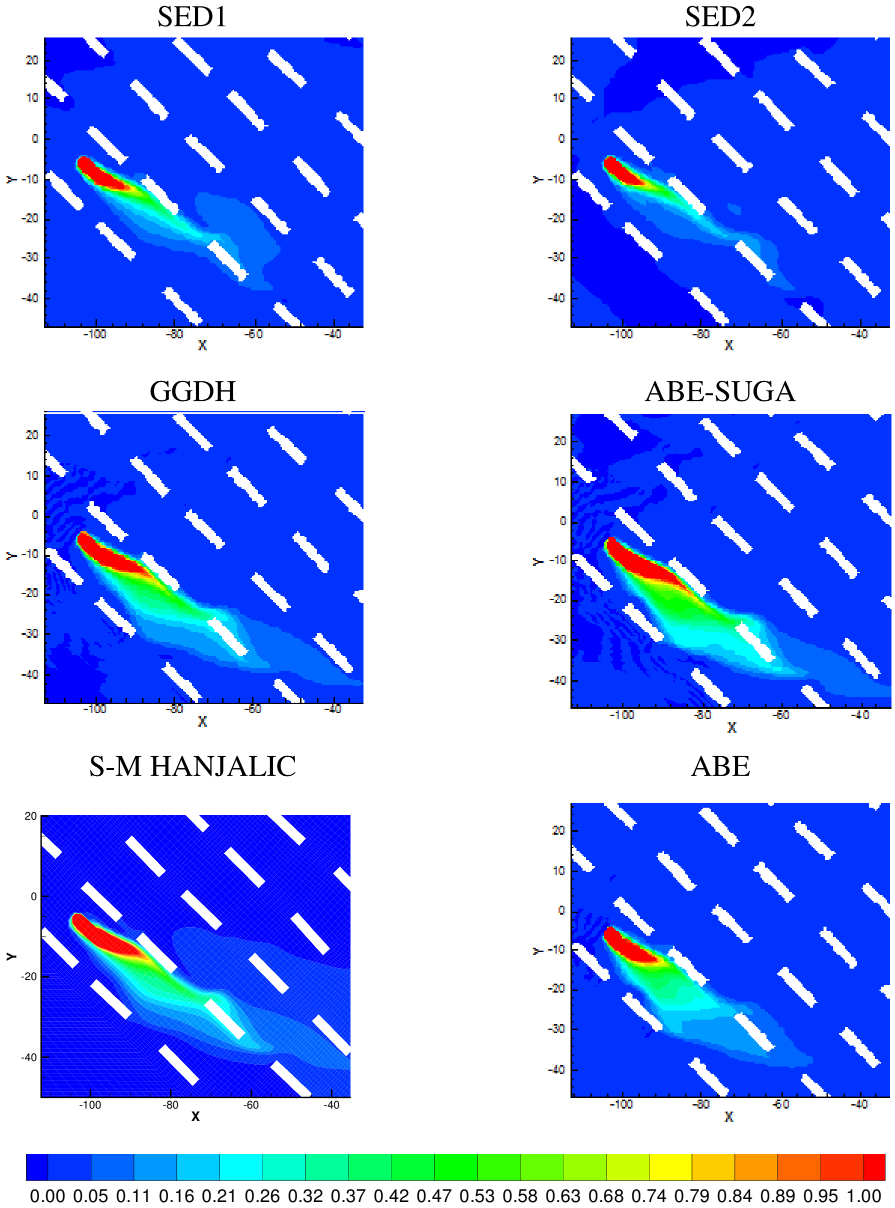
SED1

SED2

GGDH

ABE-SUGA

S-M HANJALIC

ABE

Figure C- 5. Contour plots of normalized concentration *C in MUST case using the STDDOM domain and the LRRIP turbulence model together with several scalar flux models. Plane z=H/14 (1st cell centre above bottom wall).**

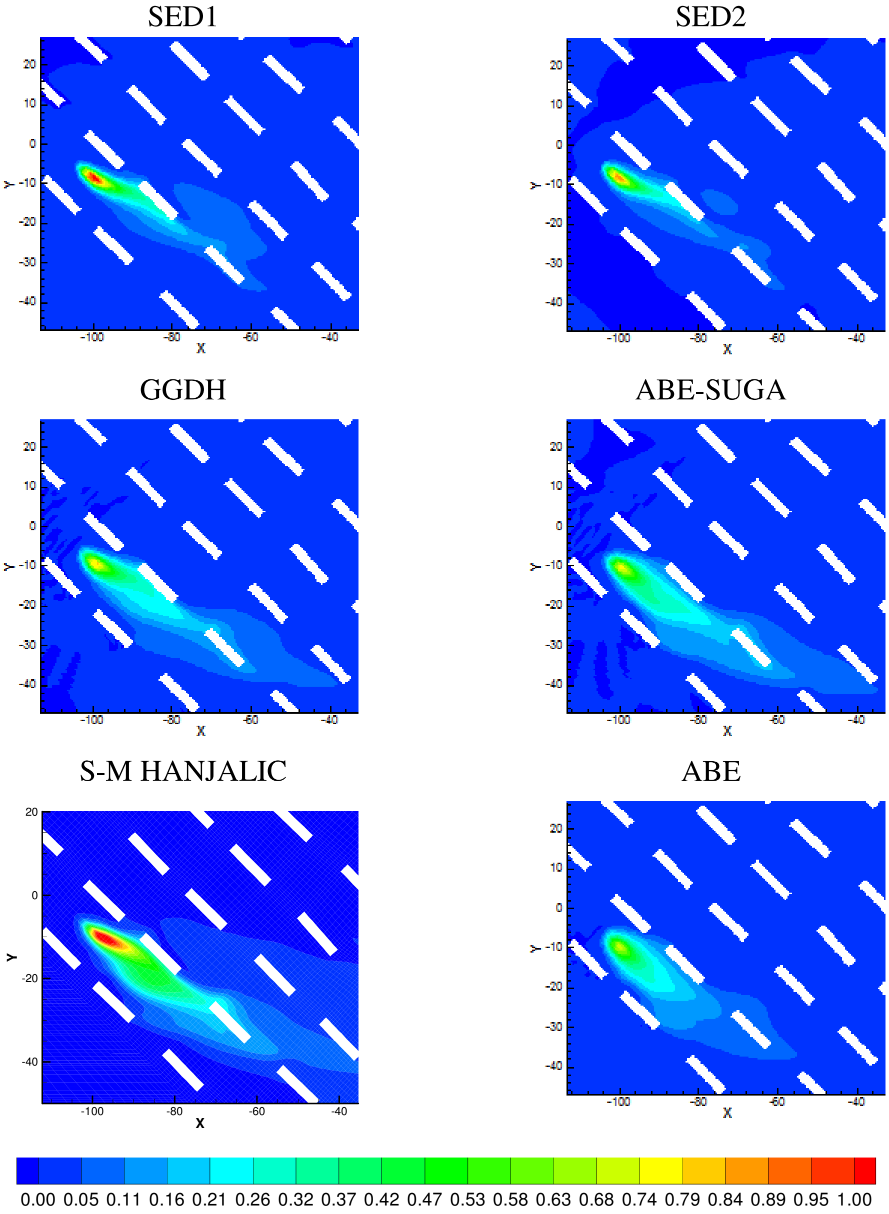

Figure C- 6. Contour plots of normalized concentration *C for LRRIP and several scalar flux models in MUST case. Plane z=H/2. See Figure C- 5 for more details of simulation setup.**

Appendix D. Source Code and Others

D.1 BOOT software output example

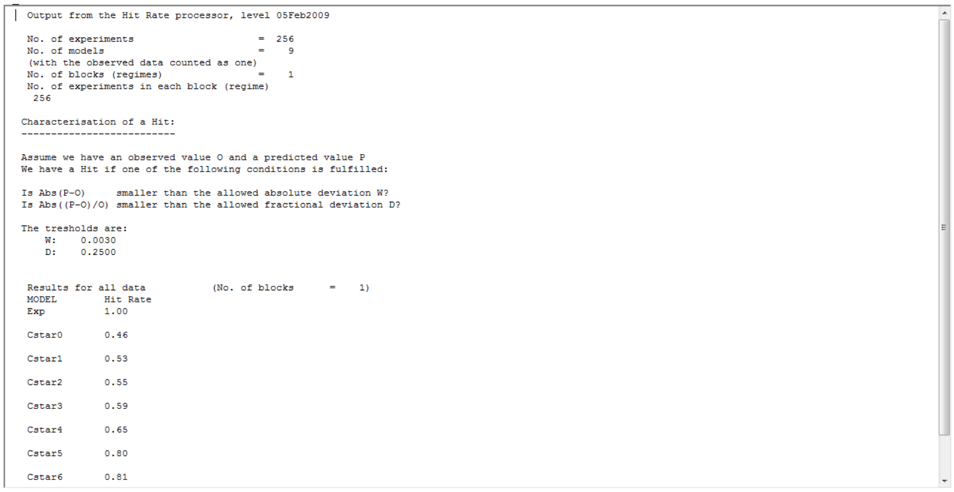

```
 Output from the Hit Rate processor, level 05Feb2009

  No. of experiments                    =  256
  No. of models                         =    9
  (with the observed data counted as one)
  No. of blocks (regimes)               =    1
  No. of experiments in each block (regime)
   256

 Characterisation of a Hit:
 --------------------------

 Assume we have an observed value O and a predicted value P
 We have a Hit if one of the following conditions is fulfilled:

 Is Abs(P-O)     smaller than the allowed absolute deviation W?
 Is Abs((P-O)/O) smaller than the allowed fractional deviation D?

 The tresholds are:
     W:    0.0030
     D:    0.2500


  Results for all data           (No. of blocks      =    1)
  MODEL        Hit Rate
  Exp          1.00

  Cstar0       0.46

  Cstar1       0.53

  Cstar2       0.55

  Cstar3       0.59

  Cstar4       0.65

  Cstar5       0.80

  Cstar6       0.81
```

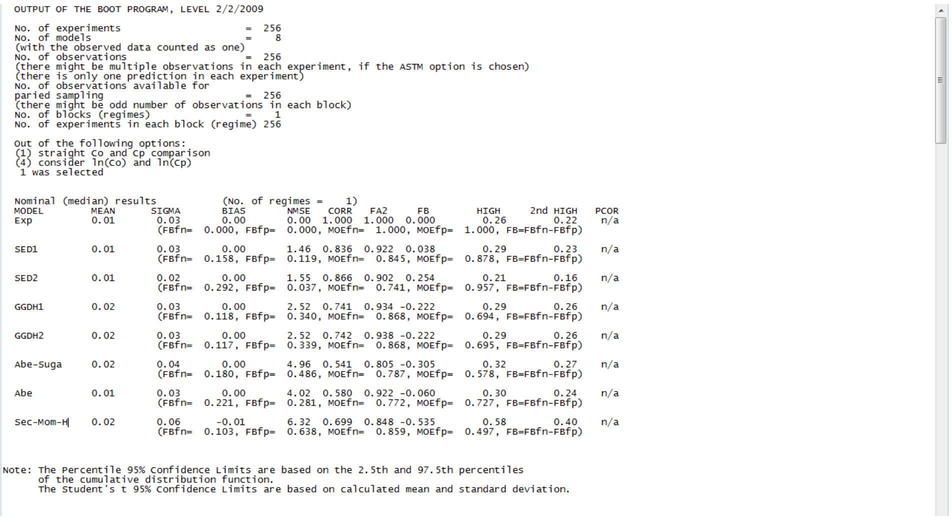

```
OUTPUT OF THE BOOT PROGRAM, LEVEL 2/2/2009

No. of experiments                         =  256
No. of models                              =    8
(with the observed data counted as one)
No. of observations                        =  256
(there might be multiple observations in each experiment, if the ASTM option is chosen)
(there is only one prediction in each experiment)
No. of observations available for
paried sampling                            =  256
(there might be odd number of observations in each block)
No. of blocks (regimes)                    =    1
No. of experiments in each block (regime) 256

Out of the following options:
(1) straight Co and Cp comparison
(4) consider ln(Co) and ln(Cp)
 1 was selected


Nominal (median) results          (No. of regimes =    1)
MODEL        MEAN       SIGMA       BIAS       NMSE   CORR   FA2     FB        HIGH     2nd HIGH   PCOR
Exp          0.01        0.03        0.00       0.00  1.000  1.000  0.000       0.26         0.22    n/a
                        (FBfn=  0.000, FBfp=  0.000, MOEfn=  1.000, MOEfp=  1.000, FB=FBfn-FBfp)

SED1         0.01        0.03        0.00       1.46  0.836  0.922  0.038       0.29         0.23    n/a
                        (FBfn=  0.158, FBfp=  0.119, MOEfn=  0.845, MOEfp=  0.878, FB=FBfn-FBfp)

SED2         0.01        0.02        0.00       1.55  0.866  0.902  0.254       0.21         0.16    n/a
                        (FBfn=  0.292, FBfp=  0.037, MOEfn=  0.741, MOEfp=  0.957, FB=FBfn-FBfp)

GGDH1        0.02        0.03        0.00       2.52  0.741  0.934 -0.222       0.29         0.26    n/a
                        (FBfn=  0.118, FBfp=  0.340, MOEfn=  0.868, MOEfp=  0.694, FB=FBfn-FBfp)

GGDH2        0.02        0.03        0.00       2.52  0.742  0.938 -0.222       0.29         0.26    n/a
                        (FBfn=  0.117, FBfp=  0.339, MOEfn=  0.868, MOEfp=  0.695, FB=FBfn-FBfp)

Abe-Suga     0.02        0.04        0.00       4.96  0.541  0.805 -0.305       0.32         0.27    n/a
                        (FBfn=  0.180, FBfp=  0.486, MOEfn=  0.787, MOEfp=  0.578, FB=FBfn-FBfp)

Abe          0.01        0.03        0.00       4.02  0.580  0.922 -0.060       0.30         0.24    n/a
                        (FBfn=  0.221, FBfp=  0.281, MOEfn=  0.772, MOEfp=  0.727, FB=FBfn-FBfp)

Sec-Mom-H    0.02        0.06       -0.01       6.32  0.699  0.848 -0.535       0.58         0.40    n/a
                        (FBfn=  0.103, FBfp=  0.638, MOEfn=  0.859, MOEfp=  0.497, FB=FBfn-FBfp)


Note: The Percentile 95% Confidence Limits are based on the 2.5th and 97.5th percentiles
      of the cumulative distribution function.
      The Student's t 95% Confidence Limits are based on calculated mean and standard deviation.
```

D.2 Code for three-dimensional algebraic scalar flux models

```
#include "udf.h"
#include "mem.h"

DEFINE_ANISOTROPIC_DIFFUSIVITY(Matrix_SED,c,t,i,dmatrix)
{
real diff,Sc,visc;
Sc=0.7;
visc=C_MU_T(c,t)/Sc;
diff=visc+C_MU_L(c,t);
 dmatrix[0][0] =diff;
 dmatrix[1][1] =diff;
 dmatrix[2][2] =diff;
 dmatrix[1][0] =0.;
 dmatrix[0][1] =0.;
 dmatrix[2][0] =0.;
 dmatrix[0][2] =0.;
 dmatrix[2][1] =0.;
 dmatrix[1][2] =0.;
}

DEFINE_ANISOTROPIC_DIFFUSIVITY(Matrix_SED2,c,t,i,dmatrix)
{
real diff,Sc,visc;
Sc=0.9;
visc=C_MU_T(c,t)/Sc;
diff=visc+C_MU_L(c,t);
 dmatrix[0][0] =diff;
 dmatrix[1][1] =diff;
 dmatrix[2][2] =diff;
 dmatrix[1][0] =0.;
 dmatrix[0][1] =0.;
 dmatrix[2][0] =0.;
 dmatrix[0][2] =0.;
 dmatrix[2][1] =0.;
 dmatrix[1][2] =0.;
}

DEFINE_ANISOTROPIC_DIFFUSIVITY(diff_GGDH,c,t,i,dmatrix)
{
  real con,Tao;
  real uu, vv, uv, vu, uw, wu, vw, wv, ww;
  uu=C_RUU(c,t);
  vv=C_RVV(c,t);
  ww=C_RWW(c,t);
  uv=C_RUV(c,t);
  vu=C_RUV(c,t);
  uw=C_RUW(c,t);
  wu=C_RUW(c,t);
  vw=C_RVW(c,t);
  wv=C_RVW(c,t);
 Tao=MAX(C_K(c,t)/C_D(c,t),6*sqrt(C_MU_L(c,t)/(C_D(c,t)*C_R(c,t))));
  con=0.3*Tao*C_R(c,t);
  dmatrix[0][0] =con*uu+C_MU_L(c,t);
  dmatrix[0][1] =con*vu;
  dmatrix[0][2] =con*uw;
  dmatrix[1][0] =con*uv;
  dmatrix[1][1] =con*vv+C_MU_L(c,t);
  dmatrix[1][2] =con*vw;
  dmatrix[2][0] =con*uw;
```

```
  dmatrix[2][1] =con*vw;
  dmatrix[2][2] =con*ww+C_MU_L(c,t);
}

DEFINE_ANISOTROPIC_DIFFUSIVITY(diff_GGDH2,c,t,i,dmatrix)
{
  real con, fmu, Rek, Ret, Tao;
  real uu, vv, uv, vu, uw, wu, vw, wv, ww;
  uu=C_RUU(c,t);
  vv=C_RVV(c,t);
  ww=C_RWW(c,t);
  uv=C_RUV(c,t);
  vu=C_RUV(c,t);
  uw=C_RUW(c,t);
  wu=C_RUW(c,t);
  vw=C_RVW(c,t);
  wv=C_RVW(c,t);
  Rek=C_R(c,t)*sqrt(C_K(c,t))*C_WALL_DIST(c,t)/C_MU_L(c,t);
  Ret=C_R(c,t)*pow(C_K(c,t),2)/(C_MU_L(c,t)*C_D(c,t));
  fmu=pow((1-exp(-0.0225*Rek)),2)*(1+(41/Ret));
 Tao=MAX(C_K(c,t)/C_D(c,t),6*sqrt(C_MU_L(c,t)/(C_D(c,t)*C_R(c,t))));
  con=0.3*fmu*Tao*C_R(c,t);
  dmatrix[0][0] =con*uu+C_MU_L(c,t);
  dmatrix[0][1] =con*vu;
  dmatrix[0][2] =con*uw;
  dmatrix[1][0] =con*uv;
  dmatrix[1][1] =con*vv+C_MU_L(c,t);
  dmatrix[1][2] =con*vw;
  dmatrix[2][0] =con*uw;
  dmatrix[2][1] =con*vw;
  dmatrix[2][2] =con*ww+C_MU_L(c,t);
}

DEFINE_ANISOTROPIC_DIFFUSIVITY(diff_Abe_Suga,c,t,i,dmatrix)
{
  real con, Tao;
  real uu, vv, uv, vu, uw, wu, vw, wv, ww;
 Tao=MAX(C_K(c,t)/C_D(c,t),6*sqrt(C_MU_L(c,t)/(C_D(c,t)*C_R(c,t))));
  con=0.45*C_R(c,t)*Tao/C_K(c,t);
  uu=C_RUU(c,t);
  vv=C_RVV(c,t);
  ww=C_RWW(c,t);
  uv=C_RUV(c,t);
  vu=C_RUV(c,t);
  uw=C_RUW(c,t);
  wu=C_RUW(c,t);
  vw=C_RVW(c,t);
  wv=C_RVW(c,t);
  dmatrix[0][0] =con*(uu*uu+uv*vu+uw*wu)+C_MU_L(c,t);
  dmatrix[0][1] =con*(uu*uv+uv*vv+uw*wv);
  dmatrix[0][2] =con*(uu*uw+uv*vw+uw*ww);
  dmatrix[1][0] =con*(vu*uu+vv*vu+vw*wu);
  dmatrix[1][1] =con*(vu*uv+vv*vv+vw*wv)+C_MU_L(c,t);
  dmatrix[1][2] =con*(vu*uw+vv*vw+vw*ww);
  dmatrix[2][0] =con*(wu*uu+wv*vu+ww*wu);
  dmatrix[2][1] =con*(wu*uv+wv*vv+ww*wv);
  dmatrix[2][2] =con*(wu*uw+wv*vw+ww*ww)+C_MU_L(c,t);
}

DEFINE_ANISOTROPIC_DIFFUSIVITY(diff_Abe,c,t,i,dmatrix)
{
```

```
  real con1,con2, Tao;
  real uu, vv, uv, vu, uw, wu, vw, wv, ww;
 Tao=MAX(C_K(c,t)/C_D(c,t),6*sqrt(C_MU_L(c,t)/(C_D(c,t)*C_R(c,t))));
  con1=0.22*C_R(c,t)*Tao;
  con2=0.45*C_R(c,t)*Tao/C_K(c,t);
  uu=C_RUU(c,t);
  vv=C_RVV(c,t);
  ww=C_RWW(c,t);
  uv=C_RUV(c,t);
  vu=C_RUV(c,t);
  uw=C_RUW(c,t);
  wu=C_RUW(c,t);
  vw=C_RVW(c,t);
  wv=C_RVW(c,t);
  dmatrix[0][0]
=con1*uu+con2*uu*uu+con2*uv*vu+con2*uw*wu+C_MU_L(c,t);
  dmatrix[0][1] =con1*uv+con2*uu*uv+con2*uv*vv+con2*uw*wv;
  dmatrix[0][2] =con1*uw+con2*uu*uw+con2*uv*vw+con2*uw*ww;
  dmatrix[1][0] =con1*vu+con2*vu*uu+con2*vv*vu+con2*vw*wu;
  dmatrix[1][1]
=con1*vv+con2*vu*uv+con2*vv*vv+con2*vw*wv+C_MU_L(c,t);
  dmatrix[1][2] =con1*vw+con2*vu*uw+con2*vv*vw+con2*vw*ww;
  dmatrix[2][0] =con1*wu+con2*wu*uu+con2*wv*vu+con2*ww*wu;
  dmatrix[2][1] =con1*wv+con2*wu*uv+con2*wv*vv+con2*ww*wv;
  dmatrix[2][2]
=con1*ww+con2*wu*uw+con2*wv*vw+con2*ww*ww+C_MU_L(c,t);
}
```

D.3 Code for three-dimensional second moment scalar flux model of HANJALIC

```
#include "udf.h"
#include "mem.h"

DEFINE_ANISOTROPIC_DIFFUSIVITY(diff_GGDH_Sec_Mom,c,t,i,dmatrix)
{
  real con, Visc, Tao; /* fmu, Rek, Ret;*/
  real uu, vv, ww, uv, uw, vw, vu, wu, wv;
  uu=C_RUU(c,t);
  vv=C_RVV(c,t);
  ww=C_RWW(c,t);
  uv=C_RUV(c,t);
  uw=C_RUW(c,t);
  vw=C_RVW(c,t);
/*  Visc=-1*C_MU_T(c,t)/C_R(c,t);
  uu=Visc*2.*C_DUDX(c,t)+(2./3.)*C_K(c,t);
  vv=Visc*2.*C_DVDY(c,t)+(2./3.)*C_K(c,t);
  ww=Visc*2.*C_DWDZ(c,t)+(2./3.)*C_K(c,t);
  uv=Visc*(C_DUDY(c,t)+ C_DVDX(c,t));
  uw=Visc*(C_DUDZ(c,t)+ C_DWDX(c,t));
  vw=Visc*(C_DVDZ(c,t)+ C_DWDY(c,t));*/
  vu=uv;
  wu=uw;
  wv=vw;
/*  Rek=C_R(c,t)*sqrt(C_K(c,t))*C_WALL_DIST(c,t)/C_MU_L(c,t);
  Ret=C_R(c,t)*pow(C_K(c,t),2)/(C_MU_L(c,t)*C_D(c,t));
  fmu=pow((1-exp(-0.0225*Rek)),2)*(1+(41/Ret));*/
  Tao=MAX(C_K(c,t)/C_D(c,t),6*sqrt(C_MU_L(c,t)/C_D(c,t)));
  con=0.15*C_R(c,t)*Tao;
```

```
  dmatrix[0][0] =con*uu;
  dmatrix[1][1] =con*vv;
  dmatrix[2][2] =con*ww;
  dmatrix[1][0] =con*uv;
  dmatrix[0][1] =con*uv;
  dmatrix[2][0] =con*uw;
  dmatrix[0][2] =con*uw;
  dmatrix[2][1] =con*vw;
  dmatrix[1][2] =con*vw;
}

DEFINE_SOURCE(source_UDS0,c,t,dS,eqn)
{
  real source;
  source =-
(C_UDSI_G(c,t,1)[0]+C_UDSI_G(c,t,2)[1]+C_UDSI_G(c,t,3)[2]);
  dS[eqn] = 0.;
 return source;
}

DEFINE_SOURCE(source_UDS1,c,t,dS,eqn)
{
  real source;
  real uu, vv, ww, uv, uw, vw, vu, wu, wv;
  real T1, T2, T3;
  uu=C_RUU(c,t);
  vv=C_RVV(c,t);
  ww=C_RWW(c,t);
  uv=C_RUV(c,t);
  uw=C_RUW(c,t);
  vw=C_RVW(c,t);
/*  Visc=-1*C_MU_T(c,t)/C_R(c,t);
  uu=Visc*2.*C_DUDX(c,t)+(2./3.)*C_K(c,t);
  vv=Visc*2.*C_DVDY(c,t)+(2./3.)*C_K(c,t);
  ww=Visc*2.*C_DWDZ(c,t)+(2./3.)*C_K(c,t);
  uv=Visc*(C_DUDY(c,t)+ C_DVDX(c,t));
  uw=Visc*(C_DUDZ(c,t)+ C_DWDX(c,t));
  vw=Visc*(C_DVDZ(c,t)+ C_DWDY(c,t));*/
  vu=uv;
  wu=uw;
  wv=vw;
T1=uu*C_UDSI_G(c,t,0)[0]+uv*C_UDSI_G(c,t,0)[1]+uw*C_UDSI_G(c,t,0)[2]
;
T2=0.45*(C_UDSI(c,t,1)*C_U_G(c,t)[0]+C_UDSI(c,t,2)*C_U_G(c,t)[1]+C_U
DSI(c,t,3)*C_U_G(c,t)[2]);
  T3=3.5*C_UDSI(c,t,1)*C_D(c,t)/C_K(c,t);
  source =-T1-T2-T3;
  dS[eqn] = -0.45*C_U_G(c,t)[0]-3.5*C_D(c,t)/C_K(c,t);
 return source;
}

DEFINE_SOURCE(source_UDS2,c,t,dS,eqn)
{
  real source;
  real uu, vv, ww, uv, uw, vw, vu, wu, wv;
  real T1, T2, T3;
  uu=C_RUU(c,t);
  vv=C_RVV(c,t);
  ww=C_RWW(c,t);
  uv=C_RUV(c,t);
  uw=C_RUW(c,t);
```

```
  vw=C_RVW(c,t);
/*  Visc=-1*C_MU_T(c,t)/C_R(c,t);
  uu=Visc*2.*C_DUDX(c,t)+(2./3.)*C_K(c,t);
  vv=Visc*2.*C_DVDY(c,t)+(2./3.)*C_K(c,t);
  ww=Visc*2.*C_DWDZ(c,t)+(2./3.)*C_K(c,t);
  uv=Visc*(C_DUDY(c,t)+ C_DVDX(c,t));
  uw=Visc*(C_DUDZ(c,t)+ C_DWDX(c,t));
  vw=Visc*(C_DVDZ(c,t)+ C_DWDY(c,t));*/
  vu=uv;
  wu=uw;
  wv=vw;
T1=vu*C_UDSI_G(c,t,0)[0]+vv*C_UDSI_G(c,t,0)[1]+vw*C_UDSI_G(c,t,0)[2]
;
T2=0.45*(C_UDSI(c,t,1)*C_V_G(c,t)[0]+C_UDSI(c,t,2)*C_V_G(c,t)[1]+C_U
DSI(c,t,3)*C_V_G(c,t)[2]);
  T3=3.5*C_UDSI(c,t,2)*C_D(c,t)/C_K(c,t);
  source =-T1-T2-T3;
  dS[eqn] = -0.45*C_V_G(c,t)[1]-3.5*C_D(c,t)/C_K(c,t);
 return source;
}

DEFINE_SOURCE(source_UDS3,c,t,dS,eqn)
{
  real source;
  real uu, vv, ww, uv, uw, vw, vu, wu, wv;
  real T1, T2, T3;
  uu=C_RUU(c,t);
  vv=C_RVV(c,t);
  ww=C_RWW(c,t);
  uv=C_RUV(c,t);
  uw=C_RUW(c,t);
  vw=C_RVW(c,t);
/*  Visc=-1*C_MU_T(c,t)/C_R(c,t);
  uu=Visc*2.*C_DUDX(c,t)+(2./3.)*C_K(c,t);
  vv=Visc*2.*C_DVDY(c,t)+(2./3.)*C_K(c,t);
  ww=Visc*2.*C_DWDZ(c,t)+(2./3.)*C_K(c,t);
  uv=Visc*(C_DUDY(c,t)+ C_DVDX(c,t));
  uw=Visc*(C_DUDZ(c,t)+ C_DWDX(c,t));
  vw=Visc*(C_DVDZ(c,t)+ C_DWDY(c,t));*/
  vu=uv;
  wu=uw;
  wv=vw;
T1=wu*C_UDSI_G(c,t,0)[0]+wv*C_UDSI_G(c,t,0)[1]+ww*C_UDSI_G(c,t,0)[2]
;
T2=0.45*(C_UDSI(c,t,1)*C_W_G(c,t)[0]+C_UDSI(c,t,2)*C_W_G(c,t)[1]+C_U
DSI(c,t,3)*C_W_G(c,t)[2]);
  T3=3.5*C_UDSI(c,t,3)*C_D(c,t)/C_K(c,t);
  source =-T1-T2-T3;
  dS[eqn] = -0.45*C_W_G(c,t)[2]-3.5*C_D(c,t)/C_K(c,t);
 return source;
}

DEFINE_SOURCE(source_UDS4,c,t,dS,eqn)
{
  real source;
  real uu, vv, ww, uv, uw, vw, vu, wu, wv;
  real T1, T2, R;
  uu=C_RUU(c,t);
  vv=C_RVV(c,t);
  ww=C_RWW(c,t);
  uv=C_RUV(c,t);
```

```
  uw=C_RUW(c,t);
  vw=C_RVW(c,t);
/*Visc=-1*C_MU_T(c,t)/C_R(c,t);
  uu=Visc*2.*C_DUDX(c,t)+(2./3.)*C_K(c,t);
  vv=Visc*2.*C_DVDY(c,t)+(2./3.)*C_K(c,t);
  ww=Visc*2.*C_DWDZ(c,t)+(2./3.)*C_K(c,t);
  uv=Visc*(C_DUDY(c,t)+ C_DVDX(c,t));
  uw=Visc*(C_DUDZ(c,t)+ C_DWDX(c,t));
  vw=Visc*(C_DVDZ(c,t)+ C_DWDY(c,t));*/
  vu=uv;
  wu=uw;
  wv=vw;
  R=0.5;
T1=-
2*(C_UDSI(c,t,1)*C_UDSI_G(c,t,0)[0]+C_UDSI(c,t,2)*C_UDSI_G(c,t,0)[1]
+C_UDSI(c,t,3)*C_UDSI_G(c,t,0)[2]);
  T2=(-C_D(c,t)/(2*R*2*C_K(c,t)))*C_UDSI(c,t,4);
  source =T1+T2;
  dS[eqn] = -C_D(c,t)/(2*R*2*C_K(c,t));
 return source;
}

DEFINE_ANISOTROPIC_DIFFUSIVITY(diff_GGDH_Variance,c,t,i,dmatrix)
{
  real con, Visc, Tao; /* fmu, Rek, Ret;*/
  real uu, vv, ww, uv, uw, vw, vu, wu, wv;
  uu=C_RUU(c,t);
  vv=C_RVV(c,t);
  ww=C_RWW(c,t);
  uv=C_RUV(c,t);
  uw=C_RUW(c,t);
  vw=C_RVW(c,t);
  vu=uv;
  wu=uw;
  wv=vw;
  Tao=MAX(C_K(c,t)/C_D(c,t),6*sqrt(C_MU_L(c,t)/C_D(c,t)));
  con=0.2*C_R(c,t)*Tao;
  dmatrix[0][0] =con*uu;
  dmatrix[1][1] =con*vv;
  dmatrix[2][2] =con*ww;
  dmatrix[1][0] =con*uv;
  dmatrix[0][1] =con*uv;
  dmatrix[2][0] =con*uw;
  dmatrix[0][2] =con*uw;
  dmatrix[2][1] =con*vw;
  dmatrix[1][2] =con*vw;
}
```

D.4 Code Profile.c

```
#include "udf.h"
DEFINE_PROFILE(inlet_u,thread,nv)
{
  face_t f;
  real x[ND_ND];
  /* loop over each of the faces of this zone */
  begin_f_loop (f,thread)
    {
      F_CENTROID(x,f,thread);
      {
```

```
F_PROFILE(f,thread,nv)=(0.068716405/0.4187)*log((x[2]+0.0165)/0.0165
);
      }
    }
  end_f_loop (f,thread)
    }
DEFINE_PROFILE(inlet_v,thread,nv)
{
  face_t f;
  real x[ND_ND];

  /* loop over each of the faces of this zone */
  begin_f_loop (f,thread)
    {
      F_CENTROID(x,f,thread);
      {
          F_PROFILE(f,thread,nv) = 0.;
      }
    }
  end_f_loop (f,thread)
    }
DEFINE_PROFILE(inlet_w,thread,nv)
{
  face_t f;
  real x[ND_ND];

  /* loop over each of the faces of this zone */
  begin_f_loop (f,thread)
    {
      F_CENTROID(x,f,thread);
      {
          F_PROFILE(f,thread,nv) = 0.;
      }
    }
  end_f_loop (f,thread)
    }
DEFINE_PROFILE(inlet_uu,thread,nv)
{
  face_t f;
  real x[ND_ND];

  /* loop over each of the faces of this zone */
  begin_f_loop (f,thread)
    {
      F_CENTROID(x,f,thread);
      {
          F_PROFILE(f,thread,nv) =0.15*0.15;
      }
    }
  end_f_loop (f,thread)
    }
DEFINE_PROFILE(inlet_vv,thread,nv)
{
  face_t f;
  real x[ND_ND];

  /* loop over each of the faces of this zone */
  begin_f_loop (f,thread)
    {
      F_CENTROID(x,f,thread);
```

```
      {
          F_PROFILE(f,thread,nv) = 0.128*0.128;
      }
    }
  end_f_loop (f,thread)
    }
DEFINE_PROFILE(inlet_ww,thread,nv)
{
  face_t f;
  real x[ND_ND];
  /* loop over each of the faces of this zone */
  begin_f_loop (f,thread)
    {
      F_CENTROID(x,f,thread);
      {
          F_PROFILE(f,thread,nv) = 0.096*0.096;
      }
    }
  end_f_loop (f,thread)
    }
DEFINE_PROFILE(inlet_uv,thread,nv)
{
  face_t f;
  real x[ND_ND];

  /* loop over each of the faces of this zone */
  begin_f_loop (f,thread)
    {
      F_CENTROID(x,f,thread);
      {
          F_PROFILE(f,thread,nv) = 0.0;
      }
    }
  end_f_loop (f,thread)
    }
DEFINE_PROFILE(inlet_uw,thread,nv)
{
  face_t f;
  real x[ND_ND];

  /* loop over each of the faces of this zone */
  begin_f_loop (f,thread)
    {
      F_CENTROID(x,f,thread);
      {
          F_PROFILE(f,thread,nv) =-0.00472;
      }
    }
  end_f_loop (f,thread)
    }
DEFINE_PROFILE(inlet_vw,thread,nv)
{
  face_t f;
  real x[ND_ND];

  /* loop over each of the faces of this zone */
  begin_f_loop (f,thread)
    {
      F_CENTROID(x,f,thread);
      {
          F_PROFILE(f,thread,nv) = 0.0;
```

```
      }
    }
  end_f_loop (f,thread)
    }
DEFINE_PROFILE(inlet_k, thread, nv)
{
  face_t f;
  real x[ND_ND], uu, vv, ww;

  /* loop over each of the faces of this zone */
  begin_f_loop (f,thread)
    {
      uu=0.15*0.15;
      vv=0.128*0.128;
      ww=0.096*0.096;
      F_PROFILE(f,thread,nv)=0.5*sqrt(uu+vv+ww);
    }
  end_f_loop (f,thread)
    }
DEFINE_PROFILE(inlet_eps, thread, nv)
{
  face_t f;
  real x[ND_ND], uu, vv, ww;
    /* loop over each of the faces of this zone */
      uu=0.15*0.15;
      vv=0.128*0.128;
      ww=0.096*0.096;
  begin_f_loop (f,thread)
    {
      F_CENTROID(x,f,thread);
          F_PROFILE(f,thread,nv) =
pow(uu+vv+ww,1.5)/pow(0.09,0.75)/0.4187/(x[2]+0.0165) ;
    }
  end_f_loop (f,thread)
    }
DEFINE_PROFILE(bottom_ks, t, i)
{
  real x1, x2, x[ND_ND];
  face_t f;

  begin_f_loop(f, t)
    {
      F_CENTROID(x,f,t);
      x1 = x[0];
      x2 = x[1];
      if (x1 < -76.05 && (x1 * x1 + x2 * x2) > 17226.5625)
        {
          F_PROFILE(f,t,i) = 0.1615845;
        }
      else
        {
          F_PROFILE(f,t,i) = 0.;
        }
    }
  end_f_loop(f, t)
}
```